Universitat Politècnica de València
I.U.I. CMT - Clean Mobility & Thermofluids

Doctoral Thesis

A comprehensive modeling toolchain for particle emissions in GDI engines.

Presented by:
Rami Abboud

Supervised by:
Prof. Raúl Payri
and
Prof. José Javier López Sánchez

in fulfillment of the requirements for the degree of
Doctor of Philosophy
Ph.D. program in Propulsion Systems for Transport
Valencia, July 2024

Ph.D. Thesis

A comprehensive modeling toolchain for particle emissions in GDI engines.

Written by: Mr. Rami Abboud
Supervised by: Prof. Raúl Payri
and
Prof. José Javier López Sánchez

Examination committee:

Chairman: Dr. José María García Oliver
Secretary: Dr. María del Pilar Dorado Pérez
Member: Dr. Dario Di Maio

Reviewing board:

Dr. Dario Di Maio
Dr. Christine Mounaïm-Rousselle

Valencia, July 2024

Abstract

Soot formation in gasoline direct injection engines is governed by complex interactions among physical processes, which vary depending on the engine operating mode. With the implementation of increasingly stringent regulations and more rigorous testing standards, the challenge of meeting particle emission limits has become exceptionally demanding. Consequently, manufacturers have resorted to post-engine outlet particle treatment methods, such as gasoline particulate filters, albeit at the expense of engine performance and fuel consumption. Moreover, there is a growing concern regarding environmental air quality due to vehicle particle emissions, with studies indicating potential cancerous risks to human health.

Modeling tools offer the benefit of diminishing the need for expensive experimental calibration campaigns aimed at finding the optimal strategy for mitigating particle emissions within acceptable limits. In this Thesis, a comprehensive modeling framework is developed that addresses three primary sources of soot formation: inadequate mixing resulting in rich pockets, fuel films on injector tips, and fuel films on combustion chamber walls due to spray impingement. By incorporating physical sub-models to address these pathways of soot formation, a comprehensive depiction of the particle size distribution becomes achievable, considering that the various sources contribute differently to overall particle emissions. Particle number, mass, and size are determined through the utilization of a detailed reaction mechanism to solve the chemical reactions occurring in rich regions defined by the multi-zone model that is integrated with a stochastic particle solver. The approach was complemented by non-reactive 3D CFD simulations to validate the formulations of the various sub-models associated with different pathways. Experimental measurements conducted on an engine test bench were then utilized to evaluate the model predictions and also served as a validation tool for certain sub-models in cases where ambiguity arose in the 3D CFD simulations. Furthermore, optical engine experiments conducted on a different engine from the one considered in this study were employed to gain further insights into the in-cylinder phenomena driving soot formation.

The modeling tool has demonstrated its capability to accurately predict the particle size distribution across various operating conditions, effectively capturing changes in engine parameter settings and thermodynamic conditions. The primary sources contributing to particle emissions stemmed from diminished mixture quality, particularly evident at higher loads due to fuel enrichment, and injector tip wetting, which manifested across all conditions. Therefore, the mixing model, based on pertinent mixing parameters proved

effective in generating equivalence ratio distributions, while the injector film evaporation model computed fuel film mass on the injector tip in a commendable way. By integrating these aspects with a thorough post-processing approach, incorporating particle counting efficiency and exhaust volume considerations, a high degree of agreement was achieved between numerical predictions and measured particle data. As a result, the tool can be leveraged to simulate particle emissions under transient driving conditions, thereby facilitating engine development in the foreseeable future.

Resumen

La formación de hollín en los motores de inyección directa de gasolina se rige por complejas interacciones entre procesos físicos, que varían en función del modo de funcionamiento del motor. Con la aplicación de normativas cada vez más estrictas, junto con ensayos de homologación más rigurosos, el reto de cumplir los límites de emisión de partículas se ha vuelto excepcionalmente exigente. En consecuencia, los fabricantes han recurrido a métodos de post-tratamiento de partículas a la salida del motor, como los filtros de partículas de gasolina, aunque a costa del rendimiento del motor y del consumo de combustible. Además, existe una creciente preocupación por la calidad del aire ambiente debido a las emisiones de partículas de los vehículos, con estudios que indican potenciales riesgos cancerígenos para la salud humana.

Las herramientas de modelización ofrecen la ventaja de disminuir la necesidad de costosos ensayos de calibración experimental destinados a encontrar la estrategia óptima para mitigar las emisiones de partículas dentro de unos límites aceptables. En esta Tesis, se desarrolla un marco de modelización exhaustivo que aborda tres fuentes principales de formación de hollín: la mezcla inadecuada que da lugar a zonas ricas, las películas de combustible en las puntas de los inyectores y las películas de combustible en las paredes de la cámara de combustión debido al impacto del chorro. Al incorporar submodelos físicos para abordar estas vías de formación de hollín, se consigue una descripción completa de la distribución del tamaño de las partículas, teniendo en cuenta que las distintas fuentes contribuyen de forma diferente a las emisiones totales de partículas. El número, la masa y el tamaño de las partículas se determinan mediante la utilización de un mecanismo de reacción detallado para resolver las reacciones químicas que se producen en las regiones ricas definidas por el modelo multizona que se integra con un solucionador estocástico de partículas. El enfoque se complementó con simulaciones CFD tridimensional no reactivo para validar las formulaciones de los diversos submodelos asociados a las distintas vías. A continuación, se utilizaron ensayos experimentales realizados en un banco de pruebas de motores para evaluar las predicciones del modelo y también sirvieron como herramienta de validación para determinados submodelos en los casos en los que surgían ambigüedades en las simulaciones CFD. Además, se utilizaron ensayos ópticos realizados en un motor distinto del considerado en este estudio para obtener más información sobre los fenómenos en el cilindro que conducen a la formación de hollín.

La herramienta de modelización ha demostrado su capacidad para predecir con exactitud la distribución del tamaño de las partículas en distintas condiciones de funcionamiento, captando eficazmente los cambios en la con-

figuración de los parámetros del motor y las condiciones termodinámicas. Se identificó que las principales fuentes que contribuían a las emisiones de partículas procedían de la disminución de la calidad de la mezcla, especialmente evidente en cargas más elevadas debido al enriquecimiento del combustible, y de la humectación de la punta del inyector, que se manifestaba en todas las condiciones. Por consiguiente, el modelo de mezcla, basado en los parámetros de mezcla pertinentes, resultó eficaz para generar distribuciones de dosados, mientras que el modelo de evaporación de la película del inyector calculó la masa de la película de combustible en la punta de forma satisfactoria. Al integrar estos aspectos con un enfoque de postprocesamiento exhaustivo, que incorpora la eficiencia del recuento de partículas y consideraciones sobre el volumen de escape, se logró un alto grado de concordancia entre las predicciones numéricas y los datos de partículas medidos. Como resultado, la herramienta puede aprovecharse para simular las emisiones de partículas en condiciones transitorias de conducción, facilitando así el desarrollo de motores en el futuro próximo.

Resum

La formació de sutge en els motors d'injecció directa de gasolina es regeix per complexes interaccions entre processos físics, que varien en funció de la manera de funcionament del motor. Amb l'aplicació de reglaments cada vegada més estrictes i normes d'assaig més rigoroses, el repte de complir els límits d'emissió de partícules s'ha tornat excepcionalment exigent. En conseqüència, els fabricants han recorregut a mètodes de tractament de partícules posteriors a l'eixida del motor, com els filtres de partícules de gasolina, encara que a costa del rendiment del motor i del consum de combustible. A més, existeix una creixent preocupació per la qualitat de l'aire ambient degut a les emissions de partícules dels vehicles, amb estudis que indiquen riscos cancerígens potencials per a la salut humana.

Les eines de modelització ofereixen l'avantatge de disminuir la necessitat de costosos assajos de calibratge experimental destinats a trobar l'estratègia òptima per a mitigar les emissions de partícules dins d'uns límits acceptables. En aquesta Tesi, es desenvolupa un marc de modelització exhaustiu que aborda tres fonts principals de formació de sutge: la mescla inadequada que dona lloc a zones riques, les pel · lícules de combustible en les puntes dels injectors i les pel · lícules de combustible en les parets de la cambra de combustió a causa de l'impacte del doll. En incorporar submodels físics per a abordar aquestes vies de formació de sutge, s'aconsegueix una descripció completa de la distribució de la grandària de les partícules, tenint en compte que les diferents fonts contribueixen de manera diferent a les emissions totals de partícules. El número, la massa i la grandària de les partícules es determinen mitjançant la utilització d'un mecanisme de reacció detallat per a resoldre les reaccions químiques que es produeixen a les regions riques definides pel model multizona que s'integra amb un solucionador estocàstic de partícules. L'enfocament es va complementar amb simulacions CFD tridimensional no reactiu per a validar les formulacions dels diversos submodels associats a les diferents vies. A continuació, es van utilitzar assajos experimentals realitzats en un banc de proves de motors per a avaluar les prediccions del model i també van servir com a eina de validació per a determinats submodels en els casos en els quals sorgien ambigüitats en les simulacions CFD. A més, es van utilitzar assajos òptics realitzats en un motor diferent del considerat en aquest estudi per a obtenir més informació sobre els fenòmens en el cilindre que condueixen a la formació de sutge.

L'eina de modelització ha demostrat la seua capacitat per a predir amb exactitud la distribució de la grandària de les partícules en diferents condicions de funcionament, captant eficaçment els canvis en la configuració dels

paràmetres del motor i les condicions termodinàmiques. Es va identificar que les principals fonts que contribuïen a les emissions de partícules procedien de la disminució de la qualitat de la mescla, especialment evident en càrregues més elevades a causa de l'enriquiment del combustible, i de la humectació de la punta de l'injector, que es manifestava en totes les condicions. Per consegüent, el model de mescla, basat en els paràmetres de mescla pertinents, va resultar eficaç per a generar distribucions de dosatges, mentre que el model d'evaporació de la pel · lícula de l'injector va calcular la massa de la pel · lícula de combustible en la punta de manera satisfactòria. En integrar aquests aspectes amb un enfocament de postprocessament exhaustiu, que incorpora l'eficiència del recompte de partícules i consideracions sobre el volum de fuita, es va aconseguir un alt grau de concordança entre les prediccions numèriques i les dades de partícules mesurades. Com a resultat, l'eina pot aprofitar-se per a simular les emissions de partícules en condicions transitòries de conducció, facilitant així el desenvolupament de motors en el futur pròxim.

"We are limited, not by our abilities, but by our vision."
- Gibran Khalil Gibran

For my beloved family and the love of my life.

Acknowledgements

This research work has been conducted at CMT – Clean Mobility & Thermofluids of Universitat Politècnica de València, Spain. The funding of this work was provided by Ministerio de Universidades through Ayudas para la formación de profesorado universitario (FPU) grant with reference FPU19/03838. Furthermore, I would like to express gratitude to the ministry for their support, notably through the Ayudas Complementarias de Movilidad grant, which facilitated my three-month research stay at the Combustion Research Facility in Sandia National Laboratories. Their contribution has been integral to the realization of this work.

I want to express my heartfelt appreciation to Professor Raul Payri for granting me the opportunity to partake in research endeavors and pursue a doctoral degree at CMT – Clean Mobility & Thermofluids. His invaluable guidance has been pivotal in advancing the progress of my thesis work, particularly in navigating and overcoming challenges inherent to the process. Additionally, his confidence in me has empowered me to explore new problem-solving approaches, significantly influencing my growth as a researcher. My co-supervisor, Professor J. Javier López, merits equal acknowledgment for our extensive and productive discussions. These interactions have been instrumental in forming the methodologies applied throughout each phase of my thesis work. Furthermore, Professor López has consistently encouraged me to explore innovative approaches to tackle challenges and find practical solutions for various issues. I can also state with confidence that my relationship with him has evolved into that of both a supervisor and a friend. This dynamic has been a source of motivation, pushing me to continuously surpass my boundaries.

During my years spent at CMT – Clean Mobility & Thermofluids, I have consistently received unwavering support from the research staff and technicians whenever it was required. Their assistance during moments of doubt and uncertainty has fostered a positive environment wherein I have never felt isolated. To my fellow doctoral students and esteemed doctors, Victor, Cesar, Sebastian, Tomas, Abian, and Maria, your camaraderie has transformed our workplace into a second home for me. This sense of tranquility has significantly enhanced my thought process throughout my journey. Jose Enrique and Omar, many thanks for your support and guidance at the injection laboratory where I have spent countless hours performing experimental measurements. Additionally, special recognition goes to Omar, as our discussions during my time in the laboratory has significantly improved my Spanish-speaking abilities, thereby enhancing my overall experience at CMT – Clean Mobility & Thermofluids and in Spain. Additionally, the efforts and support from fellow

doctoral student Jiawei Cao in the 1D spray modeling is appreciated. I would also like to extend special thanks to my colleagues Brayan, Rodrigo, Alexandra, Daiana, Francisco, and Oscar, who created an enjoyable atmosphere both in and out of the workplace. Our Friday after-work beach volleyball sessions and occasional outings were truly delightful. All in all, I extend my gratitude to everyone who, in one way or another, contributed directly or indirectly to the development of this work, whether through technical support or by creating a conducive environment for conducting research.

I would also like to thank those who facilitated my incorporation into the Combustion Research Facility at Sandia National Laboratories for my internship. Magnus, thank you for considering me as a candidate for the research stay; our scientific exchanges at the office have been enlightening. I am also grateful to Managers Paul and Isaac, whose unwavering support made the internship possible, and I appreciate your efforts to make me feel part of the research team at Sandia. Furthermore, I owe much gratitude to Eshan, who was an excellent mentor and, I am happy to say, a friend with whom I spent numerous hours conducting experiments and exchanging ideas during my three months at Sandia. Additionally, I would like to thank Dario for his supervision during the final month of my internship, providing me with the opportunity to perform measurements relevant to my thesis work. Overall, my experience at Sandia has been truly unique, and the researchers' approach to science is exemplary and educational.

Finally, I express my deepest gratitude to those who have influenced the individual I have become. To Christelle, my partner and the love of my life, your resolute support throughout my Ph.D. journey, through both challenging times and moments of joy, has been instrumental in helping me pursue and achieve not only my personal ambitions but now, our shared aspirations. To my parents, whose unwavering belief in me and provision of the necessary tools and freedom to chase my dreams have been unbounded. I look up to you both in every decision I make. To my brother Rayan and sister Lea, thank you for being the greatest siblings one could hope for. It is the support of my family that fuels my motivation and ambition, driving me forward in this wonderful journey called life.

Contents

List of Figures

List of Tables

Nomenclature

Acronyms

0D	Zero-dimensional.
1D	One-dimensional.
3D	Three-dimensional.
A_1	First aromatic ring.
A_4	Fourth aromatic ring.
A_7	Seventh aromatic ring.
AMR	Adaptive Mesh Refinement.
APC	AVL Particle Counter.
aTDC	After Top Dead Center.
BEV	Battery Electric Vehicle.
bTDC	Before Top Dead Center.
C/O	Carbon/Oxygen.
CAD	Crank angle degrees.
CFD	Computational Fluid Dynamics.
CNG	Compressed Natural Gas.
CPC	Condensation Particle Counter.
CQMOM	Conditional Quadrature Method of Moments.
DDM	Discrete Droplet Method.
DR	Dilution ratio.
ECQMOM	Extended Conditional Quadrature Method of Moments.
ED	Ejector Diluter.

EGR	Exhaust Gas Recirculation.
EOI	End of Injection.
EPA	Environmental Protection Agency.
EQMOM	Extended Quadrature Method of Moments.
EU	European Union.
EVO	Exhaust Valve Opening.
GDI	Gasoline Direct Injection.
GDP	Gross Domestic Product.
GPF	Gasoline Particulate Filter.
H/C	Hydrogen/Carbon.
HCCI	Homogenous Charge Compression Ignition.
HMOM	Hybrid Method of Moments.
HO	High olefin.
ICE	Internal Combustion Engine.
IEA	International Energy Agency.
$IMEP_n$	Net Indicated Mean Effective Pressure.
ISF	Insoluble Fraction.
IVC	Intake Valve Closure.
LIF	Laser-Induced Fluorescence.
LLNL	Lawrence Livermore National Laboratories.
MAC	Methynal Addition Cyclization.
MOMIC	Method of Moments with Interpolative Closure.
MSS	Micro-Soot Sensor.
PAH	Polycyclic Aromatic Hydrocarbons.
PCCI	Premixed Charge Compression Ignition.
PFI	Port Fuel Injection.
PID	Proportional Integral Derivative.
PISO	Pressure Implicit with Splitting of Operators.
PMI	Particulate Matter Index.
PN	Particle number.
PRF	Primary Reference Fuel.
PSDF	Particle Size Distribution Function.
PSD	Particle Size Distribution.
PSR	Perfectly-Stirred Reactor.

PTD	Porous Tube Diluter.
QMOM	Quadrature Method of Moments.
RANS	Reynolds-Averaged Navier Stokes.
RIM	Refractive Index Matching.
RNG	Re-normalized Group.
ROHR	Rate of Heat Release.
ROI	Region of Interest.
RON	Research Octane Number.
SMD	Sauter Mean Diameter.
SOC	Start of Combustion.
SOF	Soluble Organic Fraction.
$\mathrm{SoI_e}$	Electrical Start of Injection.
SOI	Start of Injection.
SRM	Stochastic Reactor Model.
SVOC	Semivolatile Organic Compound.
TEM	Transmission Electron Microscopy.
TSI	Threshold Soot Index.
TWC	Three-Way Catalyst.
VVT	Variable Valve Timing.
WLTP	World Harmonized Light Duty Test Procedure.

Greek symbols

α	Convective heat transfer coefficient.
δ_v	Vapor cushion thickness.
$\dot{\omega}$	Net chemical production rate.
λ_g	Gas thermal conductivity.
ν	Kinematic viscosity.
ϕ	Equivalence ratio (general).
ρ	Density.
σ	Surface tension.
τ_{mix}	Mixing time.

Latin symbols

$(A/F)_{st}$	Stoichiometric air-to-fuel ratio.
$\bar{h}$	Average thickness.

$\bar{m}$	Average mass.
$\bar{u}_p$	Mean piston speed.
$\dot{m}$	Mass flow rate.
$\dot{q}$	Heat transfer rate.
$\dot{Q}_d$	Heat flow rate.
$\frac{dY_{f,b}}{dt}$	Burn rate.
Re	Reynolds number.
We	Webers number.
$\triangle H_v$	Latent heat of vaporization.
$\triangle m_{st}$	Injected mass per injection step.
$\triangle p$	Pressure difference.
$\triangle \phi$	Equivalence ratio increment.
A	Area.
B	Bore diameter.
C	Species molar concentration.
c_D	Drag coefficient.
c_p	Specific heat.
CF	Temperature correction factor.
D	Diffusion coefficient.
D_p	Soot particle diameter.
d_{30}	Volume-averaged diameter.
d_{noz}	Nozzle orifice diameter.
E	Objective function error.
F	Correction factor.
f	Multiplication factor.
F_D	Drag force.
f_D	Drag correction factor.
f_v	Soot volume fraction.
FF	Fuel fraction.
G	Droplet distribution function.
I_H	Inhomogeneity index.
k	Thermal conductivity.
L_s	Liquid film thickness.
M	Moment.

m	Mass.
MW	Molecular weight.
N	Particle number density.
N_A	Avogadro's number.
$N_{d,st}$	Droplets per injection step.
n_{zones}	Number of zones exceeding the sooting threshold.
Nu	Nusselt number.
p	Pressure.
Q_r	Moment rate.
Q_{wl}	Heat flux per unit area between wall and liquid in contact.
Q_{wvl}	Heat flux per unit area between wall and liquid through vapor cushion.
R	Universal gas constant.
S	Penetration.
t	Time.
T_L	Leidenfrost temperature.
T_N	Nukiyama temperature.
u	Velocity.
U_{inj}	Injection velocity.
V	Volume.
X	Species molar fraction.
Y	Species mass fraction.

Subscripts

0	Initial.
a	Air.
ad	Adiabatic.
b	Burned.
$berno$	Bernoulli.
c	Critical.
$corr$	Corrected.
cyl	In-cylinder.
D	Drag.
d	Droplet.
e	Electrical.

eq	Equilibrium.
$evap$	Evaporated.
exh	Exhaust.
f	Fuel.
$film$	Fuel film.
g	Gas.
$global$	Global.
i	Species.
inj	Injection.
j	Zone number.
L	Liquid.
lv	Liquid-to-vapor.
mix	Mixing.
n	Normal.
p	Piston.
pyr	Pyrolysis.
r	Moment number.
ref	Reference.
res	Residual gas.
s	Surface.
sat	Saturation.
$soot$	Species production/consumption rates due to soot processes.
st	Step.
th	Thickness.
$thresh$	Threshold.
ub	Unburned.
v	Vapor.
w	Wall.

Chapter 1

Introduction

The internal combustion engine (ICE) has been the beating heart of propulsion technologies over the past century, reshaping societies and economies by bridging distances and linking people on a global scale. It is undeniable that those types of engines have been facing unprecedented scrutiny in the last decade due to growing environmental concerns. In addition to emitting greenhouse gases like carbon dioxide (CO_2) and methane (CH_4), internal combustion engines release other pollutants that adversely affect the local atmosphere and pose health risks to humans. Carbonaceous particles, historically associated with diesel engines, have become a growing concern in gasoline engines with the advent of direct injection technology. They exist as fine and ultrafine particles that can be easily inhaled by humans causing respiratory and cardiovascular complications.

1.1 General context

To provide some context, the global energy industry is grappling with the significant challenge of achieving a net-zero carbon footprint by 2050. This task is further complicated by a growing population [1] and rising Gross Domestic Product (GDP) per capita [2], as illustrated in Figure 1.1. While the adoption of renewable energy, especially in the electricity domain, indicates a decline in carbon intensity (CO_2 emissions per unit of energy), this is counterbalanced by the increasing energy demands of a growing and more affluent population. It's important to note that the presented data shouldn't be viewed as

predictions, since various factors, including geopolitical occurrences and technological innovations, have the potential to alter these trends.

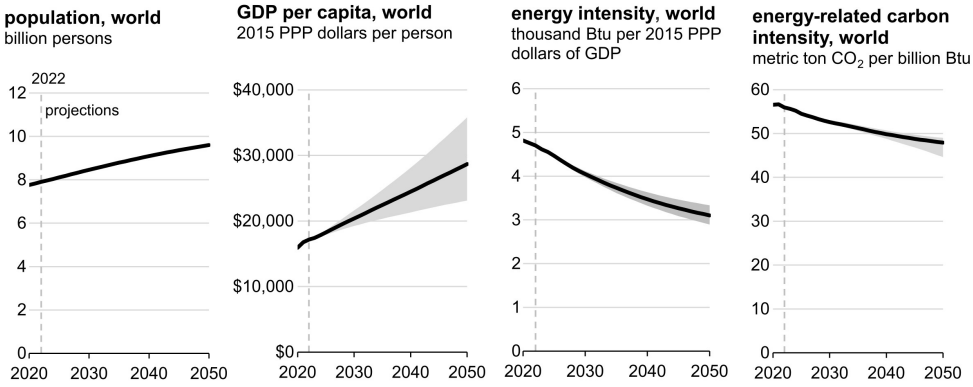

Figure 1.1: Factors driving global energy consumption and energy-related CO_2 emissions: population, average income (per capita GDP), energy intensity (energy per dollar GDP), and carbon intensity (CO_2 emissions per unit of primary energy). [2]

As stated in the 2023 International Energy Agency (IEA) report, by 2050 [2], the transportation sector is expected to account for 25% of the global energy consumption. Within this percentage, vehicles equipped with internal combustion engines (hybrid vehicles included) will still hold a significant share. However, electric vehicle sales are predicted to make up 29% to 54% of worldwide vehicle sales, with the European Union and China leading the charge in BEV adoption, spurred by their respective policies and regulations. Sale shares of BEVs and light duty ICE vehicles are further depicted in Figure 1.2.

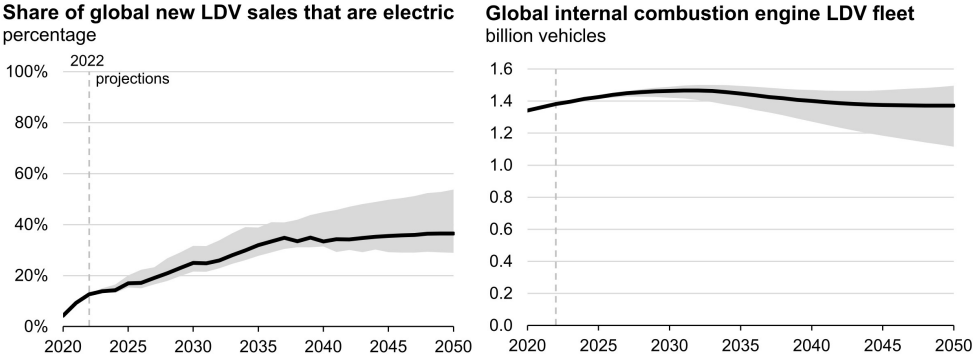

Figure 1.2: Projects for BEVs sale share and share of light duty vehicles with an internal combustion engine on-board. [2]

Reflecting on the previously discussed projections of rising income per capita, a change in transportation modes is also anticipated. As people's financial capacities grow, they lean towards more convenient, albeit less efficient, transportation methods. Figure 1.3 further underscores this trend, showcasing a more pronounced rise in light duty vehicles and air travel as compared to buses. An article published by Enerdata further digs deeper into this trend and evaluates CO_2 emissions from transport by assessing the relative contribution of five factors, namely, transport demand, modal shares, vehicle load factor, energy efficiency of modes, and carbon intensity. It was concluded that progress in energy efficiency and decarbonization is currently insufficient to offset the increase in transport demand, largely due to unfavorable trends in modal shift factor towards the most emitting transportation modes.

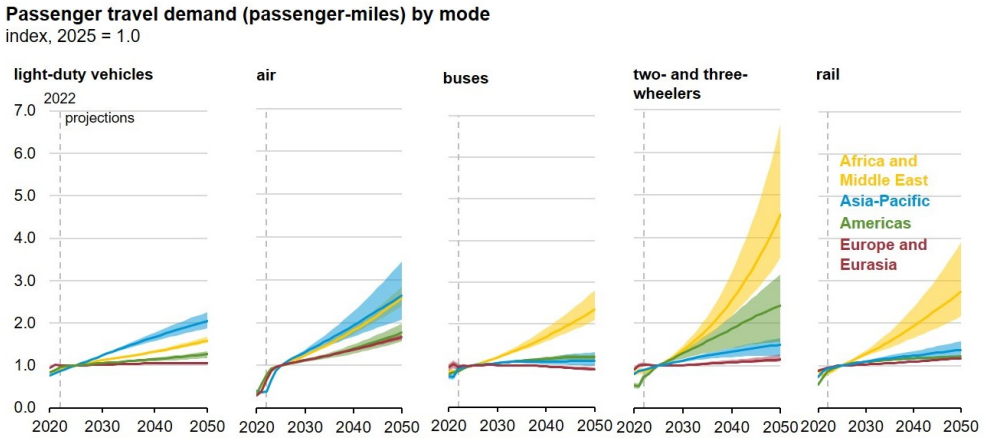

Figure 1.3: Passenger travel demand projections by mode and region [2]

The increasing share of BEVs in the global vehicle market suggests that these vehicles, which emit no tailpipe emissions, might be the key to making the transportation sector more eco-friendly. Current regulations, however, overlook emissions stemming from battery production, end-of-life processes, and critically, the primary energy sources that power these vehicles. To fairly compare the environmental impact of BEVs with that of ICE vehicles, it is essential to employ a life-cycle analysis that captures emissions produced throughout the entirety of a vehicle's lifespan. A study by Burton et al. [3], using 2019 U.S. electricity data, established a method for this comparison, finding that in several scenarios, BEVs resulted in greater greenhouse gas emissions than their HEV counterparts. Though it is true that the foreseeable share of clean electricity, generated majorly from solar and wind, is

expected to grow at high rates in the next 28 years (see Figure 1.4) supplying 54% to 67% of total electricity demand in 2050. This undoubtedly tilts the scales towards BEVs, however, projections also estimate that the share of coal and natural gas in providing that demand would still constitute a noticeable share accounting to 27% to 38%. In the High Economic Growth scenario, there is an increase in natural gas and a more significant growth in renewable energy generation, indicating that renewables become more cost-competitive when addressing higher incremental demand. When oil prices are high, the operational and production costs of natural gas also rise, making it less economically viable compared to other energy sources like renewables. This increased cost can shift investments away from natural gas towards alternative technologies that are less impacted by oil price fluctuations. As a result, the energy capacity in the high oil price scenario falls short of the levels seen in the high economic growth scenario, as higher natural gas prices make it less attractive, prompting the market to favor more cost-effective energy sources. This is also coupled with energy security considerations, particularly the preference for locally available resources such as wind and solar, which drive increased installations and planned projects for these technologies, especially in Europe and China. Additionally, electricity storage capacity, primarily in batteries, is expected to increase significantly from 52 GW to between 625 GW and 1507 GW across various scenarios, further supporting the adoption of renewable sources for electricity generation. It becomes evident that a multifaceted technological approach will be pivotal to effectively cut down the transportation sector's carbon footprint, contingent upon the forthcoming evolution in our energy mix. In light of present data and anticipated future trends, internal combustion engines will maintain a role in achieving a net-zero carbon footprint, especially in less developed regions. Current engine research is gravitating towards renewable fuels with minimal to zero carbon content, like hydrogen, as they could offer a fast route towards decarbonization [4]. This naturally raises the question: which renewable fuel is the most suitable? Given the complexity of this inquiry, there is no straightforward answer, leading to ongoing debate within the research community. The probable scenario entails the utilization of a diverse range of e-fuels, with the choice depending on the specific application and corresponding requirements.

From the regulatory perspective, and in response to increasing worries about environmental health and air quality, regulations for vehicle emissions have become notably more stringent. With the anticipated rollout of Euro 7 in 2025, automakers will be required to meet standards for particle emissions with diameters exceeding 10 nm, down from the 23 nm threshold set by Euro

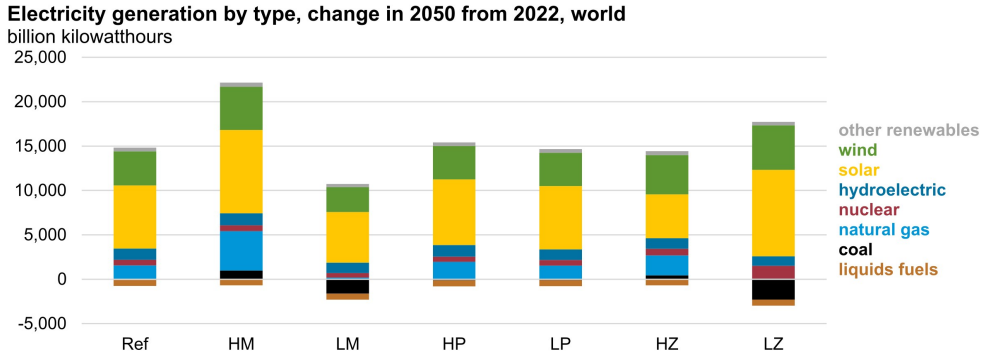

Figure 1.4: Electricity generating capacity of different technologies under different scenarios. Ref=Reference; HM=High Economic Growth; LM=Low Economic Growth; HP=High Oil Price; LP=Low Oil Price; HZ=High Zero-Carbon Technology Cost; LZ=Low Zero-Carbon Technology Cost [2]

6. Figure 1.5 illustrates the evolution of particle number and mass limits for light duty vehicles in the European Union (EU) [5].

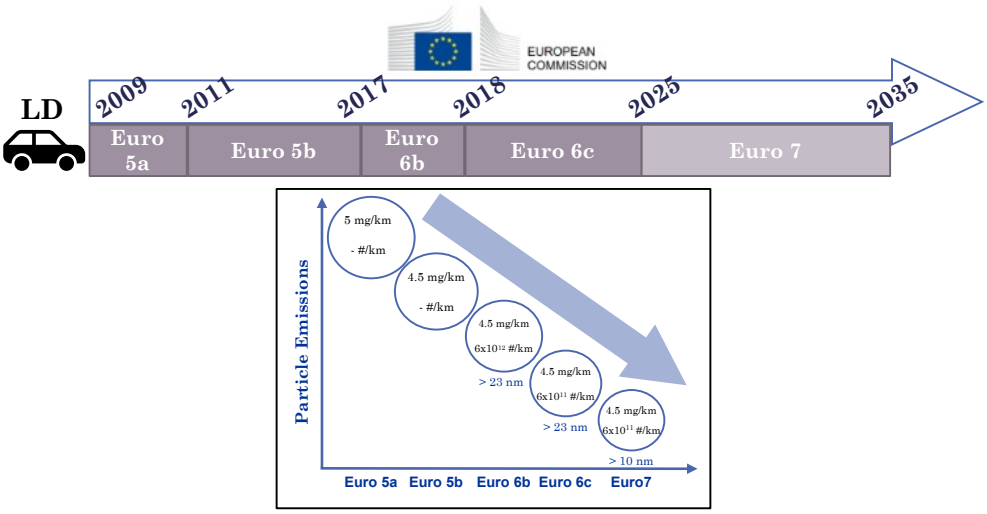

Figure 1.5: European Union particle emissions limits trajectory

The U.S. Environmental Protection Agency's (EPA) proposal for light-duty vehicles for MY2027 and beyond is anticipated to follow a comparable route, reducing particle mass emission limits from 3 mg/mi to 0.5 mg/mi [6]. This change is likely to necessitate the adoption of Gasoline Particulate Filters (GPFs), aligning with standards in the European and Chinese markets.

Alongside tighter regulations, there has been a surge in vehicle electrification ranging from mild hybrid to fully electric vehicles. Consequently, it's evident that engine development complexity is at an unprecedented level, with manufacturers striving to strike the right balance between cost and efficiency.

Amid these challenges, numerical models have traditionally been employed in engine development to cut down on experimental costs and offer insights that are difficult to obtain through measurements. Within the realm of particle emissions, three-dimensional computational fluid dynamics (3D-CFD) stands out as a promising tool for predicting engine-out particle number and mass concentrations [7–9]. However, its high computational demands can limit its applicability in certain applications. A potential alternative is the use of phenomenological and 0D/1D models based on the physical principles that characterize the primary sources of soot formation. Such models could offer a computationally efficient method for gauging the particle emission footprint of Gasoline Direct Injection (GDI) engines [10]. Moreover, they can help assess the effects of engine parameters on emissions and pinpoint strategies to reduce them.

1.2 Thesis objectives

Given the context mentioned earlier, the primary aim of this thesis is to create a detailed, computationally efficient modeling tool targeting soot emissions, with a specific emphasis on three sources: injector tip wetting, gas phase heterogeneity, and spray-wall impingement. The sources examined are limited to fuel combustion, excluding other sources such as lubrication oil. The core goal is to integrate physical models for these three main sources with a stochastic particle dynamics solver to predict particle number, mass concentration, and particle size distributions. This research aims to offer the industry a virtual testing platform for steady-state engine-out particle emissions. Once the model is validated for a specific engine, it can be applied to predict soot levels during transient driving cycles for homologation testing. This advancement will greatly facilitate engine development processes and aid researchers in fine-tuning calibration methods to reduce particle emissions.

Given the complexity of soot formation processes, few numerical studies in existing literature address all the previously mentioned sources. While many research works utilize CFD models, these methods, though detailed and quantitative in their description of complex flow phenomena, pose significant computational demands. Due to these challenges, the primary modeling framework is designed in a 0D environment.

To address the physics of soot formation from wall films and bulk gas, multiple specific objectives have been established:

- **Chemical kinetics exploration:** Focus on implementing a comprehensive chemical kinetic mechanism, emphasizing detailed PAH (Polycyclic Aromatic Hydrocarbons) formation pathways. The chemical mechanism will be integrated with a soot model to consider the impact of soot formation on the concentration of species in the gas phase. This is crucial because particle inception rates are strongly dependent on the inception species concentration, having a squared relationship.
- **Injector tip wetting analysis:** Examine the process of fuel film formation and its subsequent evaporation from the injector tip. An existing analytical evaporation model will be refined to more accurately represent the injector tip wetting behavior based on optical engine experiments.
- **Mixture formation study:** Delve into the mixture formation process to pinpoint rich areas present at the start of combustion (SOC). To achieve this, 1D and empirical approaches will be used to determine the equivalence ratio distribution at SOC.
- **Spray wall-impingement modeling:** Address the critical need for an all-encompassing soot formation model. This involves incorporating submodels in the spray-wall impingement segment to calculate the remnant fuel film mass on combustion chamber surfaces.
- **Comprehensive framework creation:** Demonstrate the primary technological outcome of this research, emphasizing its practical benefits and showcasing how the developed model can aid in future engine advancements.

1.3 Thesis outline

Following the identification of the main set of objectives in this study, the outline of the manuscript is discussed. The manuscript consists of eight chapters. It starts off with an overview of soot fundamentals and sources in GDI engines (Chapter 2) that provides the reader general knowledge on the topic and explains the theoretical aspects of soot formation.

The tools required to achieve the objectives of this research work are then outlined in Chapter 3. The usage of each tool is explained and the interconnection with other tools elaborated in order to familiarize the reader with the

overall framework. Here, the main inputs required by the model in order to compute particle emissions are depicted. Additionally, a brief overview of the experimental campaign and equipment used to measure particle number and mass concentrations are explained.

Chapter 4 then digs into the core of the model where gas phase kinetics and coupling with solid particulate phase are explained. The main considerations and assumptions taken are discussed along with the steps required to associate the chemical kinetics with the soot formation sources accounted for in this study. The post-processing methodology of the numerical results is explained here in detail in order to portray the importance of providing a 1-to-1 comparison between numerical and measured data.

Following the explanation of the main methodology, the following chapters are dedicated to each sub-model corresponding to a soot formation source. This begins with inhomogeneous mixture preparation in Chapter 5. The CFD model is first presented and along with the simulation setup that is used for calibration purposes of the mixing model, although it was also used as input in the preliminary calibration stages of the overall model. The 1D mixing model used to compute the equivalence ratio distribution, the metric used to quantify rich zones above a sooting threshold, is first explained along with the main modifications implemented to account for the assumptions that are inherent to the model. Results of the contribution of mixture induced particle emissions are then contrasted with measured data.

Chapter 6 then explains the framework used to account for injector tip wetting and the consequent particle formation processes resulting from pyrolysis reactions near the tip. Main assumptions and simplifications are explained and in-cylinder optical visualizations are used to specify important parameters affecting injector tip liquid film mass. The results of injector induced particle emissions are then depicted and their contribution summed up with the mixture induced ones. The main differences between two sources on overall particle trends are then explained.

Chapter 7 presents the final considered source of soot formation. It begins with a concise overview of the models employed, which include the spray, wall-interaction, and film evaporation models. The chapter concludes by highlighting key insights regarding the overall particle contribution.

Chapter 8 consolidates the previously constructed segments to convey the complete narrative. Within it, key discoveries are presented and the potential influence of the established modeling framework on forthcoming engine advancements is detailed. The chapter then delineates the framework's limitations, laying the groundwork for subsequent research.

References

[1] United Nations, Department of Economic and Social Affairs, Population Division. *World Population Prospects 2022: Summary of Results*. Tech. rep. 2022.

[2] U.S. Energy Information Administration. *International Energy Outlook 2023*. Tech. rep. 2023.

[3] Burton, T. et al. "A Data-Driven Greenhouse Gas Emission Rate Analysis for Vehicle Comparisons". In: *SAE International Journal of Electrified Vehicles*. Vol. 12. 1. 2022, pp. 91–128. DOI: 10.4271/14-12-01-0006.

[4] Conway, G., Joshi, A., Leach, F., García, A., and Senecal, P. K. "A review of current and future powertrain technologies and trends in 2020". In: *Transportation Engineering* 5.May (2021). DOI: 10.1016/j.treng.2021.100080.

[5] European Commission. *Euro 7 proposal from european commission*. Tech. rep. 2022.

[6] Environmental Protection Agency. *Multi-Pollutant Emissions Standards for Model Years 2027 and Later Light-Duty and Medium-Duty Vehicles*. Tech. rep. 2023.

[7] Del Pecchia, M. et al. "Development of a Sectional Soot Model Based Methodology for the Prediction of Soot Engine-Out Emissions in GDI Units". In: *SAE Technical Papers* 2020-April.April (2020). DOI: 10.4271/2020-01-0239.

[8] Held, F., Reusch, J., Salenbauch, S., and Hasse, C. "A 3D computational study of the formation, growth and oxidation of soot particles in an optically accessible direct-injection spark-ignition engine using quadrature-based methods of moments". In: *Fuel Processing Technology* 254.February 2023 (2024). DOI: 10.1016/j.fuproc.2023.107923.

[9] Wu, S., Zhou, D., and Yang, W. "Implementation of an efficient method of moments for treatment of soot formation and oxidation processes in three-dimensional engine simulations". In: *Applied Energy* 254.July (2019). DOI: 10.1016/j.apenergy.2019.113661.

[10] Frommater, S. "Phenomenological modelling of particulate emissions in direct injection spark ignition engines for driving cycle simulations". PhD thesis. TU Darmstadt, 2018.

Chapter 2

Fundamentals and literature review

This chapter delves into the processes related to soot formation and their underlying principles. It further investigates the variety of particle sources present in GDI engines and highlights their defining features. For a comprehensive understanding, various modeling techniques carried out by previous researchers addressing particle emissions are also touched upon.

2.1 Theoretical aspects of particle formation

Particulate matter is a multifaceted aerosol system, and its chemical composition is composed of solids (predominantly carbon), soluble organic fractions (SOF), and sulfates. Its exact composition is heavily influenced by the engine type, the fuel utilized, operating conditions, and even by the sample method used in the exhaust line. Elemental carbon constitutes what we refer to as soot particles, characterized by intricate aggregated crystallite structures [1–3]. Throughout this document, the term "particle" specifically denotes soot particles composed of elemental carbon.

The general consensus is that soot is formed in sub-stoichiometric regions at high temperatures. The composition of the fuel-oxidizer mixture is critical in defining the onset of soot formation. Several experimental studies have examined the critical C/O ratio for soot formation and its relationship with pressure and temperature [4–6]. Observations showed that this critical ratio

is strongly influenced by temperature, rising as temperature increases, while its dependence on pressure is relatively minimal until the carbon formation limit is reached. Beyond that, soot was observed to increase with increasing pressure [5]. Thus, it can be deduced that soot formation is governed by kinetics rather than being controlled thermodynamically, given that the critical threshold shifts based on the thermodynamic state [7]. Given the significant influence of temperature on the initiation of soot formation, Bohm et al. [8] conducted studies on premixed ethylene-air and benzene-air flames, emphasizing the lower temperature spectrum. Their findings indicated that a minimum temperature of approximately 1600 K was required for consistent soot formation. Additionally, a temperature ceiling near 2000 K was identified, beyond which the oxidation of precursors dominated over nucleation processes. The trends discussed here are depicted in Figure 2.1 and have the typical bell-shaped characteristic discussed in literature.

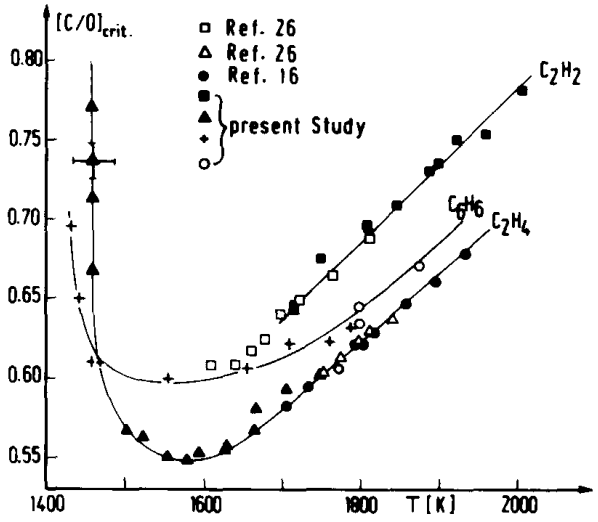

Figure 2.1: Critical sooting C/O ratio of premixed C_2H_2-air, C_6H_6-air, and C_2H_4-air flames versus flame temperature [8] [as cited in [9]]

While the routes to the emergence of initial carbon nuclei may differ based on combustion mode such as premixed or non-premixed flames, and the nature of the fuel, there is a general agreement in the literature about the multistep soot formation process. These steps, which can occur either simultaneously or in sequence, depending on the combustion mode, include: fuel fragmentation known as pyrolysis, formation of precursors, nucleation of soot precursors resulting in the inception of the first soot particle, particle growth via species

deposition on their surface, coagulation of smaller particles into larger aggregates, and oxidation reactions. These steps are further depicted in Figure 2.2. The process depicted further emphasizes the gaseous to solid phase transition and distinguishes between a gas phase molecular zone and a solid phase particle zone. A detailed description of each process is discussed in the following subsections.

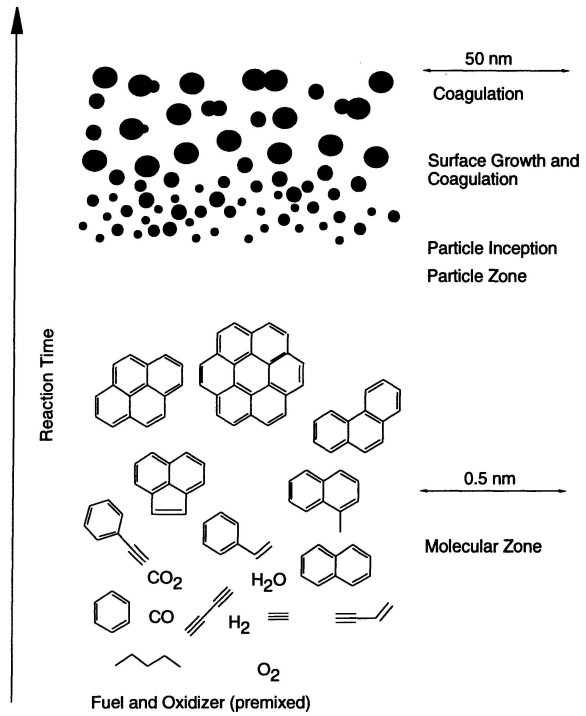

Figure 2.2: Soot formation pathway in premixed flames [9]

2.1.1 Precursor formation

The molecular gas phase soot precursors are believed to be heavy polycyclic aromatic hydrocarbons (PAHs) with a molecular weight ranging from 500-1000 amu [10]. The relative ease of molecular growth towards larger aromatic molecules generally depends on the aromatic content of the fuel, as observed in [5, 11]. Before PAHs are formed, the fuel undergoes decomposition, a process commonly referred to as pyrolysis, in which smaller hydrocarbon fragments are produced, mainly C_2 and C_3. At high temperatures and with little or no oxygen, the fuel breaks down into smaller fragments through thermal cracking and beta scission reactions. These pyrolysis reactions are usually endothermic

meaning that their rates are highly temperature dependent [1]. The radicals that result from such processes then form the first aromatic ring, known as benzene (C_6H_6). The most common pathways leading to the first aromatic ring can be summarized by the following:

- Reaction of vinyl radical (C_2H_3) and 1,3-butadiene (1,3-C_4H_6) accompanied by elimination of hydrogen [12], 1,3-C_4H_6 reaction with C_2 [13] or ethynyl (C_2H) [14]
- Reaction of 1,3-butadienyl radical (1,3-C_4H_5) with acetylene (C_2H_2) followed by hydrogen elimination [15] or ionization reactions between formyl cation (HCO+) and C_2H_2 [14]
- Recombination of propargyl radicals (C_3H_3) [16] or reaction between propargyl and 1,3-butadienyl [17]

Following the formation of the first aromatic ring, further growth to larger polyaromatic molecules begins. Bittner and Howard [18] and Frenklach et al. [15] were amongst the first to conceptualize PAH formation and growth processes. Frenklach and Wang [19] introduced the term "HACA" to describe the PAH formation process. HACA is the acronym for Hydrogen Abstraction Carbon Addition and is the most widely adopted mechanism for molecular growth to PAHs. It is basically a two-step process representing the abstraction of hydrogen and the addition of acetylene (C_2H_2). Figure 2.3 is a schematic of such reaction mechanism which begins with the creation of the first aromatic ring and then grows to the PAH molecule pyrene ($C_{16}H_{10}$) containing four aromatic rings. Radicals were also found to play a role in PAH formation. Through their experiments of toluene/acetone pyrolysis, Shukla et al. [20] highlighted the importance of methyl radicals in the formation of PAHs in which a new formation mechanism, methynal addition cyclization (MAC), was proposed. The process encompasses the addition of a methyl radical to an existing aromatic ring, coupled with hydrogen abstraction, resulting in a stabilized radical. The radical subsequently undergoes cyclization, giving rise to the formation of a new aromatic ring and thereby expanding the size of the system. For a comprehensive review of all the mechanisms involved in the formation of the first aromatic ring and the subsequent growth to PAHs, the reader is referred to the review of Rezeir et al. [21].

2.1.2 Soot Particle Inception

The transition from the molecular gas phase to the solid phase has long perplexed scientists. Experimental investigations in premixed flames have been

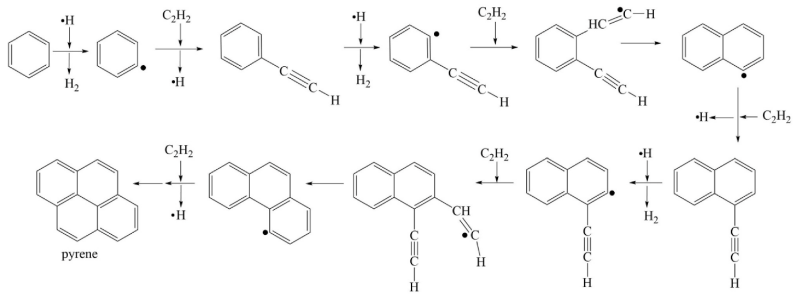

Figure 2.3: Hydrogen abstraction acetylene addition mechanism [21]

restricted to observing soot, since they couldn't detect molecules smaller than soot due to their limited sensitivity. Yet, recent breakthroughs in experimental techniques have allowed researchers to delve deeper into this intricate process. Several pathways towards the creation of nascent soot nanoparticles have been proposed by researchers, the most commonly adopted mechanism being the coalescence of PAH molecules to form stacked clusters which later on grow by surface growth and coagulation [15, 19, 22]. Weiner and Harris [23] optically investigated a premixed ethylene-oxygen-argon sooting flame and observed that PAHs in the 500-1000 amu range were depleted when an increase in soot volume fraction was detected. The authors then concluded that those molecules are being incorporated into incipient soot particles and are thus the precursors of soot. This mechanism has been discussed recently in more detail by D'Anna [24] where a review of chemical and spectroscopic analysis was shown. The findings suggest that small particles, associated to incipient soot particles, may be conceptualized as layered PAH structures originating from PAH dimerization. This mechanism is commonly used in literature to model the nucleation process [25–27]. Thus, it can be asserted that for precise modeling of the initial soot formation stages, a comprehensive kinetic mechanism that includes fuel decomposition and the creation of soot precursors is essential [28].

2.1.3 Surface Growth

Particles formed during the nucleation process typically measure around 2 nm in diameter and only have a marginal contribution to the total soot mass [3]. The bulk of soot mass is then due to surface growth processes that contribute to an overall increase in the particle mass without any change in the number density of particles. The growth process primarily stems from the attachment of gas-phase molecules to the particle surface, with acetylene addition

playing a significant role. Larger polymers tend to deposit more rapidly than their smaller counterparts [29]. Additional processes contributing to surface growth include the condensation of PAHs on the particle surface [5]. However, it was evident that the dehydrogenation of the soot particle is also necessary to explain the typical hydrogen mole fraction of soot particles which is in the 0.1-0.2 range. Hence, a combination of mechanisms attributed to HACA and PAH condensation would then be responsible for surface growth. When this event takes place, the H/C ratio of the particles diminishes until a stable value emerges, as demonstrated in Prado and Lahaye [30]. Their findings highlighted that the ultimate soot volume fraction is predominantly influenced by surface growth. The decrease in H/C ratio further supports the theory of dehydrogenation, or hydrogen abstraction, that occurs along with carbon addition. As particles mature, they exhibit a diminished reactivity to acetylene, a trend evident in older particles. This leads to the stabilization of the H/C ratio, causing it to essentially plateau [1]. Another mechanism contributing to size growth is termed coagulation, however, contrary to surface growth, the total particle mass remains constant. This mechanism is further elaborated in the following section.

2.1.4 Coagulation and agglomeration

When an abundant number of particles are formed in the system, their probability to collide and merge increases. During the early stages, smaller particles coagulate and form spheroids. This process usually occurs simultaneously with surface growth which further contributes to the overall spherical shape of the coalesced particle [1]. This in turn affects the total number density of particles in the system and can be visualized by the trends outlined in Figure 2.4.

Initially, a rapid increase in number density is shown which can be attributed to the nucleation process. During this stage, soot volume fraction remains almost constant, as previously discussed in subsection 2.1.2. When the nucleation process ends, surface growth processes contribute to a growth in soot volume fraction (on the right side of the peak in number density). Coagulation of relatively small particles also contribute to increase in particle diameter. As surface growth declines due to the depletion of gas phase molecules, larger particles colliding result in a chain of spherical particles through a process referred to as aggregation [1]. The overall shape of soot particles now changes and a chain-like structure is created. The primary particles that stick together maintain their spherical geometry [31]. An example of such structure is shown in Figure 2.5.

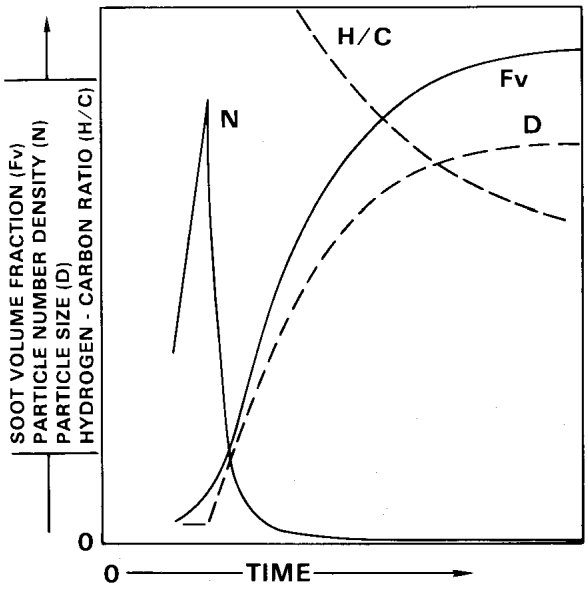

Figure 2.4: Particle number density N, soot volume fraction F_v, particle diameter D, and particle hydrogen/carbon (H/C) ratio trends in a flame [2]

2.1.5 Oxidation

The oxidation process occurs throughout the different particle stages depending on the availability of oxidation species, namely oxygen (O_2) and hydroxil radicals (OH). Under fuel rich conditions in premixed flames, OH is the predominant radical participating in oxidation reactions. Lahaye [33] reported that the oxidation route involving OH is more probable, leading to a more substantial mass reduction and even aggregate destruction, in contrast to oxidation with oxygen.

2.2 Sources of particle emissions in GDI engines

Gasoline direct injection presents multiple benefits compared to port fuel injection (PFI). One such advantage is an enhanced volumetric efficiency, stemming from charge cooling during fuel vaporization. This system also permits higher compression ratios and more advanced spark timing, enhancing overall performance and efficiency. Furthermore, leveraging the scavenging effect with GDI can boost the low-end torque in turbocharged engines. By using variable valve timing (VVT) technology, it not only amplifies performance but also offers fuel economy benefits [34–36]. The drawback, however, is the rise

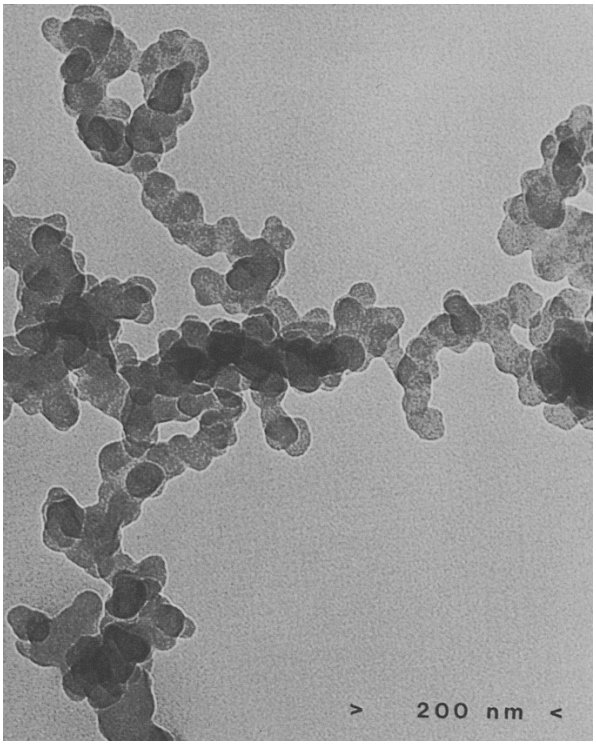

Figure 2.5: Micrograph depicting the chain-like structure of a soot particle [32]

in particulate matter emissions [37–39], primarily attributed to wall films and inadequate mixing, which will be elaborated upon in subsequent sections.

2.2.1 Wall films

In GDI engines, the formation of liquid fuel film is a primary contributor to particle emissions. This category of particle formation encompasses spray impingement on the piston surface and/or liner, spray impinging on the intake valve during injection, and the formation of fuel film on the injector tip. A common issue with these sources is that not all the deposited fuel vaporizes before combustion begins. This remnant fuel film is then the origin of particle formation. The likelihood of fuel-wall interactions is influenced by several factors including spray penetration length, injection timing, and injector location, with these parameters further varying based on engine operating conditions.

Kim et al. [40] visualized the wall-wetting behavior of an optically accessible GDI engine operating under stratified charge mode and quantified the total wetted area by the refractive index matching (RIM) technique. Their

conclusions highlight the dependence of plume-to-plume interaction on spray collapse which ultimately led to higher wall wetting. Furthermore, it was proposed that shorter injection durations provide limited time for inter-spray interactions, thereby preventing spray collapse and subsequently reducing wall wetting. Steeper and Stevens [41] utilized Laser-Induced Fluorescence (LIF) imaging to observe piston wetting. Subsequently, they assessed the interaction between the remaining fuel film and the approaching flame front, leading to the formation of pool fires, a diffusion-like flame observed on the piston crown, which persists until exhaust valve opening (EVO). In their research, it is evident that the use of late injection strategies increases the likelihood of fuel films persisting until the SOC. However, it's worth noting that with early injection and depending on the fuel's characteristics, a fuel film on the piston crown may also be present at SOC. The spray has also been shown to impact the intake valve during the intake stroke [42]. Additionally, abundant studies exist literature where the formation of liquid films on the injector tip is investigated [43–46]. It is agreed upon that the formation of deposits is more prone to maintain the liquid fuel and vapor in the pores of the deposit layer. This is the reason that comparisons between clean and fouled injectors have demonstrated significant differences where a more pronounced sooting flame was visualized on the injector tip for the fouled injector. Medina et al. [47] put forth different mechanisms of tip wetting and evaluated their dependence on engine operating parameters. Liquid fuel can stick to the injector tip due to wide plume wetting, in which the liquid fuel comes in contact with the edges of the counterbore and sticks on the injector tip due to adhesive forces. Fuel dribble wetting was also mentioned, and is characterized by a process in which a ligament breaks off of the main liquid spray and is deposited on the tip. The authors found that with increasing injection pressure, particle number emissions were reduced due to reduced tip wetting by the wide plume wetting mechanism. The higher momentum of fuel exiting the nozzle hole is more likely to occupy a greater area on the injector tip, thus increasing the evaporation rate. Figure 2.6 portrays the effect of tip wetting on soot formation as per the yellow luminous flame visualized in the bottom figures.

Barone et al. [48] characterized particle emissions from a GDI engine using Transmission Electron Microscopy (TEM). The analysis of the captured images led them to conclude that particle morphology strongly relies on injection timing. Early injection (320 CAD bTDC) was found to result in larger aggregate primary particle sizes, mainly due to increased wall impingement. On the other hand, delaying the SOI altered the particle morphology shifting the primary particles towards smaller sizes. A similar observation was made by Sabathil et al. [49], who found that the use of the earliest injection timing re-

(a) Large tip wetting (b) Small tip wetting

(i) Visualization of injector tip wetting without deposit

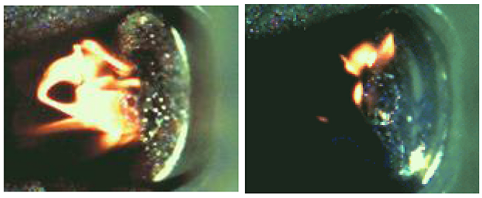

(a) Large tip wetting (b) Small tip wetting

(ii) In-cylinder visualization

Figure 2.6: Injector tip wetting and in-cylinder soot visualizations [45]

sulted in the emission of larger particles, attributed to fuel impingement. The particle size distribution for different SOI timings is depicted in Figure 2.7.

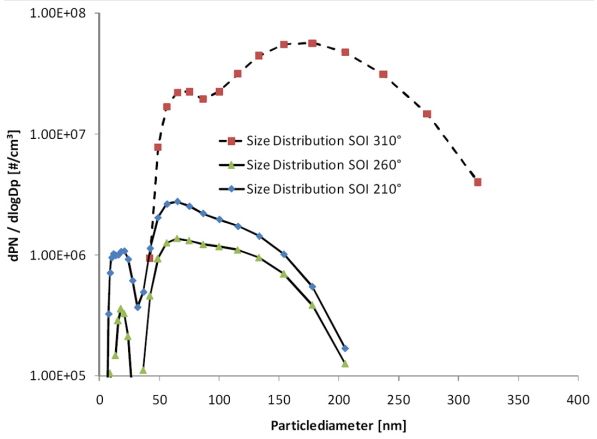

Figure 2.7: Particle size distribution for a SOI sweep [49]

In this particular case, the lowest particle number concentration was achieved at 260 CAD bTDC. This is likely attributed to reduced fuel impingement in comparison to the earlier injection timing and a greater duration available for mixing compared to the later injection timing. A similar trend

was also observed in TEM analysis of Lee at al. [50]. Based on these TEM images, in conjunction with data acquired on particle size distribution, they reached the conclusion that larger particles generated during the earliest injection timing are more likely to result in a higher particle mass concentration compared to a timing that is more delayed. As a result, a more comprehensive understanding of the sources of particle emissions can be derived by considering their morphology and size. Another significant aspect that warrants attention is the bimodal size distribution observed in all SOI timings, as depicted in Figure 2.7, which suggests the involvement of multiple emission sources that are in play.

2.2.2 Insufficient mixing

Another primary contributor to particle emissions in GDI engines is the presence of sub-stoichiometric regions within the combustion chamber [39, 49, 51–53]. Given the direct injection of fuel into the cylinder, it is necessary for the fuel to undergo sequential steps of evaporation and subsequent mixing with the surrounding gas to achieve homogenization. Consequently, the time available for this process plays a critical role in ensuring the formation of a homogeneous mixture prior to the initiation of combustion. Several factors come into play regarding engine operating parameters in this context. Extended injection durations, typically occurring at higher engine loads, tend to reduce the time available for mixing, resulting in decreased mixture quality. However, this effect could possibly be offset by higher injection pressure, which has the potential to enhance the mixing process due to elevated injection velocities, although it may have adverse effects on wall wetting depending on the injection timing. When engine speed increases, the potential for mixture homogeneity can be improved, thanks to enhanced turbulent mixing, although it is constrained by a shorter mixing duration. Surely, other factors related to the fuel properties affecting the evaporation process are also significant. Consequently, the mixing process in GDI engines is a multifaceted phenomenon, characterized by various parameters that often compete with one another. The evolution of the mixture formation is depicted in Figure 2.8 for various SOI timings. It is evident that in the case of the latest injection timing (left column), the mixture distribution at spark timing exhibits non-uniformity, characterized by rich pockets of fuel concentration near the liner. These regions, with elevated fuel concentration, are likely to result in a high concentration of soot precursors in the gas phase, ultimately contributing to soot formation [53]. Furthermore, despite the fact that the earliest SOI timing exhibits a greater level of mixture uniformity (as seen in the right column), it

also reveals a more noticeable presence of liquid film mass. The presence of liquid film mass could potentially outweigh the benefits of mixture homogeneity. In the presented example, the baseline SOI taking place midway through the intake stroke, represents the most favorable compromise.

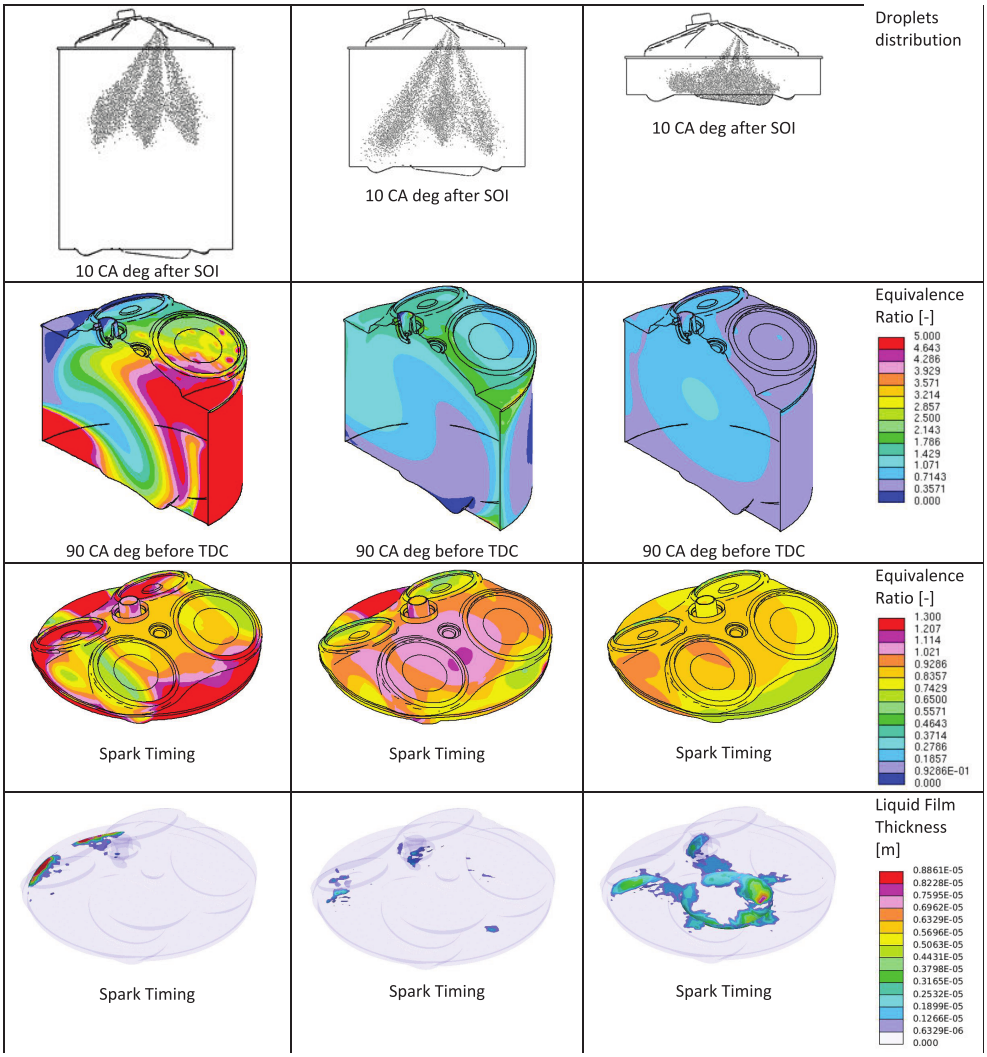

Figure 2.8: Spray, equivalence ratio and liquid film thickness distribution at different instances for SOI=180 CAD bTDC (left), SOI=baseline (middle), and SOI=330 CAD bTDC (right). [52]

Jiao and Reitz performed an equivalence ratio sweep for a premixed charge of iso-octane with 28% toluene by volume by means of 3D CFD simulations

[54]. Figure 2.9 plots the soot mass evolution from SOC until 80 CAD aTDC in addition to the particle size distribution acquired at 80 CAD aTDC. The first important observation to be made is that after a certain C/O threshold (around 0.44), the soot mass was shown to increase significantly, similarly to what was observed in other studies [55]. This was also the soot threshold observed in [56]. Another noticeable feature is that with increasing equivalence ratio, particle number predominantly increases in the nucleation mode (D_p<30 nm).

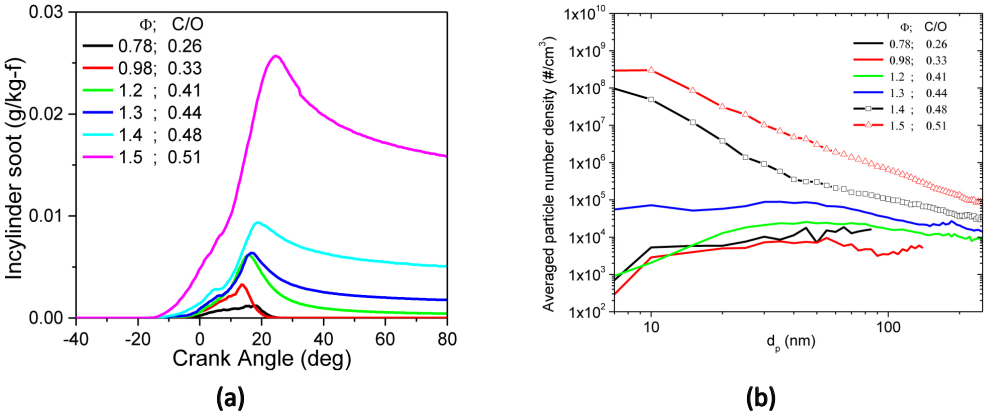

Figure 2.9: Soot mass (a) and PSD (b) for an equivalence ratio sweep. [54]

2.2.3 Unvaporized Fuel

In certain situations, the in-cylinder conditions pose challenges for the vaporization of the injected liquid fuel, particularly during cold engine states. As a result, a residual fuel mass persists in the liquid state, unable to evaporate and thoroughly mix with the bulk gas. This lingering liquid fuel may undergo carbonization, making liquid droplets an additional source of particle emissions. Furthermore, when liquid droplets impact the piston or liner surface with extended penetration, they may experience rebound or splashing, breaking into smaller droplets that remain in the liquid state until ignition. Additionally, liquid film stripping late during the compression phase causes some of the liquid fuel to detach from the film. This stripped mass would then have a limited amount of time to evaporate before combustion [57].

2.2.4 Fuel Effect

The aromatic content of the fuel is a decisive factor in the pyrolysis and precursor formation stages discussed in subsection 2.1.1. With an increased

aromatic content, the process towards the formation of the first aromatic ring is bypassed resulting in an easier path towards PAHs. Hence, the soot nucleation rate increases, ultimately leading to higher number of particles formed [58]. Alternatively, the fuel's oxygen content could facilitate in the oxidation of fragmented hydrocarbons, breaking the paths toward cyclization processes [59]. Apart from this, different fuel blends could influence the macroscopic characteristics of the spray itself, having a direct impact on spray penetration and impingement. In addition, the fuel's ease of evaporation plays a vital role both in mixture formation and evaporation of liquid films formed on the walls. A higher latent heat of vaporization would lead to a prolonged evaporation process which would consequently result in higher particle formation. Singh et al. [60] observed the sooting propensity of different fuels in an optical engine and correlated spray characteristics observed in a spray chamber with soot pathways. Their comparison of high olefin (HO) fuel with diisobutylene blends showed that the higher penetration lengths of diisobutylene, associated with its distillation curves, density, and viscosity, led to more impingement on the piston surface and thus higher soot formed from this region. However, the higher boiling point of HO caused it to evaporate more slowly which could explain the higher sooting tendency that was observed from the injector tip.

2.2.5 Lubrication Oil

Particle emissions from the lubricating oil, or more commonly known as motor oil, has been found to be a source of particle emissions comprising mainly of the organic fraction of particle mass [61]. A study showed that the elevated metal additives in the oil, such as Zinc, Calcium, and Magnesium, contributed to higher particle number emissions as compared with oil counterparts with reduced additives [62]. Their results also showed that a 10% decrease in Zinc content may lead to a reduction of 9-11% of non-volatile particle emissions. Additionally, semivolatile organic compounds (SVOCs) can desorb from the oil layer coating the liner during the expansion stroke leading to particle emissions [63]. Lubricating oil can also find its way into the combustion chamber via reverse blow-by through the piston rings, particularly during load transients. Lubricating oil can also find its way into the combustion chamber via reverse blow-by through the piston rings, particularly during load transients. Improved piston ring designs, which significantly reduced particle emissions, have revealed this process as a major contributor to soot emissions in CNG applications [64, 65]. Although oil consumption in modern GDI engines is low [66], some oil can evaporate from the liner and burn with the fuel [67]. Hence, lubrication oil properties and their impact on particle emissions are

an ongoing subject of study since both their properties and aging effects can impact particle emissions [68]. Guido et al. [64] investigated the influence of various oil compositions on particle number and soot emissions in a CNG engine. They started with a base oil formulation of SAE grade 10w40 and subsequently formulated two additional oils: one with 50% less ash content and another with optimized base oil properties. The findings indicated a reduction of approximately 35% in PN and soot emissions for the low-ash oil, while the optimized oil showed a more significant reduction of around 70-80%. Moreover, the particle size distribution maintained the same shape for all three oils, with reductions observed in all particle modes compared to the reference oil formulation.

2.3 Modeling techniques

2.3.1 Chemical Kinetics

As previously elaborated in subsection 2.1.1, it is crucial to incorporate the consideration of soot precursor formation, extending to include larger PAHs, in order to effectively model the inception of particles. One of the primary challenges frequently encountered in the development of such chemical mechanisms pertains to the complexities associated with measuring the concentrations of these large PAHs [69]. This challenge stems from the commonly accepted understanding that these larger PAHs are responsible for particle formation and, consequently, the emergence of nascent soot particles. This, in turn, presents difficulties in the simultaneous tracking and assessment of both larger PAHs and soot particles [70]. When it comes to fuel definition, simplifications are commonly applied when dealing with the complexity of fuel composition. To model fuels like gasoline and diesel, surrogate fuels or a combination of surrogates are often employed. One well-known example of such surrogates is the use of primary reference fuels (PRF), which includes iso-octane and n-heptane. These PRF blends are extensively utilized to replicate the combustion and knock characteristics of internal combustion engines running on gasoline [71]. In scenarios where it is necessary to represent the aromatic components of gasoline, toluene is frequently introduced into the PRF mixture, particularly when researchers aim to study soot emissions [72]. Various kinetic mechanisms have been well established in literature for gas-phase soot precursor estimation, such as the ABF mechanism [73], mechanism of Blanqaurt et al. [28], CRECK mechanism [74], KAUST mechanism [75], all of which have been validated under a wide range of experimental data. The arising question pertains to identifying the optimal size of PAH species for

an efficient modeling of soot inception, as discussed in subsection 2.1.2. It is a common belief in literature that modeling inception typically requires the inclusion of PAH reactions up to the fourth aromatic ring (A4). Therefore, it is reasonable to contemplate pyrene ($C_{16}H_{10}$) as the candidate species for inception. Pyrene is a favorable choice because it is formed early in the combustion process and exhibits significantly higher concentrations in comparison to larger aromatic ring species, as noted in [69]. In addition, experimental studies discussed in subsection 2.1.2 further support the choice of pyrene as the inception species. The concentration profiles of other species involved in soot-related processes are of equal significance to pyrene. For example, acetylene plays a pivotal role in both the surface growth of soot particles and the molecular growth of PAHs.

Blanquart et al. [28] developed a mechanism that encompasses fuel surrogates and tested it for both premixed and diffusion flames. They based their work on the widely recognized GRI-MECH v3.0 mechanism [76] for methane combustion, then extended it to encompass larger hydrocarbons, including iso-octane. The mechanism for PAH growth up to pyrene was constructed based on the pathways outlined in subsection 2.1.1. Furthermore, the oxidation chemistry for iso-octane was adapted from Lawrence Livermore National Laboratories (LLNL) mechanism [77], with a reduction to eliminate low-temperature combustion reactions that were irrelevant to their research. The initial validation of this mechanism involved a comprehensive examination across a wide range of equivalence ratios and pressures, considering laminar burning velocities and ignition delay times. In terms of soot precursors, two rich laminar premixed flames—n-heptane/air and iso-octane/air with an equivalence ratio of 1.9 were investigated. Their chemical mechanism demonstrated effectiveness in predicting molar concentrations of PAH precursors. The primary pathways leading to benzene formation closely resemble those mentioned in subsection 2.1.1, where smaller hydrocarbons are generated through iso-octane decomposition, leading to the production of ethylene molecules and, later on, acetylene. Additionally, C_3 and C_3 isomers are formed from the decomposition process. The dominant pathway considered in their mechanism for benzene formation involves the recombination of propargyl radicals, or the reaction between propargyl and allyl radicals.

2.3.2 Soot Modeling in GDI Engines

Based on the information presented thus far, it is evident that the modeling of soot formation in ICEs is an intricate undertaking, encompassing complex chemical kinetics and interactions between the gas and solid phases. Soot for-

mation models generally vary in complexity depending on their level of detail in describing the physical processes and range from empirical, semiempirical, and detailed models [78].

Empirical models typically establish a direct relationship between a physical soot property, such as soot mass density, and experimental measurements conducted under various conditions. These models typically take the form of equations with multiple constants that require calibration to obtain the best fit. While this category of models often exhibits strong agreement with experimental results within specific conditions, they do not offer insights into soot morphology or size characteristics, as discussed in [79]. An example of this method is detailed in the study of Khan et al. [80], where they established a correlation between soot mass density and in-cylinder parameters, such as pressure, temperature, and local equivalence ratio. Their approach was based on the assumption that the primary factor influencing particle formation is inception, and excluded the oxidation processes from the analysis. This necessitated the adjustment of several variables in their equation to align with these assumptions, using a measured dataset obtained from a diesel engine operating across various engine speeds. Empirical models have also found application in the gas turbine field, where Edelman and Harsha employed a more sophisticated methodology compared to that of Khan et al. [81]. They took into consideration soot oxidation by introducing a corresponding negative term, similar in form to the one used for soot formation. The implementation of one equation for soot formation and one equation for soot oxidation is commonly referred to in literature as two-equation empirical models. Hiroyasu and Kadota [82] adopted this approach where soot formation was considered in the both vapor and liquid phases. In a more recent investigation conducted by Dong et al. [83], the authors utilized the two-equation empirical model taking ethylene concentration as the precursor for soot formation, differently from the conventional approach that considers fuel concentration as the precursor, as outlined in [82]. These models are appealing due to their computational efficiency and prove useful in scenarios where the assessment of particle emissions is solely focused on mass concentration. Nevertheless, they do not furnish any insights into particle number density or size variations over time.

Semi-empirical models further add a degree of detail by encompassing some physical and chemical considerations. They use simplified chemistry in order to compute the rate equations for reactions involving soot precursors and soot particles [79]. The works of Tesner et al. [84] have been widely adopted in soot modeling studies. The authors proposed a two step mechanism that

describes the formation rate of the soot nuclei and the particle number density. The modeling strategy was complemented with measurements of particle formation in an acetylene-hydrogen laminar diffusion flame. Other models include the physical processes of nucleation, surface growth, and oxidation, and represented them with rate expressions as well [85]. The limitation lies in the fact that these models are inherently constrained to particular conditions that closely match the empirical constants' derivation [79]. Therefore, to achieve generality, it is essential to have a comprehensive inclusion of fuel pyrolysis and PAH growth in the gas phase kinetics coupled with the dynamics of soot particle growth.

Detailed soot models often differ in the way the particle size distribution function (PSDF) is solved. One approach to solve the soot population balance equation for a stochastic particle system is the Monte-Carlo method [86]. In this method, the processes contributing to particle formation, growth, and oxidation are treated randomly based on their rates. The outcome is a detailed description of the PSDF time evolution. Another method of solving for the PSDF is the sectional method in which the size distribution is divided into a finite number of bins [87]. In each bin, all particles are represented by a scalar, soot volume fraction (f_v) for instance, from which the number density can be derived [88]. A third and less computationally expensive approach is the method of moments. In this method, the population balance equation is represented by the transport equations of its moments [89]. A comprehensive representation of the PSDF necessitates an infinite number of moments. Nevertheless, for practical reasons, only a finite number of moments are solved and provide satisfactory results. The drawback of this approach is that the moment rates remain unclosed because they depend on moments that are not explicitly solved for in the equations. As a solution, various closure methods have been devised, with the most common one being the Method of Moments with Interpolative Closure (MOMIC) as introduced by Frenklach and his colleagues [25, 73, 89, 90]. MOMIC utilizes logarithmic interpolation techniques to close the moment rate equations. However, a limitation of this method is its inability to account for bimodal number density distributions. To address this, alternative variations of the Method of Moments have been introduced, such as the Quadrature Method of Moments (QMOM) [91]. It's important to note that although the QMOM approach provides accurate solutions, it has been found to be ill-posed and challenging to implement [27]. In response to these challenges, Mueller et al. [27] developed the Hybrid Method of Moments (HMOM). The HMOM aims to combine the strengths of both the MOMIC and QMOM techniques, offering a more robust and versatile approach to moment closure in soot modeling while simultaneously capturing bimodal

number density distributions. Other approaches that have been recently developed include Conditional Quadrature Method of Moments (CQMOM) [92], Extendend Quadrature Method of Moments (EQMOM) [93], and Extended Conditional Quadrature Method of Moments (ECQMOM) [94]. For more details of the aforementioned models, the reader is referred to the corresponding papers.

When applying models of differing complexity to GDI engines, the conventional trade-off between precision and computational time emerges as a crucial determinant. The issue extends beyond the approach to soot modeling and involves the processes of gas exchange, mixture formation, and combustion prior to the onset of soot formation. Wallesten et al. [95] serves as an example of coupling a detailed engine model with an empirical soot model. They conducted simulations under low load conditions, considering three distinct injection timings using a 3D CFD model of the engine and employed the Kennedy-Hiroyasu-Magnussen model to calculate soot mass fractions. The overall pattern of a rise in soot mass fraction with delayed injection timing, due to the decrease in mixture homogeneity, was successfully replicated, although there was a notable overestimation for the most delayed timing. The authors' conclusion is that the soot model demands further fine-tuning, which basically impairs its predictive accuracy under changing operating conditions. In a more recent study, Etheridge et al. [96] used the Stochastic Reactor Model (SRM) engine code coupled with a detailed soot model. The model was first calibrated with experimental measurements and was then used to investigate different SOI timing implications on exhaust emissions. The simulation effectively reproduced the change in particle number and size with SOI, although the model displayed a more pronounced presence of smaller particles in the 10 nm range. The authors further explain this discrepancy by stating that the simulation data is extracted at EVO, which precedes the time at which exhaust gas is sampled in the experimental study. Consequently, this could imply that coagulation processes, which continue through the exhaust port, are somewhat truncated in the simulation, resulting in a higher number density of smaller particles. Moreover, this study did not take into account spray-wall impingement, a factor that could have implications on particles in the accumulation mode, as observed in subsection 2.2.1. In a more recent investigation, Wang et al. [97] extended the SRM engine model to incorporate spray-wall impingement. This was accomplished by dividing the cylinder into a bulk zone and a wall zone. In this manner, the temperature and equivalence ratio gradient within the wall zone could be known, thus accounting for particles induced by the wall film. Contrary to Etheridge et al. [96] who considered acetylene as the inception species, corenene ($C_{24}H_{12}$) was the inception

species in their study. Experimental measurements were conducted at various injection timings, with particular interest in the case of early injection at 330 CAD bTDC, which exhibited the highest particle number density. The simulated particle size distribution fell within the same order of magnitude as the experimental results, although it underpredicted the size of the main mode by a factor of two. Much like the approach in [96], particles were sampled at EVO in the simulation, potentially explaining the discrepancy in particle size. Therefore, it is evident that numerical simulations should extend beyond EVO to achieve a closer alignment with measurements, as particle mass concentration is significantly influenced by size.

Tan et al. [57] utilized a combined 3D-CFD model and chemical kinetic mechanism that employed the sectional method to address soot formation. Their extensive investigation led to a comprehensive conceptual grasp of soot pathways, primarily originating from fuel-rich zones resulting from the evaporation of liquid films and unvaporized liquid fuel droplets at ignition time. At a constant load and with an increase in engine speed, the simulations and experimental measurements both indicated a reduction in particle number density. Examination of tumble flow velocity and turbulent kinetic energy revealed an augmentation with the increase in engine speed, which, in turn, proved to enhance the spray vaporization and mixing processes. The interplay here appears to revolve around the competing factors of the available mixing time, which shortens at higher engine speeds, and the spray vaporization and mixing rate. Under constant engine speed and increasing engine load, the increase in injection pressure resulted in a higher swirl ratio and an increased level of turbulent kinetic energy after the injection ended. These effects facilitated the mixing processes, ultimately reducing the mixture's non-uniformity at the point of ignition. The numerical model successfully replicated trends in particle number density. However, in both sets of parameters, the particle mass density consistently fell below the measured values. The authors propose that the underestimation of particle size may be attributed to the assumption that particles are spherical in nature, without considering agglomeration in the modeling process. Furthermore, the potential contribution of coagulation beyond the exhaust valve opening, which was not factored into the simulations, could also impact the overall particle size and mass. Nonetheless, the sectional method has demonstrated its suitability for accurately predicting particle number, particulate mass, and particle size distribution to a noteworthy extent. However, it falls short in providing additional insights into the morphology of soot particles, as is achieved by the stochastic method. Fontanesi et al. [98] implemented the sectional method in 3D CFD simulations as well. They used an optimized reaction mechanism developed by

Cai et al. [99] to account for oxygenated fuels in the PAH formation mechanisms since the surrogate fuel they utilized contained ethanol. This basically mimicked the gasoline fuel's threshold soot index (TSI) used in acquiring the measurements on the engine test bench. In their study, three different SOIs were compared at 2000 RPM and full load condition. Similarly to previous studies, the earliest injection timing (340 CAD bTDC) led to the highest PN and PM values due to higher liquid film formation on the piston top. Additionally, soot mass concentration was also underestimated in their study and further clarified by examining the particle size distribution which was dominated by particles in the 5.6-10 nm range, 5.6 nm being the minimum diameter detectable by the particle sampling system. The authors establish a connection between the underestimation of soot mass and the utilization of a constant soot density across all sections within the sectional method. However, they contend that soot density decreases with particle size [88], which would, in turn, result in a higher mass concentration due to the conservation of mass in each section. An interesting note to point out here, the authors in [98] performed a correction on the particle number and mass concentrations by considering an equivalent volume at reference pressure, temperature, and dilution ratio (DR) in the exhaust sampling system. This equivalent volume was then used to compute the final number and mass concentrations. In this way, a one-to-one comparison was assured between experimental and numerical results. A later study by Berni et al. [100] used the same methodology for calculating gaseous and particle emissions from an eight cylinder high performance GDI engine. An additional adjustment were made in their study on the computed particle number and mass densities. The efficiency of the particle counter, used in the experimental acquisition campaign, was factored into each section to further equalize the comparison between measured and numerical values. This effectively brought down the difference between numerical and experimental results to one order of magnitude.

Liang et al. [101] implemented the method of moments in FORTÉ CFD code first applied on fundamental spray combustion experiments and then used the model for a soot particle tracking in a spray-guided GDI engine. In their study, they used a 7-component surrogate blend to match the chemical and physical characteristics of gasoline. By tracking the soot cloud, they were able to observe the initiation of the soot in the spark plug region, due to the presence of some liquid fuel there, and the growth of the soot cloud during the expansion stroke. The authors pointed out that the flame propagation speed is much faster than the soot cloud growth indicating that soot formation processes are a post-flame phenomena. This was also observed in controlled spray chamber premixed combustion experiments [60].

Other researchers opted for simpler approaches by coupling semi-detailed soot models with CFD. An example of such an approach was elaborated in [102] which used a soot model that was initially developed for soot modeling in low temperature diesel combustion [103].The impetus behind developing a semi-detailed soot model arose from the necessity to streamline the model's complexity and accelerate the simulation process in engine CFD-based approaches. In their soot model, pyrene was considered to be the inception species, surface growth was attributed to both acetylene and PAH (A_4), coagulation was modeled by the normal square dependence, and oxidation was due to O_2 and OH radicals. Additionally, soot species density and number density were treated as passive species for which their transport equations were solved. Regarding the gas phase chemistry, the authors modified an existing multi-surrogate mechanism of n-heptane/iso-octane/toluene by adding reactions to model PAH formation up to pyrene and toluene pyrolysis. A preliminary validation was carried out with respect to the chemistry mechanism for four laminar premixed flames. For all flames considered, the chemical mechanism predicted molar fractions of C_2H_2, C_2H_4, and A_1 quite satisfactorily. Additionally, it was shown in the toluene flame simulations that the C_2H_2 and A_1 molar fractions are within the same order of magnitude as compared with n-heptane flame where A_1 molar fraction was three order of magnitudes lower than C_2H_2. This emphasizes the importance of inclusion of toluene in the fuel composition to accurately model the aromatic content of gasoline. They compared their simulation of lean burned stratified combustion strategy with a simulation using the two-step soot model of Hiroyasu [82]. Interestingly, no soot mass was formed when using Hiroyasu's soot model whereas soot mass was formed and continuously increased in the case of Jiao and Reitz's approach. Their depiction of soot-related variables show how the fuel rich regions near the wall film provide ideal conditions for soot formation due to the absence of oxidizing species of OH and O_2 and a relatively lower temperature due to wall film vaporization. In a different study [54], the authors highlighted the effect of the multicomponent fuel on wall film vaporization where the low volatility fuel contributed to wall film formation and consequent soot formation. In certain scenarios, the computational resources required for the aforementioned modeling techniques can be excessively demanding. Giovannoni et al. [104] adopted a CFD analysis of the mixture formation process and wall impingement to establish a qualitative correlation between these aspects and soot formation. This approach allowed them to distinguish the quality of the mixture and the fuel film deposits at spark timing across different cases, serving as an initial assessment of their tendency to generate soot. However,

it's important to note that this approach does not yield detailed insights into the dynamics of soot and serves as a preliminary evaluation.

It can be inferred from the modeling techniques discussed above that common routes to soot formation exist within GDI engines, and these pathways differ based on engine parameters. While these models are effective in predicting particle formation and oxidation to varying degrees of detail and accuracy, they typically cannot be extended to simulations involving transient driving cycles or dynamic engine operation. In addressing this challenge, Frommater et al. [105] introduced a phenomenological model that integrates physically grounded models for fuel film deposits and the computation of mixture non-uniformity with detailed chemical kinetic mechanisms and a stochastic soot model. The main modeling framework extracts thermodynamic data from an engine process simulation, which is then input into the multi-zone block. Within this block, sub-stoichiometric zones and pyrolysis zones are defined resulting from incomplete mixing and liquid films, respectively. Each block independently evolves based on the chemical kinetics specific to that zone. The temporal evolution of species involved in nucleation, surface growth, coagulation, and oxidation is subsequently passed on to the stochastic Monte Carlo tool for the calculation of particle number, particulate mass, and particle size distribution across various operational conditions. The validation of the model was based on a set of measured steady-state operational points, where the numerical model exhibited strong capabilities. In this regards, the dominant sooting pathway was found to be injector tip wetting. The model was further extended to simulate particle emissions during a customized highway driving cycle, with PN and PM measurements falling within 20% of the observed values. However, there are some limitations associated with this model, primarily concerning its applicability to other engine types and combustion modes. Notably, the sub-models responsible for accounting for the different soot pathways incorporate numerous coefficients that are not necessarily based on physical principles; rather, they are calibrated to align with experimental measurements. Hence, it is highly probable that a reparametrization of these coefficients will be necessary when applying the model to a different engine scenario. It's worth noting that the model exhibited a positive response to changes in actuator settings, thus paving the way for a computationally efficient and comprehensive approach to soot modeling in GDI engines.

2.4 Summary

This chapter commenced by delineating the fundamental elements linked to particle formation processes in fuel-rich combustion. The advancement of

experimental and optical techniques has facilitated a more profound and extensive comprehension of the soot formation process. The chemical reactions initiating from the fuel and leading to the formation of aromatic rings were initially discussed, with a specific focus on aliphatic fuels, although the breakdown of the fuel and the formation of cyclic rings are analogous in fuels with aromatic content. The transition from the gaseous phase to the emergence of the nascent soot particle was then elucidated, along with insights into the growth and oxidation processes.

Optical visualizations and particle sampling play a dual role by not only facilitating an understanding of the theoretical aspects of soot dynamics but also providing insights into the sources that foster favorable conditions for particle formation in GDI applications. The characteristics of these sources can be correlated with specific particle morphology and structures, revealing how diverse sources exert distinct physical and chemical influences on soot. Throughout the development of models, experimental findings have consistently guided conceptualizations. Main model hypotheses are evaluated by comparing numerical results with experimental measurements, forming a symbiotic relationship between theoretical frameworks and observations. A review of the main literature work concerning particle emissions sources in GDI engines revealed that mixture quality leading to fuel rich pockets and remaining liquid films in the combustion chamber at ignition timing were the main particle formation pathways. Depending on operating conditions and the engine's thermodynamic state, the different sources contribute to overall particle number and mass in varying proportions.

The subsequent discussion delved into the intricacies of soot modeling techniques. Originally designed for premixed and diffusion flames within controlled laboratory settings, these models were initially employed in diesel engine applications before being adapted to predict particle emissions in GDI engines. Given the significant role of PAH precursor formation in soot inception, the majority of currently applied models identify A_4 as the inception species, and in some cases, even A_7. The models vary in complexity, ranging from straightforward empirical equations to more comprehensive descriptions that encompass nucleation, surface growth, coagulation, and oxidation processes. Moreover, the majority of numerical approaches entail 3D CFD engine simulations coupled with detailed soot models. However, these models often demand substantial computational resources and may not encompass all soot pathways due to constraints, such as computational limitations hindering the inclusion of injector tip wetting, for instance. The work of Frommater et al. [105] represents a new way of approaching the issue by utilizing phenomenological sub-models accounting for the main soot pathways that are directly

linked with detailed chemical kinetics and a stochastic soot model. However, the model requires a prior optimization of coefficients with CFD results and particle measurements.

The research endeavors presented in this study were inspired by the modeling framework introduced by the authors in [105]. Several adjustments were made to enhance the model's generality and minimize parameterization, aiming to extend its applicability to diverse engine concepts. The subsequent chapter delves into the primary tools employed, integral to the model structure, and provides a detailed explanation of the key theoretical aspects underpinning them.

References

[1] Smith, O.I. "Fundamentals of soot formation in flames with application to diesel engine particulate emissions". In: *Progress in Energy and Combustion Science* 7:4 (1981). DOI: 10.1016/0360-1285(81)90002-2.

[2] Amann, C. A. and Siegla, D. C. "Diesel particulates—What they are and why". In: *Aerosol Science and Technology* 1.1 (1981), pp. 73–101. DOI: 10.1080/02786828208958580.

[3] Heywood, J. B. *Internal Combustion Engine Fundamentals*. New York: McGraw-Hill, 1988.

[4] Mansurov, Z.A. "Soot formation in combustion processes (Review)". In: *Combustion, Explosion, and Shock Waves* 41.6 (2005), pp. 727–744. DOI: 10.1007/s10573-005-0083-2.

[5] Haynes, B.S. and Wagner, H.Gg. "Soot formation". In: *Progress in Energy and Combustion Science* 7.4 (1981), pp. 229–273. DOI: https://doi.org/10.1016/0360-1285(81)90001-0.

[6] Bönig, M. et al. "Soot formating in premixed C2H4 flat flames at elevated pressure". In: *Symposium (International) on Combustion* 23.1 (1991), pp. 1581–1587. DOI: https://doi.org/10.1016/S0082-0784(06)80429-7.

[7] Warnatz, J., Mass, U., and Dibble, R.W. *Combustion: Physical and Chemical Fundamentals, Modeling and Simulation, Experiments, Pollutant Formation*. Springer Berlin Heidelberg New York, 2006.

[8] Böhm, H. et al. "The influence of pressure and temperature on soot formation in premixed flames". In: *Symposium (International) on Combustion* 22.1 (1989), pp. 403–411. DOI: https://doi.org/10.1016/S0082-0784(89)80047-5.

[9] Bockhorn, H. *Soot Formation in Combustion: Mechanisms and Models*. Ed. by V. I. Toennies, F. P. Goldanskii, and J. P. Schafer. 59. Springer-Verlag, 1994. DOI: 10.1007/978-3-642-85167-4.

[10] Richter, H. and Howard, J. B. "Formation of polycyclic aromatic hydrocarbons and their growth to soot-a review of chemical reaction pathways". In: *Progress in Energy and Combustion Science* 26.4 (2000), pp. 565–608. DOI: 10.1016/S0360-1285(00)00009-5.

[11] Schug, K. P., Manheimer-Timnat, Y., Yaccarino, P., and Glassman, I. "Sooting Behavior of Gaseous Hydrocarbon Diffusion Flames and the Influence of Additives". In: *Combustion Science and Technology* 22.5-6 (1980), pp. 235–250. DOI: 10.1080/00102208008952387.

[12] Lindstedt, R. and Skevis, G. "Benzene Formation Chemistry in Premixed 1,3-Butadiene Flames". In: *Twenty-Sixth Symposium (International) on Combustion/The Combustion Institute* 26.1 (1996), pp. 703–709.

[13] Zhang, F. et al. "Formation of the phenyl radical [C6H5(X 2A1)] under Single collision conditions: A crossed molecular beam and ab initio study". In: *Journal of the American Chemical Society* 132.8 (2010), pp. 2672–2683. DOI: 10.1021/ja908559v.

[14] Woods, P. M., Millar, T. J., Zijlstra, A. A., and Herbst, E. "The Synthesis of Benzene in the Proto–planetary Nebula CRL 618". In: *The Astrophysical Journal* 574.2 (2002), pp. L167–L170. DOI: 10.1086/342503.

[15] Frenklach, M., Clary, D. W., Gardiner, W. C., and Stein, S. E. "Detailed kinetic modeling of soot formation in shock-tube pyrolysis of acetylene". In: *Symposium (International) on Combustion* 20.1 (1984), pp. 887–901. DOI: 10.1016/S0082-0784(85)80578-6.

[16] Miller, J. A. and Klippenstein, S. J. "The Recombination of Propargyl Radicals and Other Reactions on a C6H6 Potential". In: *Journal of Physical Chemistry A* 107.39 (2003), pp. 7783–7799. DOI: https://doi.org/10.1021/JP030375H.

[17] Wang, E. and Ding, J. "Reaction between the i-C4H5 radical and propargyl radical (C3H3): A theoretical study". In: *Chemical Physics Letters* 768 (2021), p. 138407. DOI: 10.1016/j.cplett.2021.138407.

[18] Bittner, J. D. and Howard, J. B. "Composition profiles and reaction mechanisms in a near-sooting premixed benzene/oxygen/argon flame". In: *Symposium (International) on Combustion* 18.1 (1981), pp. 1105–1116. DOI: 10.1016/S0082-0784(81)80115-4.

[19] Frenklach, M. and Wang, H. "Detailed modeling of soot particle nucleation and growth". In: *Symposium (International) on Combustion* 23.1 (1991), pp. 1559–1566. DOI: 10.1016/S0082-0784(06)80426-1.

[20] Shukla, B., Miyoshi, A., and Koshi, M. "Role of Methyl Radicals in the Growth of PAHs". In: *Journal of the American Society for Mass Spectrometry* 21.4 (2010), pp. 534–544. DOI: 10.1016/j.jasms.2009.12.019.

[21] Reizer, E., Viskolcz, B., and Fiser, B. "Formation and growth mechanisms of polycyclic aromatic hydrocarbons: A mini-review". In: *Chemosphere* 291 (2022), p. 132793. DOI: 10.1016/j.chemosphere.2021.132793.

[22] Herdman, J. D. and Miller, J. H. "Intermolecular potential calculations for polynuclear aromatic hydrocarbon clusters". In: *Journal of Physical Chemistry A* 112.28 (2008), pp. 6249–6256. DOI: 10.1021/jp800483h.

[23] Weiner, A. M. and Harris, S. J. "Optical detection of large soot precursors". In: *Combustion and Flame* 77.3-4 (1989), pp. 261–266. DOI: 10.1016/0010-2180(89)90133-8.

[24] D'Anna, A. "Combustion-formed nanoparticles". In: *Proceedings of the Combustion Institute* 32.1 (2009), pp. 593–613. DOI: 10.1016/j.proci.2008.09.005.

[25] Frenklach, M. and Wang, H. "Detailed Mechanism and Modeling of Soot Particle Formation". In: *Soot Formation in Combustion: Mechanisms and Models*. Ed. by Henning Bockhorn. Berlin, Heidelberg: Springer Berlin Heidelberg, 1994, pp. 165–192. DOI: 10.1007/978-3-642-85167-4_10.

[26] Mueller, M.E., Blanquart, G., and Pitsch, H. "A joint volume-surface model of soot aggregation with the method of moments". In: *Proceedings of the Combustion Institute* 32.1 (2009), pp. 785–792. DOI: 10.1016/j.proci.2008.06.207.

[27] Mueller, M. E., Blanquart, G., and Pitsch, H. "Hybrid Method of Moments for modeling soot formation and growth". In: *Combustion and Flame* 156.6 (2009), pp. 1143–1155. DOI: 10.1016/j.combustflame.2009.01.025.

[28] Blanquart, G., Pepiot-Desjardins, P., and Pitsch, H. "Chemical mechanism for high temperature combustion of engine relevant fuels with emphasis on soot precursors". In: *Combustion and Flame* 156.3 (2009), pp. 588–607. DOI: 10.1016/j.combustflame.2008.12.007.

[29] Homann, K.H. "Carbon formation in Pre-Mixed flames". In: *Combustion and Flame* 11.4 (1967), pp. 265–287. DOI: https://doi.org/10.1016/0010-2180(67)90017-X.

[30] Prado, G. and Lahaye, J. "Physical Aspects of Nucleation and Growth of Soot Particles". In: *Particulate Carbon: Formation During Combustion*. Ed. by Donald C. Siegla and George W. Smith. Boston, MA: Springer US, 1981, pp. 143–175. DOI: 10.1007/978-1-4757-6137-5_6.

[31] Tree, D. R. and Svensson, K. I. "Soot processes in compression ignition engines". In: *Progress in Energy and Combustion Science* 33.3 (2007), pp. 272–309. DOI: 10.1016/j.pecs.2006.03.002.

[32] Dobbins, R. A. and Subramaniasivam, H. "Soot Precursor Particles in Flames". In: *Soot Formation in Combustion: Mechanisms and Models*. Ed. by Henning Bockhorn. Berlin, Heidelberg: Springer Berlin Heidelberg, 1994, pp. 290–299. DOI: 10.1007/978-3-642-85167-4_10.

[33] Lahaye, J. "Mechanisms of soot formation". In: *Polymer Degradation and Stability* 30.1 (1990), pp. 111–121. DOI: 10.1016/0141-3910(90)90121-M.

[34] Zhao, F., Lai, M. C., and Harrington, D. L. "Automotive spark-ignited direct-injection gasoline engines". In: *Progress in Energy and Combustion Science* 25.5 (1999), pp. 437–562. DOI: 10.1016/S0360-1285(99)00004-0.

[35] Knop, V. and Essayem, E. "Comparison of PFI and DI operation in a downsized gasoline engine". In: *SAE International Journal of Engines*. Vol. 6. 2. 2013, pp. 941–952. DOI: 10.4271/2013-01-1103.

[36] National Research Council. *Cost, effectiveness, and deployment of fuel economy technologies for light-duty vehicles*. Washington, DC: The National Academies Press, 2015. DOI: 10.17226/21744.

[37] He, X., Ratcliff, M. A., and Zigler, B. T. "Effects of gasoline direct injection engine operating parameters on particle number emissions". In: *Energy and Fuels* 26.4 (2012), pp. 2014–2027. DOI: 10.1021/ef201917p.

[38] Bahreini, R. et al. “Characterizing emissions and optical properties of particulate matter from PFI and GDI light-duty gasoline vehicles”. In: *Journal of Aerosol Science* 90 (2015), pp. 144–153. DOI: 10.1016/j.jaerosci.2015.08.011.

[39] Chen, L., Liang, Z., Zhang, X., and Shuai, S. “Characterizing particulate matter emissions from GDI and PFI vehicles under transient and cold start conditions”. In: *Fuel* 189 (2017), pp. 131–140. DOI: 10.1016/j.fuel.2016.10.055.

[40] Kim, N., Vuilleumier, D., and Sjoberg, M. “Effects of Injection Timing and Duration on Fuel-Spray Collapse and Wall-Wetting in a Stratified Charge SI Engine”. In: *SAE Technical Paper* (2021). DOI: 10.4271/2021-01-0544.

[41] Stevens, E. and Steeper, R. “Piston wetting in an optical DISI engine: Fuel films, pool fires, and soot generation”. In: *SAE Technical Papers* 2001.724 (2001). DOI: 10.4271/2001-01-1203.

[42] Guinther, G. and Smith, S. “Formation of Intake Valve Deposits in Gasoline Direct Injection Engines”. In: *SAE International Journal of Fuels and Lubricants* 9.3 (2016), pp. 558–566. DOI: 10.4271/2016-01-2252.

[43] Berndorfer, A., Breuer, S., Piock, W., and Von Bacho, P. “Diffusion combustion phenomena in GDi engines caused by injection process”. In: *SAE Technical Papers* 2 (2013). DOI: 10.4271/2013-01-0261.

[44] Leick, P., Bork, B., and Geiler, J. N. “Experimental characterization of tip wetting in gasoline DI injectors”. In: *ICLASS 2018 - 14th International Conference on Liquid Atomization and Spray Systems* July (2018).

[45] Imaoka, Y., Hashizume, Y., Inoue, T., and Shiraishi, T. “A Study of Particulate Emission Formation Mechanism from Injector Tip in Direct-Injection Gasoline Engines”. In: *SAE International Journal of Advances and Current Practices in Mobility* 2.1 (2020), pp. 376–384. DOI: 10.4271/2019-01-2244.

[46] Fischer, A. “Experimental and Numerical Investigation of Injector Tip Wetting in Modern Gasoline Engines as predecessor for particle emissions”. PhD thesis. TU Graz, 2018. DOI: 10.51202/9783186807120-725.

[47] Medina, M., Alzahrani, F. M., Fatouraie, M., Wooldridge, M. S., and Sick, V. "Mechanisms of fuel injector tip wetting and tip drying based on experimental measurements of engine-out particulate emissions from gasoline direct-injection engines". In: *International Journal of Engine Research* 22.6 (2021), pp. 2035–2053. DOI: 10.1177/1468087420916052.

[48] Barone, T., Storey, J., Youngquist, A., and Szybist, J. "An analysis of direct-injection spark-ignition (DISI) soot morphology". In: *Atmospheric Environment* 49 (2012), pp. 268–274. DOI: 10.1016/j.atmosenv.2011.11.047.

[49] Sabathil, D., Koenigstein, A., Schaffner, P., Fritzsche, J., and Doehler, A. "The influence of DISI engine operating parameters on particle number emissions". In: *SAE World Congress and Exhibition*. 2011. DOI: 10.4271/2011-01-0143.

[50] Lee, K. O., Seong, H., Sakai, S., Hageman, M., and Rothamer, D. "Detailed morphological properties of nanoparticles from gasoline direct injection engine combustion of ethanol blends". In: *11th International Conference on Engines & Vehicles*. Vol. 6. SAE International, 2013. DOI: 10.4271/2013-24-0185.

[51] Farron, C. et al. "Particulate characteristics for varying engine operation in a gasoline spark ignited, direct injection engine". In: *SAE World Congress and Exhibition* (2011). DOI: 10.4271/2011-01-1220.

[52] Biagiotti, F. et al. "Modelling liquid film in modern GDI engines and the impact on particulate matter emissions – Part 1". In: *International Journal of Engine Research* 23.10 (2022), pp. 1634–1657. DOI: 10.1177/14680874211024476.

[53] Kayes, D. and Hochgreb, S. "Mechanisms of particulate matter formation in spark-ignition engines. 1. Effect of engine operating conditions". In: *Environmental Science and Technology* 33.22 (1999), pp. 3968–3977. DOI: 10.1021/es981100w.

[54] Jiao, Q. and Reitz, R. "Modeling of equivalence ratio effects on particulate formation in a spark-ignition engine under premixed conditions". In: *SAE Technical Papers* (2014). DOI: 10.4271/2014-01-1607.

[55] Alessio, A. D., Gambi, G., Minutolo, P., Russo, S., and D'Anna, A. "Optical characterization of rich premixed CH4/O2 flames across the soot formation threshold". In: *Twenty-Fifth Symposium (International) on Combustion* 25.1 (1994), pp. 645–651. DOI: https://doi.org/10.1016/S0082-0784(06)80696-X.

[56] Hageman, M. and Rothamer, D. "Sensitivity analysis of particle formation in a spark-ignition engine during premixed operation". In: *8th US National Combustion Meeting 2013* 1 (2013), pp. 500–514.

[57] Tan, J. Y., Bonatesta, F., Ng, H. K., and Gan, S. "Numerical Investigation of Particulate Matter Processes in Gasoline Direct Injection Engines through Integrated Computational Fluid Dynamics-Chemical Kinetic Modeling". In: *Energy and Fuels* 34.4 (2020), pp. 4909–4924. DOI: 10.1021/acs.energyfuels.9b03945.

[58] Short, D. Z., Vu, D., Durbin, T. D., Karavalakis, G., and Asa-Awuku, A. "Components of Particle Emissions from Light-Duty Spark-Ignition Vehicles with Varying Aromatic Content and Octane Rating in Gasoline". In: *Environmental Science and Technology* 49.17 (2015), pp. 10682–10691. DOI: 10.1021/acs.est.5b03138.

[59] Price, P., Twiney, B., Stone, R., Kar, K., and Walmsley, H. "Particulate and hydrocarbon emissions from a spray guided direct injection spark ignition engine with oxygenate fuel blends". In: *SAE Technical Papers* 724 (2007), pp. 776–790. DOI: 10.4271/2007-01-0472.

[60] Singh, E. et al. "Particulate Matter Emissions in Gasoline Direct-Injection Spark-Ignition Engines: Sources, Fuel Dependency, and Quantities". In: *Fuel* 338.October 2022 (2023). DOI: 10.1016/j.fuel.2022.127198.

[61] Kleeman, M. J., Riddle, S. G., Robert, M. A., and Jakober, C. A. "Lubricating oil and fuel contributions to particulate matter emissions from light-duty gasoline and heavy-duty diesel vehicles". In: *Environmental Science and Technology* 42.1 (2008), pp. 235–242. DOI: 10.1021/es071054c.

[62] Pirjola, L. et al. "Effects of fresh lubricant oils on particle emissions emitted by a modern gasoline direct injection passenger car". In: *Environmental Science and Technology* 49.6 (2015), pp. 3644–3652. DOI: 10.1021/es505109u.

[63] Sonntag, D. B., Bailey, C. R., Fulper, C. R., and Baldauf, R. W. "Contribution of lubricating oil to particulate matter emissions from light-duty gasoline vehicles in Kansas City". In: *Environmental Science and Technology* 46.7 (2012), pp. 4191–4199. DOI: 10.1021/es203747f.

[64] Guido, C., Di Maio, D., Napolitano, P., and Beatrice, C. "Sub-23 particle control strategies towards Euro VII HD SI natural gas engines". In: *Transportation Engineering* 10 (2022), p. 100132. DOI: 10.1016/j.treng.2022.100132.

[65] Napolitano, P., Di Maio, D., Guido, C., Merlone Borla, E., and Torbati, R. "Experimental investigation on particulate filters for heavy-duty natural gas engines: Potentialities toward EURO VII regulation". In: *Journal of Environmental Management* 331 (2023), p. 117204. DOI: 10.1016/j.jenvman.2022.117204.

[66] Jung, H., Kittelson, D. B., and Zachariah, M. R. "The influence of engine lubricating oil on Diesel nanoparticle emissions and kinetics of oxidation". In: *SAE Technical Papers* 724 (2003). DOI: 10.4271/2003-01-3179.

[67] De Petris, C., Giglio, V., and Police, G. "Some insights on mechanisms of oil consumption". In: *SAE Technical Papers* 412 (1996). DOI: 10.4271/961216.

[68] Christianson, M., Bardasz, E., and Nahumck, W. "Impact of lubricating oil condition on exhaust particulate matter emissions from light duty vehicles". In: *SAE Technical Papers* 3.2 (2010), pp. 476–488. DOI: 10.4271/2010-01-1560.

[69] Thomson, M. J. "Modeling soot formation in flames and reactors: Recent progress and current challenges". In: *Proceedings of the Combustion Institute* 39.1 (2023), pp. 805–823. DOI: 10.1016/j.proci.2022.07.263.

[70] Pejpichestakul, W. et al. "Examination of a soot model in premixed laminar flames at fuel-rich conditions". In: *Proceedings of the Combustion Institute* 37.1 (2019), pp. 1013–1021. DOI: 10.1016/j.proci.2018.06.104.

[71] Morgan, N. et al. "Mapping surrogate gasoline compositions into RON/MON space". In: *Combustion and Flame* 157.6 (2010), pp. 1122–1131. DOI: 10.1016/j.combustflame.2010.02.003.

[72] Pitz, W. J. et al. "Development of an experimental database and chemical kinetic models for surrogate gasoline fuels". In: *SAE Technical Papers* 2007.724 (2007), pp. 776–790. DOI: 10.4271/2007-01-0175.

[73] Appel, J., Bockhorn, H., and Frenklach, M. "Kinetic modeling of soot formation with detailed chemistry and physics: Laminar premixed flames of C2 hydrocarbons". In: *Combustion and Flame* 121.1-2 (2000), pp. 122–136. DOI: 10.1016/S0010-2180(99)00135-2.

[74] Ranzi, E. et al. "Hierarchical and comparative kinetic modeling of laminar flame speeds of hydrocarbon and oxygenated fuels". In: *Progress in Energy and Combustion Science* 38.4 (2012), pp. 468–501. DOI: 10.1016/j.pecs.2012.03.004.

[75] Wang, Y., Raj, A., and Chung, S. H. "A PAH growth mechanism and synergistic effect on PAH formation in counterflow diffusion flames". In: *Combustion and Flame* 160.9 (2013), pp. 1667–1676. DOI: 10.1016/j.combustflame.2013.03.013.

[76] Smith, G. P. et al. *http://www.me.berkeley.edu/gri_mech/*. Accessed on 2023-11-06.

[77] Ó Conaire, M., Curran, H. J., Simmie, J. M., Pitz, W. J., and Westbrook, C. K. "A comprehensive modeling study of hydrogen oxidation". In: *International Journal of Chemical Kinetics* 36.11 (2004), pp. 603–622. DOI: 10.1002/kin.20036.

[78] Tan, J. Y., Bonatesta, F., Ng, H. K., and Gan, S. "Developments in computational fluid dynamics modelling of gasoline direct injection engine combustion and soot emission with chemical kinetic modelling". In: *Applied Thermal Engineering* 107 (2016), pp. 936–959. DOI: 10.1016/j.applthermaleng.2016.07.024.

[79] Kennedy, I. M. "Models of soot formation and oxidation". In: *Progress in Energy and Combustion Science* 23.2 (1997), pp. 95–132. DOI: 10.1016/S0360-1285(97)00007-5.

[80] Khan, I.M., Greeves, G., and Probert, D.M. "Prediction of soot and nitric oxide concentrations in diesel engine exhaust". In: *Air Pollution Control in Transport Engines C* 142 (1971), pp. 205–217.

[81] Edelman, R. B. and Harsha, P. T. "Laminar and turbulent gas dynamics in combustors-current status". In: *Progress in Energy and Combustion Science* 4.1 (1978), pp. 1–62. DOI: 10.1016/0360-1285(78)90010-2.

[82] Hiroyasu, H. and Kadota, T. "Models for Combustion and Formation of Nitric Oxide and Soot in Direct Injection Diesel Engines." In: *SAE Prepr* 760129 (1976). DOI: 10.4271/760129.

[83] Dong, Z., Shuai, S., Wang, Z., and Zhao, H. "CFD Modeling of Mixture Preparation and Soot Formation in a Downsized Gasoline Direct Injection Engine". In: *SAE Technical Paper* (2016). DOI: 10.4271/2016-01-0586.

[84] Tesner, P. A., Smegiriova, T. D., and Knorre, V. G. "Kinetics of dispersed carbon formation". In: *Combustion and Flame* 17.2 (1971), pp. 253–260. DOI: 10.1016/S0010-2180(71)80168-2.

[85] Kennedy, I. M., Yam, C., Rapp, D. C., and Santoro, R. J. "Modeling and measurements of soot and species in a laminar diffusion flame". In: *Combustion and Flame* 107.4 (1996), pp. 368–382. DOI: 10.1016/S0010-2180(96)00092-2.

[86] Balthasar, M. and Kraft, M. "A stochastic approach to calculate the particle size distribution function of soot particles in laminar premixed flames". In: *Combustion and Flame* 133.3 (2003), pp. 289–298. DOI: 10.1016/S0010-2180(03)00003-8.

[87] Gelbard, F. and Seinfeld, J. H. "Simulation of multicomponent aerosol dynamics". In: *Journal of Colloid And Interface Science* 78.2 (1980), pp. 485–501. DOI: 10.1016/0021-9797(80)90587-1.

[88] Netzell, K., Lehtiniemi, H., and Mauss, F. "Calculating the soot particle size distribution function in turbulent diffusion flames using a sectional method". In: *Proceedings of the Combustion Institute* 31 I.1 (2007), pp. 667–674. DOI: 10.1016/j.proci.2006.08.081.

[89] Frenklach, M. "Method of moments with interpolative closure". In: *Chemical Engineering Science* 57.12 (2002), pp. 2229–2239. DOI: 10.1016/S0009-2509(02)00113-6.

[90] Frenklach, M. and Harris, S. J. "Aerosol dynamics modeling using the method of moments". In: *Journal of Colloid And Interface Science* 118.1 (1987), pp. 252–261. DOI: 10.1016/0021-9797(87)90454-1.

[91] McGraw, R. "Description of aerosol dynamics by the quadrature method of moments". In: *Aerosol Science and Technology* 27.2 (1997), pp. 255–265. DOI: 10.1080/02786829708965471.

[92] Yuan, C. and Fox, R. O. "Conditional quadrature method of moments for kinetic equations". In: *Journal of Computational Physics* 230.22 (2011), pp. 8216–8246. DOI: 10.1016/j.jcp.2011.07.020.

[93] Yuan, C., Laurent, F., and Fox, R. O. "An extended quadrature method of moments for population balance equations". In: *Journal of Aerosol Science* 51 (2012), pp. 1–23. DOI: 10.1016/j.jaerosci.2012.04.003.

[94] Salenbauch, S. et al. "Modeling soot formation in premixed flames using an Extended Conditional Quadrature Method of Moments". In: *Combustion and Flame* 162.6 (2015), pp. 2529–2543. DOI: 10.1016/j.combustflame.2015.03.002.

[95] Wallesten, J., Lipatnikov, A., and Chomiak, J. "Simulations of Fuel / Air Mixing , Combustion , and Pollutant Formation in a Direct Injection Gasoline Engine". In: *SAE Technical Paper Series* (2002).

[96] Etheridge, J., Mosbach, S., Kraft, M., Wu, H., and Collings, N. "Modelling soot formation in a DISI engine". In: *Proceedings of the Combustion Institute* 33.2 (2011), pp. 3159–3167. DOI: 10.1016/j.proci.2010.07.039.

[97] Wang, B. et al. "Modelling soot formation from wall films in a gasoline direct injection engine using a detailed population balance model". In: *Applied Energy* 163 (2016), pp. 154–166. DOI: 10.1016/j.apenergy.2015.11.011.

[98] Fontanesi, S., Del Pecchia, M., Pessina, V., Sparacino, S., and Di Iorio, S. "Quantitative investigation on the impact of injection timing on soot formation in a GDI engine with a customized sectional method". In: *International Journal of Engine Research* 23.4 (2022), pp. 624–637. DOI: 10.1177/1468087421993955.

[99] Cai, L., Ramalingam, A., Minwegen, H., Alexander Heufer, K., and Pitsch, H. "Impact of exhaust gas recirculation on ignition delay times of gasoline fuel: An experimental and modeling study". In: *Proceedings of the Combustion Institute* 37.1 (2019), pp. 639–647. DOI: 10.1016/j.proci.2018.05.032.

[100] Berni, F. et al. "Modeling of gaseous emissions and soot in 3D-CFD in-cylinder simulations of spark-ignition engines: A methodology to correlate numerical results and experimental data". In: *International Journal of Engine Research* 24.5 (2023), pp. 2149–2174. DOI: 10.1177/14680874221112564.

[101] Liang, L., Naik, C. V., Puduppakkam, K. V., Modak, A. U., and Meeks, E. "Application of Detailed Soot-Particle Model to Simulations of Fundamental Spray Experiments and GDI Engine". In: *International Multidimensional Engine Modeling User's Group Meeting* (2014).

[102] Jiao, Q. and Reitz, R. D. "Modeling soot emissions from wall films in a direct-injection spark-ignition engine". In: *International Journal of Engine Research* 16.8 (2015), pp. 994–1013. DOI: 10.1177/1468087414562008.

[103] Vishwanathan, G. and Reitz, R. D. "Development of a practical soot modeling approach and its application to low-temperature diesel combustion". In: *Combustion Science and Technology* 182.8 (2010), pp. 1050–1082. DOI: 10.1080/00102200903548124.

[104] Giovannoni, N. et al. "CFD Analysis of the Effects of Fuel Composition and Injection Strategy on Mixture Preparation and Fuel Deposit Formation in a GDI Engine". In: *SAE Technical Papers* 2015-September.September (2015). DOI: 10.4271/2015-24-2408.

[105] Frommater, S., Neumann, J., and Hasse, C. "A phenomenological modelling framework for particle emission simulation in a direct-injection gasoline engine". In: *International Journal of Engine Research* 22.4 (2021), pp. 1166–1179. DOI: 10.1177/1468087419895161.

Chapter 3

Resources and tools

This chapter depicts the main tools utilized throughout this thesis along with their implementation into the modeling framework. First, the tool which processes the engine test bench measurements providing key thermodynamic variables is discussed. Second, the 3D CFD model used for validating various sub-models that are developed in this thesis is presented. Third, the open-source tool Cantera is described. Fourth, the particle formation modeling techniques adopted are elaborated. Finally, the experimental campaign for soot emissions, carried out by a previous PhD candidate at CMT – Clean Mobility & Thermofluids at Universitat Politècnica de València, will be briefly depicted.

3.1 Combustion diagnostic tool

Crank angle and cycle resolved thermodynamic variables are the main inputs to the model. It is of utmost importance to ensure the accuracy of such variables as they have a great influence on particle formation processes. The input data were derived from an experimental campaign carried out by a previous PhD student at CMT – Clean Mobility & Thermofluids [1]. On the one hand, the instantaneous intake and exhaust pressures were measured by a Kistler 4045A5 piezoresistive pressure sensor with a Kistler Type 4603 amplifier. The in-cylinder pressure, on the other hand, was measured with a Kistler 6961A250 piezoelectric pressure sensor with a Kistler Type 5015 amplifier. For a more detailed description of the experimental facility, the reader

is referred to the doctoral thesis of Manuel E. Rivas Perea [1]. After acquiring the in-cylinder pressure, the signal is filtered and pegged with the intake pressure signal at Intake Valve Closure (IVC). With this information, the first law of thermodynamics is then applied between IVC and EVO coupled with the ideal gas equation of state for calculating the rate of heat release (ROHR) and mean gas temperature in the chamber. In addition to these equations, several sub-models are also implemented into the 0D thermodynamic model, called CALMEC, to compute the in-cylinder volume, mass, and wall temperatures. These sub-models include, but are not limited to, the following:

- A simplified filling and emptying model is used for calculating the trapped mass [2].
- A blow-by model based on the consideration of an adiabatic nozzle is used to compute the blow-by mass [3].
- A volume calculation model that takes into account mechanical deformations and piston eccentricity [4].
- A variation of the Woschni correlation is used for computing the heat transfer coefficient [5]. A lumped nodal model is used to calculate average wall temperatures [6].

The energy balance, shown in Equation 3.1, is then applied according to the first law of thermodynamics to compute the heat release.

$$dHR = pdV + dQ_w + m_c du_c - (h_{f,inj} - u_{f,g})dm_{f,ev} + R_c T dm_{bb} \tag{3.1}$$

The terms on the right hand side of Equation 3.1 represent the work done by the gas, heat transfer to the walls, sensible internal energy of the gas, energy related to fuel injection, evaporation, and heating up to the gas temperature, and the work done by the blow-by leakage, respectively. The rate of heat release can then be computed by directly dividing the dHR by the angle increment as $ROHR = dHR/d\alpha$. In order to close the energy balance, the equation of state is used:

$$pV = mR_c T \tag{3.2}$$

Equation 3.1 and Equation 3.2 are solved for each crank angle, depending on the resolution of the measured pressure signal, to obtain the instantaneous

pressure and temperature. In addition to pressure and temperature, additional variables are also calculated and include the instantaneous in-cylinder mass and composition, heat flux to walls, and cycle-averaged wall temperatures.

The main hypotheses that are considered by CALMEC are enumerated in the following:

- A uniform pressure throughout the combustion chamber is considered. This is valid since the flame propagation speed is much slower than the speed of sound.
- The gas in the chamber is composed of air, fuel, and burned products from stoichiometric combustion. Hence, in the calculation of gas thermodynamic properties, three species are considered.
- The gas mixture is assumed to behave as a perfect gas.
- Temperature correlations are used to calculate the sensible internal energy of the gas mixture.
- A mean and uniform gas temperature is employed for the calculation of internal energy. This is a very strong assumption, especially in the early phase of combustion, where the temperature of the burned products exceeds the mean temperature. Nevertheless, as combustion advances, the error diminishes owing to heat transfer and dilution which tend to make the temperature uniform.

Other variables of interest, calculated by CALMEC, are also required and fed to the PN/PM model. A summary of the main input variables obtained from CALMEC are tabulated in Table 3.1.

Table 3.1: Input variables obtained from CALMEC.

Instantaneous	Cycle average
In-cylinder pressure	Start of combustion
Gas temperature	Residual gas mass fraction
Cylinder volume	Global equivalence ratio
Burn rate	Exhaust temperature
Piston position	Wall temperatures*

* Wall temperatures include cylinder head, piston, and liner temperatures.

3.2 3D CFD model

A 3D CFD model of the engine under investigation was constructed specifically for validation purposes in this thesis. The experimental measurement campaign involved utilizing a metal engine setup to analyze engine-out soot particles, and so no information on in-cylinder processes was available as this would necessitate complex optical access. In such cases, 3D CFD proves invaluable, offering a means to visualize in-cylinder processes like mixture formation and spray-wall impingement. The primary focus was on simulating processes occurring before combustion begins, specifically addressing gas exchange, fuel injection, mixing, and wall film formation. Consequently, simulations were conducted from EVO to SOC and subsequently compared with dedicated sub-models developed in this research.

The engine is a *2.0 L Euro V* turbocharged gasoline direct injection engine with detailed geometrical and performance characteristics listed in Table 3.2. The side mounted injector is typical of wall-guided engines that re-directs the spray to the spark region, operating under the so-called stratified charge. However, in the operating conditions considered in this study, the engine operated under homogeneous combustion mode, meaning that the injection process occurred early during the intake stroke so as to achieve a homogenous mixture at spark timing. Furthermore, the engine operates with a fuel enrichment strategy under full load conditions to lower the exhaust gas temperature, thereby safeguarding the turbine of the turbocharger.

Table 3.2: Engine characteristics.

Engine	4-stroke SI
Number of cylinders	4
Valves per cylinder	4
Bore/Stroke	87.5/83.1 mm
Connecting rod length	156.15 mm
Compression ratio	10.2:1
Maximum power/speed	143/5000 kW/RPM
Maximum torque/speed	310/1750 Nm/RPM
Injection position/no. of holes	Side-mounted/7

Regarding the 3D CFD engine model, Converge CFD v3.1 [7], a commercial computational fluid dynamics software developed by Convergent Science, was the adopted software to perform the simulations. This code is broadly adopted in the internal combustion engine community due to its flexibility and simplicity in mesh generation and its capability of describing complex flow and

combustion processes. Additionally, it incorporates an adaptive mesh refinement (AMR) tool which scales the mesh in run-time to enhance the resolution of the numerical solution. A planar cut taken at the center of the cylinder depicting the mesh at different regions is shown in Figure 3.1. A base grid cell size of 4 mm was used with fixed embedding throughout the different regions. The regions near the walls of the piston, liner, and cylinder head were reduced to a minimum cell size of 1 mm to improve boundary layer predictions. Additionally, AMR was applied differently in two stages, an embedding level of 3 was first used from EVO until SOI achieving a minimum cell size of 0.5 mm. The solution was then mapped at SOI with the simulation now adopting four embedding levels. The AMR was applied based on velocity and temperature sub-grid scales of 1 m/s and 2.5 K, respectively. In this way, the mixing processes from SOI up to SOC was simulated with a greater level of detail while maintaining an acceptable computational time for the overall simulation.

The solution of the differential equations governing the fluid flow is achieved by the finite volume method. The Pressure Implicit with Splitting of Operators (PISO) algorithm is used to resolve the system of equations in each cell. Additionally, the discretization in space is performed by the central difference method whereas time discretization is of the first order implicit scheme. In addition to the numerical solution approach, appropriate models are also needed to describe the physical processes occurring during gas exchange and mixing. In this regards, the Reynolds-Averaged Navier Stokes (RANS) k-ϵ model was used to model turbulence. The Re-normalized Group (RNG) variant of the k-ϵ model was used to model the turbulent viscosity and close the equation of the strain rate tensor [8]. The Discrete Droplet Method (DDM), an Eulerian-Lagrangian coupling where the discrete liquid phase evolves and interacts with the Eulerian field, was used to model fuel injection [9]. Parcels were initialized with a diameter equal to the injector orifice diameter. Additionally, the liquid fuel species chosen to represent commercial gasoline in the experimental campaign was pure iso-octane. Consequently, a modification to the stoichiometric equivalence ratio of iso-octane was required when constructing the equivalence ratio distribution histogram. This adjustment was necessary because the inducted air mass and injected fuel mass in the simulation closely mirrored the measurements. The remaining sub-models, addressing aspects such as spray breakup and spray-wall interaction, are further detailed in Table 3.3.

In terms of initialization, the engine model was segmented into three regions: intake, exhaust, and cylinder. The simulation began at EVO, and therefore, the initial pressure values in the various regions were directly derived from the measured pressure signal. The temperatures were also measured in

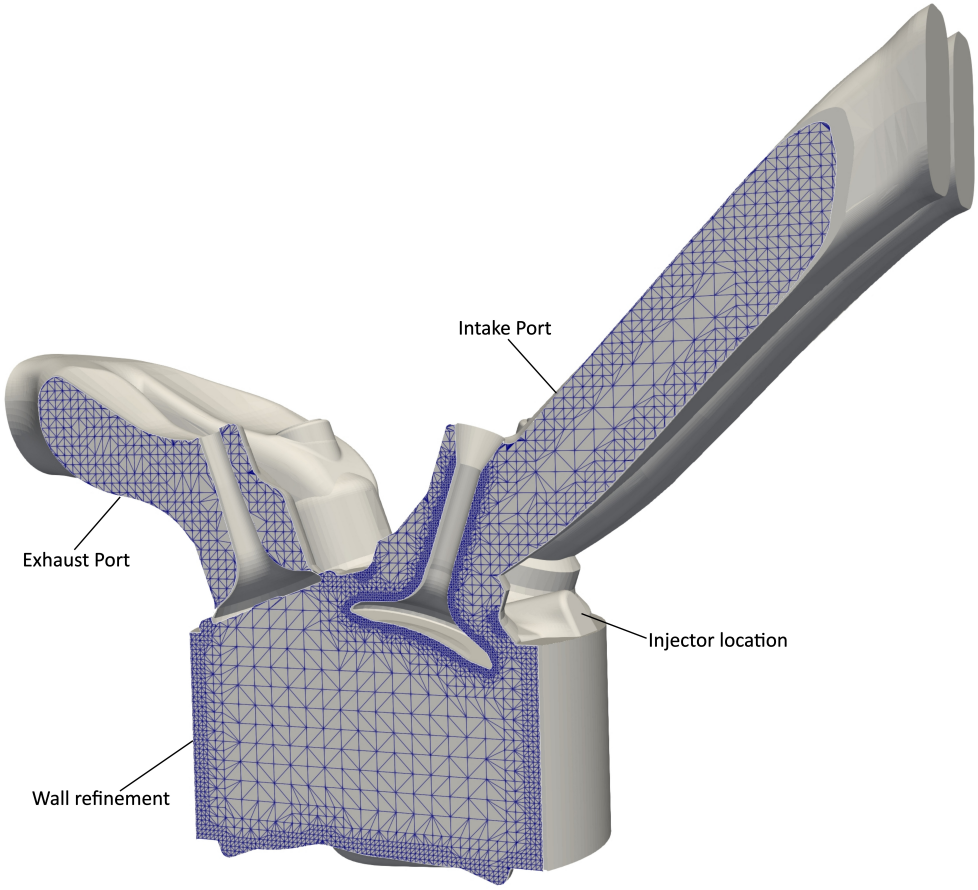

Figure 3.1: Computational domain and mesh details @ -277 bTDC.

the intake and exhaust regions so the values obtained from the thermocouples were used to initialize these domains. The in-cylinder temperature, however, was not measured but was obtained from CALMEC by the equation of state as explained in section 3.1 Additionally, the measured instantaneous pressure signals in the intake and exhaust manifold were applied as inflow and outflow boundary conditions, respectively. For this reason, Figure 3.1 shows intake and exhaust geometries that were cut-off at the point of the pressure sensor of the experimental set-up. Wall temperatures, obtained from the lumped model embedded in CALMEC, were utilized to define the temperatures of various engine components. The intake was initialized with a gas composition corresponding to pure air, given the absence of exhaust gas recirculation (EGR) for the considered operating points. Meanwhile, the gas composition of the cylinder and exhaust was initialized based on the burned products result-

Table 3.3: 3D CFD model setup.

Sub-models	
Spray	Langrange with KHRT breakup
Evaporation	Frossling
Drag	Dynamic drop drag
Equation of state	Redlich-Kwong
Turbulence	RNG k-ϵ
Wall-interaction	Bai-Gosman
Boundary conditions	
Inlet	pressure, temperature
Outlet	pressure, temperature
Wall	temperature
Moving	piston, valve lift

ing from combustion at the corresponding operating point's equivalence ratio. The evaluation of the 3D CFD simulations' accuracy was conducted by comparing the in-cylinder pressure with the measured signal from EVO to SOC. Figure 3.2 illustrates the achieved overall precision, indicating a numerical in-cylinder pressure within 5-7% of the measured values at SOC. This alignment ensures the reliability of the mixing process modeled by the numerical approach.

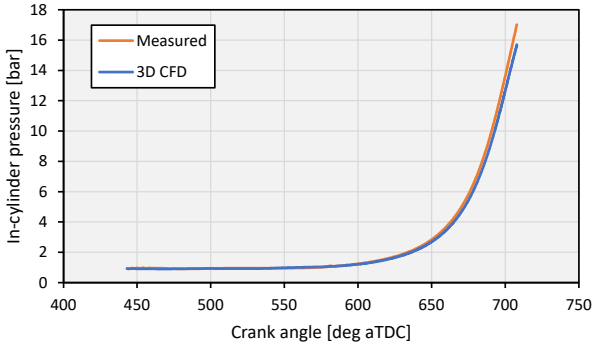

Figure 3.2: Comparison between measured and 3D CFD pressure trace.

3.3 Cantera

Cantera is an open-source tool for used for solving chemical kinetics, thermodynamics, and transport problems [10]. It has multiple interfaces and can be

conveniently installed as a MATLAB toolbox, which is particularly advantageous in the present context of the thesis. It automates the chemical kinetic and thermodynamic calculations so that detailed chemical mechanisms can be easily incorporated into the computations. In this regards, the chemical mechanism employed in this thesis has been transformed from the Chemkin format to a CTI file, which is compatible with Cantera for reading and processing. The mechanism used was that of Blanquart et al. [11] consisting of 149 species and 1651 reactions. The mechanism includes iso-octane as a fuel and encompasses reactions leading to the formation of precursors up to the fourth aromatic ring, pyrene (A_4). It has been validated for both diffusion and premixed flames with measured laminar burning velocities and ignition delay times. The results align closely with measurements across a wide range of equivalence ratios and pressures. Furthermore, the inclusion of chemistry pertinent to aromatic combustion and the combustion of larger alkanes, such as iso-octane, makes this mechanism a strong candidate for use in this investigation.

Cantera plays a pivotal role within the modeling framework, serving various purposes. Its primary function involves the creation of gas objects with specific compositions and thermodynamic states, facilitating the calculation of essential properties such as mixture density, gas molecular weight, and species reaction rates. Furthermore, Cantera is instrumental in determining adiabatic flame temperatures across different mixture compositions (equivalence ratios), a crucial aspect of one of the sub-models. Additionally, it proves useful for computing the composition of the burned gas mixture through the utilization of an equilibrium solver for given gas objects. As a result, its utility extends across multiple facets of the framework, establishing itself as an integral component of the overall model.

3.4 Method of moments

The application of the method of moments with interpolative closure in GDI soot modeling has been discussed previously in 2.3.2. The implementation of this method into the modeling framework will be discussed here. As mentioned before, MOMIC approximates the soot population balance equation by a discrete number of moments of soot transport [12]. The evolution of the soot particle size distribution can be depicted by the following equation:

$$\frac{\partial N(t,k)}{\partial t} = R(t)\delta_i^* + G(t,k) + W(t,k) \tag{3.3}$$

where *N(t,k)* is the particle number density for particle size k and time t, *R(t)* is the rate of particle inception, δ_i^* is the smallest particle size upon inception, *G(t,k)* is rate of particle coagulation, and *W(t,k)* is the rate of surface reactions. In MOMIC the particle size distribution can be represented by a series of moments:

$$M_r = \sum_{i=1}^{\infty} m_i^r N_i \tag{3.4}$$

where m_i is the mass of the particle of size i, r represents the r^{th} moment and N_i is the number density of particles in the i^{th} (diameter) bin. It can then be deduced that the zeroth moment (M_0) represents the particle number density. The first moment, M_1, is related to the soot volume fraction, the second and third moments of the particle size distribution represent the variance and skewness, respectively. If one would consider an infinite number of moments, then the full particle size distribution would be obtained. However, in most applications only a few moments are sufficient to obtain useful information about the properties of the PSD. The transport equation for moments can then be expressed in general form as:

$$\frac{\partial M_r}{\partial t} = f(M_r, \frac{\partial M_r}{\partial x_i}, Q_r), r = 0, ..., N_m - 1 \tag{3.5}$$

where M_r is the r^{th} moment, $\frac{\partial M_r}{\partial x_i}$ is the spatial variation of the r^{th} moment with respect to coordinate x_i, Q_r is the formation rate of the r^{th} moment, and N_m being the number of moments. Revzan et al. [13] developed a MOMIC routine in FORTRAN which calculates the moment rates, depending on the processes of inception, coagulation, and surface reactions, and also computes the species consumption/production rates due to particle formation. This routine was translated into MATLAB in order to better fit into the modeling framework and be easily coupled with the species conservation equations that will be detailed in the next chapter. Hence, the main inputs to the routine are the pressure, temperature, and the concentration of PAH, C_2H_2, CO, H, H_2, H_2O, O_2, and OH.

MOMIC routine models the soot particle inception by the dimerization of two PAH molecules, as expressed in:

$$R_0 = 2.2\sqrt{\frac{4\pi k_b T}{m_c n_{C,PAH}}} d_{PAH}^2 N_A^2 N_{PAH}^2 \tag{3.6}$$

where R_0 is the inception rate for the zero-th moment, k_b is the Boltzmann constant, T is the gas temperature, m_c is the mass of a carbon atom, $n_{C,PAH}$ is the number of carbon atoms in the PAH molecule, d_{PAH} is the diameter of the PAH molecule, N_A is the Avogadro's number, and N_{PAH} is the concentration of the PAH molecule. The inception rate for the following moments are then expressed as:

$$R_r = 2n_{C,PAH}R_{r-1} \quad r = 1, ..., N_m - 1 \tag{3.7}$$

A spatially homogenous particle ensemble is then considered for coagulation. The G source term in Equation 3.3 is evaluated for r number of moments. The coagulation source terms are represented by the following equations:

$$G_0 = \frac{1}{2}\sum_{i=1}^{\infty}\sum_{j=1}^{\infty}\beta_{ij}N_iN_j \tag{3.8}$$

$$G_r = \frac{1}{2}\sum_{k=1}^{r-1}\binom{r}{k}\left(\sum_{i=1}^{\infty}\sum_{j=1}^{\infty}m_i^k m_j^{r-k}\beta_{ij}N_iN_j\right) \quad r = 2, 3, ..., N_m - 1 \tag{3.9}$$

where β_{ij} is the collision coefficient between particle of size i and j. The specific form of β depends on the coagulation regime defined by the Knudsen number:

$$K_n = \frac{2\lambda_f}{d_s} \tag{3.10}$$

where λ_f is the gas mean free path and d is the soot particle diameter. The difficulty in solving the coagulation terms is due to the appearance of fractional order moments and due to the non-additive nature of the collision coefficient. This will be first demonstrated for the continuum regime ($K_n << 1$). In the continuum regime, the collision coefficient is expressed according to Seinfeld and Pandis [14] as:

$$\beta_{ij}^c = K_c\left(\frac{C_i}{m_i^{\frac{1}{3}}} + \frac{C_j}{m_j^{\frac{1}{3}}}\right)(m_i^{\frac{1}{3}} + m_i^{\frac{1}{3}}) \tag{3.11}$$

where $K_c = 2k_BT/3\eta$ and C is the Cunningham slip correction factor. Substituting Equation 3.11 into Equation 3.8, the following equation is obtained:

$$G_0 = K_c[M_0^2 + M_{\frac{1}{3}} M_{-\frac{1}{3}} + K_c^{'}(M_{-\frac{1}{3}} M_0 + M_{\frac{1}{3}} M_{-\frac{2}{3}})] \tag{3.12}$$

where $K_c^{'} = 2.514\lambda(\pi\rho/6)^{(\frac{1}{3})}$, ρ is the particle material density, and the moment order r is extended to include any real value. The appearance of this fractional moments introduce the so-called closure problem since these moment values are not solved for directly. Hence, a logarithmic interpolation scheme is applied among whole order moments to compute the fractional moments.

In the free-molecular regime (K_n»1), β_{ij} is expressed as:

$$\beta_{ij}^c = K_f \sqrt{\frac{1}{m_i} + \frac{1}{m_j}} (m_i^{\frac{1}{3}} + m_j^{\frac{1}{3}})^2 \tag{3.13}$$

where $K_f = \epsilon\sqrt{6k_BT/\rho}(3/4\pi\rho)^{\frac{1}{6}}$ and ϵ is the Van der Waals enhancement factor. The non-additive nature of the collision coefficient is thus evident and a specific treatment must be done in the free-molecular regime. First, a grid function in general form can be defined as:

$$f_l^{(x,y)} = \sum_{i=1}^{\infty}\sum_{j=1}^{\infty}(m_i + m_j)^l m_i^x m_j^y \left(m_i^{\frac{1}{3}} + m_i^{\frac{1}{3}}\right)^2 N_i N_j \quad l = 0, 1, 2, ... \tag{3.14}$$

Solving for the 0-th moment coagulation term requires $l = \frac{1}{2}$. Thus, Equation 3.8 can then be written as a function of the grid function:

$$G_0 = \frac{1}{2} K_{fm}^{'} M_0^2 f_{\frac{1}{2}}^{(0,0)} \tag{3.15}$$

Hence, a double interpolation is required here where the first consists of interpolating amongst the integer order grid function values at $l = 0, 1, 2, ..$, which in the case of $f_{\frac{1}{2}}$ would yield:

$$f_{\frac{1}{2}} = f_0^{\frac{3}{8}} f_1^{\frac{3}{4}} f_2^{-\frac{1}{8}} \tag{3.16}$$

Integer order grid functions (e.g f_0, f_1, etc.) can then be evaluated in terms of fractional-order moments again through interpolation as previously shown in the continuum regime.

Surface growth is modeled by the mass deposition on particle surface from the species present in the gas phase. To account for this, C_2H_2 is used in

HACA reactions while O_2 and OH are used in oxidation reactions. A total of six reactions are accounted for in the surface growth processes as displayed in Table 3.4.

Table 3.4: Surface growth reaction schemes.

Number	Reaction scheme
1	$C_{soot}H + H \overset{\leftarrow}{\rightarrow} C_{soot}\bullet + H_2$
2	$C_{soot}H + OH \overset{\leftarrow}{\rightarrow} C_{soot}\bullet + H_2O$
3	$C_{soot}\bullet + H \rightarrow C_{soot}H$
4	$C_{soot}\bullet + C_2H_2 \rightarrow C_{soot}H + H$
5	$C_{soot}\bullet + O_2 \rightarrow 2CO$ + products
6	$C_{soot}\bullet + OH \rightarrow CO$ + products

$C_{soot}\bullet$ denotes a radical site.

The surface reaction rates are then expressed as follows:

$$W_r^{C_2H_2} = k_4[C_2H_2]\alpha\chi C_{soot} \cdot \pi C_s^2 M_0 \sum_{l=0}^{r-1}(rl)\mu_{l+\frac{2}{3}}(2)^{r-l} \tag{3.17}$$

$$W_r^{O_2} = k_5[O_2]\alpha\chi C_{soot} \cdot \pi C_s^2 M_0 \sum_{l=0}^{r-1}(rl)\mu_{l+\frac{2}{3}}(-2)^{r-l} \tag{3.18}$$

$$W_r^{OH} = \gamma_{OH}[OH]\sqrt{\frac{\pi k_b T}{2m_{oh}}} N_A C_s^2 M_0 \sum_{l=0}^{r-1}(rl)\mu_{l+\frac{2}{3}}(-1)^{r-l} \tag{3.19}$$

where k_4 and k_5 are the kinetic rate coefficients for C_2H_2 and O_2, respectively. The species in braces represent the molar concentrations of the corresponding species, γ_{OH} is the collision efficiency for an OH radical, m_{oh} is the mass of an OH radical, C_s is the particle diameter, χC_{soot} is the number density of surface radicals, and α is the steric factor. The rate of surface reactions are mainly influenced by the overall surface area of particles and their corresponding number of active reaction (radical) sites available. Additionally, the fraction of reactive sites available for surface growth and oxidation reactions depends on the steric factor α which is calculated as a function of temperature and the first order reduced moment according to Appel et al. [15]. The reduced moments (μ_r) are defined as $\mu_r = M_r/M_0$. Finally, the r^{th} moment source term (Q_r) can be computed as the sum of the nucleation, coagulation, and surface growth and oxidation source terms as follows:

$$\frac{dM_r}{dt} = R_r + G_r + W_r \tag{3.20}$$

It must be noted that the zero-th moment (M_0) is only effected by the nucleation and coagulation source terms as there is no contribution from surface growth and oxidation reactions to particle number density in MOMIC.

As mentioned previously, the routine developed in [13] was translated into MATLAB language. Two main functions are incorporated into the routine. The first function, *initSoot*, must be called first. This function initializes the routine with the user input variables, such as the number of moments, coagulation regime considered (the user has the option to specify that the calculation of coagulation rates should only apply to the free-molecular regime), PAH inception species, diameter of the PAH species, etc. In this thesis, the number of moments was chosen to be six, all coagulation regimes were considered based on Knudsen number, and the inception species was considered to be the four-ring PAH molecule pyrene ($A4 - C_{16}H_{10}$). After the call to *initSoot*, a certain number of global coefficients are also made available in the MATLAB workspace and are necessary for the calculation of the different rate terms. The second function, *soot*, can then be called once the moment rates (Q_r) and the gas phase species source terms are to be computed. The moment rates are necessary for the moment conservation equations and the gas species source terms directly modify the chemical production rates of the species participating in nucleation and surface reactions. Hence, the input parameters to the *soot* function are the pressure, temperature, and the molar concentration of $C_{16}H_{10}$, C_2H_2, CO, H, H_2, H_2O, O_2, and OH, all of which must also be present in the chemical mechanism implemented in Cantera. In this way, the *soot* routine is called at each time step during combustion with the current thermodynamic state and species concentrations in order to obtain the moment rates and species source terms. The coupling between MOMIC and the species conservation equations will be detailed in the following chapter.

3.5 SWEEP

A population balance solver for particle systems was developed based on the Monte-Carlo method by researchers in the COMO group at the University of Cambridge [16]. The solver was implemented in FORTRAN90. To integrate it with the thesis model framework, an executable was generated and called from the MATLAB environment. In this way, the user would not have to perform the particle simulation separately in order to obtain the PSD at

simulation end. The gas phase chemistry profile obtained from the coupling between species conservation and MOMIC is provided to SWEEP along with the pressure and temperature profiles. The solver handles the population balance without being coupled to the gas phase. This poses no concern in this scenario, as MOMIC has already accounted for the effect of soot processes on species concentrations.

As mentioned in 2.3.2, the approach of the stochastic method does not require any assumptions to the shape of the size distribution function. No interpolation is required since the solver tracks individual particles and simulates their interaction over time in a probabilistic manner. Similarly to MOMIC, inception is two-body species collisions using the transition kernel of [17]:

$$R_{\text{inception}} = \frac{1}{2} k_{tr} N_A^2 C_A C_B \tag{3.21}$$

where k_{tr} is the transition regime coagulation kernel constant, N_A is the Avogadro's number, and C_A and C_B are the concentrations of the first and second inception species, respectively. The transition kernel is defined as:

$$k_{tr} = \frac{k_{fm} k_{sf}}{k_{fm} + k_{sf}} \tag{3.22}$$

The constant for the free-molecular kernel (k_{fm}) is defined as follows:

$$k_{fm} = 2.2 \sqrt{\frac{\pi k_B T}{2} (\frac{1}{m_A} + \frac{1}{m_B})} (d_A + d_B)^2 \tag{3.23}$$

where k_B is the Boltzmann constant, T is the temperature, m_i is the mass of the species i, and d_i is the collision diameter of species i. Moreover, the slip-flow kernel (k_{sf}) is defined as:

$$k_{sf} = \frac{2 k_b T}{3 \mu} (\frac{1 + 1.257 K_{n_A}}{d_A} + \frac{1 + 1.257 K_{n_B}}{d_B}) (d_A + d_B) \tag{3.24}$$

where μ is the viscosity of the gas, and K_{n_i} is the Knudsen number which quantifies the relative importance of the molecular mean path with respect to a characteristic length scale, taken at the diameter of the inception species in this case and calculated by:

$$K_{n_i} = (4.74 \times 10^{-8}) \frac{T}{P d_i} \tag{3.25}$$

where P is the pressure and d_i is the diameter of species i.

Coagulation, which decreases the particle number density, is modeled by the Smoluchowski coagulation equation which takes the form:

$$\frac{d}{dt}n(x) = \sum_{y=1}^{x-1} \beta(x-y,y)n(x-y)n(y) - \sum_{y=1}^{\infty} \beta(x,y)n(x)n(y) \tag{3.26}$$

where $n(x)$ is the number density of particles of type x and $\beta(x,y)$ is the coagulation kernel between particles of type x and y. The coagulation kernels for the different regimes have already been discussed earlier by the equations of inception.

Surface reactions involving C_2H_2 addition, through the HACA mechanism, and oxidation reactions by OH and O_2 have the general Arrhenius form:

$$R_{\text{surface}} = AT^n exp(-\frac{E}{RT}) \prod_{j=1}^{J} \theta_j^{p_j} \prod_{i=1}^{I} C_i^{\nu_i} \tag{3.27}$$

where A, n, and E represent the Arrhenius pre-exponential factor, temperature exponent, and activation energy, respectively. R is the gas constant and T is the temperature. θ_j is a property of the particle (e.g. volume (V), mass (m), diameter (d), active surface area (A_s), etc.) which is raised to some power p_j given by the reaction mechanism. J is the number of soot particle properties used in the rate expression. C_i is the concentration of species i, ν_i is the forward stoichiometric coefficient of species i, and I is the number of species on the reactant side of the reaction. The specific terms of each reaction are listed here below:

$$C_2H_2\, addition : 8.0 \times 10^7 T^{1.56}\, exp\left(\frac{-3.8}{RT}\right) \quad \theta = A_s, p = 1 \tag{3.28}$$

$$OH oxidation : 8.0 \times 10^{10} T^{0.734}\, exp\left(\frac{-1.43}{RT}\right) \quad \theta = d, p = 2 \tag{3.29}$$

$$O_2\, oxidation : 2.2 \times 10^{12}\, exp\left(\frac{-7.5}{RT}\right) \quad \theta = A_s, p = 1 \tag{3.30}$$

SWEEP has the possibility of it implementing different surface area models. The options include a constant value for the active surface area fraction (α), another option exists where the user can provide a profile with the chemistry inputs, or the ABF correlation can be used to compute α. Within this

thesis, α was used as a calibration constant as will be explained in the following chapters. Condensation reactions, which also fall under the umbrella of surface reactions, involve a free-molecular collision between the inception species and a soot particle. The condensation rate is represented by the following equation:

$$R_{\text{condensation}} = 2.2\eta C\sqrt{\frac{\pi k_B T}{2m}}(d^2 + 2dd_p + d_p^2) \tag{3.31}$$

where C, m, and d are the gas phase concentration (mol/cm^3), mass (g), and collision diameter (cm) of the condensing species respectively. d_p is the collision diameter of the particle and η being the efficiency of the collision.

The solver also requests the maximum stochastic particle count to be supplied by the user. This number represents the number of virtual soot particles that one stochastic particle encompasses. The choice of this value is a trade-off between computational time and accuracy. The property of the algorithm follows the law of large numbers in which the exact solution is approached as this parameter goes to infinity. A value of 2048 particles deemed adequate for this work. Additionally, the algorithm requires an estimation of the zero-th moment (M_0) to be provided as input and is used to set the internal scaling of the solver. This number should be set according to the expected maximum number density of the simulation. Setting a low estimation would result in SWEEP removing particles from the ensemble which would lead to possible inaccuracies in volume fraction calculations and high computational times. If it is set too low, then a complete removal of the particle ensemble results. If the estimation is set too high, the particle doubling algorithm would not work and one would risk not having enough particles to get a statistically meaningful solution. Hence, the developers of SWEEP [16] suggest an iterative process that begins by running a simulation with a value larger than the expected maximum zero-th moment and note the actual maximum value of M_0 observed. The simulation is then suggested to be relaunched with a slightly higher value for the maximum zero-th moment (5% higher) than the observed value. However, this might require numerous iterations until an acceptable value is reached. For this reason, the methodology suggested by Frommater [18] was used and convergence was reached in only a couple of iterations. Furthermore, it is commonly recommended to conduct multiple runs of the SWEEP solver to achieve a statistically comprehensive solution due to the probabilistic nature of the chosen physical processes. Nevertheless, a single execution of the solver demonstrated its reliability, resulting in a reduced time effort for each operating point.

At simulation end, CSV files are generated by the solver along with 99% confidence intervals. The output file contains statistical information and rate processes at each time step. In addition, particle size distributions could be saved at time steps of the user's choosing. This file is called the particle size list (PSL) output file where the volume, surface area, and diameter of each particle in the ensemble is given. The post-processing is then carried out offline in order to build the particle size histogram.

3.6 Experimental test bench

The measurements for characterizing particle size distributions under different engine speeds and loads was the main focus of a previous PhD student at CMT – Clean Mobility & Thermofluids. A brief description of the facility and sampling procedure will be discussed in the following paragraphs, however, for a complete detailed description of the campaign, the reader is referred to the thesis of Daniel Campos [19].

The GDI engine, whose specifications were outlined in section 3.2, was installed on a test bench equipped with a SCHENCK-Dynas3 LI250 asynchronous dynamometric brake that simulates a resistant load. The setup also has a tachometer that allows the measurement of the engine rotational speed and is able to measure speed in the range of 0 ± 1 to 10000 ± 1 RPM in addition to a torque meter that operates in the range of ± 650 Nm. The setup enables the engine to operate under constant speeds and loads as well as transient operation. The engine coolant and fuel are thermally controlled by heat exchangers with water supplied from a cooling tower. Proportional Integral Derivative (PID) controllers are used to regulate the engine coolant temperature by varying the water mass flow rate coming from the cooling tower. This system also allows the control of the intake air temperature thanks to an air-water heat exchanger. The intake air flow rate was measured by two methods. The first was through the engine's air flow meter that records the values in the ECU. The second method was through a hot plate anemometer, the ABB Sensycom Sensyflow-P 720 DN-80, which measures the airflow rate in the range of 40 to 720 kg/h [20].

The fuel in the experimental campaign was Gasoline with Research Octane Number (RON) 98 and was supplied by *Repsol S.A.* The fuel was characterized in a certified laboratory in order to identify its main properties, as a strong correlation between fuel properties and pollutant emissions exist as discussed in 2.2.4. A summary of the fuel properties is shown in Table 3.5. The fuel flow rate was also evaluated by a gravimetric system which incorporates the AVL-

733S Dynamic Fuel Meter. The measurement range of this device is between 0 and 75 kg/h with an accuracy of 0.12%, and permits a fuel consumption measurement frequency of 1 Hz [21].

Table 3.5: Fuel Properties.

Gasoline		
RON	[–]	98
Density @ 15 °C	[kg/m^3]	735.7
Lower heating value	[MJ/kg]	44.09
Sulphur content	[ppm]	4.3
Oxygen content	[wt%]	2
PAH content	[vol%]	22.9
Benzene content	[vol%]	0.68
$T_{10\%\ vol.}$ distillation temperature	[°C]	51.3
$T_{50\%\ vol.}$ distillation temperature	[°C]	85.8
$T_{90\%\ vol.}$ distillation temperature	[°C]	142.9

In this research, four operating conditions served as the foundation for validating the model. These conditions involve two different engine speeds and loads. Under full load conditions, the studied engine employs fuel enrichment to ensure that the exhaust gas temperature remains below the turbine's thermal limit. As a result, the global equivalence ratio falls below stoichiometry, exerting a notable impact on particle formation processes. Hence, analyzing the transition from medium to high load conditions provides a means to evaluate the collective influence of alterations in injector parameters and mixture formation on particle emissions. Moreover, variations in engine speed affect the mixture formation process, accelerating charge motion and mixing at higher speeds. Conversely, this acceleration shortens the time available for mixture preparation and wall film evaporation. Ultimately, the examination of all four operational points enables a thorough assessment of how changes in engine parameters impact soot formation pathways, establishing a robust database for validating simulations. A summary of the four operating conditions is provided in Table 3.6.

For each operating condition, the engine speed and load are first fixed. Subsequently, adjustments are made to the values of EGR rate, spark advance, variable valve timing, or throttle position based on the specific test requirements. The engine is operated for a specified duration until key parameters, including engine coolant temperature, exhaust temperature, injected fuel mass flow, intake temperature, and, if applicable, EGR rate and EGR outlet temperature, reach a stable state. After this duration, the particle emission

Table 3.6: Operation conditions.

Operating conditions	A50	A100	B50	B100
Engine speed [rpm]	2000	2000	3000	3000
BMEP [bar]	9.41	19.14	9.83	19.4
Injected fuel [mg/cc]	31.87	75.42	33.35	78.32
λ [-]	1.010	0.898	1.006	0.824
Spark timing [CAD bTDC]	17.1	5.25	21	13.5
Start of injection [CAD bTDC]	279.5	299.5	290.25	310.25
Intake pressure [bar]	0.947	1.708	0.977	1.746
Coolant temperature [°C]	90.5	90.5	90.87	91.17
EGR [%]	0	0	0	0

measurement system and exhaust gas analyzer are initiated, necessitating an additional stabilization period to ensure the accurate measurement of exhaust emissions. Once all the stabilization periods are achieved, the data acquisition process starts. The average signals are captured over a 60-second duration with a resolution of 0.1 seconds, while the instantaneous signals are recorded for 100 engine cycles with a resolution of 0.25 CAD.

3.6.1 Particle mass concentration

Particulate matter measuring instruments enable the distinction between the physical and chemical composition of soot, specifically the soluble organic fraction (SOF) and the insoluble fraction (ISF). The utilized device was the *HORIBA MEXA 1230-PM* analyzer, which continually assesses these two distinct fractions [22]. The measurement process is illustrated in Figure 3.3, where the exhaust gas sample passes through two main channels. The first channel directs the sample towards two HFID detectors, measuring light and heavy hydrocarbon components of SOF. The solid soot fraction is evaluated using the *TSI DCS-100* diffusion charger [23]. This device operates on the Brownian diffusion principle, where particles acquire a charge through collisions with electric ions. Once charged, the particles precipitate in an insulated electric filter, and the resulting current is amplified. The intensity of this current is then proportional to the mass of soot in the analyzed gas sample.

3.6.2 Particle number concentration

The particle number measurement process involved two devices located in series to each other. First, the exhaust gas sample is diluted by *DEKATI FPS-4000* [24] before it is introduced into the spectrometer, the *TSI EEPS-3090*

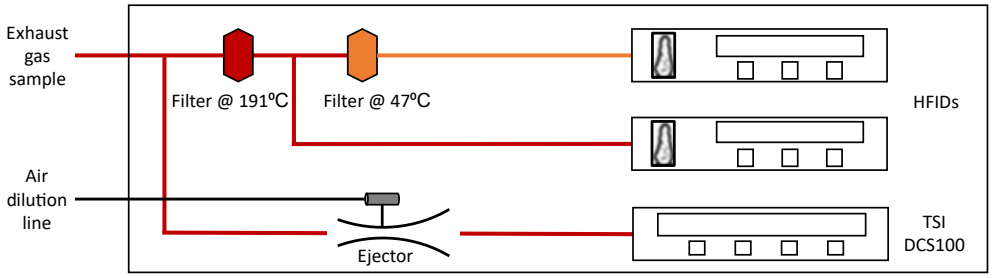

Figure 3.3: Horiba Mexa 1230-PM analyzer scheme. Adapted from [19].

[25], where the particle size distribution is measured. The exhaust gas sample undergoes two dilution stages in the *DEKATI FPS-4000*. The first occurs at a temperature similar to that of the exhaust gas in a porous tube diluter (PTD), allowing for an isothermal reduction of volatile concentration without generating new particles (process A to B in Figure 3.4). It should be mentioned that no catalytic stripper was used, as the experimental setup adhered to the Particle Measurement Program (PMP) protocol conditions. Before entering the second dilution stage, the particles pass through a heated residence chamber. Once stabilized, the second dilution stage takes place in an ejector diluter (ED), where mixing with cold air reduces the sample temperature and particle concentration (point D). The conditioned sample is then introduced into the spectrometer, which measures the particle concentration within a range spanning from 5.6 to 560 nm, utilizing 32 electrometers (representing particle diameters) for discretization. In this process, the measurement principle relies on the electrical mobility (Z_p) acquired by the particles, with the electrical mobility being a function of particle diameter. Initially, two unipolar chargers, arranged in series, impart a net positive charge to the particles. Subsequently, the charged particles traverse an electrostatic classification region, causing them to segregate based on their electrical mobility. This separation facilitates the instrument in determining particle size. The stages that the particles undergo are depicted in Figure 3.5. Once the particles are classified according to their sizes, a condensation particle counter (CPC) detects the quantity of particles within each size range, thereby continuously generating the particle size distribution. Figure 3.6 depicts the exhaust sampling procedure outlining the particle mass and number concentration measurements downstream of the three-way catalyst (TWC).

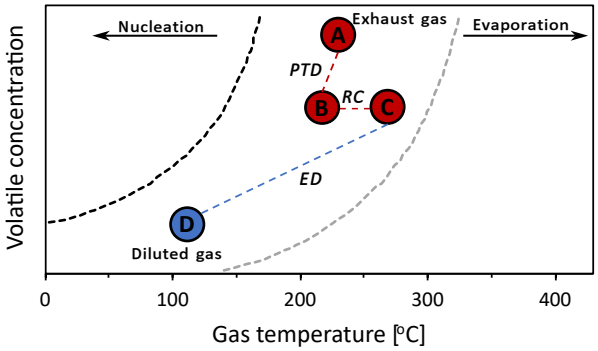

Figure 3.4: Phase diagram of the exhaust aerosol sample in the different stages of the dilution system. Adapted from [19].

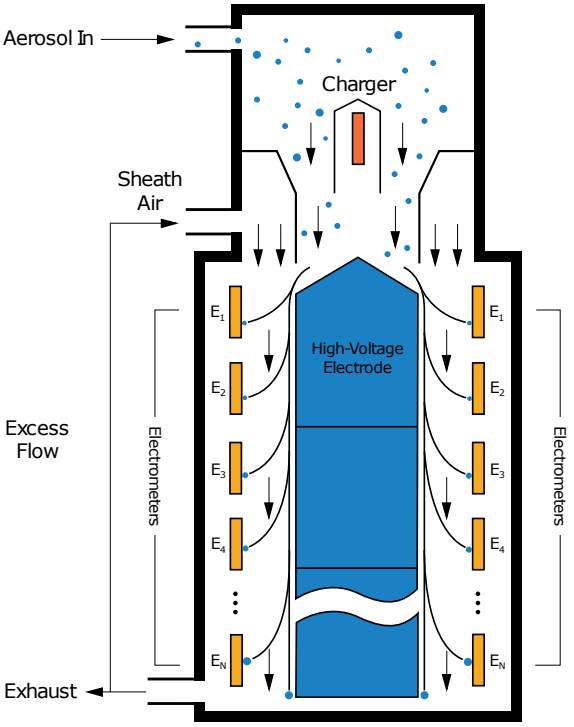

Figure 3.5: Engine exhaust particle sizer flow schematic. Source: TSI [26].

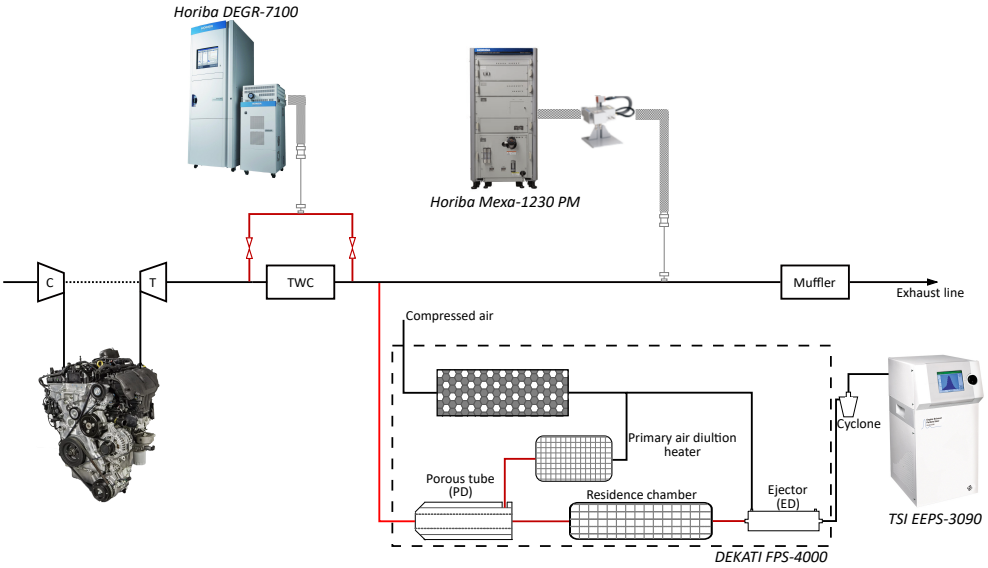

Figure 3.6: Schematic representation of the different equipment used for measuring PN/PM. Adapted from [19].

3.7 Summary

The numerical tools necessary to carry out the fundamental studies of soot formation were discussed along with the experimental test bench used to provide a set of validation data. The numerical framework was seen to comprise a set of tools that communicate with one another to provide a detailed understanding of particle formation processes in GDI engines. The model is based on a simplified mass based multi-zone approach developed in MATLAB that is coupled with a combustion diagnostic tool for providing main input variables, and a soot population balance Monte-Carlo tool for calculating particle processes. In addition, chemical kinetics was implemented into the main framework in MATLAB using Cantera's MATLAB toolbox.

An in-house combustion diagnostic tool, named CALMEC, employs the measured in-cylinder pressure obtained from the experimental test bench to derive key combustion variables, including the heat release law. Furthermore, CALMEC provides crucial output data, such as burned gas temperature, which serve as inputs to the particle model.

This chapter also included a detailed description of a 3D CFD engine model specifically developed for the study. The 3D CFD model functions as a validation tool for various soot pathway sub-models. Its primary role is to offer

insights into the spray mixing process, generating crucial information about equivalence ratio distributions. The model employs an RNG k-ϵ model for turbulence and adopts an Eulerian-Lagrangian approach for modeling liquid-gas phase interaction. Given its application in simulating gas exchange processes and fuel injection, the model's validation is conducted using the experimental pressure trace from EVO to SOC, meaning that only non-reactive simulations were performed, and no combustion model was applied.

The chemical mechanism was implemented by Cantera's MATLAB toolbox and was essentially dedicated to provide properties such as species formation rates, burned mixture density, and mean molecular weights. It does so by creating a gas object with the mixture composition at the current thermodynamic state. The chemical mechanism developed by Blanquart et al. [11] was used for this purpose since it involves a detailed description of the aromatic ring formation and growth up to the fourth aromatic ring considering iso-octane as fuel. Encompassing detailed PAH formation and growth has already been shown to be essential for predicting particle formation processes in Chapter 2.

Particle formation processes were approached by two modeling techniques. The first, the method of moments with interpolative closure, was primarily used to account for the effect of soot formation on gas phase species concentration. A detailed description of the method was provided along with its main simplifications of the soot population balance equation. The second, the Monte-Carlo tool called SWEEP, was described and the advantage of the stochastic method was portrayed in the mathematical formulations. Due to its nature, SWEEP is able to generate a stochastic set of particles at specific time steps that represent the soot population. In that way, one can build the soot size distribution evolution from SOC up to exhaust phase TDC.

Possessing a collection of experimental measurements is essential when the aim is to evaluate the accuracy of a model under development. The experimental campaign focused on validating a model under four operating conditions involving varying engine speeds and loads. Full load conditions included fuel enrichment to maintain exhaust gas temperature below the turbine's limit, impacting particle formation. Analyzing transitions from medium to high load conditions helps assess the effects of injector and mixture formation changes on particle emissions. Engine speed variations affect mixture formation, influencing charge motion and mixing. Examining all operating points enables a comprehensive evaluation of engine parameter changes on soot formation pathways. The experimental setup involves stabilizing key parameters before measuring exhaust emissions using a particle analyzer and gas analyzer. The measurement distinguishes between the physical and chemical composition of

soot, utilizing a HORIBA MEXA 1230-PM analyzer. The particle number measurement involves DEKATI FPS-4000 dilution stage before the exhaust gas sample is introduced into a TSI EEPS-3090 spectrometer, assessing particle size distribution. The measurement strategy established a robust particle emission database for validating the numerical simulations.

References

[1] Rivas Perea, M. E. "Assessment of fuel consumption reduction strategies on a gasoline turbocharged direct injection engine with a cooled EGR system". PhD thesis. Universitat Politècnica de València, 2016.

[2] Payri, F., Galindo, J., Martín, J., and Arnau, F. J. "A simple model for predicting the trapped mass in a DI diesel engine". In: *SAE Technical Papers* 2007.724 (2007). DOI: 10.4271/2007-01-0494.

[3] Payri, F., Olmeda, P., Martín, J., and García, A. "A complete 0D thermodynamic predictive model for direct injection diesel engines". In: *Applied Energy* 88.12 (2011), pp. 4632–4641. DOI: 10.1016/j.apenergy.2011.06.005.

[4] Payri, F., Molina, S., Martín, J., and Armas, O. "Influence of measurement errors and estimated parameters on combustion diagnosis". In: *Applied Thermal Engineering* 26.2-3 (2006), pp. 226–236. DOI: 10.1016/j.applthermaleng.2005.05.006.

[5] Payri, F., Margot, X., Gil, A., and Martin, J. "Computational study of heat transfer to the walls of a DI diesel engine". In: *SAE Technical Papers* 2005.724 (2005). DOI: 10.4271/2005-01-0210.

[6] Torregrosa, A. J., Olmeda, P., Martín, J., and Romero, C. "A tool for predicting the thermal performance of a diesel engine". In: *Heat Transfer Engineering* 32.10 (2011), pp. 891–904. DOI: 10.1080/01457632.2011.548639.

[7] *Converge CFD v3.1.* https://www.convergecfd.com/. Convergent Science Inc. 2022.

[8] Yakhot, V. and Orszag, S. "Renormalization group analysis of turbulence. I. Basic theory". In: *Journal of scientific computing* 1.1 (1986), pp. 3–51. DOI: 10.1007/BF01061452.

[9] Kong, S. C., Senecal, P. K., and Reitz, R. D. "Developments in spray modeling in diesel and direct-injection gasoline engines". In: *Oil and Gas Science and Technology* 54.2 (1999), pp. 197–204. DOI: 10.2516/ogst:1999015.

[10] Goodwin, D. G., Moffat, H. K., Schoegl, I., Speth, R. L., and Weber, B. W. *Cantera: An Object-oriented Software Toolkit for Chemical Kinetics, Thermodynamics, and Transport Processes*. `https://www.cantera.org`. Version 3.0.0. 2023. DOI: `10.5281/zenodo.8137090`.

[11] Blanquart, G., Pepiot-Desjardins, P., and Pitsch, H. "Chemical mechanism for high temperature combustion of engine relevant fuels with emphasis on soot precursors". In: *Combustion and Flame* 156.3 (2009), pp. 588–607. DOI: `10.1016/j.combustflame.2008.12.007`.

[12] Frenklach, M. "Method of moments with interpolative closure". In: *Chemical Engineering Science* 57.12 (2002), pp. 2229–2239. DOI: `10.1016/S0009-2509(02)00113-6`.

[13] Revzan, K. L., Brown, N. J., and Frenklach, M. `http://www.me.berkeley.edu/soot/`. 1999.

[14] Seinfeld, J. H., Pandis, S. N., and Noone, K. "Atmospheric Chemistry and Physics: From Air Pollution to Climate Change". In: *Physics Today* 51.10 (1998), pp. 88–90. DOI: `10.1063/1.882420`.

[15] Appel, J., Bockhorn, H., and Frenklach, M. "Kinetic modeling of soot formation with detailed chemistry and physics: Laminar premixed flames of C2 hydrocarbons". In: *Combustion and Flame* 121.1-2 (2000), pp. 122–136. DOI: `10.1016/S0010-2180(99)00135-2`.

[16] Patterson, R.I. and Celnik, M. *SWEEP2: Cambridge Soot Simulator*. `http://como.cheng.cam.ac.uk`. 2006.

[17] Patterson, R. I., Singh, J., Balthasar, M., Kraft, M., and Wagner, W. "Extending stochastic soot simulation to higher pressures". In: *Combustion and Flame* 145.3 (2006), pp. 638–642. DOI: `10.1016/j.combustflame.2006.02.005`.

[18] Frommater, S. "Phenomenological modelling of particulate emissions in direct injection spark ignition engines for driving cycle simulations". PhD thesis. TU Darmstadt, 2018.

[19] Campos, D. "Estudio De Las Emisiones De Escape En Motores De Combustion Interna Alternativos Utilizando Diferentes Sistemas De Control De Contaminantes". PhD thesis. Universitat Politècnica de València, 2016.

[20] ABB Sensyflow. *Thermal air-mass flowmeter for test rigs and quality assurance. Operation and Service manual.*

[21] AVL 733S Dynamic Fuel Meter. *AVL LIST GMBH. Graz. User Manual.*

[22] HORIBA MEXA 1230-PM. *Particle Matter Exhaust Gas Analyzer. HORIBA GmbH. user Manual.*

[23] TSI. *Model DCS-100. Diffusion charging sensor. Operation and Service Manual.*

[24] DEKATI. *Model FPS-4000. Fine Smart Particle Sampler. User manual.*

[25] TSI. *Model EEPS-3090. Engine Exhaust Particle Sizer Spectrometer. Operation and Service Manual.*

[26] TSI. *Engine Exhaust Particle Sizer Spectrometer Model 3090 Spec Sheet.*

Chapter 4

Modeling methodology

The previous chapter delved into the primary tools, encompassing both numerical and experimental aspects, essential for conducting the current study. This chapter will now outline and elaborate on the central aspects of the modeling methodology. Initially, it involves an examination of gas phase kinetics using a multi-zone approach to calculate the evolution of species profiles throughout combustion until the exhaust phase top dead center. Within this framework, the conservation equations will be presented and the interaction between the gas and solid phase explained. Following that, an overview of the simulation chain will be provided, highlighting the various soot pathways considered in this investigation. Finally, the validation process and comparison with experimental measurements will be discussed.

4.1 Gas phase initialization

The utilization of multi-zone modeling has been widely adopted for the prediction of gaseous emissions in diverse combustion modes [1–3]. In numerous applications, CFD simulations are employed to model the gas exchange process, serving as the basis for initializing the zones. This approach enables the application of detailed chemistry in combustion while still maintaining a reasonable computational time. This methodology has already been applied in various combustion modes, such as Homogeneous Charge Compression Ignition (HCCI) and Premixed Charge Compression Ignition (PCCI), where temperature and fuel stratification serve as inputs for multi-zone 0D models

[4, 5]. These models are particularly well-suited for these engine types as the division of the chamber into homogeneous zones aligns well with the characteristics of HCCI and PCCI combustion, making it a robust assumption. In Baratta et al. [1], a multi-zone thermodynamic model was coupled with a detailed chemical mechanism for Compressed Natural Gas (CNG) combustion in which each zone was considered as a 0D homogenous batch reactor. Their modeling strategy showed better engine-out species prediction compared to simplified chemical reaction schemes and equilibrium assumptions. Similarly to the aforementioned methodologies, a multi-zone approach was adopted in this study in order to identify zones within the combustion chamber that exceed the soot threshold for iso-octane combustion. The zones are based on the gas phase mixture and liquid films. The idea here is that each zone would consist of a pair of Perfectly-Stirred Reactors (PSR) with an entrainment from the unburned reactor to the burned reactor based on the zone specific mass flow.

Initially, the definition of zones is based on the Probability Density Function (PDF) of the equivalence ratio at SOC. This data can be derived either from 3D CFD simulations, simplified 1D spray models, or empirical models. The specifics of these models will be discussed in the subsequent chapter, particularly in the context of the mixing model. Thus, the modeling framework commences by considering the fuel mass versus equivalence ratio distribution function, which assesses the quantity of fuel mass at different equivalence ratio values. In such a scenario, a perfectly homogeneous mixture would yield a single zone at the overall ϕ value, while inadequate mixture preparation would lead to a greater number of zones. An example of such a distribution function is shown in Figure 4.1, in which a total of 6 zones were defined. Zone definition is first based on the selection of a fixed $\Delta\phi$ increment and by specifying the maximum fuel fraction value $f(\phi_{max})$.

In this study, the $\triangle\phi$ was taken to be 0.05, whereas the maximum value of the integral fuel fraction was considered to be 0.999. The ϕ_{max} is then obtained at this fuel fraction value. Additionally, a soot threshold must be defined in order to perform the division of zones between this value and the maximum equivalence ratio ϕ_{max}. The studies previously mentioned in section 2.2 have shown that the soot mass concentration notably increased for C/O higher than $\approx$ 0.44-0.46 when performing a ϕ sweep of a premixed charged of iso-octane and toluene [6]. Additionally, a similar threshold was observed in CH_4/O_2 flames investigated optically by Alessio et al. [7]. This range of values correspond to an equivalence ratio of about 1.4 for iso-octane combustion. Hence, this was the sooting threshold considered in this study for all operating

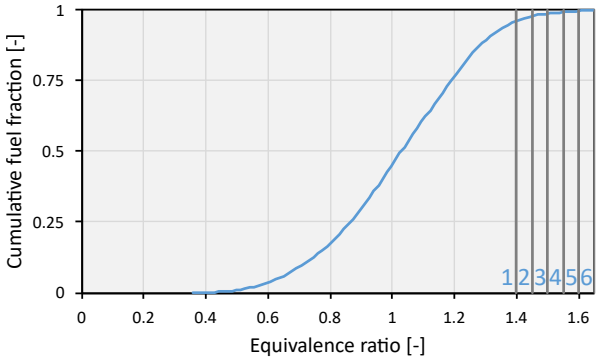

Figure 4.1: Integral fuel fraction with respect to ϕ. Zone boundaries are depicted by the vertical gray lines.

conditions. With the sooting threshold now defined, the number of zones can be determined using the following equation:

$$n_{zones} = \frac{\phi_{max} - \phi_{thresh}}{\Delta\phi} + 1 \tag{4.1}$$

In the case illustrated in Figure 4.1, a total of six zones were identified, with five surpassing the sooting threshold. After establishing the boundaries for these zones, it becomes possible to extract the mean ϕ within each zone, along with the associated total fuel fraction. Given the sufficiently small selected $\Delta\phi$, the mean value converges towards the mass-averaged ϕ value within each zone. Regarding the fuel mass below the sooting threshold, the total mass is lumped into one zone at the global ϕ value of the operating point.

This procedure is only aimed at defining the mixture induced rich zones. However, liquid film zones are initialized in a different way. The treatment of these zones will be thoroughly discussed in the respective sub-model chapters later on. Nevertheless, the initialization of the zones is done in the same way as the gas phase zones. The details of the zone mixture composition will be outlined next.

4.1.1 Zone composition

Now that each zone is identified by integral fuel fraction and the equivalence ratio, the gas composition of each zone can then be derived. First, the total fuel mass in each zone can be calculated since the total fuel fraction and total injected fuel mass are known quantities:

$$m_{f_j} = FF_j \cdot m_{f,total} \quad j = 1, 2, ..., n_{zones} \tag{4.2}$$

where FF_j is the total fuel fraction in each zone, $m_{f,total}$ is the total injected fuel mass, and j is the zone number. The air mass in each zone can then be calculated with the knowledge of the zone specific ϕ_j according to the following equation:

$$m_{a_j} = \frac{m_{f_j} (A/F)_{st}}{\phi_j} \tag{4.3}$$

where m_{f_j} is the zone fuel mass, $(A/F)_{st}$ is the stoichiometric air-to-fuel ratio of iso-octane, and ϕ_j being the zone specific equivalence ratio. Then, the residual mass in each zone is defined based on the knowledge of the ϕ_j and the residual gas mass fraction (Y_{res}) of the operating point. The residual gas mass is the sum of the exhaust gas recirculated (EGR) mass and the residual mass remaining in the clearance volume. Hence, the residual gas mass in each zone is computed according to the following equation:

$$m_{res_j} = \frac{Y_{res} \left(\frac{(A/F)_{st}}{\phi_j} + 1 \right)}{1 - Y_{res}} m_{f_j} \tag{4.4}$$

Finally, the total unburned mass in each zone can be calculated as the sum of the fuel, air, and residual gas mass:

$$m_{ub_j} = m_{f_j} + m_{a_j} + m_{res_j} \tag{4.5}$$

The sum of unburned masses in each zone should equate to the trapped mass at intake valve closure obtained from CALMEC. With the knowledge of the mass, the volume in each zone can also be computed by the ideal gas law at the current thermodynamic state:

$$V_{ub_j} = \frac{m_{ub_j} R T_{ub}}{MW_{global} p_{cyl}} \tag{4.6}$$

where R is the universal gas constant of the unburned mixture, T_{ub} is the unburned mixture temperature, MW_{global} is the mean molecular weight, and p_{cyl} is the in-cylinder pressure. The composition of the residual gas is obtained through the utilization of an equilibrium solver in Cantera with the thermodynamic state at SOC time and the zone's equivalence ratio. The stoichiometric coefficients of iso-octane combustion with air are used according to the following chemical reaction:

$$I - C_8H_{18} + \frac{25}{2}(O_2 + 3.76N_2) \longrightarrow 8CO_2 + 9H_2O + 3.76\frac{25}{2}N_2 \tag{4.7}$$

The residual gas is considered to be constituted of CO, CO_2, H_2O, and O_2, while the rest of the minor species are lumped into N_2. The equilibrium solver returns the species mass fractions of the previously mentioned burned species which enables the calculation of the species mass in the burned state. In a specific zone, the burned mass of a species can be computed by:

$$m_{b_i} = Y_{b_{i,eq}} m_{res} \tag{4.8}$$

where $Y_{b_{i,eq}}$ is the equilibrium concentration of species i. The total species mass fraction in the unburned reactor can then be computed as the sum of the fresh species mass fractions (representing the fresh charge) and the burned species mass fractions (accounting for the residuals):

$$Y_{O_2} = \frac{0.233 m_a + m_{b_{O_2}}}{m_{ub}} \tag{4.9}$$

$$Y_{N_2} = \frac{0.767 m_a + m_{b_{N_2}}}{m_{ub}} \tag{4.10}$$

$$Y_{[CO,CO_2,H_2O]} = \frac{m_{b_{[CO,CO_2,H_2O]}}}{m_{ub}} \tag{4.11}$$

$$Y_{IC_8H_{18}} = \frac{m_f}{m_{ub}} \tag{4.12}$$

Carrying out this deduction for all zones $j = 1, ..., n_{zones}$, one would define the unburned mixture composition at SOC.

Each zone comprises an unburned reactor, initialized through the previously described procedure, and a burned reactor. The burned reactor within each zone is initialized using the equilibrium solution obtained from the unburned zone. Specifically, a Cantera gas object is created with the composition of the unburned mixture and is evolved to equilibrium. This methodology is commonly adopted due to the unknown initial species concentrations in the burned zone. Additionally, setting the initial burned zone volume to a small but non-zero value, 10^{-30} m^3 in this study, is necessary to prevent stability issues. It is important to note that the initial burned zone volume at the SOC is effectively zero since the entire chamber is in an unburned state. As combustion progresses, the burned volume increases as the unburned volume is consumed.

The reactor pairs within each zone operate independently, implying a lack of interaction between different pairs. In each reactor pair, there is a mass flow from the unburned reactor to the burned reactor, carrying the unburned mixture composition and regulated by the physical combustion speed. This variable, known as the burn rate or the derivative of the burned fuel mass fraction, mirrors the propagation of the flame front and the consumption of unburned mass in two-zone SI combustion models.

4.1.2 Mass flow variable

The unburned mass flow connecting the reactor pair in each zone dictates the unburned species mass transfer to the burned zone. This process in illustrated schematically by Figure 4.2.

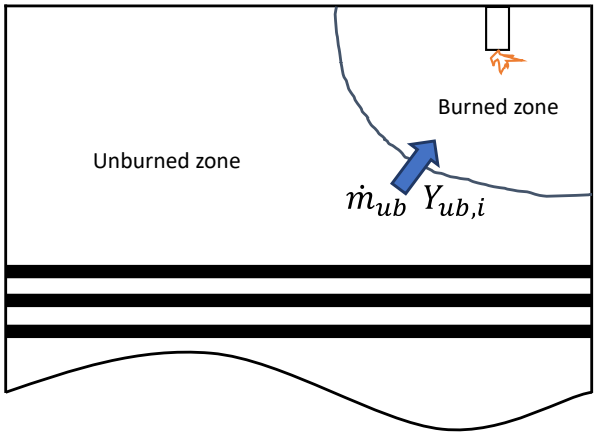

Figure 4.2: Unburned mass flow rate from the unburned to burned reactor with the unburned mixture composition.

The flow consists of the fuel, air, and residual gas mass flows, which are to be computed for each zone. Hence, the fuel mass flow between the reactors depends on the burn rate, derived from the measured in-cylinder pressure signal, and the fuel mass in a given zone which is obtained from the equivalence ratio distribution function. In mathematical terms, this is represented by the following equation:

$$\frac{dm_{f_j}}{dt} = m_{f_j} \frac{dY_{f,b}}{dt} \tag{4.13}$$

where $\frac{dY_{f,b}}{dt}$ is the burn rate.

Since the equivalence ratio in each zone is known, the air mass flow can then be deduced:

$$\frac{dm_{a_j}}{dt} = \frac{dm_{f_j}}{dt}\frac{(A/F)_{st}}{\phi_j} \tag{4.14}$$

And similarly to Equation 4.4, the residual gas mass flow from the unburned reactor to the burned reactor can be computed from the knowledge of the global residual gas mass fraction Y_{res}:

$$\frac{dm_{res_j}}{dt} = \frac{Y_{res}\left(\frac{dm_{f_j}}{dt} + \frac{dm_{a_j}}{dt}\right)}{1 - Y_{res}} \tag{4.15}$$

The total unburned mass flow is then the sum of Equation 4.13, Equation 4.14, and Equation 4.15:

$$\frac{dm_{ub_j}}{dt} = \frac{dm_{f_j}}{dt} + \frac{dm_{a_j}}{dt} + \frac{dm_{res_j}}{dt} \tag{4.16}$$

4.2 Conservation equations

The conservation equations are developed and solved for the burned reactor in zones where soot formation is expected, namely those exceeding the sooting threshold. The conservation equations in the burned reactor are analogous to those of a PSR. The species participating in the reactions have very high mixing rates and are assumed to be spatially uniform. Such type of reactors have been frequently used in order to predict particle size distributions under varying parameter sweeps, such as equivalence ratios and fuel aromatic content [8, 9]. The conservation equations of mass, species, and energy are detailed in the following sections.

Mass conservation

Mass is conserved between the unburned and burned reactors meaning that the inflow mass and outflow mass equate to the rate of change of mass in the reactor. This is mathematically represented by the following equation:

$$\frac{d(\rho V)}{dt} = \dot{m}_{in} - \dot{m}_{out} \tag{4.17}$$

In the burned zone of an ICE, the only mass flow is from the unburned reactor (Equation 4.16). The second term on the right hand side of Equation 4.17 is omitted, and the equation becomes:

$$\frac{dm_b}{dt} = \dot{m}_{ub} \tag{4.18}$$

where the term $\frac{dm_b}{dt}$ represents the rate at which mass changes in the burned reactor. Consequently, with the advancement of the combustion process, unburned mass transforms into burned mass until the entire unburned mass is depleted, terminating combustion. It is essential to note that blow-by is not considered in this model, meaning that there is no assumed gas leakage beyond the piston rings. Having information about the mass variation in the burned zone, the volume can be determined using the ideal gas law, as demonstrated earlier in Equation 4.6. However, in this context, the computation involves specifying the mass, temperature, and mean molecular weight of the burned gases. The mass within each zone remains constant once combustion concludes, with the cumulative mass of all zones equaling the in-cylinder trapped mass. Conversely, the combined volume of all zones aligns with the in-cylinder volume only until EVO, after which the volume expands into the exhaust. Accurate volume calculations are crucial for determining particle number and mass concentrations. Since the measured particle data was collected downstream of the exhaust manifold, the simulation extends beyond EVO to the TDC exhaust phase. This approach ensures that particle processes occurring in the exhaust manifold are appropriately considered by the model.

Energy conservation

The system of differential equations doesn't include a separate energy equation as the burned gas temperature, calculated using CALMEC, is applied. Given that CALMEC already incorporates energy conservation while determining gas temperature, the temperature profile serves as input for the model. However, this temperature profile represents the average value in the cylinder at the global equivalence ratio. To address the expected lower temperature values in fuel rich zones compared to the global value, a correction is necessary for this global temperature profile. The correction is made by utilizing the adiabatic flame temperature of the fuel rich zones. This is done in order to provide a reference value of the burned gas temperature in fuel rich zones under idealized conditions.

The procedure is to first create an ideal gas mixture for each zone with the zone specific equivalence ratio. Then, the system of ordinary differential

equations for a constant volume, adiabatic, zero-dimensional reactor is solved by an *ode*15*s* function in MATLAB. In this way, the computed temperature would represent the adiabatic flame temperature of the zone. Additionally, the adiabatic flame temperature of the global zone at the global equivalence ratio is obtained. The adiabatic flame temperatures of each zone are then divided by the global adiabatic temperature value. Consequently, a global correction factor for zones exceeding the sooting threshold is computed as the mass-averaged value, as shown in the following equation:

$$CF = \frac{\sum_{j=2}^{n_{zones}} \frac{T_{ad,j}}{T_{ad,global}} \cdot m_{ub_j}}{\sum_{j=2}^{n_{zones}} m_{ub_j}} \tag{4.19}$$

The summation iterator in Equation 4.19 initiates from $j = 2$ due to the exclusion of the correction factor for the global zone (below the sooting threshold) from the averaging process. The temperature reduction in fuel-rich zones is achieved by multiplying the correction factor with the overall temperature profile. Subsequently, since the burned gases propagate into the exhaust manifold post-EVO, a minimum temperature profile is enforced, corresponding to the average exhaust temperature. Consequently, the final temperature profile utilized is illustrated in Equation 4.20. It's worth noting that the methodology outlined here has been previously employed in the works of Frommater et al. [10].

$$T_b = max(T_{global} \cdot CF, T_{exh}) \tag{4.20}$$

Species conservation

The equations governing species conservation bear a resemblance to those applied in well-stirred reactors. The progression of mass fractions for each species in a burned state is contingent upon both the molar production rate of that species and the incoming mass flow from the unburned mixture. Consequently, the species conservation equations encompass two primary phenomena. The first pertains to the chemical processes, relying on the existing thermodynamic state and the composition of the burned gas, influencing the creation or depletion of the species. The second is associated with the combustion rate, characterized by the inflow of mass from the unburned mixture into the burned reactor. For each species i, the rate of change of mass fraction can be written as:

$$\frac{dY_{b,i}}{dt} = \frac{\dot{\omega}_i MW_i}{\rho_b} + \frac{\dot{m}_{ub}}{m_b} \left(Y_{ub,i} - Y_{b,i}\right) \tag{4.21}$$

where $\dot{\omega}_i$ represents the net chemical production rate for species i, MW_i denotes the molecular weight of species i, ρ_b stands for the density of the burned mixture, and $Y_{b,i}$ signifies the mass fraction of species i in the burned state. The variables influencing the term associated with reaction chemistry are acquired through a Cantera gas object call. In each iteration, a gas object is generated with the current thermodynamic state and burned mixture composition. Utilizing this information, Cantera returns the chemical production term for each species and the density of the burned mixture. Moreover, a closer examination of Equation 4.21 underscores the necessity to initialize the burned reactor volume with a non-zero value, given that the burned mass appears in the denominator. Furthermore, after combustion ends, the term on the right-hand side of Equation 4.21 approaches zero, resulting in the species evolution being solely contingent on their chemical formation rate.

Moment conservation

Equation 4.21 does not consider the effect of particle formation on gas phase species mass fractions. As mentioned in Chapter 3, the method of moments is incorporated into the framework in order to evaluate the influence of species formation or consumption due to soot processes. To do so, six additional equations are added to the 149 equations (1 equation for mass conservation and 148 for species conservation) for the moment transport. The moment rates are represented by:

$$\frac{dM_r}{dt} = Q_r \tag{4.22}$$

where r represents the moment number within the range of 0 to 5 (it is customary for moment indices to commence with 0). The rate of the r^{th} moment, denoted as Q_r, encompasses the summation of nucleation, coagulation, and surface reaction rate terms, as defined by Equation 3.20. Consequently, Equation 4.22 mirrors Equation 3.20, except that the right-hand side expression is expressed as a single term. The challenge arises from the fact that the moment values and rates are orders of magnitude larger than species mass fractions, leading to a stiffness issue in solving the system of differential equations. To address this concern, Equation 4.22 is reformulated in terms of the natural logarithm of the moment value:

$$Y_r = log(M_r) \tag{4.23}$$

which re-structures the moment rate equation to:

$$\frac{dY_r}{dt} = \frac{Q_r}{M_r} \tag{4.24}$$

This significantly reduces the stiffness of the system of equations since the moment rates are normalized by the moment values. A call to the MOMIC routine also returns adjustments to the rates ($\dot{\omega}_i$) of certain species to account for the consumption or production of these species due to particle formation, coagulation, surface growth, and oxidation. Therefore, Equation 4.21 is re-written in terms of the adjusted chemical rate term:

$$\frac{dY_{b,i}}{dt} = \frac{\dot{\omega}_i^{'} M_i}{\rho_b} + \frac{\dot{m}_{ub}}{m_b}\left(Y_{ub,i} - Y_{b,i}\right) \tag{4.25}$$

where $\dot{\omega}_i^{'}$ is expressed as:

$$\dot{\omega}_i^{'} = \dot{\omega}_i + \dot{\omega}_{soot} \tag{4.26}$$

Here, $\dot{\omega}_{soot}$ represents an array of soot production rates pertaining to chemical species involved in particle processes, and it is imperative that these species are included in the chemical mechanism.

The process of solving the system of differential equations to compute mass, species, and moments is integrated into the primary modeling framework. Addressing the system of equations involves establishing initial conditions during each iteration. The time step is determined by the resolution of the input dataset and spans from SOC up to the exhaust phase TDC. While the initial values for mass and species have been previously detailed, the initialization of moment values requires specific attention. Even though no particles are present at SOC, it is crucial to set these initial moment values to a certain non-zero value to prevent division by zero (refer to Equation 4.24). To adhere to this requirement, the initial values for moments in log-space were defined in accordance with the recommendations of the MOMIC routine developers [11], as depicted in Table 4.1.

During each time step, the integrated solver for stiff differential equations in MATLAB, namely $ode15s$, is invoked. An array of inputs is required to effectively solve the system of differential equations, encompassing pressure, temperature, burned mass, species mass fractions, and moment values. Within an iteration of $ode15s$, the MOMIC routine is called with the primary inputs (refer to section 3.4), yielding the moment rates Q_r and adjustments to the species production rates $\dot{\omega}_{soot}$. With this information, the system of differential

Table 4.1: Moment initial conditions.

Moment	Initial Value
M_0	1
M_1	4.47
M_2	7.93
M_3	11.40
M_4	14.87
M_5	18.34

equations can be solved. Additionally, within an iteration, it's common to make multiple calls to the MOMIC routine until the solution of the equation system meets the specified tolerances. In this particular investigation, the relative and absolute tolerances were set at 1E-08 and 1E-10, respectively. The solution of the differential equations is done for all zones of the multi-zone framework and renders the mass and species profiles. The species profiles are then transferred to the Monte-Carlo tool (SWEEP) for calculating the particle size distribution. Since the gas phase species profiles are in mass fraction, they need to be converted into molar concentration values in order to be effectively provided to SWEEP. This is done by first converting the mass fractions into molar fractions:

$$X_{b,i} = \frac{Y_{b,i}}{MW_i \cdot \sum_{i=1}^{n_{species}} \frac{Y_{b,i}}{MW_i}} \tag{4.27}$$

Followed by a conversion to molar concentration:

$$C_{b,i} = \frac{X_{b,i}\rho_b}{MW_{global}} \tag{4.28}$$

4.3 Simulation chain

An initial overview of the simulation chain can be inferred from the earlier discussion regarding model initialization and equation development. Before initiating SWEEP, valuable insights can be gleaned from solving the system of differential equations. By addressing the conservation of moment equations, one can derive profiles ranging from the zeroth to the fifth moment. As the zeroth moment is the particle number density (refer to section 3.4), it becomes possible to deduce the final particle number density at the end of the simulation. Furthermore, the volume fraction (or soot mass density) can be computed using the first moment:

$$f_v = M_1 \frac{m_c}{\rho_{soot}} \tag{4.29}$$

and the soot mass density by:

$$M_d = M_1 \cdot m_c \tag{4.30}$$

Additional insightful attributes of the soot distribution can also be calculated, including the mean diameter of soot. This computation is performed using the following equation:

$$d_{mean} = \frac{M_{1/3}}{M_0} \left(\frac{6 m_c}{\pi \rho_{soot} N_A} \right)^{1/3} \tag{4.31}$$

By juxtaposing these parameters with the outcomes of the SWEEP solution, one can evaluate the validity of the coupling between the species conservation equations and the method of moments. Furthermore, if the specific interest lies not in the particle size distribution, MOMIC could be exclusively employed to generate particle number and mass densities, along with the average diameter of the distribution, assuming the two sets of results are comparable. This becomes particularly relevant when experimental measurements are limited to particle number and mass densities. Nevertheless, delving into the size distribution provides an additional layer of insight into the analysis, as sooting pathways typically encompass a range of particle sizes.

Returning to the simulation chain, the initial step involves retrieving input data from CALMEC into MATLAB. The input variables were previously defined in section 3.1. Supplementary inputs pertain to various sub-models that directly interact with the main model. For example, the sub-model dedicated to generating the equivalence ratio distribution is directly linked to the primary framework. The distribution is initially analyzed, involving the partitioning of zones according to the procedure outlined in section 4.1. The distinction between sub-models lies in the information conveyed to the main framework. Liquid film zones, also referred to as pyrolysis zones in this work, whether located on the injector tip or on the walls, lack a dedicated equivalence ratio distribution. Instead, they compute the remaining fuel mass on the walls at SOC. This value is transmitted to the main framework, where an additional zone is created for each wall film pathway. Subsequently, this fuel mass is employed to initialize the gas phase and facilitate the subsequent solution of the system of differential equations. Consequently, the remainder of the simulation chain remains identical across the various pathways. The simulation chain is summarized by the block diagram shown in Figure 4.3.

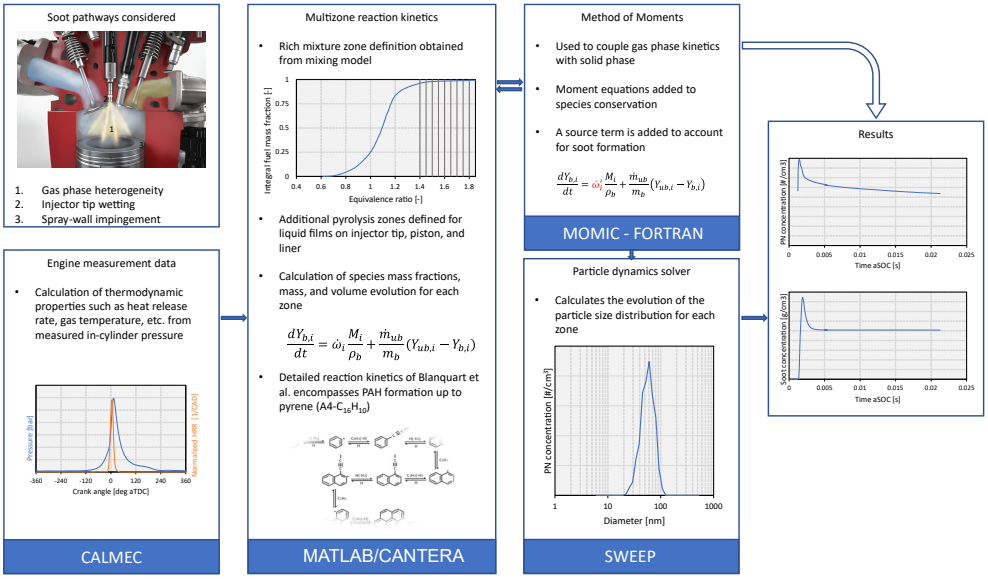

Figure 4.3: Overview of the modeling framework.

4.4 Validation strategy

Establishing a basis for comparing numerical and measured particle emissions is a complex undertaking. The particle number and mass density profiles derived from SWEEP necessitate several post-processing steps to facilitate a direct comparison with the measured data. It is crucial to consider volume as the starting point, given that particle measurements are sampled volumetrically. Consequently, the computed number and mass densities must be adjusted to concentration values for a single cylinder. This adjustment is made by considering the cylinder volume during the closed cycle and the exhaust volume when the exhaust valve opens. Since the cylinder volume is divided into distinct zones, each zone's volume is individually processed to transform the zone number density, derived from SWEEP, into the total number of particles per zone. The particle counts from each zone are subsequently summed to obtain the overall particle count for the cylinder. This summed value is then divided by the exhaust volume to calculate the particle number density. The procedure is represented by the following equation:

$$N_{total} = \frac{\sum_{j=1}^{n_{zones}} (N_{SWEEP,j} V_j)}{V_{exh}} \tag{4.32}$$

where N_{SWEEP} is the particle number density calculated by SWEEP, V_j is the volume of zone j, V_{exh} is the exhaust volume for one cylinder (total exhaust

volume divided by the number of cylinders), and N_{total} is the total number density for one cylinder. Here, V_{exh} is utilized, but it can alternatively be substituted with the sum of all zone volumes at the end of simulation. This substitution is guaranteed by the principle of mass conservation. Equation 4.32 represents particle number density but the mass density is also computed in the same way.

The second point to consider is the counting efficiency of the particle counter device. The counting efficiency curve is depicted in Figure 4.4. As evident, the counting efficiency is suboptimal at smaller diameters. For the specific device under consideration, the counting efficiency attains 50% at a diameter of 23 nm, aligning with the standards established by regulatory frameworks. To incorporate the counting efficiency of the device from a numerical standpoint, the channel (or bin) efficiency was employed to adjust the total number of particles within that channel. This implies that the binning process applied to the numerical data mirrors the procedure used in EEPS-3090 device. A total of 32 channel sizes were utilized within a diameter range of 5-560 nm, with the channel width matching that of the device. The efficiency considered in each channel was considered to be that corresponding to the value at the midpoint diameter of the channel.

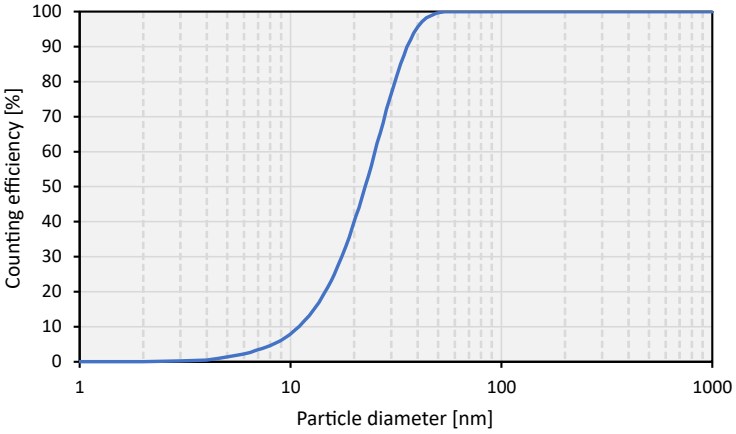

Figure 4.4: Particle counting efficiency.

By following these procedures, a more consistent comparison between numerical and experimental values can be achieved, as the sampling process the particles undergo in the exhaust has been replicated in the correction of the numerical values. Accounting for the particle counting efficiency of the

measurement device is essential, as particle number concentrations are significantly influenced by it, particularly for particles at the smaller end of the spectrum. Additionally, no further adjustments were required for the dilution ratio used in the measurements, as the final measured particle emission values, which will be used for model validation, were already adjusted according to this ratio.

4.5 Summary

This chapter has provided an overview of the modeling framework, delineating the assumptions and considerations employed in modeling precursor reaction chemistry and particle formation. The mathematical expressions showcased earlier were implemented into a MATLAB script, wherein the primary calculations for each zone of the multi-zone framework were executed. Although the SWEEP tool functioned as an independent executable file, it was integrated into the MATLAB script through a call to the SWEEP executable using the *system* function. Given that SWEEP outputs results in *.csv* format, they can be imported back into MATLAB for further analysis.

In section 4.1, the gas phase initialization process was detailed, commencing with the definition of the gas mixture at ignition. Additionally, the use of Cantera for establishing residual gas composition was demonstrated. This information was then employed to define the unburned gas composition, incorporating zone-specific equivalence ratios derived from the equivalence ratio distribution. Each zone was subsequently subdivided into unburned and burned reactors connected by a mass flow variable, computed based on air, fuel, and residual gas mass flows.

The subsequent section, section 4.2, outlined the system of ordinary differential equations representing the conservation of mass, species, and moments. Developed for the burned reactor, this system was solved from SOC up to the exhaust phase TDC. The coupling between species conservation equations and the method of moments was explained, along with details of the numerical ODE solver.

In section 4.3, the simulation chain was summarized, emphasizing the numerical execution strategy. Although the primary modeling framework was presented based on inputs from the mixing sub-model, a brief mention was made of the integration of other sub-models, with further details to be touched upon in subsequent chapters.

Finally, the validation strategy was presented in section 4.4, highlighting the procedures employed for an even comparison between numerical and ex-

perimental results. This step is crucial, as the validity of the results hinges on their proper utilization.

References

[1] Baratta, M., Ferrari, A., and Zhang, Q. "Multi-zone thermodynamic modeling of combustion and emission formation in CNG engines using detailed chemical kinetics". In: *Fuel* 231 (2018), pp. 396–403. DOI: 10.1016/j.fuel.2018.05.088.

[2] Babajimopoulos, A., Lavoie, G. A., and Assanis, D. N. "Modeling HCCI Combustion With High Levels of Residual Gas Fraction – A Comparison of Two VVA Strategies". In: *SAE Technical Paper*. 2003. DOI: https://doi.org/10.4271/2003-01-3220.

[3] Vasudev, A., Mikulski, M., Balakrishnan, P. R., Storm, X., and Hunicz, J. "Thermo-kinetic multi-zone modelling of low temperature combustion engines". In: *Progress in Energy and Combustion Science* 91 (2022), p. 100998. DOI: 10.1016/j.pecs.2022.100998.

[4] Kodavasal, J. et al. "An accelerated multi-zone model for engine cycle simulation of homogeneous charge compression ignition combustion". In: *International Journal of Engine Research* 14.5 (2013), pp. 416–433. DOI: 10.1177/1468087413482480.

[5] Babajimopoulos, A., Assanis, D. N., Flowers, D. L., Aceves, S. M., and Hessel, R. P. "A fully coupled computational fluid dynamics and multi-zone model with detailed chemical kinetics for the simulation of premixed charge compression ignition engines". In: *International Journal of Engine Research* 6.5 (2005), pp. 497–512. DOI: 10.1243/146808705X30503.

[6] Jiao, Q. and Reitz, R. "Modeling of equivalence ratio effects on particulate formation in a spark-ignition engine under premixed conditions". In: *SAE Technical Papers* (2014). DOI: 10.4271/2014-01-1607.

[7] Alessio, A. D., Gambi, G., Minutolo, P., Russo, S., and D'Anna, A. "Optical characterization of rich premixed CH4/O2 flames across the soot formation threshold". In: *Twenty-Fifth Symposium (International) on Combustion* 25.1 (1994), pp. 645–651. DOI: https://doi.org/10.1016/S0082-0784(06)80696-X.

[8] Manzello, S. L. et al. "Soot particle size distributions in a well-stirred reactor/plug flow reactor". In: *Proceedings of the Combustion Institute* 31.1 (2007), pp. 675–683. DOI: 10.1016/j.proci.2006.07.013.

[9] Lenhert, D. B. and Manzello, S. L. "Effects of benzene and naphthalene addition on soot inception in a well-stirred reactor/plug flow reactor". In: *Proceedings of the Combustion Institute* 32.1 (2009), pp. 657–664. DOI: 10.1016/j.proci.2008.07.016.

[10] Frommater, S. "Phenomenological modelling of particulate emissions in direct injection spark ignition engines for driving cycle simulations". PhD thesis. TU Darmstadt, 2018.

[11] Revzan, K. L., Brown, N. J., and Frenklach, M. http://www.me.berkeley.edu/soot/. 1999.

Chapter 5

Gas-phase heterogeneity

This chapter will explore the first soot pathway examined by the model, focusing on the formation of soot originating from rich regions within the combustion chamber due to insufficient mixture homogeneity. Various methodologies for modeling mixture formation and fuel distribution at the onset of combustion were explored. Utilizing 3D CFD simulations, a comprehensive database was established to validate these modeling approaches. Initially, a 1D spray model was employed and compared against 3D CFD trends across different operating points. Subsequently, the advantages and limitations of this approach were discussed to justify its application as a tool for assessing equivalence ratio distribution. An empirical model was then devised based on observed trends from 3D CFD simulations, incorporating calibration parameters correlated with key variables influencing mixture formation, such as engine speed, injection pressure, and mixing time. The contribution of gas-phase induced particle emissions on overall particle number and mass densities is also thoroughly discussed.

5.1 3D-CFD virtual database

The details of the CFD setup used to simulate mixture formation has already been detailed in section 3.2. In the particle formation context, the equivalence ratio distribution at SOC is the instant that governs the consequent soot formation processes. Thus, the distribution is captured at SOC and divided into zones exceeding the sooting threshold. The four operating conditions vary

in mixing nature as they differ in injection timing, in-cylinder themodynamic conditions, injection pressure, and gas velocity, all of which influence fuel evaporation and fuel-air mixing. Moreover, fuel impingement on the piston and liner walls also play a role in mixture preparation as liquid films formed on combustion chamber walls tend to evaporate in the late stages of the cycle before combustion begins [1].

The CFD simulation results are illustrated in Figure 5.1 as integral fuel fraction plotted against equivalence ratio. These distributions were derived through a binning method, wherein the fuel mass of cells within specified equivalence ratio ranges was accumulated. A total of 100 bins were generated for each case, spanning the full range from the minimum to maximum equivalence ratio value. Here, a clear observation emerges, illustrating the enrichment strategy employed by this engine under higher loads. A shift in the distribution curve can be seen at A100 and B100 towards higher equivalence ratio values, where 50% of fuel mass is at the proximity of the global ϕ of the corresponding operating point. Moving from 2000 to 3000 rpm at medium load, a change in slope of the distribution is noted, characterized by a steeper slope for the higher engine speed. Considering that the injection process occurs during the intake stroke, a higher incoming gas velocity enhances the distribution of fuel within the cylinder resulting in more rapid mixing. Additionally, the higher in-cylinder turbulent intensity would also contribute to achieving a mixture with higher homogeneity. The result of this is a narrower range of equivalence ratios. Moving from medium to high load at fixed engine speed, the injected fuel quantity is almost doubled, making it harder for the fuel to mix with the gas since less time is available for mixing a larger quantity of fuel.

Comparing A50 with A100, it is evident that the last portion of the curve, ϕ values greater than 1.4, reaches unity much later for the higher load case. This indicates the presence of a higher degree of fuel rich regions with respect to medium load. Even though the high load case has a higher maximum equivalence ratio value, the curve is relatively steeper around the global ϕ value indicating more mixture uniformity. This is attributed to the higher injection pressure that improves spray atomization and breakup leading to smaller liquid droplets that are easier to evaporate. Additionally, higher injection pressures result in increased liquid velocities, enhancing the entrainment of air into the spray. Figure 5.2 plots the sauter mean diameter (SMD) evolution during injection. It can be observed that the cases with higher injection pressures exhibit smaller SMD values which justifies the difference in slope observed between A50 and A100. This trend, however, is not observed when

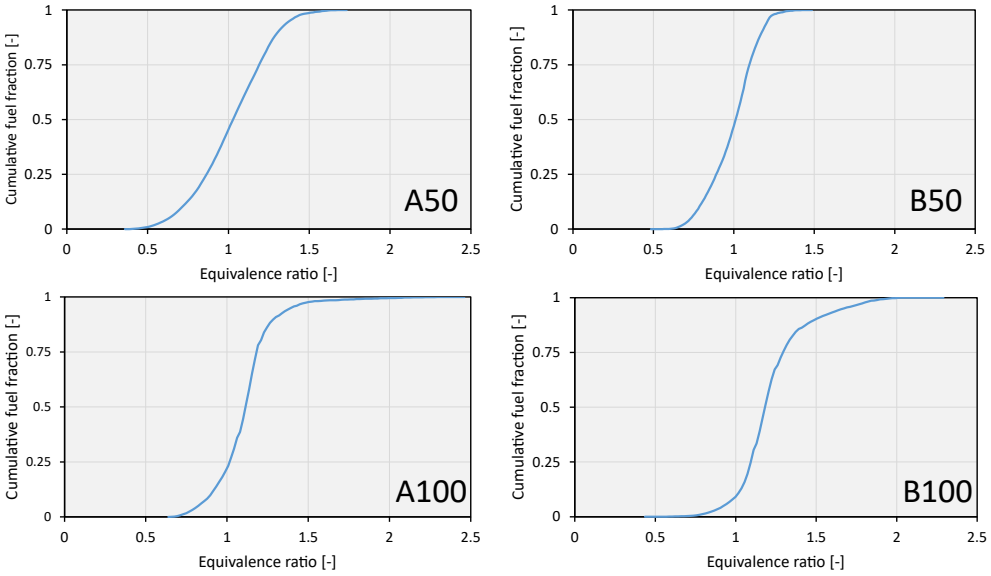

Figure 5.1: Equivalence ratio distributions for the four operating points at SOC.

moving from medium to high load at 3000 rpm indicating that another phenomenon comes into play that counteracts the benefit of a higher injection velocity. B100 exhibits the earliest SOI timing (-303 °CA), suggesting that spray-wall impingement may be more prominent compared to other operating conditions with more delayed SOIs. This factor, coupled with a shorter mixing time relative to B50 and the 2000 rpm cases, contributes to a higher concentration of fuel in rich zones.

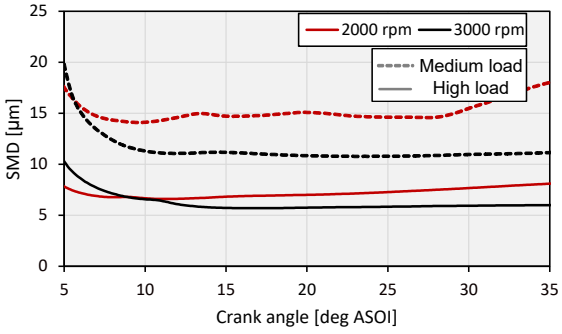

Figure 5.2: Sauter mean diameter for the four operating points during the early phase of injection.

Figure 5.3 shows the mixture formation evolution at different instances aEOI. The impact of intake air velocity is evident at the early stage of the mixing process (EOI+100 °CA). The higher speed cases have fuel dispersed around most of the cylinder, whereas lower engine speed cases exhibit greater areas of very lean mixtures on the exhaust side. On the intake side, most cases experience a rich zone on the liner likely due to the tumble flow dispersing liquid droplets. At 150 °CA aEOI, higher load cases exhibit rich zones on the inlet side, as the larger fuel mass is still being mixed with the gas driven by the tumble flow (evidenced more clearly in A50). At SOC, A50 relatively has more zones with low fuel concentration, which explains the higher fuel mass between ϕ of 0.5 and 1 (see Figure 5.1). In terms of mixture homogeneity, A50 demonstrates the poorest behavior. However, this isn't anticipated to result in increased soot formation, as the maximum ϕ values do not reach high levels. At higher loads, the mixture at SOC reveals rich pockets near the injector region, more pronounced in the B100 case. This is expected given that the B100 case operates with the highest degree of enrichment. Consequently, these rich pockets become a source for soot formation processes due to reduced mixing time resulting from longer injection durations.

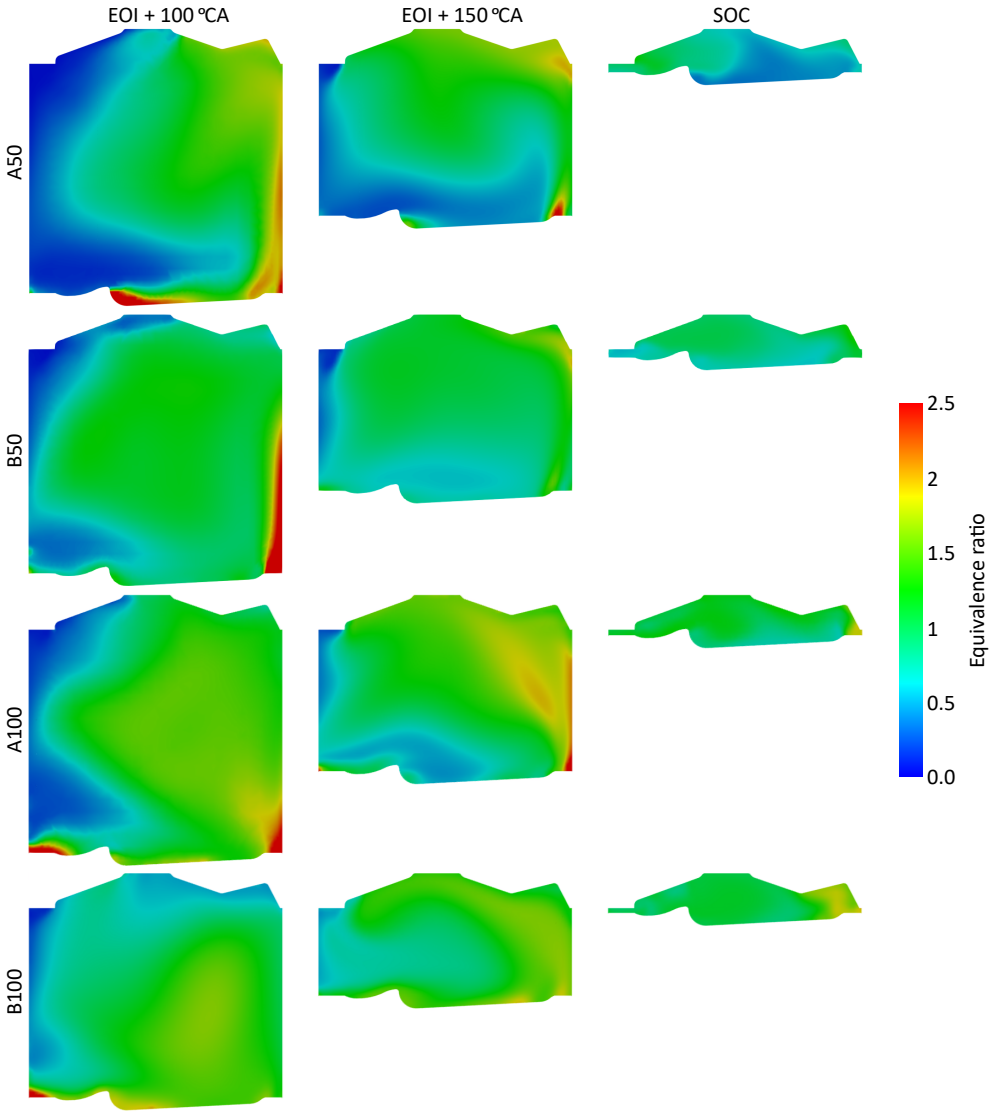

Figure 5.3: Evolution of the mixture formation process at different instances throughout the cycle up to SOC.

It is important to note that CFD simulations utilize inputs derived from the average values of multiple engine cycles. Consequently, the presented results solely reflect the average engine behavior, without considering cycle-to-cycle variability. While the implications of these considerations could impact soot formation, they fall outside the scope of this study.

5.2 1D mixing model development

One-dimensional CFD tools have been widely employed to predict spray behavior in conditions resembling those of an engine. These tools could be expanded to assess variables that are more expensive to obtain through 3D CFD means. Their advantage lies in their low computational cost, facilitated by the model's reliance on assumptions and simplifications. In the context of this work, a 1D spray model developed at CMT – Clean Mobility & Thermofluids was used to model the spray interaction with the gas in the combustion chamber so as to evaluate the mixing process and obtain the equivalence ratio distribution throughout the mixing process. The model, called DICOM, has been developed for diesel spray applications both under inert and reaction conditions [2–4]. The model has also been extended to simulate multicomponent fuels and was validated based on spray macroscopic variables such as liquid length and vapor penetration [5].

5.2.1 1D Model assumptions and modifications

The model operates based on several key principles. Fuel is injected into a sufficiently large quiescent chamber, ensuring no interaction with the walls. Additionally, the spray evolution does not alter the conditions of the gas far away from the nozzle. The fuel stream is assumed to possess a spatially uniform velocity profile at the nozzle exit. The interaction between the fuel and ambient gas is represented by the widening of the spray as it traverses the chamber. This radial expansion is directly correlated with the cone angle θ, which is an input parameter to the model. Together with the nozzle diameter d_0, the spray angle determines the virtual origin of the spray, such that at the nozzle exit, $x = x_0 = d_0/2/tan(\theta/2)$. The main configuration of the modeling approach is illustrated in Figure 5.4. It can be seen that the spray domain is segmented axially into cells, each with a specific thickness $\triangle x$.

The conservation equations of momentum, fuel, and energy are developed and solved for each cell. The solution of the equations yield the axial velocity u, mixture fraction f (equal to the fuel mass fraction for non-reactive jets), and enthalpy h. The main hypotheses adopted by the model are listed below:

- No swirl motion is accounted for and therefore the spray is symmetrical on its axis.
- Self-similar radial profiles are defined for the conserved variables. This implies that the ratio of a conserved variable with respect to the cen-

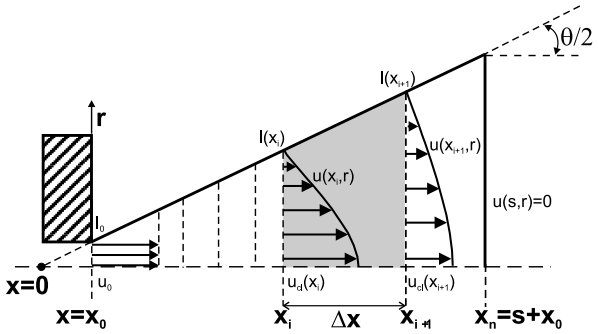

Figure 5.4: Schematic depicting DICOM's modeling approach [2].

terline value does not depend on the axial distance. A Gaussian radial function is used to describe the radial profile of the spray.

- A local equilibrium exists for both thermal and velocity conditions.
- The pressure field is assumed to be constant over all the spray.
- State relationships establish the local composition, temperature, and density of the spray based on the mixture fraction. The determined local density is then supplied as an input to the conservation equations.

Inputs to the model, including boundary conditions like fuel injection rate and momentum profile, are typically derived from experimental measurements. The model assumes an adiabatic mixing process between the fuel and air streams as the fuel enters the chamber, allowing for the calculation of the local mixture composition. For a comprehensive understanding of the model and its underlying assumptions, readers are directed to Pastor et al. [2].

Adapting the 1D spray model for the context of spray mixing in a GDI engine necessitated some modifications. Given that the injection process in the engine takes place within a confined volume, the evaporated fuel mass would be re-entrained into the spray. Consequently, the spray not only entrains air from the surrounding environment but also vapor fuel. To account for the re-entrainment of vapor fuel in DICOM, at a given time instant, the surrounding gas was considered to be consisted of air and residuals, in addition to the evaporated fuel mass injected in the previous time step. The application of this correction is schematically represented by Figure 5.5. At time t_0, injection has not begun and the chamber consists only of air and residuals. At the next time step t_1, a quantity of fuel is injected according to the injection rate. That fuel mass is assumed to be evaporated instantaneously and perfectly

mixed with the ambient gas. This is a very optimistic assumption that leads to an overestimation of the mixing process, which required the introduction of a calibration parameter to limit mixing, as will be shown later on in subsection 5.2.2. Following this method, the entrained gas in the next time step t_2 consists of air, residuals, and fuel vapor.

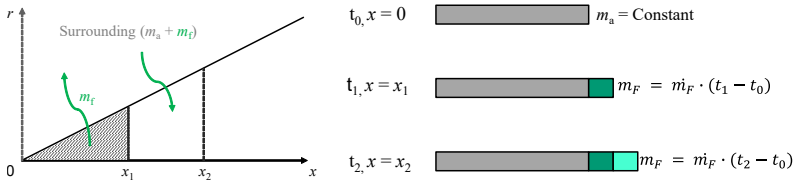

Figure 5.5: Schematic depicting the modification of the ambient gas composition during fuel injection.

The implementation of the aformentioned assumption was done by rescaling the fuel mass fraction as follows:

$$Y_f = Y_{f,\infty}(1 - f) + Y_{f,0} \cdot f \tag{5.1}$$

where f is the fuel mass fraction, $Y_{f,0}$ is the fuel mass fraction in the fuel stream, and $Y_{f,inf}$ is the instantaneous fuel mass fraction in the ambient gas computed by Equation 5.2.

$$Y_{f,\infty}(t) = \frac{m_f(t)}{m_f(t) + m_a(t) + m_{res}(t)} \tag{5.2}$$

The instantanoues fuel mass is obtained from the injection rate, whereas the instantaneous air and residual gas masses were taken from the CFD simulation. This was done to exclude any difference in masses and gas composition that may arise due to the gas exchange process during the model validation phase. Once validated, CALMEC would be used to supply the 1D mixing model with time history of the in-cylinder masses.

5.2.2 1D model results and calibration

In this context, instead of employing the equivalence ratio, the fuel mass fraction was utilized as it is the default variable in DICOM. The spray cone angle serves as a crucial parameter for the model, exerting significant influence on the spray mixing process. A larger spray cone angle corresponds to a broader spray plume width, which promotes air entrainment, thereby enhancing mixture formation. It is assumed within the framework of fuel mass

fraction distributions, that a larger cone angle would result in a more uniform distribution, leading to a more upright curve.

The A50 case was first considered for comparing fuel mass fraction distributions computed by the 1D model with CFD results. In Figure 5.6, distributions at various time instants of the cycle were plotted, beginning from EOI and extending to SOC. Here, a spray cone angle of 5° was chosen, which was necessary due to the rapid mixing predicted by the 1D model, as will be evident shortly. Figure 5.6b illustrates the impact of the correction applied to the fuel mass fraction, as described by Equation 5.1. Due to the finite mass available in-cylinder for mixing with the fuel, the curves are adjusted towards the global fuel mass fraction. Trends from the 1D model indicate that the mixing process immediately following EOI progresses more rapidly compared to the CFD case, which necessitates a very small cone angle to be able to predict a sensible distribution at SOC. If the cone angle was adjusted to produce a plausible distribution between SOI and EOI, conditions most similar to a diesel engine, then the mixing process after EOI would be significantly overestimated. Since the distribution at SOC is the one that directly impacts soot, the focus was set on replicating the trend at that instant.

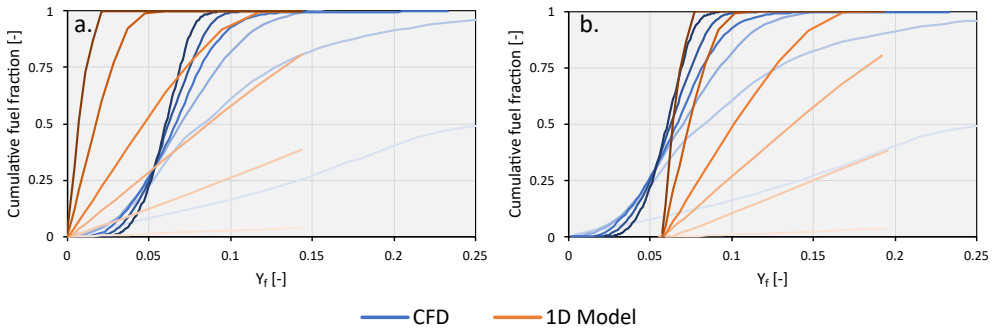

Figure 5.6: CFD versus 1D model fuel mass fraction distribution prior to Y_f modification (a) and after (b). The shades of colors are for different time instants in the cycle, ranging from EOI (lightest) to SOC (darkest) separated by 50 °CA.

While the Y_f distribution at SOC closely resembles that of the CFD case, a noticeable deviation in the final segment of the curve exists, which is the most vital portion as far as particle formation is concerned. Consequently, the spray cone angle was decreased to 1° to further minimize the mixing capacity of the 1D model. Figure 5.7 presents the outcomes for the modified spray cone angle, demonstrating an enhancement in the curve at SOC. However, this adjustment results in the global fuel mass fraction shifting towards a richer value. Equation 5.1 was thus revised and a tuning parameter ($vFactor$) was

introduced to shift the curve towards the global fuel mass fraction value, as shown in Equation 5.3.

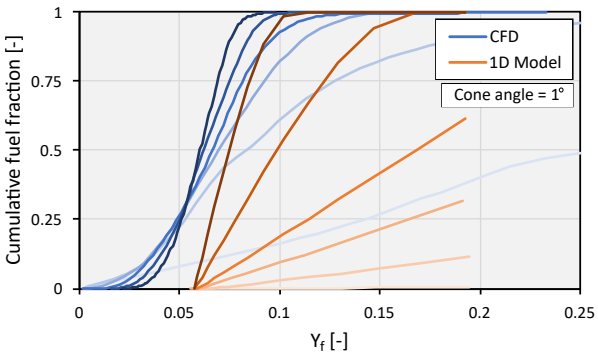

Figure 5.7: Spray cone angle effect on fuel mass fraction distribution. The shades of colors are for different time instants in the cycle, ranging from EOI (lightest) to SOC (darkest) separated by 50 °CA.

$$Y_{fv} = vFactor \cdot Y_{f,\infty}(1 - f) + Y_{f,0} \cdot f \tag{5.3}$$

The $vFactor$ is time-dependent, since the global fuel mass fraction evolves over time, gradually approaching the global value, defined by the total air and fuel mass at IVC. The effect of the $vFactor$ is depicted in Figure 5.8, where an adjustment has been applied on the distribution at SOC and SOC-50 °CA. The evolution of the trends are improved, especially at the lower fuel mass fraction values. It is clearly observed that when adjusting the spray cone angle to ensure a good fit of the distribution at SOC, the penultimate one deviates significantly from the CFD trend. This suggests that DICOM predicts an overly rapid mixing process starting from EOI. Initially during injection, the mixing progresses slowly, it then appears to accelerate significantly until it aligns with the CFD distribution at SOC. Evidently, the entire evolution is not accurately predicted, except for the instant of primary interest (SOC).

Therefore, it is reasonable to disregard the data points from time instants preceding SOC, given the constraints of the 1D model which lacks a comprehensive physical assessment of the phenomena influencing mixture formation (such as spray-air interaction, spray-wall impingement, etc.). Keeping this in consideration, the calibration procedure proceeded for all four operating points, adjusting both the spray cone angle and $vFactor$ to minimize the error between the 1D model and CFD results. The procedure entailed manually adjusting the values and assessing the resulting outcomes. Figure 5.9 depicts

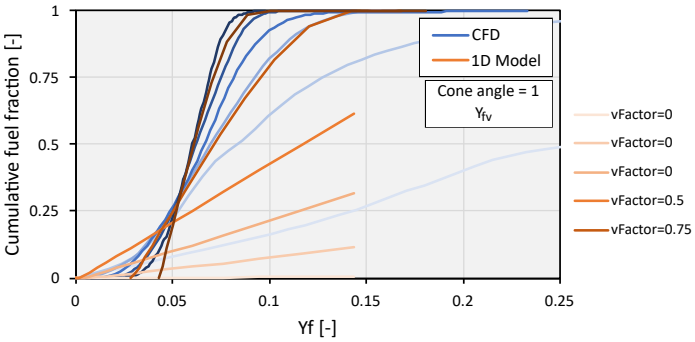

Figure 5.8: Effect of the vFactor on fuel mass fraction distributions. The shades of colors are for different time instants in the cycle, ranging from EOI (lightest) to SOC (darkest) separated by 50 °CA.

the trends for all four operating points and the corresponding cone angle and *vFactor* for each case. There seems to be a good agreement between CFD and 1D model predictions at medium load, for the given set parameters, whereas larger deviations are observed at high load conditions. These differences appear at higher fuel mass fraction values, indicating that high uncertainties in particle formation prediction would result.

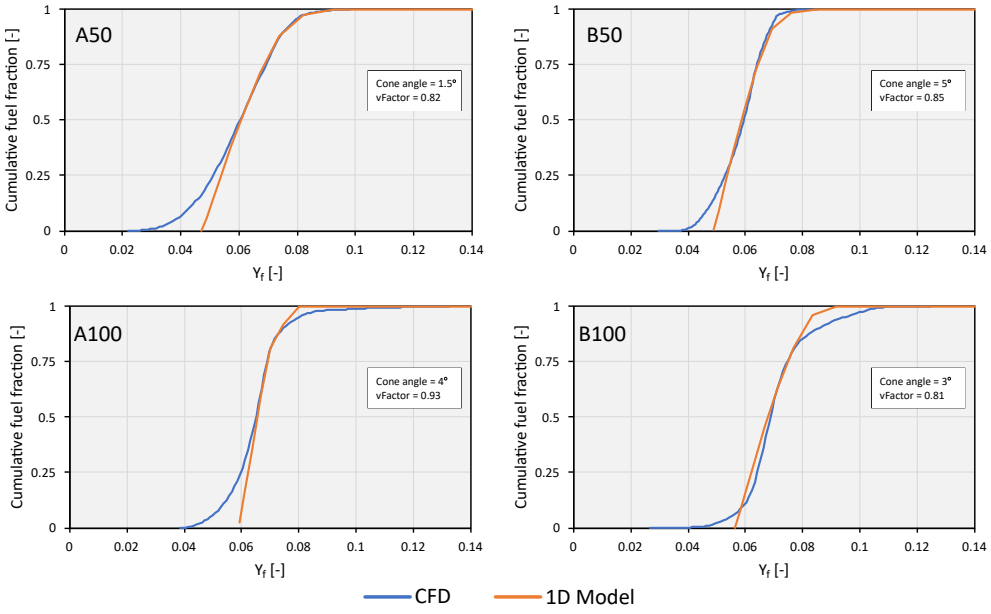

Figure 5.9: Parameter calibration of the 1D model. The optimization of each case was done individually.

Certainly, the goal was then to investigate whether a correlation exists between the tunable parameters of the 1D model (cone angle and $vFactor$) and the pertinent variables that influence mixture formation within the engine. Figure 5.10 plots the $vFactor$ and cone angle versus an indicator of available mixing time, which in this case, is considered to be the time between SOC and EOI normalized by the injection duration. No clear conclusion could be drawn from Figure 5.10a and Figure 5.10b as no correlation exists between the pair of parameters and the mixing time.

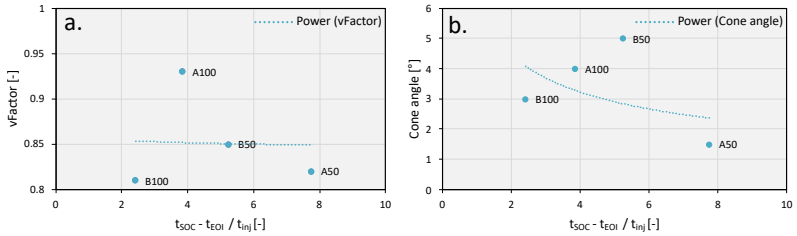

Figure 5.10: Correlation of the vFactor and spray cone angle with mixing time.

In Figure 5.10b, case A50 appears to be the anomaly in the dataset. The remaining cases appear to exhibit a consistent pattern suggesting that the spray cone angle widens as mixing durations increase, resulting in an improved mixture formation process. A50 operates under the lowest injection pressure (80 bar), which from Figure 5.10b, seems to be a limiting factor since A50 requires the smallest cone angle. Hence, a new correlating parameter was computed that accounts for the injection pressure, and is defined as:

$$Param = \sqrt{P}_{inj} \cdot (SOC - EOI) \tag{5.4}$$

where P_{inj} is the injection pressure, SOC and EOI are in units of crank angle degrees. Figure 5.11 depicts the cone angle plotted against the newly computed parameter. The impact of injection pressure is evident in the A50 case; nevertheless, no clear correlation seems to emerge.

While the 1D model inherently incorporates certain physical aspects of fuel-air mixing, it's important to acknowledge that the model was originally designed for diesel spray applications. As such, it is probable that parameters like mixing time, in-cylinder bulk flow, and spray-wall impingement, which significantly influence the resulting mixture in GDI applications, cannot be fully considered. Despite the injection pressure being included in the correlated parameter, which led to a slight improvement in the correlation with respect to cone angle, it was insufficient to establish a meaningful trend. Hence,

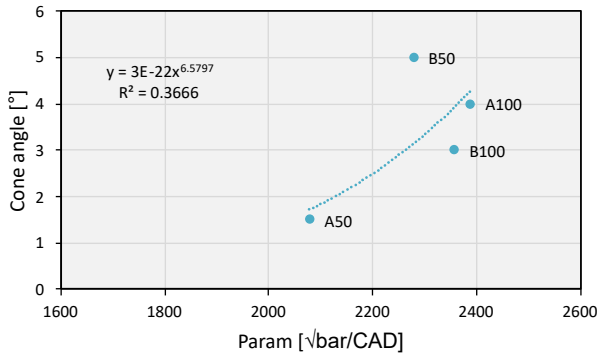

Figure 5.11: Correlation of the spray cone angle with new parameter.

the utilization of the 1D model for predicting fuel mass fraction distributions appears to be unsuitable within the context of this modeling framework. An alternative approach was then devised and is detailed in the following section.

5.3 Empirical mixing model

After recognizing the limitations of the 1D modeling approach, particularly regarding its applicability across all operating points, an alternative approach was formulated. Here, an empirical equation was devised to replicate the equivalence ratio distribution trends. From observing the trends (see Figure 5.1) it can be said that an exponential formulation would best fit the curves. Hence, the mathematical form of the equivalence ratio distribution was represented by the following equation:

$$f(\phi) = \frac{1}{1 + exp(-A(\phi - B))} \tag{5.5}$$

where f is the cumulative fuel fraction value at a given ϕ, A is the parameter that affects the slope of the curve, whereas B modifies the horizontal displacement. From the nature of the curve, parameter B is most suited to represent the global equivalence ratio of a given operating point, hence, Equation 5.5 could be reformulated into:

$$f(\phi) = \frac{1}{1 + exp(-A(\phi - \phi_{global}))} \tag{5.6}$$

Regarding the A parameter, it is clear that the slope of the curve would depend on physical variables affecting the mixing process, such as spray velocity, in-cylinder gas velocity, and available time for mixing. Gong and Rutland

[6] proposed a homogeneity model to characterize the air-fuel mixing process in a SIDI gasoline engine. The authors formulated an inhomogeneity index, correlating three dimensionless numbers which capture the effects of injection timing, in-cylinder flow, and spray-air interaction during injection. The first dimensionless number, mixing time τ_{mix}, is shown in the following equation:

$$\tau_{mix} = \frac{t_{SOC} - t_{EOI}}{\triangle t_{inj}} \tag{5.7}$$

where t_{SOC} is the start of combustion, t_{EOI} is the end of injection, and $\triangle t_{inj}$ is the injection duration. In this work, and similarly to the work of Frommater [7], mixing is accounted for directly from the onset of injection since the spray entrains and mixes with the surrounding gas while the injection is taking place. Therefore, t_{EOI} in Equation 5.7 is replaced with t_{SOI}. The second dimensionless number accounting for in-cylinder flow is the Reynolds number (Re). The Reynolds number is directly proportional to the mean piston speed ($\overline{u}_p$) and is calculated by the following equation:

$$Re = \frac{\overline{u}_p B}{\nu} \tag{5.8}$$

where B is the engine bore and ν is the kinematic viscosity. The kinematic viscosity (ν) is computed by means of a Cantera gas object assuming pure air as the gas with the current in-cylinder thermodynamic conditions. The third dimensionless number accounting for the spray-air interaction during injection is the Weber number (We). The Weber number is scaled with the injection velocity, which in turn is a function of injection pressure. The spray Weber number is calculated according to Equation 5.9

$$We = \frac{\rho_f U_{inj}^2 d_{noz}}{\sigma} \tag{5.9}$$

where ρ_f is the fuel density, U_{inj} is the injection velocity, d_{noz} is the nozzle orifice diameter, and σ is the fuel surface tension. The injection velocity is computed from the injection rate, which is known for each operating condition. The surface tension (σ) in Equation 5.9 is calculated from Poling et al. [8], according to the Brock and Bird correlation, at the injected fuel temperature. Finally, the inhomogeneity index is then represented by the dimensionless numbers as:

$$I_H = exp(-C_2 \cdot \tau_{mix}^X \cdot Re^Y \cdot We^Z) \tag{5.10}$$

where C_2 is a steepness factor that controls how the inhomogeneity index varies with the three dimensionless numbers. It could then be noted that higher mixture homogeneity tends to yield smaller values for the index I_H. The utility of such an index can then be incorporated into Equation 5.6 by substituting parameter A directly with the inverse of I_H. Therefore, a higher mixture homogeneity, and consequently a smaller inhomogeneity index value, would lead to a steeper curve, and vice versa. The final equation characterizing the equivalence ratio distribution inside the combustion chamber at SOC is then expressed as:

$$f(\phi) = \frac{1}{1 + exp(-1/I_H(\phi - \phi_{global}))} \tag{5.11}$$

The equation could also be structured to calculate the fuel fraction values prior to the start of combustion (SOC). To achieve this, τ_{mix} would be computed up to the specified time at which the equivalence ratio distribution is to be determined. This entails replacing t_{SOC} in Equation 5.7 with the corresponding desired time.

To implement the equation into the current framework, an optimization procedure is necessary to obtain a suitable set of parameters C_2, X, Y, and Z that would fit all operating points. To achieve this, a multidimensional unconstrained nonlinear minimization function called $fminsearch$ was utilized in the MATLAB environment in order to find the set of parameters that would minimize the error (E) of the objective function. The objective function was defined as the summation of the squared difference between the values predicted by Equation 5.11 and the CFD distributions for all operating points, as shown in Equation 5.12:

$$E = \sum (f(\phi) - f(\phi)_{CFD})^2 \tag{5.12}$$

where $f(\phi)_{CFD}$ is the cumulative fuel mass fraction value obtained from CFD. The error function is calculated solely based on the distribution at SOC, ignoring data from earlier time steps in the optimization process. This approach is justifiable because it is the distribution at SOC that determines the subsequent zone definition and particle formation. Furthermore, all exponents were constrained to be greater than zero, as increasing any of the dimensionaless numbers would enhance mixture homogeneity.

The result of the optimization process is tabulated in Table 5.1. The exponents indicate that the mixing time and Weber number hold a greater influence on mixture formation compared to the Reynolds number.

Table 5.1: Optimization results for inhomogeneity index parameters.

C_2	X	Y	Z
2.423e−4	0.425	0.142	0.560

Figure 5.12 illustrates the distribution of equivalence ratios resulting from the empirical model. The model demonstrates satisfactory accuracy across four distinct operating points. Nevertheless, a deviation is apparent in the A50 case. This condition operates at the lowest injection pressure (80 bar) and displays the greatest variance from the global equivalence ratio, as observed by the slope of the curve. It is likely that this scenario exerted the most influence on the optimization process regarding the Z parameter.

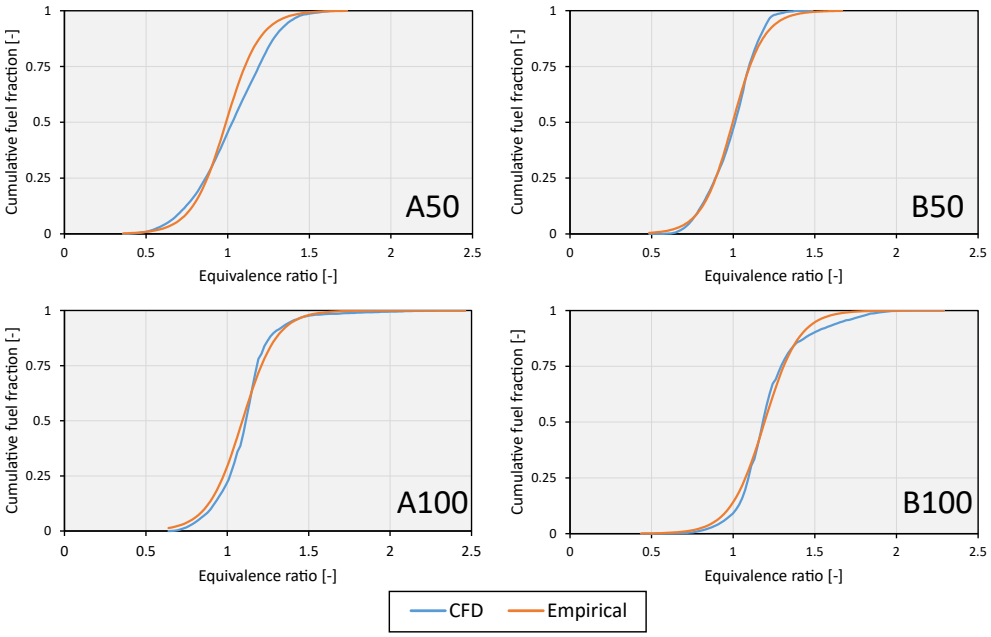

Figure 5.12: Equivalence ratio distributions for the four operating points at SOC, as calculated from the empirical model compared to those obtained from CFD.

5.4 Gas-phase particle formation

The empirical model demonstrated proficient capabilities in replicating equivalence ratio trends under varied operating conditions. Specifically, it effectively responded to alterations in engine speed and load, accurately capturing

the changes in mixture homogeneity stemming from variations in engine parameters, such as injection timing and injection pressure. The model could subsequently be employed to define rich zones exceeding the sooting threshold, thereby achieving the primary goal of its application: calculating gas-phase-induced particle emissions.

Figure 5.13 plots the partition of the equivalence ratio distributions after the sooting threshold into zones with a ϕ width of 0.05 (see section 4.1). As expected, the higher engine speed and load case (B100) exhibits the highest number of zones after the sooting threshold with a maximum ϕ of 1.93.

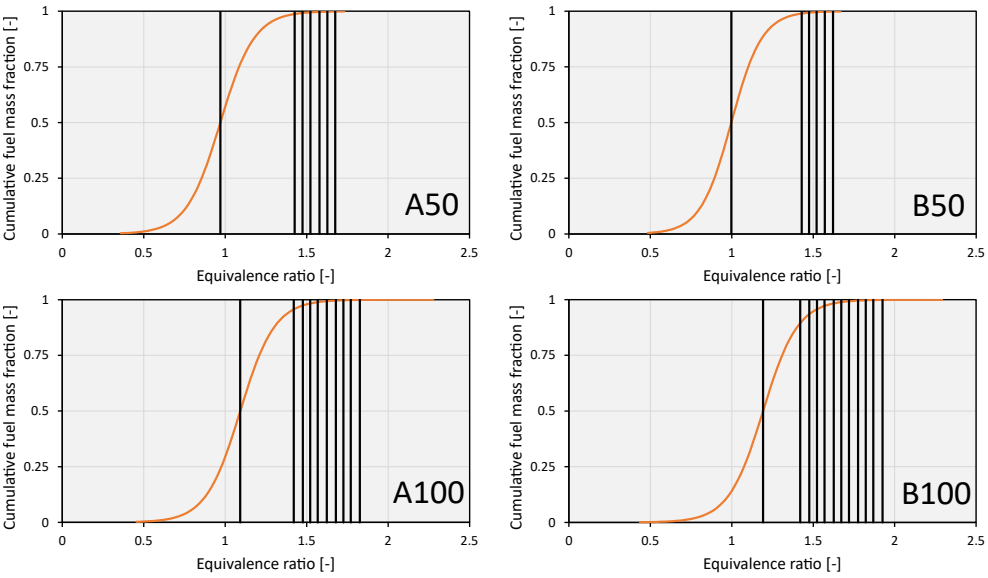

Figure 5.13: Equivalence ratio distributions for the four operating points at SOC, as calculated from the empirical model compared to those obtained from CFD.

The temperature correction factor (Equation 4.19) for each operating condition and its associated peak in-cylinder temperature are displayed in Table 5.2. As anticipated, the medium load cases exhibit higher correction factors due to fewer rich zones compared to the higher load cases, resulting in higher peak in-cylinder temperatures. Additionally, before correction, the in-cylinder temperature is already higher for the medium load cases since they operate with a stoichiometric charge. Conversely, the higher load cases utilize fuel enrichment to reduce exhaust gas temperatures, consequently lowering the in-cylinder temperature. The variations in temperature trends are anticipated to impact particle formation processes.

Table 5.2: Temperature correction factor and peak in-cylinder temperatures for the different cases.

Operating point	Correction factor [-]	Peak in-cyl temp [K]
A50	0.94	2360
A100	0.90	2131
B50	0.93	2356
B100	0.92	2245

Figure 5.14 shows the particle number and soot mass concentrations for all cases. For medium load cases, no particles were detected at calculation end. However, this absence does not necessarily signify that no particle formation occured early during the power stroke. Instead, these particles likely have undergone complete oxidation, often referred to as "burnout", which resulted in their elimination. On the other hand, in the high load cases, particles emitted accounted for 32% and 65% of total particle number density for 2000 rpm and 3000 rpm, respectively. Figure 5.14b shows that these particles primarily have smaller diameters, as evidenced by their minimal contribution to the overall soot mass.

To gain further insights into the distinctions between particle number and mass, an examination of the particle size distribution is conducted. Figure 5.15 illustrates the PSDs for cases where particles were detected at the conclusion of the simulation. The total numerical PSD encompasses the collective contributions of individual zones responsible for particle emissions. Despite numerous zones surpassing the soot formation threshold (refer to Figure 5.13), only a few zones retain particles until the exhaust phase TDC. Furthermore, although the B100 case exhibits a higher maximum equivalence ratio (1.925 compared to 1.826 for A100), the model shows that emitted particles from A100 are both larger and higher in number. This difference is directly linked to the in-cylinder temperature, which not only affects the oxidation rate, leading to a higher reduction in particle size, but also influences the pyrene concentration in the gas phase. Consequently, this impacts the rate of pyrene inception, thereby influencing the particle number concentration. The oxidation rate, however, only affects soot mass in the early stages of soot formation. This is showcased by Figure 5.16b and Figure 5.16d, where a higher peak temperature for the B100 case results in more intense oxidation (see Figure 5.16a) and therefore a lower soot mass concentration, as compared to A100. In both cases, soot mass concentration stabilizes when the in-cylinder temperature drops to 1600 K and remains constant for the remainder of the cycle. Hence, coagulation processes, which increase particle size while keeping particle mass

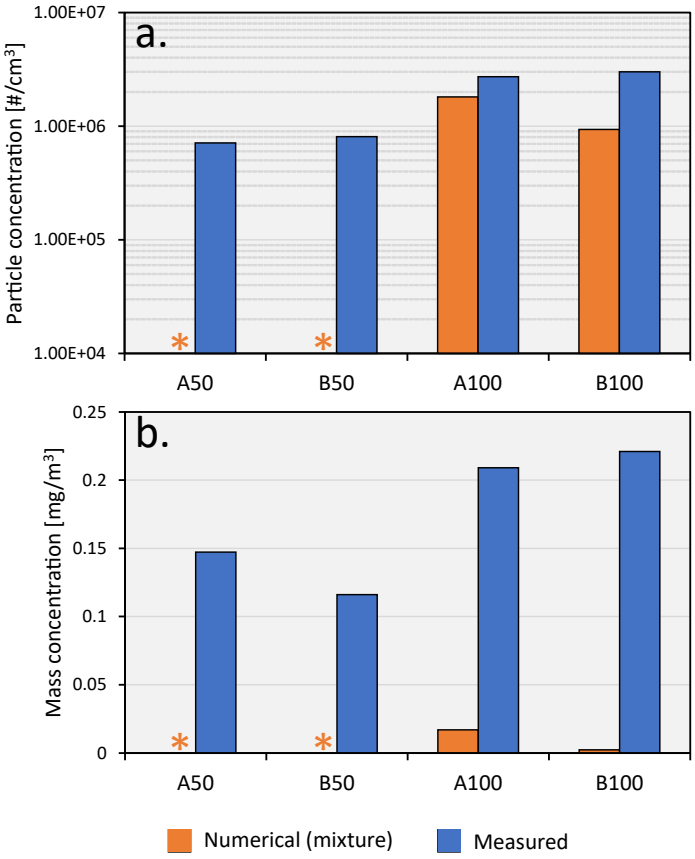

*Figure 5.14: Particle concentration (a) in logarithmic scale and soot mass concentration (b) in linear scale for the four cases. The asterisk * indicates that no particle emissions existed at calculation end (TDC exhaust phase).*

constant, are likely to play a role in final particle number and size. Since B100 runs at a higher engine speed of 3000 rpm compared to 2000 rpm for A100, there is less time for particle growth processes leading to particles with relatively smaller diameters. This is seen in Figure 5.16e where the particle number concentration continues to decrease for the A100 for 8 ms beyond the B100 case. This reduction, at a constant soot mass, would signify larger particle sizes. There is no significant contrast in the coagulation rates between the two cases, as illustrated in Figure 5.16c. However, the peak value is marginally greater for the B100 case owing to its higher initial fuel concentration, thereby augmenting the likelihood of particle collisions. It is important to highlight that the trends in mass and particle concentration, depicted in Figure 5.16d and Figure 5.16e, are presented without the application of bin

efficiency. Consequently, the values at the end of the calculation are higher than those in Figure 5.14.

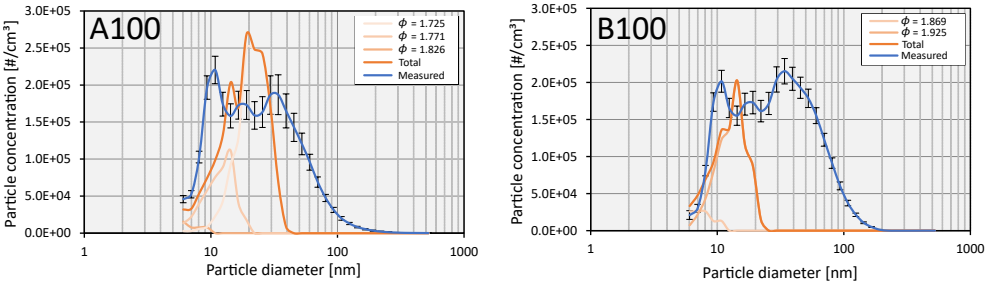

Figure 5.15: Particle size distributions of the high load cases. Individual zones contributing to total particle emissions are also plotted.

The particle size distributions also highlight the impact of equivalence ratio on particle diameters. At higher equivalence ratios, the PSD shifts towards larger particles. This phenomenon is influenced by chemical kinetics, particularly through the formation of pyrene in the gas phase. For higher fuel concentrations, a higher formation rate of pyrene leads to elevated soot inception rates, resulting in more particles initially formed. This, in turn, amplifies particle growth processes such as coagulation, surface growth, and pyrene condensation, ultimately contributing to larger particle sizes. Moreover, particles emitted from rich zones are mostly in the nucleation mode (D_p < 30 nm). Therefore, the particle number concentrations are categorized into nucleation mode and accumulation mode to provide a more meaningful comparison between numerical and experimental results. Figure 5.17 displays the measured and numerical particle number emitted in each mode. In B100, only particles below 30 nm were observed in the numerical results, whereas a minor portion of particles emitted by the A100 case exceeded 30 nm. A better agreement between the simulated and experimental values is now evident, providing additional support for the notion that particles emitted from gas phase inhomogeneities are likely to fall in the nucleation mode, while particles in the accumulation mode predominantly stem from alternative sources of soot, as will be shown in the following chapters.

5.5 Summary

The chapter investigates the formation of soot originating from rich regions within the combustion chamber due to inadequate mixture homogeneity. It

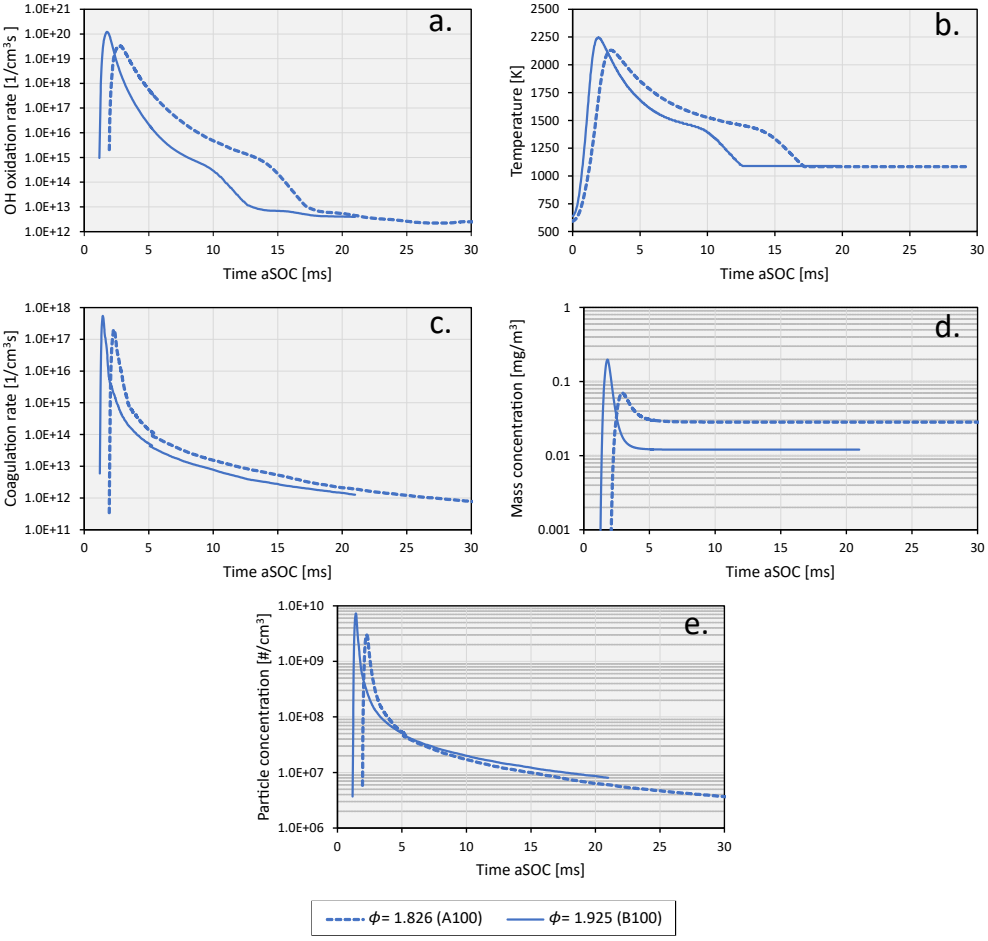

Figure 5.16: Comparison of particle oxidation (a) and coagulation (c) rates, in-cylinder temperature (b), mass concentration (d) and particle concentration (e) evolution from SOC up to calculation end. The richest zone in each case are selected for comparison.

explores various methodologies for modeling mixture formation and fuel distribution at combustion onset, employing 3D CFD simulations to validate these approaches.

The distribution of equivalence ratios at start of combustion was examined, revealing distinct variations across operating conditions influenced by factors such as injection timing, injection pressure, and gas velocity. CFD simulation results illustrated enrichment strategies at higher loads, resulting in higher maximum equivalence ratios. The results also emphasized the importance of injection pressure in promoting spray atomization and breakup,

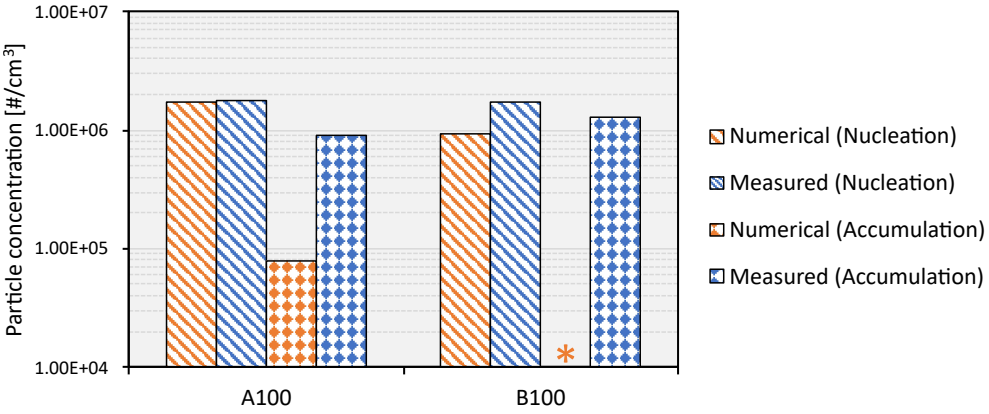

Figure 5.17: Analysis of particle concentration in nucleation and accumulation modes.

thereby affecting the slope of the distribution curves. The equivalence ratio profiles observed at various moments along a plane cutting through the cylinder illustrated how engine speed influences the dispersion of fuel within the cylinder, promoting mixing.

Initially, a 1D spray model was utilized and compared against 3D CFD trends across different operating points to assess fuel mass fraction distribution. An empirical model was subsequently developed based on observed trends from 3D CFD simulations, incorporating calibration parameters correlated with key variables influencing mixture formation.

Furthermore, the chapter highlights the limitations of the 1D model in replicating mixture formation accurately. Despite attempts to adjust the fuel mass fraction to accommodate the finite gas volume, these refinements fell short in capturing the evolution of the mixing process. Consequently, an empirical equation was developed to better capture trends in equivalence ratio distribution. Optimization techniques were utilized to derive parameters for this empirical model. The findings revealed that the mixing process in a given engine could be characterized by three dimensionless numbers. While less grounded in physical principles compared to the 1D model, the empirical approach proved more suitable within the present framework.

Particle number and soot mass concentrations were examined, indicating significant differences across operating conditions. Particle size distributions highlighted the influence of equivalence ratio on particle diameters, with higher fuel concentrations leading to larger particle sizes. Additionally, it was observed that only the most enriched zones emitted particles that persisted until the end of the calculation. Conversely, zones with lower equivalence

ratios experienced rapid burnout shortly after formation, attributed to high temperatures (> 1600 K). Below this threshold, the soot mass concentration remained constant until exhaust phase TDC.

Finally, the comparison between simulated and experimental results provided further validation for the model's efficacy, particularly in categorizing particles into nucleation and accumulation modes, thus enhancing understanding of particle formation mechanisms in GDI engines.

References

[1] Costa, M., Sorge, U., and Allocca, L. "Numerical study of the mixture formation process in a four-stroke GDI engine for two-wheel applications". In: *Simulation Modelling Practice and Theory* 19.4 (2011), pp. 1212–1226. DOI: 10.1016/j.simpat.2010.07.006.

[2] Pastor, J. V., Lopez, J. J., Garcia-Oliver, J. M., and Pastor, J. M. "A 1D model for the description of mixing-controlled inert diesel sprays". In: *Fuel* 87.13-14 (2008), pp. 2871–2885. DOI: 10.1016/j.fuel.2008.04.017.

[3] Desantes, J. M., Pastor, J. V., Garcia-Oliver, J. M., and Pastor, J. M. "A 1D model for the description of mixing-controlled reacting diesel sprays". In: *Combustion and Flame* 156.1 (2009), pp. 234–249. DOI: 10.1016/j.combustflame.2008.10.008.

[4] Pastor, J. V., Payri, R., Garcia-Oliver, J. M., and Nerva, J. G. "Schlieren measurements of the ECN-spray a penetration under inert and reacting conditions". In: *SAE Technical Papers*. 2012. DOI: 10.4271/2012-01-0456.

[5] Pastor, J. V., García-Oliver, J. M., Pastor, J. M., and Vera-Tudela, W. "One-dimensional diesel spray modeling of multicomponent fuels". In: *Atomization and Sprays* 25.6 (2015), pp. 485–517. DOI: 10.1615/AtomizSpr.2014010370.

[6] Gong, J. and Rutland, C. "A quasi-dimensional NOx emission model for spark ignition direct injection (SIDI) gasoline engines". In: *SAE Technical Papers* (2013). DOI: 10.4271/2013-01-1311.

[7] Frommater, S. "Phenomenological modelling of particulate emissions in direct injection spark ignition engines for driving cycle simulations". PhD thesis. TU Darmstadt, 2018.

[8] Poling, B. E., Prausnitz, J. M., and O'Connell, J. P. *The Properties of Gases and Liquids*. Fifth Edit. New York: McGraw Hill, 2001.

Chapter 6

Injector tip wetting

This chapter introduces the second pathway leading to soot formation, considered to be injector tip wetting in this study. An analytical liquid film evaporation model was employed to track the evolution of fuel film mass on the injector tip. Optical engine experiments conducted in a single-cylinder research engine provided valuable insights into the formation of sooting flames originating from the injector tip region under varying operating conditions. These experiments were conducted during a three-month research stay at Sandia National Laboratories. Leveraging these insights, adjustments were made to the tip wetting model to enhance its ability to capture the underlying physics of tip sooting. The chapter then outlines the contribution of injector-induced particle emissions, which are combined with mixture-induced particle ones to construct a more comprehensive particle size distribution.

6.1 Optical engine experiments

Studying in-cylinder phenomena optically offers a valuable approach to comprehending the fundamental physics underlying combustion and the formation of soot. Recent advancements in laser-based diagnostic techniques have introduced innovative methods for conducting in-situ measurements of the combustion process. For instance, one such advancement resulted in the development of the conceptual model of diesel combustion [1]. In the realm of soot formation in GDI engines, in-cylinder visualizations offer an in-depth view of the various pathways contributing to particle emissions. At the simpler end of the

optical technique spectrum, natural combustion and soot luminosity images, acquired by high speed cameras, facilitate the identification of soot sources and offer a qualitative evaluation of soot quantity [2, 3].

The experimental study was conducted in a DISI single-cylinder research engine with optical accessibility at Sandia National Laboratories. This engine differs from the one used to measured the particle size distribution for which model development has been validated with. However, the results from these experiments provide insight into injector-induced particle emissions and their sensitivity to changes in engine load and injection pressure. Those parametric variations are highly relevant to the operating conditions investigated in this thesis. A brief description of the engine characteristics and experimental methodology will be given in the following section.

6.1.1 Engine characteristics and operating conditions

The engine is equipped with a centrally mounted injector close-coupled with the spark plug and features a bowl in the piston. Additionally, the engine has a pent-roof cylinder head with two intake valves and two exhaust valves. Table 6.1 provides an overview of the main characteristics of the engine. The engine was operated at 1400 rpm under all conditions. An overall stoichiometric mixture was maintained throughout the testing campaign, although local in-cylinder deviations from stoichiometry occurred due to imperfect mixture formation. To protect the integrity of the optical windows, the thermal load on the quartz windows was reduced by operating the engine under a skip-fired sequence. A 20:80 schedule was employed, 20 fired cycles followed by 80 motored cycles, wherein the in-cylinder pressure of 23 cycles was recorded in each batch consisting of 3 motored cycles and 20 fired cycles. Of the 23 cycles, only the fired ones were recorded by the cameras. The measurement devices used to measure engine-out particle number and mass concentration were the AVL Particle Counter (APC) 489 and AVL Micro-Soot Sensor (MSS) 483, respectively.

Concerning the injector, it is equipped with six orifices and has undergone a fouling campaign to establish a specific deposit state on the tip. However, specific details and the precise condition of fouling are not provided here due to confidentiality agreements with the supplying company. Additionally, the fuel utilized in this study is regular-grade gasoline with a low Particulate Matter Index (PMI), and the specific properties of the fuel are also not disclosed here for confidentiality reasons.

Three different injection pressures were tested: 60 bar, 120 bar, and 180 bar. The variation was implemented in a way that at each value of injection

Table 6.1: Engine specifications and operating parameters.

Engine displacement	**552 cc**
Bore	86 mm
Stroke	95.1 mm
Connecting rod length	166.7 mm
Geometric compression ratio	10
Injector installation angle	5° (relative to cylinder axis)
Intake valve diameter	35.1 mm
Intake valve angle	18° (relative to cylinder axis)
Exhaust valve diameter	30.1 mm
Exhaust valve angle	16° (relative to cylinder axis)
Engine speed	1400 rpm
Coolant temperature	90 °C

pressure, the SoI_e was swept from -330 °CA to -90 °CA with 60 °CA increments. The discussion of the results will focus solely on SoI_e of -330 °CA. The tests were carried out at medium load with an Indicated Mean Effective Pressure ($IMEP_n$) of approximately 955 kPa. The injected mass was kept constant among the different injection pressures by adjusting the injection duration. Intake pressure was maintained at 96 kPa by setting the intake air mass-flow rate to 5.96 g/s. This mimicked wide-open throttle engine operation minimizing pumping losses.

As mentioned earlier, transient operation involved operating the engine under a skip-fired sequence to reduce the thermal load on the quartz windows. This mode of operation is referred to as transient operation and is more representative of conditions experienced in light-duty vehicles. For an in-depth explanation and comprehensive analysis of the impacts of this mode on combustion behavior, readers are directed to [4].

A load variation was also investigated, involving the implementation of both single and double injection strategies. The SoI_e was set at -310 °CA for single injection strategy. In the case of double injection, two pulses with equal split ratio were implemented with the first at -310 °CA and the second at -280 °CA. A medium load condition, with the same settings as the ones in the injection pressure sweep, was tested. For the higher load condition, the intake air mass-flow rate was increased to 8.3 g/s, which corresponded to an intake pressure of approximately 128 kPa. A stoichiometric mixture was maintained for the two cases by varying the injection duration at 180 bar of injection pressure. A summary of the two load conditions is provided in Table 6.2.

Table 6.2: Summary of the two load conditions.

Parameter	Medium load	High load
Intake temperature [°C]	35	35
Intake air mass-flow rate [g/s]	5.96	8.3
ϕ [-]	1	1
Intake pressure [kPa]	95	128
ST single/double injection [°CA]	-1.8/-1.4	-1.0/-0.6
First/second SoI_e [°CA]	-310/-280	-310/-280
Injection duration single/double injection [μs]	2830/1410	3828/1915

6.1.2 Optical setup

High speed direct imaging of combustion and soot luminosity was carried out using two high-speed cameras. The colored Phantom v611 camera was used to acquire images from the Bowditch type piston, which encompasses a quartz window with an outer diameter of 44.5 mm, an aperture of 37.4 mm, and a thickness of 22.2 mm, via a 45° reflection mirror. The camera operated with aperture f/5.6 and a frame rate of 4200 frames per second, corresponding to one image every 2 °CA at 1400 rpm. The image resolution was 512 × 512 pixels and the exposure time was set at 50 μs. A high-power pulsed LED illuminated the spray plumes via the pent-roof window during the injection duration and was synchronized with the SoI_e. As for the side-view images, the Phantom v710 was used for imaging through the pent-roof plano-concave diverging lens, enlarging the field of view as shown in Figure 6.1. The camera aperture was also set at f/5.6 and the image resolution was 432 × 200 pixels. In this case, two high-power pulsed LED were used to illuminate the liquid spray through the piston-window. A cylindrical plano-concave lens with a focal length of 50 mm was added to the pent-roof imaging setup in order to avoid astigmatism and distortion. Details of the optical setup are depicted in Figure 6.2.

6.1.3 Image processing

Different image processing techniques were applied in order to extract the variables of interest, such as sooting flame intensity, sooting flame area, and sooting flame frequency.

The calculation of sooting flame intensity involved summing the red channel intensity (R value in RGB channels) of all pixels in an image. To differentiate between sooting flames originating from different regions in the cylinder,

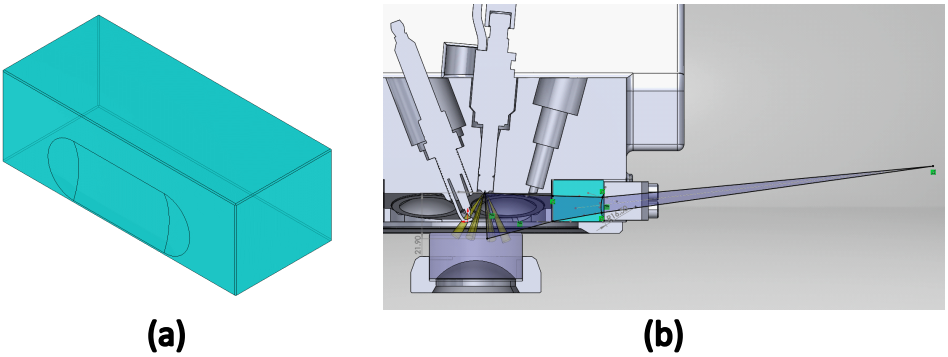

Figure 6.1: Schematic of the diverging plano-concave lens (a) and the field of view through the cylinder head (b).

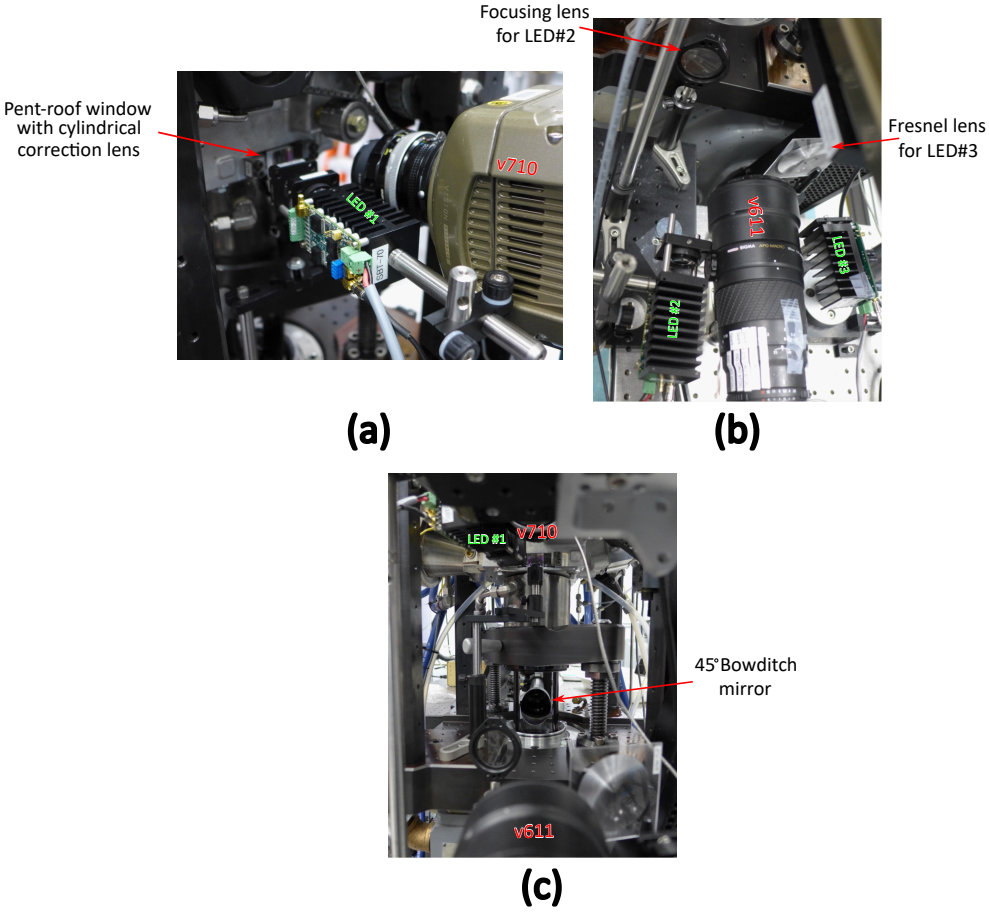

Figure 6.2: Optical set up for side view imaging (a) and bottom view (b), (c).

specific regions of interest (ROIs) were assigned to each source. Three distinct regions were identified as illustrated in Figure 6.3. ROIs were designated at the injector tip, the intake valve location, and the periphery of the piston bowl. This method facilitated the examination and comparison of how parametric variations impact particular sources of soot.

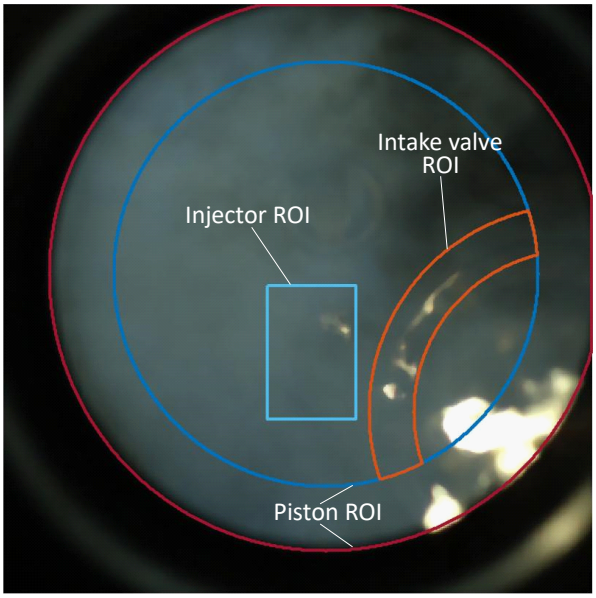

Figure 6.3: Regions of interest in bottom-view imaging captured by the colored v611 camera.

To calculate the sooting flame area, pixels with an intensity value R $\geq$ 153.6 (out of 256) were counted, corresponding to 60% of maximum bit depth. Sooting flame frequency was obtained by averaging binarized images at a specific crank angle, using the same threshold used for computing flame area. This average image would then be a statistical representation of the yellow flame occurrence. The lateral images used the maximum intensity value as the threshold to account for the saturation of pixel luminosity emitted by the sooting flame. Careful consideration led to the adoption of this maximum threshold to prevent the inclusion of hot combustion gases as sooting flames.

6.1.4 Engine load effect on injector zone soot emissions

Changes in engine load are interconnected with adjustments in actuator settings, particularly involving variations in injected fuel mass, spark timing, and intake air mass flow. These alterations contribute to a variation in the engine's

thermodynamic state, a change in the dynamics of fuel film formation on combustion chamber walls, consequently influencing particle formation processes. In this study, moving from medium to high load operation involved an increase in injection duration, at a fixed injection pressure, to maintain stoichiometric combustion. In this way, a greater quantity of fuel was injected to meet the high load power demand.

Figure 6.4 depicts the particle number concentration for two load conditions. To ensure a comprehensive examination, the single and double injection strategies were plotted individually. Furthermore, the values represent the peak for 20 consecutive fired cycles. It is evident that particle emission values are initially high and gradually decrease as the engine's thermal state stabilizes. It is thus crucial to note that the comparison here can only be made on a qualitative basis, given the highly transient nature of the measurements. The forthcoming optical analysis will be based on the last two batches (40 cycles) of the test campaign.

As can be observed in Figure 6.4, moving from medium to high load results in roughly three-fold increase in PN. The reason behind this increase could be attributed to different possible factors. Certainly, the extended injection duration increases the likelihood of a greater amount of fuel interacting with the combustion chamber walls, whether it be the liner, piston, or intake valve. Moreover, knowing that the injector used has undergone a specific fouling procedure rendering it susceptible to injector tip wetting, a portion of the injected fuel is likely to remain at the injector tip at SOC. Images illustrating this point will be shown shortly. With that in mind, the higher injected fuel mass at higher engine load would then lead to a higher fuel mass remaining on the injector tip at SOC. The higher remaining fuel mass would consequently lead to higher particle emissions.

Regarding soot mass concentration, Figure 6.5 further portrays that the higher load condition leads to an overall higher mass concentration. Soot mass further involves more complex phenomena related to surface reactions and oxidation processes. These are dependent on the soot precursor species concentration and the in-cylinder thermodynamic conditions. At higher load, the larger film mass on the injector tip is more likely to lead to zones with dense fuel concentration in the tip vicinity, an ideal scenario for soot formation.

It is also worth noting the difference between single and double injection strategies in terms of particle number and mass concentration. No appreciable difference can be observed in terms of particle number, on the other hand, soot mass concentration is higher for double injection at both medium and high loads. Since injector tip sooting is known to be a source of soot emissions

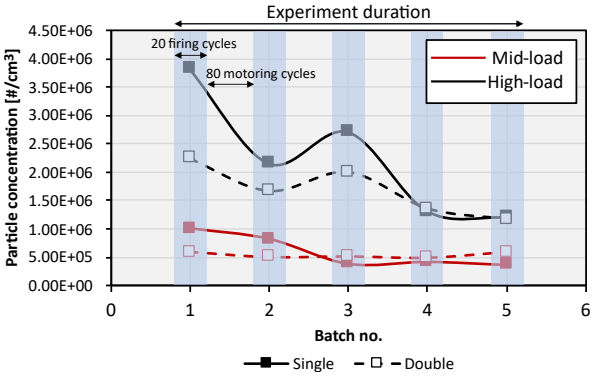

Figure 6.4: Particle number at medium and high load conditions.

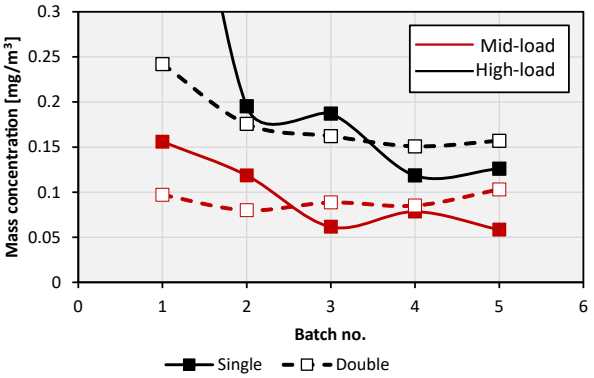

Figure 6.5: Soot mass concentration at medium and high load conditions.

for fouled injectors, it is probable that single and double injection strategies exhibit different effects on injector tip wetting. In a study by Berndorfer et al. [5], it was shown that split injection strategies led to higher amount of fuel on the injector tip after end of injection (aEOI). They arrived at their conclusion by analyzing flame intensity images captured at the injector tip during both single and split injections. The correlation observed indicated that elevated flame intensities at the injector tip were linked to increased tip wetting. This association may be attributed to the relatively low fuel flow velocities during the opening and closing phases of the injector needle. The reduced momentum during these stages makes it more likely for the fuel exiting the nozzle to remain attached to the nozzle tip and be deposited on the injector tip surface [6]. As a result, an increase in the frequency of opening and closing events would likely result in a higher degree of tip wetting.

Based on the examination of images captured from the bottom and lat-

eral windows, it was evident that the sooting flame predominantly originated from the injector tip. This is further supported by Figure 6.6a, which puts in evidence a greater luminosity radiated from the injector zone. There was a minor contribution from the piston, particularly in the high load case, as evidenced in Figure 6.6b. Soot formation originating from the piston was primarily noticeable from the lateral view, characterized by a limited area of the sooting flame. Other sources in Figure 6.6 correspond to flames originating from regions excluding the injector and piston ROIs. Under both load conditions, the occurrence of sooting flames in such regions were scarce. Channel intensity and percentage of occurrence were taken for 80 cycles, including both single and double injection strategies. Owing to the predominance of the luminosity from the injector tip region, the yellow flame area in the injector ROI was then examined to identify any discernible trends between single and double injection strategies. The evolution of the yellow flame area during the cycle is depicted in Figure 6.7. The curve represents the average of the last two batches (40 cycles). Firstly, the earlier analysis comparing medium and high loads can now be validated, as high load cases manifest larger yellow flame areas. Secondly, a difference between single and double injection cases is apparent, with double injection cases exhibiting greater flame areas. All instances decay around comparable crank angle values as the sooting flame separates from the injector tip during the expansion stroke and ultimately exits the region of interest and then into the exhaust at EVO. It should be noted here that the early increase in yellow flame area at high load, highlighted by the light blue zone, is unreliable since hot combustion gases emit high red channel intensities comparable to soot luminosity.

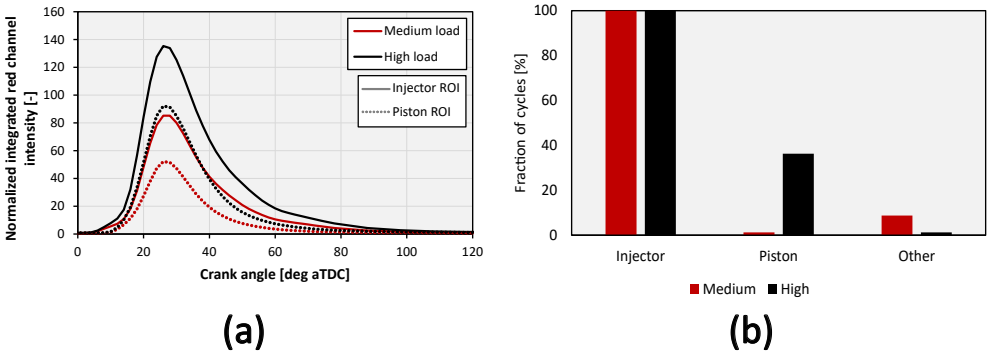

Figure 6.6: Integrated red channel intensities in the injector and piston regions (a) and the fraction of cycles exhibiting sooting flames from each region (b). The red channel intensities are normalized by the respective area of the ROI.

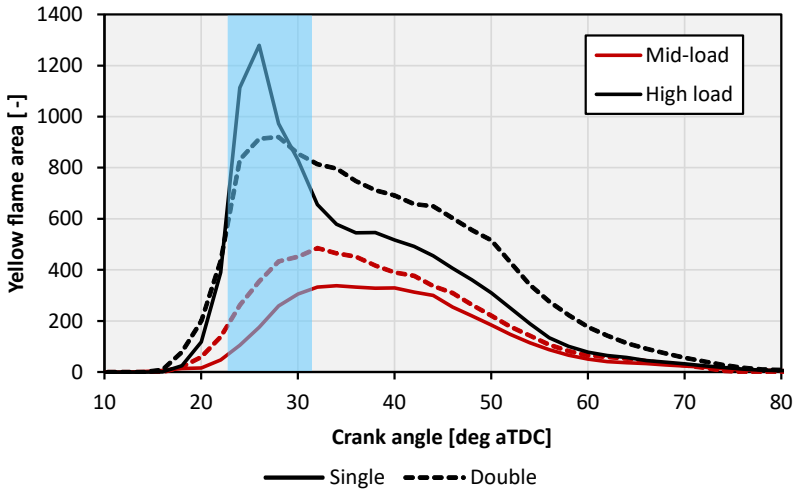

Figure 6.7: Yellow flame area at medium and high loads for both injection strategies in the injector ROI.

An illustrative cycle highlighting the distinctions between the load conditions is presented in Figure 6.8. Images depicting the bottom and lateral views are shown at two distinct instances: the initial emergence of the soot flame and a later stage during the expansion stroke. Utilizing both bottom and lateral views facilitates a thorough examination of the observed sooting flame, enabling not only the identification of its origin but also an assessment of its size. In the portrayed instances, it is apparent that the higher load scenario exhibits a larger yellow flame area connected to the injector tip.

6.1.5 Injection pressure effect on injector zone emissions

While many studies have concentrated on the improvement of mixture quality through increased spray velocity and atomization, it is equally intriguing to investigate the injection pressure effect on injector film and wall wetting behavior. As observed in the preceding section, the main contributor to soot formation is the residual liquid film on the injector tip. Thanks to the optimal injection timing (-310° CA), ample time is provided for achieving mixture homogeneity along with minimal spray-wall interaction. In this section, the results pertaining to injection pressure variation are presented at a fixed SoI_e.

In this analysis, the injection timing has been advanced by 20 degrees as it was part of a sweep campaign examining the SoI_e at different injection pressures. The discussion on the impact of SoI_e variation on soot was part of this study but will not be addressed here. Figure 6.9 plots the particle number

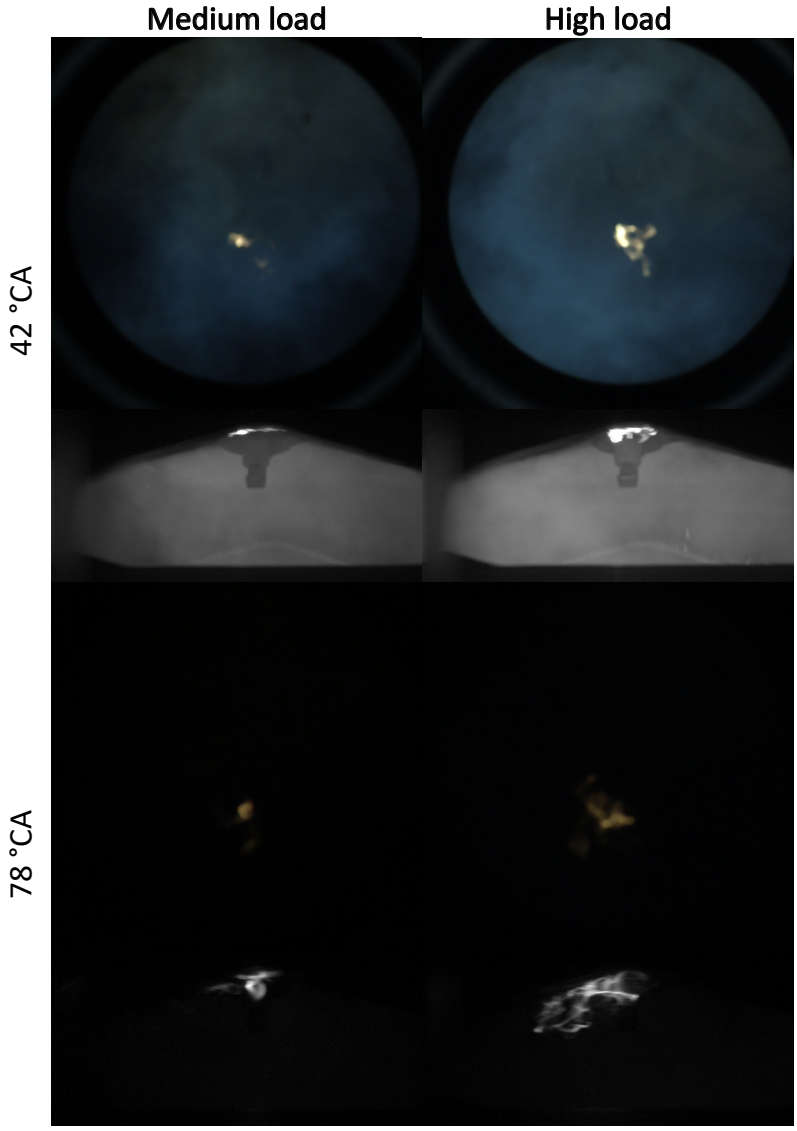

Figure 6.8: Soot flame imaging at different instants throughout the cycle.

and mass concentrations versus injection pressure. Both particle number and mass concentrations follow the same trend. Particle emissions initially increase when moving from 60 bar to 120 bar of injection pressure then decrease, at the highest injection pressure. The values shown represent peak values of the second batch of SoI_e sweeps, as explained in subsection 6.1.1. It is interesting to note that the use of the lowest injection pressure led to reduced particle emissions, which goes against the conventional expectations. As the injection timing is well advanced relative to spark timing, the lower injection pressure still possesses ample time to achieve mixture homogeneity, suggesting other factors may be contributing to soot formation. At such an advanced timing, it is anticipated that wall impingement is likely to become significant. Additionally, the combined effects of injector tip wetting suggest that these two factors are more likely to be the determining contributors.

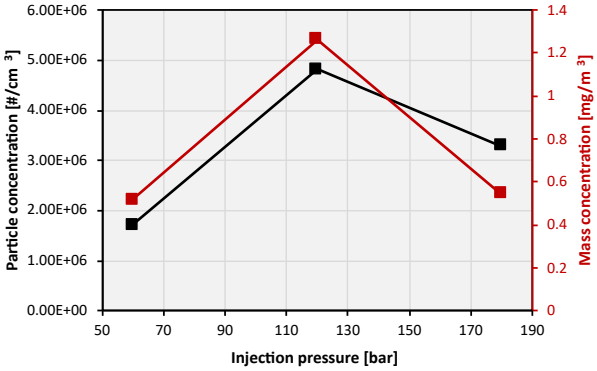

Figure 6.9: Particle concentration (left axis) and soot mass concentration (right axis) variation with injection pressure.

Figure 6.10 depicts the integrated red channel intensity for the injection pressures tested. Individual cycles are plotted as gray curves whereas the average intensity is represented by the dark red curve. The peak intensity consistently diminishes with higher injection pressure. Likely, the fuel film on the injector tip at the start of combustion is less pronounced in cases of higher injection pressure, due to the increased momentum of the fuel as it exits the nozzle orifices, restricting the deposition on the tip surface. Referring back to Figure 6.9, despite the fact that less soot is visualized from the injector tip at 120 bar compared to 60 bar, it is noteworthy that the 120 bar case exhibits particle number and mass concentrations that are twice as high as those at 60 bar injection pressure.

To further support film mass differences, the frequency of yellow flame occurrence was computed at 32 °CA and is shown in Figure 6.11. The fre-

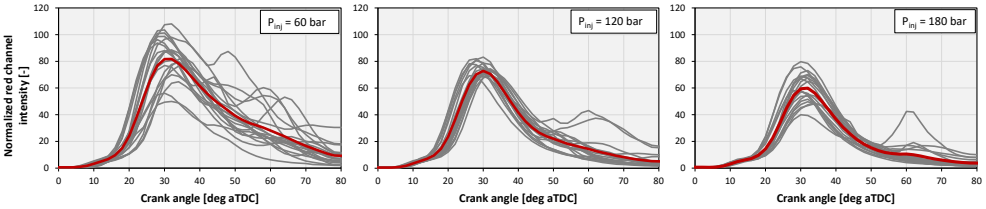

Figure 6.10: Injector zone integrated red channel intensity at the tested three injection pressures. SoI_e was fixed at -330 ° aTDC.

quency images indicate an increased presence of a sooting flame coming from the injector tip in the case with the lowest injection pressure. Furthermore, when examining the lateral image at 60 bar, it is observed that a few instances of yellow flames are scattered near the liner on the right-hand side and above the piston. These occurrences may stem from rich pockets in this region due to inadequate mixture preparation. However, they could also be formed as a result of rich areas arising from the evaporation of the liquid fuel film on the piston. At 120 bar, a larger fraction of cycles exhibit soot in the piston-bowl region. It is noteworthy to mention that the inlet side consistently exhibited higher soot occurrence. This could be attributed to the interaction of the spray with the incoming charge during the intake phase. On the one hand, it can be inferred that the increased spray-wall impingement at 120 bar, counteracted the advantages observed in soot reduction from the injector tip, when compared to the 60 bar case. On the other hand, elevating the injection pressure to 180 bar resulted in a decrease in soot around the piston-bowl region compared to the 120 bar case. However, the overall reduction in tip soot was not significant enough to achieve particle number/mass values comparable to those of the lowest injection pressure at 60 bar. Consequently, it can be asserted that spray-wall impingement exerted a greater influence on overall particle emissions in contrast to injector tip sooting. It is essential to note that the sooting dynamics may vary under different injection timings, however, injector-induced sooting flames are more likely to show a consistent trend with injection pressure at various SoI_e.

6.2 Injector film formation and evaporation

The injector film formation model adopted in this thesis is based on the work of Alzahrani et al. [7] who developed an analytical model for injector film evaporation. For a more thorough explanation of the mathematical formulations and physical assumptions taken, the reader is referred to their work.

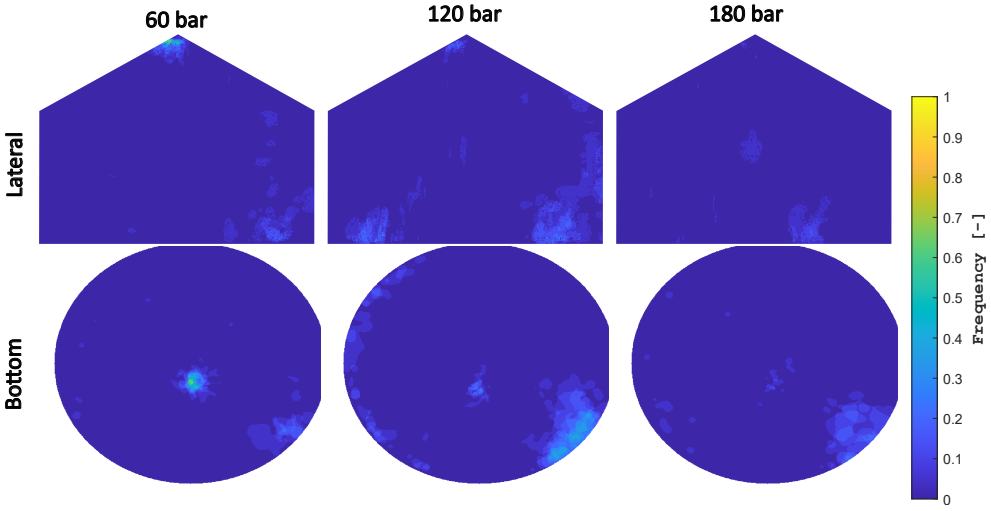

Figure 6.11: Frequency of yellow flame occurence as observed from the lateral (upper row) and bottom (bottom row) views for the different injection pressures.

The evaporating behavior of the film is governed by diffusion from the liquid film to the gas phase. The difference in vapor pressure between the liquid and the gas determines the mass transfer as shown below

$$\frac{dm}{dt} = \frac{\overline{MW} A_s D}{RTL_s}(p_{v,L} - p_{v,g}) \tag{6.1}$$

where $\overline{MW}$ is the average molecular weight of the vapor phase, R is the universal gas constant, T is the vapor phase temperature, A_s is the surface area of evaporation, D is the diffusion coefficient, L_s is the film thickness, $p_{v,L}$ is the liquid vapor pressure, and $p_{v,g}$ is the vapor pressure taken as the in-cylinder pressure. The liquid vapor pressure is computed by the Antoine Equation for temperatures up to T_{min} of 398 K for liquid phase iso-octane and the Extended Antoine equation for liquid film temperatures between T_{min} and T_{max} of 398 and 543 K, respectively. Antoine equation coefficients were obtained from Poling et al. [8]. Moreover, the diffusion coefficient is calculated based on the theory describing diffusion in binary gas mixtures at low to moderate pressures [8].

Resolving Equation 6.1 requires the knowledge of the film temperature. The change of film temperature was assumed to be due to conduction from the injector tip surface only. The injector tip is exposed to the hot combustion gases in each cycle contributing to a heating effect of the newly deposited fuel

film. Conduction from the injector tip surface to the fuel film is represented by the following heat conduction equation:

$$q(t) = kA_s(\frac{T_w - T_L(t)}{L(t)}) \tag{6.2}$$

where k is the thermal conductivity of the fuel film, T_w is the injector tip temperature, T_L is the fuel film temperature, and L is the fuel film thickness. The injector tip temperature was considered to be the same as the cylinder head temperature. The rate of heat conduction can be expressed as a function of the liquid film temperature as:

$$q(t) = \rho(t)V(t)c_p\frac{dT_L}{dt} \tag{6.3}$$

where $\rho(t)$ is the fuel film density and $V(t)$ is the fuel film volume. The fuel film thickness changes according to:

$$L(t) = \frac{m(t)}{\rho(t)A_s} \tag{6.4}$$

where $m(t)$ is the fuel film mass. In addition, liquid properties such as thermal conductivity, density, and specific heat were calculated as a function of temperature according to the expressions in [8]. It must be mentioned that the analytical model does not incorporate the effect of local air velocity on liquid film evaporation which could be a drawback at higher engine speeds. Nevertheless, detailed assessment of the phenomenon requires 3D CFD simulations of the injector geometry and velocity field around the injector tip which is out of the scope of the present study. The approach assumes that a certain mass of fuel remains on the injector tip after EOI, which evaporates due to heat transfer from the tip surface and mass diffusion until SOC. The liquid film is assumed to be cylindrical covering a surface area of A_s. A schematic summarizing the fuel film evaporation from the injector tip is depicted in Figure 6.12.

The difficulty remains in the consideration of the constant surface area for evaporation A_s. From the findings of the optical study, two main conclusions are drawn:

- Increasing the injected fuel mass when transitioning from medium to high load conditions correlates with higher luminosity emitted from the injector region. At higher loads, a larger sooting flame area suggests

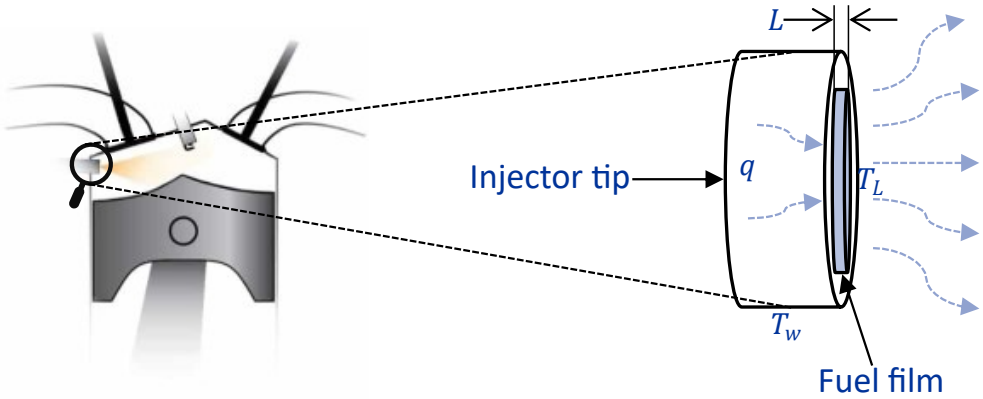

Figure 6.12: Schematic showing heat transfer from the injector tip to liquid fuel film by conduction and evaporation by mass diffusion to gas phase.

increased fuel mass deposition on the injector tip, corresponding to the elevated fuel mass levels.

- Increasing injection pressure demonstrates a mitigating effect on injector-induced particle emissions, as evidenced by the diminishing intensity of the red channel within the injector ROI. Under equivalent injected fuel masses, this phenomenon indicates a reduced deposition of fuel on the injector tip, attributable to the higher momentum of fuel as it is discharged from the nozzle.

The first observation is duly accommodated within the analytical model, as it encompasses the retention of 0.1% of the injected fuel mass on the injector tip at the end of injection. This value comes from the experimental observations of Leick et al. [9], where the observed fuel tip volume varried between 0.012 – 0.035 mm^3 as back pressure decreased, corresponding to 0.1% of the injected volume. Consequently, the higher injected fuel mass inherently leads to an increased mass deposition on the injector tip. Regarding the surface area A_s, a sensitivity analysis was conducted based on measured particle number and soot concentrations, constituting the sole available data for model validation in this instance. Given that mixture heterogeneities primarily emit particle emissions in the nucleation mode, the analysis focused on particles in the accumulation mode (D_p>30 nm). Thus, the sensitivity analysis aimed to match simulated particle emissions with measured ones in the accumulation mode. Moreover, it was assumed that only the injector tip wetting soot pathway contributes to accumulation mode particles. Another significant consideration is the zone temperature. Analogous to rich mixture

zones, temperature correction becomes imperative to account for temperature boundary layers near the wall zone. No additional sub-model was employed for this purpose and the temperature correction factor was incorporated into the sensitivity analysis, along with A_s.

6.2.1 Computation of A_s and $F_{corr,pyr}$

The extent of surface area available for evaporation influences the residual fuel film at the start of combustion, consequently impacting the volume of the injector zone for pyrolysis reactions. As a result, this parameter directly influences the scaling of both final particle number and mass concentration values in the exhaust. The influence pertains solely to the scaling of the zone volume and does not introduce alterations to chemical kinetics or particle formation processes. Conversely, the temperature correction factor plays a pivotal role in soot chemistry and particle processes, as it adjusts the temperature profile within the zone. Unlike gas-phase fuel rich zones, the temperature correction factor is determined through a more empirical approach, utilizing a tunable temperature threshold value.

$$F_{corr,pyr} = \frac{T_{thresh}}{max(T_{cyl})} \tag{6.5}$$

where T_{thresh} is computed from the sensitivity analysis and T_{cyl} is the burned gas temperature.

The results of the sensitivity analysis are first shown for the surface area for evaporation in Table 6.3. The values were obtained from a calibration procedure done with respect to the measured particle number concentration in the accumulation mode.

Table 6.3: Surface area for evaporation A_s.

Case	A50	A100	B50	B100
Area	2.33e-06	6.00e-06	2.80e-6	7.60e-6

Two trends emerge in this context: one contingent upon load and the other reliant on injection pressure. When engine load is increased at constant speed, both the injection pressure and injected fuel mass increase. Higher injection pressure necessitates a larger surface area for evaporation to achieve the desired outcome of reduced injector tip sooting. Nevertheless, it is important to note that a higher injection pressure does not necessarily correspond to a

greater surface area in reality. However, within the framework of the simplified evaporation model, it represents the most straightforward method to attain the desired outcome. The higher injected fuel mass would also cover a larger portion of injector tip thereby contributing to an increase in A_s. This is explained by the difference in areas between the A100 and B50 cases, where both operate with 100 bar of injection pressure.

Figure 6.13 plots the surface area for evaporation against the relevant variables, in this case, injected mass and Weber number. The first parameter accounts for the engine load, while the second accounts for the injection pressure. A strong correlation exists indicating a robust relationship between injector-induced particle emissions and both the injected mass and injection pressure. However, it cannot be definitively asserted that injection pressure directly results in an increase in surface area in practice. The influence may primarily affect the mass of the fuel film rather than its area. Nonetheless, the model addresses this by accounting for changes in the surface area.

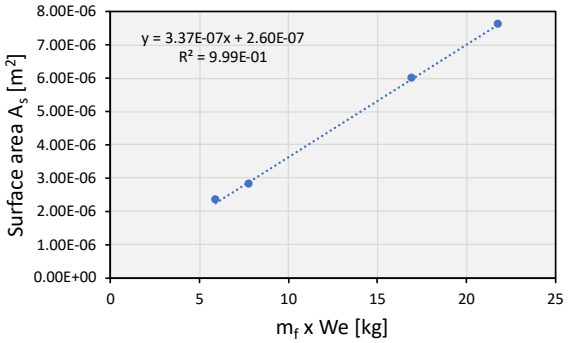

Figure 6.13: Correlation of the surface area for evaporation and the product of the injected mass and Weber number.

The obtained values of A_s lie within the order of magnitude of those observed by Leick et al. [9], who measured the injector tip film thickness under different combinations of injection pressures and back pressures.

Regarding the temperature correction factor, a threshold temperature of 2180 K deemed suitable for the four cases. The correction factors are then computed according to the maximum in-cylinder temperature. Table 6.4 shows the corresponding correction factors for each operating condition. Medium load cases required smaller temperature correction factors since they exhibited higher in-cylinder temperatures due to stoichiometric combustion.

The particle number and mass concentrations in the accumulation mode are depicted in Figure 6.14. A higher level of concordance between simulated

Table 6.4: Temperature correction factors for the injector zone.

Case	A50	A100	B50	B100
$F_{corr,inj}$	0.8651	0.9239	0.8601	0.8929

and measured values is observable for particle number concentration compared to mass concentration. This discrepancy is likely attributed to the method of computation for the temperature correction factor, which notably influences soot mass. As depicted in Figure 6.14b, it is apparent that medium loads exhibit an overestimation of temperature, whereas high load injector zone temperatures are underestimated.

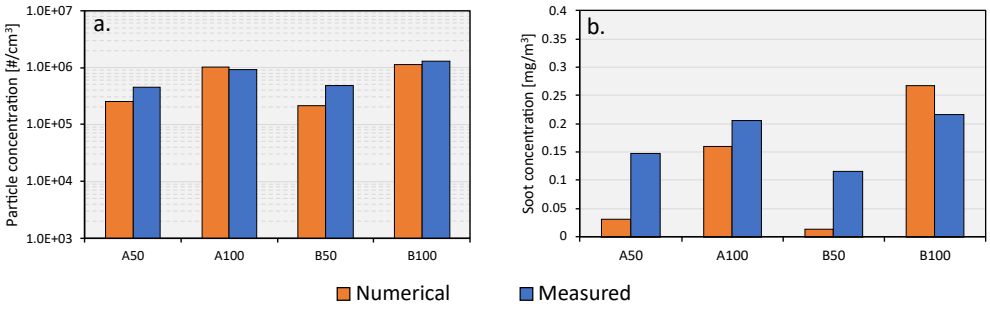

Figure 6.14: Particle number (a) and soot mass concentration (b) in the accumulation mode (D_p>30 nm).

6.2.2 Film mass evolution

As mentioned earlier, the initial film mass at EOI constitutes of 0.1% of the injected fuel mass. The computed surface area for evaporation is kept constant throughout the evaporation process and only the film thickness varies according to the evaporated mass. The evolution of the film mass is shown in Figure 6.15 for all four cases.

The figures depict the instantaneous film mass, cylinder pressure, and liquid vapor pressure. A similar trend is observed in all cases in which the fuel film mass decreases in an exponential form until it reaches a minimum value after which it starts to increase. That increase corresponds to the time at which the in-cylinder pressure becomes higher than the liquid vapor pressure as the piston approaches TDC during the compression phase. This process would lead to the vapor fuel condensing back into the liquid film on the injector tip. The simplified evaporation model, however, does not incorporate bulk gas

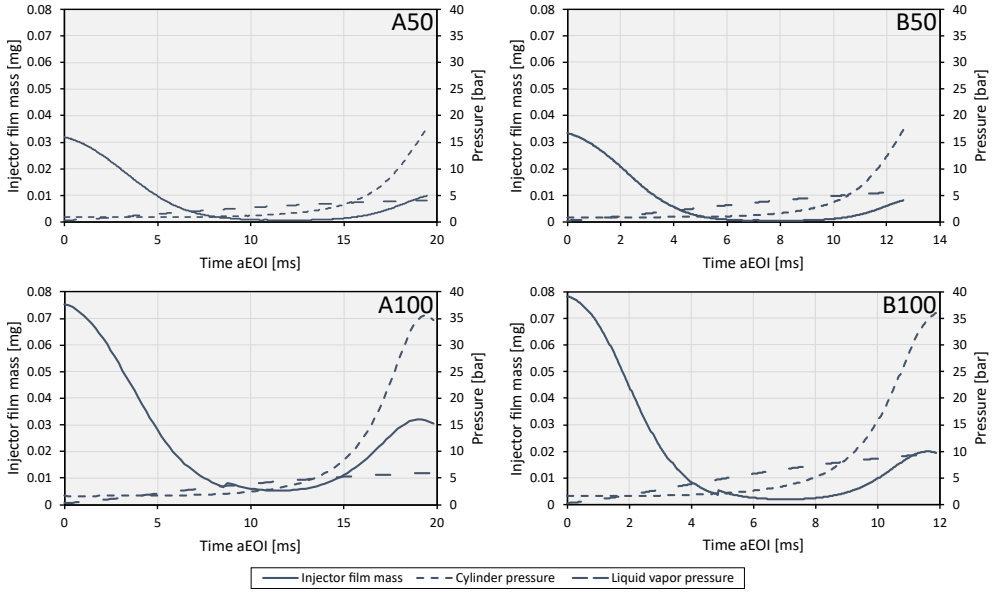

Figure 6.15: Injector fuel film mass evolution from end of injection up to start of combustion.

motion in the cylinder, which, in a real engine scenario, would disperse the newly evaporated film mass away from the injector tip. Consequently, the minimum film mass observed in the trend is regarded as the film mass at the start of combustion. Subsequently, this film mass is transferred to the particle model for calculating particle emissions. It should be noted that a minor discontinuity occurs in the film mass trends coinciding with IVC event, marking the transition for CALMEC from solving the mass conservation equation for an open cycle to a closed cycle. This transition introduces a correction in cylinder trapped mass calculations, consequently affecting gas temperature calculations.

6.2.3 Injector zone mass and volume considerations

Given that the 0D model does not incorporate local information, certain assumptions were required to calculate the necessary variables, such as the injector zone mass and volume. Before delving into these considerations, it is imperative to address the physical aspects of soot formation within the injector zone.

A recent study by Singh et al. [10] looked into soot formation via pool-fire mechanism. The authors used diffused back illumination (DBI) to visual-

ize the interaction of the fuel film with the approaching stoichiometric flame front in a spray vessel. Experimental observations showed the slow formation of soot after the flame front has passed, suggesting a decoupling from thin premixed flame combustion processes and a primary role of pyrolysis driven by hot combustion-product gases. In an oxygen-depleted environment, soot formation would primarily occur through pyrolysis reactions. Their DBI images also revealed the presence of a lift-off height above which soot formation occurred. This indicates the existence of a significant gradient in fuel mass fractions above the wall, driven by film evaporation due to conduction from the wall and the high temperature of combustion gases. Further away from the wall, fuel concentration would be lower, but a temperature exceeding 1400 K would be adequate for soot formation, provided that the timescales are long enough. In an actual engine, the timescales are expected to be shorter owing to the rapid propagation of turbulent flames, leading to much faster film evaporation.

An example of a sooting flame emerging from the injector tip in is depicted in the sequence of images shown in Figure 6.16. The appearance of a sooting flame only occurs after the flame has consumed all the gas in the field of view (22 °CA). As the piston recedes downwards, the sooting flame area expands and grows by diffusion from the hot combustion products. The sooting flame persists late through the expansion stroke and exits the cylinder at EVO.

To model these processes in the current framework, certain assumptions are required [11]. Firstly, the fuel film mass at SOC ($m_{film,SOC}$) is assumed to evaporate instantaneously. Secondly, the equivalence ratio gradient above the injector tip is neglected and all the fuel mass is lumped into a single zone at a single fuel mass fraction value $Y_{f,pyr}$. Lastly, the sooting flame grows only by expansion according to the zone volume which is computed by the ideal gas law. In this way, soot is formed by pyrolysis behind the flame front by reacting with the residual gas from combustion at the global ϕ value. The pyrolysis zone mass is assumed to remain constant throughout the cycle and is defined by the film mass at SOC and the calibrated pyrolysis zone fuel mass fraction value:

$$m_{pyr} = \frac{m_{film,SOC}}{Y_{f,pyr}} \tag{6.6}$$

where m_{pyr} is the pyrolysis zone mass, $m_{film,SOC}$ is obtained from the film evaporation model, and $Y_{f,pyr}$ is obtained from the molar fuel fraction value in the pyrolysis zone $X_{f,pyr}$. The parameter $X_{f,pyr}$ was adjusted within the range of 0.005 to 0.02 (±30% of the value used in [11]), and a value of 0.01

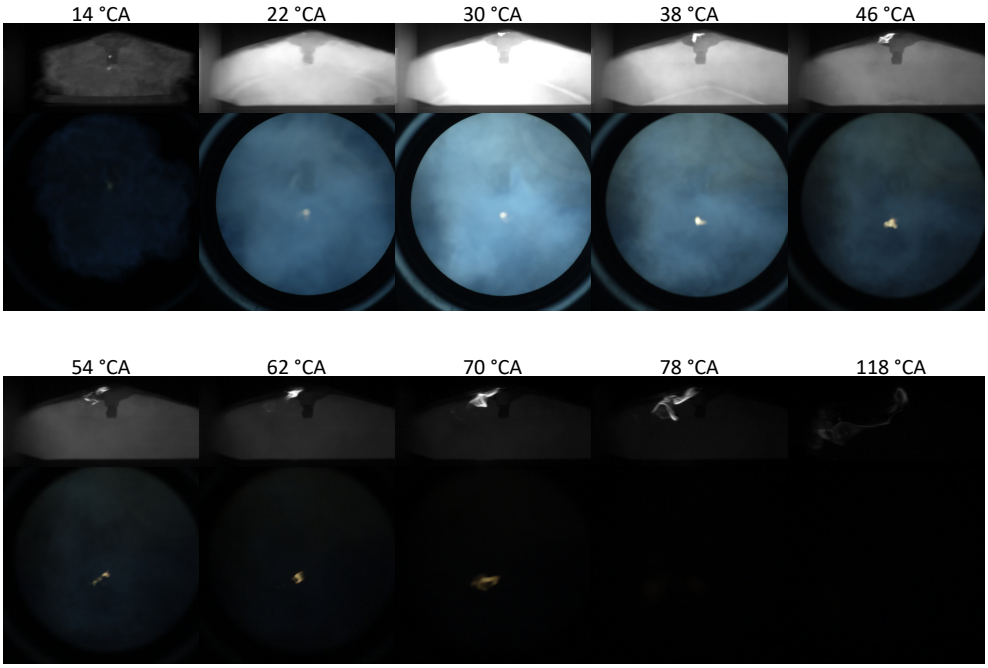

Figure 6.16: Injector tip sooting flame evolution at 1400 RPM and 13 bar.

was determined to be appropriate for the purposes of this study. The fuel mass fraction in the pyrolysis zone can then be computed according to:

$$Y_{f,pyr} = \frac{X_{f,pyr} \cdot MW_{IC8H18}}{\overline{MW}_{pyr}} \tag{6.7}$$

where MW_{IC8H18} is the molecular weight of isooctane and $\overline{MW}_{pyr}$ is the mean molecular weight of the gas in the pyrolysis zone.

With the constant mass of the pyrolysis zone, the instantaneous volume can be calculated according to the ideal gas law:

$$V_{pyr}(t) = \frac{m_{pyr} R T_{pyr}(t)}{\overline{MW}_{pyr}(t) p_{cyl}(t)} \tag{6.8}$$

where R is the gas constant, $T_{pyr}(t)$ is the injector zone temperature after correction, and $p_{cyl}(t)$ is the in-cylinder gas pressure. The pyrolysis zone volume directly influences the final particle number and soot concentrations by scaling the emission values obtained from the particle model, similarly to the zones arising from mixture inhomogeneity. At SOC, the pyrolysis zone is initialized with the pyrolysis zone fuel mass fraction value and burned gas

from combustion at the global equivalence ratio. Therefore, the zone is already considered to be burned and reacts by pyrolysis, so the rightmost term in the species conservation equation is omitted and Equation 4.21 becomes:

$$\frac{dY_{b,i}}{dt} = \frac{\dot{\omega}_i MW_i}{\rho_b} \tag{6.9}$$

6.3 Injector induced particle emissions

With the assumption that particle emissions formed from injector tip fuel films contribute to particles in the accumulation mode, the complete particle size distribution can now be represented. Figure 6.17 plots the simulated and measured PSD showing only the contribution of injector-induced particles. The trends, previously shown by the bar graphs in Figure 6.14a and Figure 6.14b, are further clarified here by the PSD. At high load conditions, particle diameters in the accumulation mode tend to be overestimated compared to the measurements, resulting in an overestimation of the soot mass concentration for the B100 case. This highlights the high sensitivity of the soot mass concentration on particle size. Better agreement is observed at medium load conditions, where peak concentration values are attained at very comparable diameters. The discrepancies observed at higher loads are likely due to the method adopted for computing the temperature correction factor. The temperature threshold does not account for enrichment, which already decreases the global gas temperature in the cylinder. Hence, the correction factor excessively reduces the temperature leading to larger average particle size.

When transitioning from 2000 rpm to 3000 rpm under constant engine load (from A50 to B50 or A100 to B100), an increase in the particle concentration of the second mode (accumulation mode) is evident in both the measured data and the predicted numerical PSD. This phenomenon is likely due to a decreased duration for particle growth processes, particularly coagulation, which stands as the primary factor influencing the final particle count. This is further illustrated in Figure 6.18, where a higher particle count is observed at the end of the calculation for the 3000 rpm case due to its shorter duration to reach the TDC exhaust phase. As a result, particle size is expected to lean towards smaller diameters, as indicated by the comparison of the numerical PSDs of A50 and B50.

Calibrating multiple parameters is crucial for the numerical model, as achieving a full physical depiction of the phenomenon is unattainable through

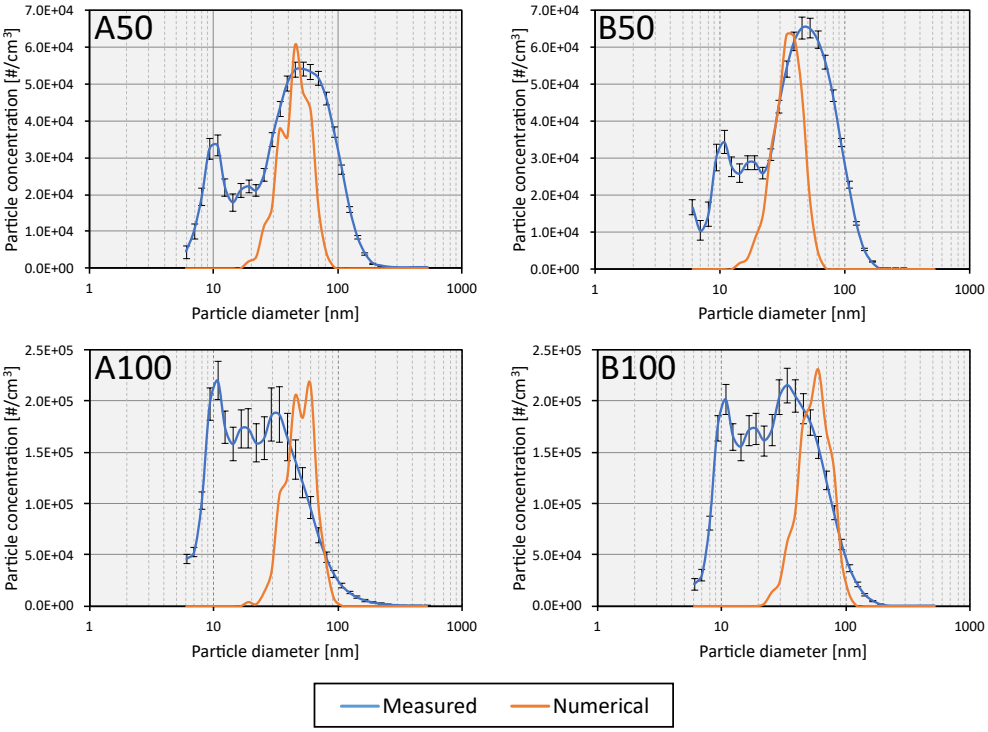

Figure 6.17: Particle size distribution comparison between measured and numerical values. Only the injector tip wetting soot pathway is shown in the numerical trends.

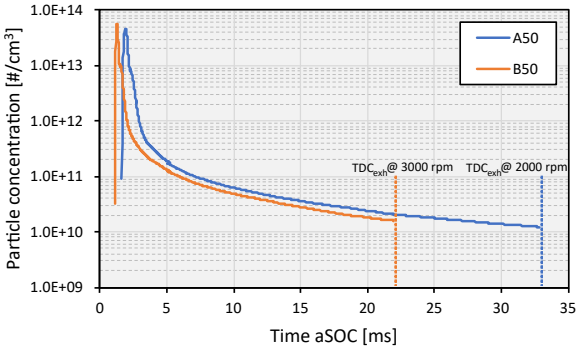

Figure 6.18: Engine speed effect on particle number concentration at 50% load.

a 0D approach alone. To gain a better understanding of how the results are influenced by the adopted simplifications, a sensitivity analysis was conducted on parameters relevant to soot, such as the temperature correction factor and fuel molar fraction. In this study, the gasoline fuel, utilized in the measurement campaign, was simulated with iso-octane. Unlike gasoline, iso-octane lacks any aromatic content, which could introduce discrepancies in the results. Nevertheless, concerning injector-induced particles, this variation could be addressed by adjusting the $X_{f,pyr}$ parameter. The subsequent sections elaborate on the investigated parametric variations and their effects on particle number and mass concentration.

6.3.1 Influence of the temperature correction factor

Figure 6.19 illustrates the impact of temperature correction factor variations on the sensitivity of particle number concentration and mass concentration. The sensitivity analysis focuses on the A50 case. During this analysis, the temperature correction factor was adjusted within 4% of the calibrated value for this operating condition.

As anticipated, variations in temperature exhibit a more pronounced effect on soot mass concentration. This outcome is attributed to the significant influence of temperature on surface reactions, which in turn affects soot oxidation rates. Lower temperatures are expected to result in decreased oxidation rates, consequently leading to higher soot mass concentrations.

Furthermore, it is anticipated that lower temperatures will lead to higher concentrations of A_4 in the gas phase due to reaction kinetics, potentially resulting in elevated condensation rates. This phenomenon contributes to an increase in particle mass and size. Notably, when the temperature correction factor was increased by 4%, particles were eliminated due to the low concentration of A_4 in the gas phase, coupled with high oxidation rates.

6.3.2 Influence of the fuel concentration

The fuel concentration was varied within 15% of the calibrated value of 0.01. Generally, increasing the initial fuel concentration in the injector zone would lead to higher nucleation rates. This is shown in Figure 6.20a where higher final particle concentrations are evident in most cases. However, an increase of 5% resulted in around 20% reduction in particle concentration, likely attributed to the higher coagulation rate which led to final particle number that are lower than the baseline case. This is supported by a higher maximum value exhibited when increasing $X_{f,pyr}$ by 5%, increasing the probability of

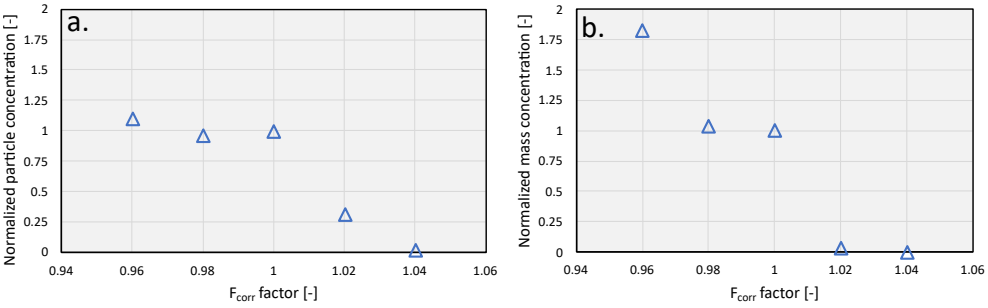

Figure 6.19: Sensitivity of particle concentration (a) and soot mass concentration (b) on the temperature correction factor. Temperature correction factor varied within 4% of base value for the A50 case.

coagulation and thus reducing particle number. Another aspect affecting final emission levels of particles is the mass of the pyrolysis zone. As $X_{f,pyr}$ rises, and correspondingly $Y_{f,pyr}$, the mass of the pyrolysis zone diminishes (refer to Equation 6.6), consequently leading to a reduction in the overall particle concentration within the cylinder. The mass concentration exhibits a similar pattern to the particle number. In this context, reaction kinetics likely play a role, where higher fuel mass fraction is expected to yield more OH radicals, thereby explaining the observed trend by a factor of 1.05. Hence, it is evident that the phenomenon entails competing physical processes that contribute to the final emissions of particle number and mass.

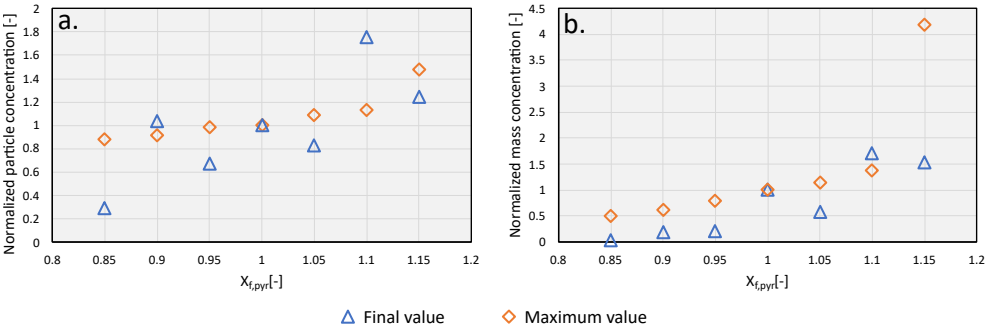

Figure 6.20: Sensitivity of particle concentration (a) and soot mass concentration (b) on the injector zone fuel molar fraction. $X_{f,pyr}$ varied within 15% of base value for the A50 case.

6.4 Analysis of gas phase inhomogeneities and injector-induced particles

To complete the numerical PSD, the particles emitted due to combustion of fuel rich regions are added to the previously shown injector-induced particles. Figure 6.21 shows the particle size distributions of all operating conditions. The PSD is in better agreement with measured data at higher loads, as expected, since the rich zones, detected by the mixing model at medium load, did not contribute to particle emissions at simulation end. The first peak in the nucleation mode is likely due to another source of soot formation that is not covered by the model. Additionally, neglecting the gradient of equivalence ratios and temperatures above the injector tip fuel film is likely to affect the PSD, however, it cannot be ascertained what the particle morphology would be nor it can be analyzed by the current modeling approach. At high load, B100 exhibits a gap between the two particle formation modes possibly attributed to the gas phase. This indicates that the model is very sensitive to the tail of the equivalence ratio distribution curve. While those zones occupy a very small mass fraction of the total cylinder mass, their impact on soot formation seems notable.

To assess the influence of the final portion of the equivalence ratio distribution on particle formation, the distribution computed by CFD for B100 was provided as input to the particle model. In this case, a total of 14 zones were identified exceeding the sooting threshold with a maximum ϕ value of 2.02 (1.93 in the case of the empirical model). Figure 6.22 shows that the numerical model significantly overestimates the particle number density by almost two orders of magnitude. The equivalence ratio distribution affects the final results in different ways. The higher number of zone results in a smaller temperature correction factor leading to larger particles. In addition, the equivalence ratio computed by CFD simulations showed more fuel mass in zones exceeding the sooting threshold (see Figure 5.12) which directly impacts the final emission values. Although the shape of the PSD improves (the PSD trend now spans all particle diameter values between 5.6 nm and 100 nm), a larger disparity exists in total particle emissions values between numerical and measured values.

The nature of the soot formation process occurring in the bulk gas compared to the injector film zones are expected to be different. Soot formation in the rich zones of the bulk gas are formed early on as the flame consumes the unburned gas leading to diffusion-like combustion. In the injector film zones, soot is formed by pyrolysis reactions in the burned gas region after the

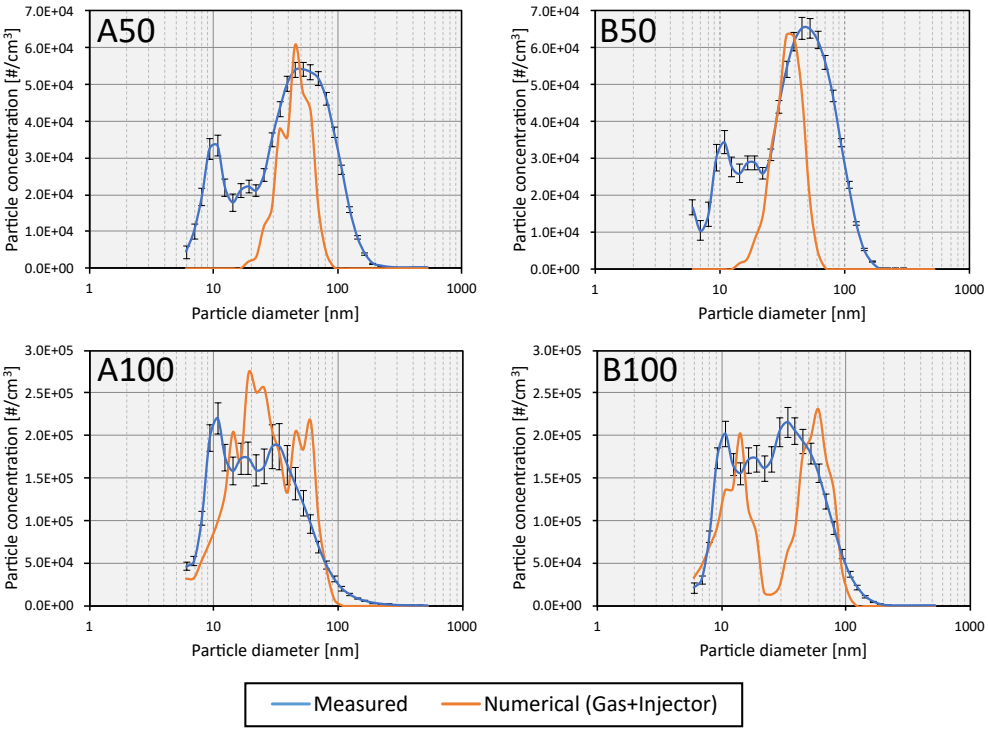

Figure 6.21: Particle size distributions of the four operating points. Numerical curves show the sum of particles emitted from the gas phase and injector films.

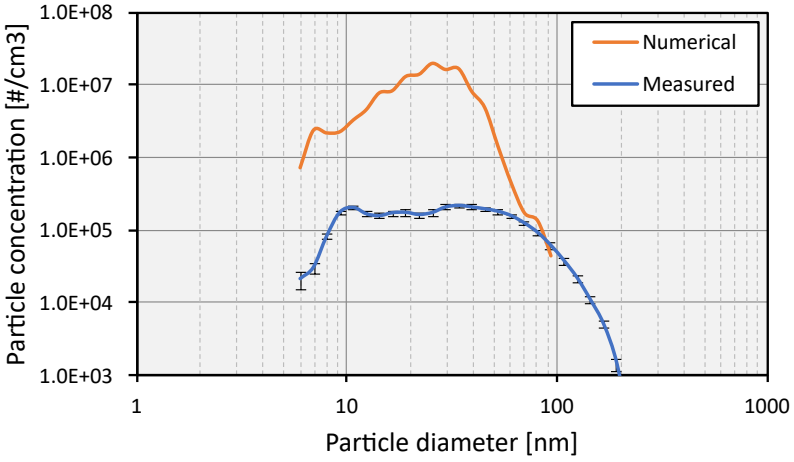

Figure 6.22: PSD of B100 case due to gas phase inhomogeneities and injector tip wetting. Gas phase particles are computed from the equivalence ratio distribution obtained from CFD.

flame front has already passed. Compared to the bulk gas, lower OH and O_2 concentratiosn are expected in the pyrolysis zone. Moreover, the temperature in the pyrolysis zone is lower than the temperature in the richest zone (see Figure 6.23) because these processes occur in the near-wall region, leading to relatively less intense oxidation. These factors collectively contribute to the differences observed.

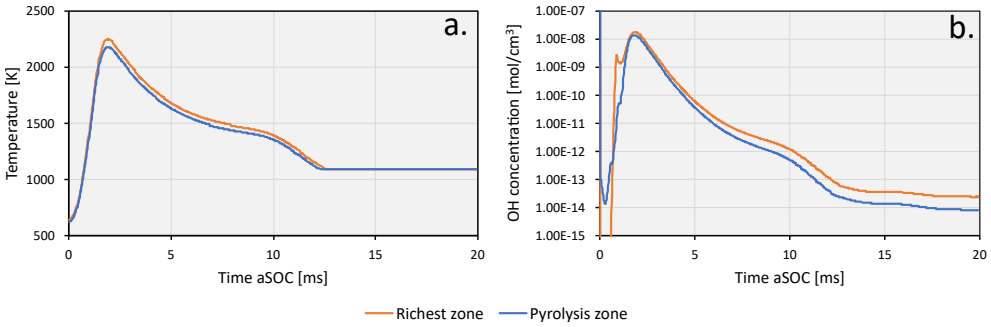

Figure 6.23: In-cylinder temperature (a) and OH concentration (b) in the richest and pyrolysis zones for the B100 operating point.

6.5 Summary

The first part of this chapter was intended to portray the physical considerations behind soot formation from injector films by means of optical engine experiments. High-speed direct imaging of combustion and soot luminosity were taken from two optical access points, the pent-roof and the piston bowl. The effects of engine load and injection pressure on injector zone soot emissions were outlined, emphasizing the interplay between engine parameters and combustion dynamics. At higher engine loads, larger sooting flame was observed at the injector tip signifying a greater wetted area when injected fuel mass is increased. Furthermore, increasing injection pressure was shown to decrease soot formation from the injector tip likely linked to the higher momentum of the fuel leading to lower fuel deposition.

From the observations of the engine experiments, an existing injector film evaporation model in literature was modified to account for the physical aspects of the film formation and evaporation processes. A correlation was found between the surface area for evaporation and the product of the injected fuel mass and Weber number. In this way, engine load and injection pressure variations are accounted for in the model affecting the final fuel film mass remaining at SOC.

The remnant fuel film mass is then passed to the particle formation model to evaluate engine-out particle emission. At high engine load conditions, particle diameters in the accumulation mode were shown to be overestimated compared to measurements, leading to an overestimation of soot mass concentration. This discrepancy was attributed to the method used to compute the temperature correction factor of the injector zone, which fails to account for enrichment, resulting in an excessive reduction of temperature and larger average particle size. Transitioning from 2000 rpm to 3000 rpm under constant engine load revealed an increase in the concentration of particles in the accumulation mode, attributed to a decreased duration for particle growth processes, particularly coagulation. A sensitivity analysis on parameters relevant to soot, such as the temperature correction factor and the initial fuel molar fraction, highlights the necessity of calibrating several parameters in the numerical model, given the inherent simplifications of the 0D approach used.

The complete PSD was then built by summing the contributions of gas phase inhomogeneities and injector tip wetting. The numerical model showed a suitable agreement with measured values and highlighted the different physical aspects associated with particle morphology from the two sources. Soot formation from injector films occur via pyrolysis reactions in the burned gas, leading to lower oxidation rates and larger particles compared to soot formation from rich pockets in the bulk gas. This difference was supported by differences in oxidation rates exhibited between the injector pyrolysis zone and the richest zone in the gas phase.

References

[1] Dec, J. E. “A conceptual model of di diesel combustion based on laser-sheet imaging”. In: *SAE Technical Papers* (1997). DOI: 10.4271/970873.

[2] Etikyala, S. and Dahlander, P. “Soot Sources in Warm-Up Conditions in a GDI Engine”. In: *SAE Technical Papers* (2021). DOI: 10.4271/2021-01-0622.

[3] Martinez, S., Merola, S., and Irimescu, A. “Flame front and burned gas characteristics for different split injection ratios and phasing in an optical GDI engine”. In: *Applied Sciences* 9.3 (2019). DOI: 10.3390/app9030449.

[4] Vuilleumier, D. and Sjöberg, M. "The Use of Transient Operation to Evaluate Fuel Effects on Knock Limits Well beyond RON Conditions in Spark-Ignition Engines". In: *SAE Technical Paper*. 2017. DOI: 10.4271/2017-01-2234.

[5] Berndorfer, A., Breuer, S., Piock, W., and Von Bacho, P. "Diffusion combustion phenomena in GDi engines caused by injection process". In: *SAE Technical Papers* 2 (2013). DOI: 10.4271/2013-01-0261.

[6] Medina, M., Alzahrani, F. M., Fatouraie, M., Wooldridge, M. S., and Sick, V. "Mechanisms of fuel injector tip wetting and tip drying based on experimental measurements of engine-out particulate emissions from gasoline direct-injection engines". In: *International Journal of Engine Research* 22.6 (2021), pp. 2035–2053. DOI: 10.1177/1468087420916052.

[7] Alzahrani, F. M., Fatouraie, M., and Sick, V. "Analytical model for liquid film evaporation on fuel injector tip for the mitigation of injector tip wetting and the resulting particulate emissions in gasoline direct-injection engines". In: *International Journal of Engine Research* 23.1 (2022), pp. 49–63. DOI: 10.1177/1468087420973897.

[8] Poling, B. E., Prausnitz, J. M., and O'Connell, J. P. *The Properties of Gases and Liquids*. Fifth Edit. New York: McGraw Hill, 2001.

[9] Leick, P., Bork, B., and Geiler, J. N. "Experimental characterization of tip wetting in gasoline DI injectors". In: *ICLASS 2018 - 14th International Conference on Liquid Atomization and Spray Systems* July (2018).

[10] Singh, E. et al. "Particulate Matter Emissions in Gasoline Direct-Injection Spark-Ignition Engines: Sources, Fuel Dependency, and Quantities". In: *Fuel* 338.October 2022 (2023). DOI: 10.1016/j.fuel.2022.127198.

[11] Frommater, S., Neumann, J., and Hasse, C. "A phenomenological modelling framework for particle emission simulation in a direct-injection gasoline engine". In: *International Journal of Engine Research* 22.4 (2021), pp. 1166–1179. DOI: 10.1177/1468087419895161.

Chapter 7

Spray-wall interaction

The third pathway to soot formation is discussed in this chapter. Initially, optical engine experiments are introduced to shed light on the physical phenomena driving spray-wall interaction. Subsequently, a simplified spray model is explained, essential for computing the relative distance between spray evolution and combustion chamber walls. The modeling methodologies for film deposition and evaporation are then detailed, outlining the strengths and limitations of the models. Finally, the chapter concludes with an examination of the extent to which this pathway contributes to soot formation.

7.1 Optical engine experiments

A brief overview of the results obtained from a SoI_e sweep carried out on the optical engine, whose characteristics have been previously presented in Chapter 6, will be shown here.

Particle number and mass concentrations are first compared at a SoI_e of -330 °CA for three different injection pressures. At this injection timing, the distance between the piston and the injector is short, hence, spray contact with the wall is likely to occur. Figure 7.1 shows the spray evolution for the different injection pressures. The red contour depicts the envelope of the liquid spray as seen through the pent-roof window. The spray at the highest injection pressure penetrates the fastest due to the higher momentum. Higher injection pressure cases may then result in a greater fuel deposition on the piston surface. This observation aligns with the particle number and mass trends when moving

from 60 bar to 120 bar of injection pressure (see Figure 7.2). However, the case at 180 bar demonstrated lower particle emission values compared to 120 bar, likely from improved atomization yielding smaller-diameter droplets than those at 120 bar. This would facilitate film evaporation and lower fuel film mass at the start of combustion. Moreover, owing to the higher droplet Weber number, a greater mass is likely to rebound, contributing to an overall lower film mass deposition on the piston surface.

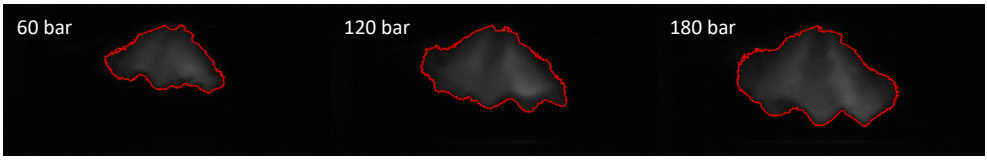

Figure 7.1: Spray evolution for different injection pressures at 4 °CA $aSoI_e$ captured from the pent-roof window.

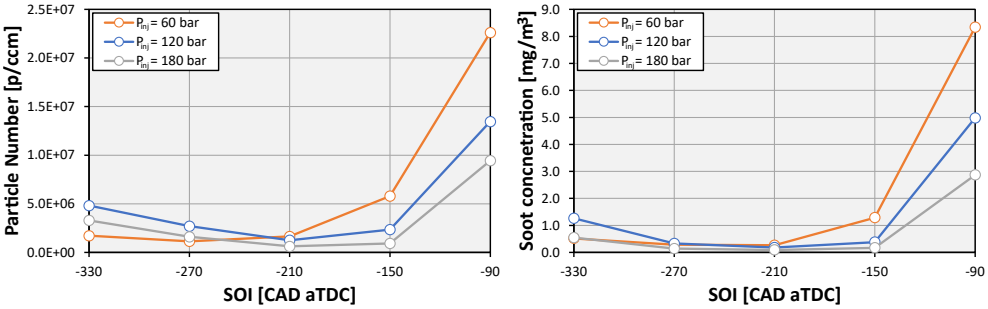

Figure 7.2: Particle number and mass concentrations at different SoI_es and injection pressures.

At -270 °CA, spray-wall impingement is reduced as the piston is farther downward at this timing, lowering the particle number and mass concentrations for the higher injection pressure cases. However, valve wetting is inevitable as the intake valve is around its maximum lift. This would be true for all cases of injection pressure and is probably why there is no noticeable decrease for the lowest injection pressure case. By SoI_e of -210 °CA, it would be safe to say that spray-wall interaction becomes much less significant and only constrained to a few cycles. The particle emission results remain comparable to values at -270 °CA due to contributions from other sources, such as injector tip wetting and mixture inhomogeneity. Further delaying the SoI_e to -150 °CA shows a noticeable increase for the 60 bar case while values remain almost the same for 120 and 180 bar. This is likely attributed to the longer injection duration of the 60 bar case resulting in more contact with the piston

as it moves upwards during the compression stroke. Mixture inhomogeneity also becomes a significant contributor at this timing since a reduced time is available for mixing. A visual representation is presented in Figure 7.3 to facilitate the interpretation of differences in durations among the various injection pressures.

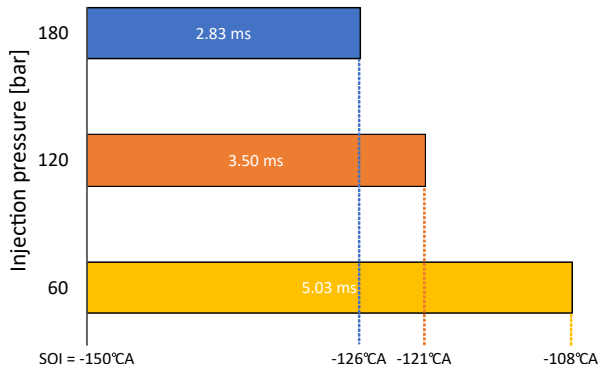

Figure 7.3: Injection durations for the different injection pressures. Each case illustrates the injection duration in milliseconds, along with the EOI timing in °CA aTDC for a SOI of -150 °CA.

At -90 °CA, all injection pressure cases show a significant increase in particle number and mass concentrations, as expected. At this very retarded injection timing, the likelihood of spray-wall impingement rises. Mixture inhomogeneity and injector film evaporation also play a role here since mixing time and film evaporation time are highly reduced.

From the observed results, it could be said that soot induced from spray-wall impingement depends on the interplay between injection timing and spray velocity. Other parameters that could influence wall wetting, especially at low load operation, is flash boiling, which in some cases could lead to spray collapse thus extending the penetration length [1, 2]. The temperature of the chamber also influences spray-wall impingement, with lower chamber temperatures, such as during cold starts, resulting in extended spray penetrations and consequently increased wall wetting [3].

7.2 Overview of simplified spray model

Examining the spray evolution during the injection process is a widely studied topic in engine research. Spray characteristics affect mixture formation and spray-wall interaction, subsequently influencing combustion behavior. In the

context of spray-wall interaction, spray development in the gas phase needs to be computed to assess whether contact with the wall occurs or not. Different spray models with varying level of detail exist ranging from simple empirical equations to more complex three-dimensional computational fluid dynamics approaches. Empirical correlations rely on experimental observations offering advantages in terms of simplicity, although being only applicable to certain conditions and injectors [4, 5]. Those correlations are often limited to providing information on spray macroscopic variables, such as spray penetration, although some also include spray microscopic details, such as the sauter mean diameter. Other more complex fluid dynamics approaches consider two-phase flows, liquid and gas. This can be done by considering both fields as continuous, as in the Eulerian-Eulerian approach, or considering the liquid phase as discrete and dispersed in the continuous gas phase, termed as the Eulerian-Lagrangian approach. An example of the latter is the Discrete Droplet Method (DDM) [6], where the liquid phase is represented by a finite number of parcels consisting of droplets having the same properties, such as velocity and size. The parcels are tracked in the Eulerian field and evolve based on the interaction with the gas phase. The approach has been widely used to model gasoline direct injection under different operating conditions and fuels [7, 8].

In this sub-model, the Eulerian-Lagrangian methodology is employed to track the evolution of liquid fuel within the gas phase. This involves solving conservation equations for mass, momentum, and energy for individual liquid parcels, each assumed to possess uniform temperature and composition. Due to the neglect of droplet atomization and breakup, an assumption is necessary: a finite number of droplet diameters is defined, derived from the calculated SMD value under the specified operating condition, effectively representing the entire droplet population within the spray (as will be explained later in more detail). Consequently, the conservation equations are solved for each defined droplet diameter. The treatment of liquid droplets and the gas phase is segregated, with thermal equilibrium assumed at their interface. Gas phase properties are defined using a Cantera gas object to specify thermodynamic and transport properties. Evaporation in the liquid phase is modeled through a mass-based diffusion approach. Additionally, the fuel injection is assumed to occur within a quiescent environment.

7.2.1 System of equations

A system of ordinary differential equations (ODEs) are developed for the liquid droplet to compute its position, mass, velocity, and temperature. The system of equations are solved by the built-in MATLAB ODE solver called ode15s.

Mass conservation

The rate of change of a droplets mass is equal to the evaporation rate mass flow rate $\dot{m}_{evap}$:

$$\frac{dm_d}{dt} = -\dot{m}_{evap} \tag{7.1}$$

where the negative sign indicates a loss of mass due to evaporation. The evaporating mass flow rate is defined based on the Spalding mass transfer number B, according to the following:

$$\dot{m}_{evap} = \pi d_d D \rho_v Sh B \tag{7.2}$$

where d_d is the droplet diameter, D is the diffusion coefficient, ρ_v is the vapor fuel density, and Sh is the Sherwood number. The Spalding number B is defined as:

$$B = \frac{Y_{f,s} - Y_{f,\infty}}{1 - Y_{f,s}} \tag{7.3}$$

where $Y_{f,s}$ is the vapor fuel mass fraction at the droplet surface at saturation conditions and $Y_{f,\infty}$ is the vapor fuel mass fraction in the far field. The fuel vapor mass fraction at the droplet surface is obtained by assuming ideal gas behavior and can be computed according to Equation 7.4 and Equation 7.5. This evaporation model is valid for evaporating conditions without flash boiling. Under flash boiling conditions, the fuel mass fraction at the surface of the droplet would approach unity leading to non-physical evaporation rates. The consideration of flash boiling requires the consideration of other evaporation models, such as the Adachi-Rutland flash boiling model [9, 10], into the framework which is out of the current scope.

$$X_{f,s} = \frac{p_v(T_s)}{p_g} \tag{7.4}$$

$$Y_{f,s} = \frac{M_f}{M_f + M_a(\frac{1}{X_{f,s}} - 1)} \tag{7.5}$$

A saturation state is assumed to exist at the droplet surface and the local partial vapor pressure is equal to the droplets saturation vapor pressure. Hence, p_v is the vapor pressure of the liquid at its surface temperature T_s, which is equal to the droplet temperature since it is considered to be uniform.

The Extended Antoine equation, taken from Poling et al. [11], is used for the vapor pressure. p_g is the ambient pressure of the gas and thus is equal to the in-cylinder pressure. The conversion from molar fraction to mass fraction is then carried out by considering the molecular weight of the fuel M_f and air M_a.

Energy conservation

Solving the energy equation is necessary for computing the droplet temperature. The change in droplet temperature depends on the heat flow rate between the ambient gas and the droplet surface $\dot{Q}_d$ and the latent heat of vaporization H_v, as shown below:

$$m_d c_{p,l} \frac{dT_d}{dt} = \dot{Q}_d - \triangle H_v \dot{m}_{evap} \tag{7.6}$$

The heat flow rate $\dot{Q}_d$ is calculated by:

$$\dot{Q}_d = \alpha A_s (T_\infty - T_s) \tag{7.7}$$

where α is the convective heat transfer coefficient, A_s is the droplet surface area, T_∞ is the gas temperature and T_s is the droplet surface temperature. α is computed from the Nusselt number (Nu) [12]:

$$Nu = \frac{\alpha d_d}{\lambda_g} = 2 + (0.4\sqrt{Re} + 0.06\sqrt[3]{Re^2})\sqrt[3]{Pr} \tag{7.8}$$

where λ_g is the gas thermal conductivity computed by Cantera.

The latent heat of vaporization H_v is calculated according to the Watson relation which accounts for the influence of temperature and can be found in the book of Poling et al. [11].

Momentum conservation

The droplet motion within the ambient gas is slowed down to a drag force that is exerted on it. The drag force can be computed according to:

$$F_D = c_D \frac{\rho_g u_d^2 A_s}{2} \tag{7.9}$$

where c_D is the drag coefficient calculated according to [13]:

$$c_D = \begin{cases} \frac{24}{Re}(1 + 0.15Re^{0.687}) & \text{for } Re \leq 1000, \\ 0.44 & \text{for } Re > 1000. \end{cases} \tag{7.10}$$

The conservation equation for momentum can then be written as shown in Equation 7.11, where the negative sign indicates a deceleration due to the drag force.

$$\frac{du_d}{dt} = \frac{-F_D}{m_d} \tag{7.11}$$

The droplet penetration can then be computed from the knowledge of its velocity according to:

$$\frac{dS_d}{dt} = u_d \tag{7.12}$$

All gas properties are computed by the $\frac{1}{2}$-rule taken at the following reference conditions [14]:

$$T_{ref} = T_s + \frac{1}{2}(T_\infty - T_s) \tag{7.13}$$

$$Y_{f,ref} = Y_{f,s} + \frac{1}{2}(Y_\infty - Y_{f,s}) \tag{7.14}$$

Solving the ODEs

The system of ODEs are then developed for each droplet diameter and injected with an initial velocity calculated according to the theoretical Bernoulli velocity and the velocity coefficient:

$$u_{d,0} = C_v \cdot u_{berno} \quad \text{with} \quad u_{berno} = \sqrt{\frac{2\triangle p}{\rho_l}} \tag{7.15}$$

The injection event is divided into different intervals to account for the changing boundary conditions the droplets would be exposed to. At each interval, all the diameter classes are injected into the cylinder and are subjected to ambient conditions that are averaged over a time interval equal to the injection duration (i.e. $t_i + \triangle t_{inj}$). The differential equations are solved for each diameter until ignition timing or complete evaporation, whichever happens

first. The output of the spray model would then be vectors m_d, S_d, u_d, and T_d for each droplet diameter and injection step.

Solving the system of equations is only representative of the respective droplet diameter evolution. However, it does not have any information about the total injected mass. To scale the diameter classes to the complete spray mass, the information of the droplet size distribution is used where each droplet diameter is weighted according to its probability. As mentioned earlier, the injection period is divided into several injection steps ($N_{st} = \frac{t_{inj}}{\triangle t_{st}}$) with an injected mass $\triangle m_{st}$. This mass is then divided by the number of orifices to obtain the injected mass per orifice and per injection step. To obtain the injected mass for each diameter class, the number of droplets for each diameter class is first obtained. The total number of droplets injected at each time step are first obtained:

$$N_{d,st} = \frac{\triangle m_{st}}{\bar{m}_d} \tag{7.16}$$

where $\bar{m}_d$ is the average droplet mass computed from the volume-averaged diameter of the droplet size distribution:

$$\bar{m}_d = \frac{\pi}{6}\rho_l d_{30}^3 \quad \text{with} \quad d_{30} = \left(\frac{\sum_{i=1}^{n_{class}} G(i) \cdot d_i^3}{\sum_{i=1}^{n_{class}} G(i)} \right)^{1/3} \tag{7.17}$$

The probability of each diameter can then be applied in order to obtain the number of droplets injected per diameter class, injection step, and orifice ($N_{d,i}$) according to:

$$N_{d,i} = G(i) \cdot \frac{N_{d,st}}{N_{orif}} \tag{7.18}$$

The injected mass per injection step, orifice, and diameter class ($m_{d,i}$) can then be computed:

$$m_{d,i} = N_{d,i} \cdot \frac{\pi}{6}\rho_l d_i^3 \tag{7.19}$$

The knowledge of the total injected mass per diameter class is essential to the spray-wall impingement model since droplet diameters influence the behavior of wall interaction.

The droplet position in the 3D space can be computed with the knowledge of the location and orientation of each injector orifice within the engine:

$$\vec{x}_d = \vec{x}_{orif} + S_d(t) \cdot \vec{d}_{orif} \tag{7.20}$$

where $\vec{x}_{orif}$ is the location of an orifice and $\vec{d}_{orif}$ is the direction vector. The axial spray distance can then be extracted and compared with the instantaneous piston position to identify whether impact has occurred or not. The distance to the liner can also be computed with the knowledge of the cylinder bore and the radial distance of the droplet r_d.

$$r_d(t) = \sqrt{x_d^2 + y_d^2} \tag{7.21}$$

The impacted mass per time step and diameter is then transferred to the spray-impingement model along with the information of droplet velocity and temperature at the moment of impingement, as will be described in the following section.

7.2.2 Droplet size distribution

Since no atomization or breakup modeling is included in the simplified spray model, the droplet size distribution is predefined as a function of the SMD, as previously mentioned. The SMD represents the diameter of a sphere having the same volume-to-area ratio of the population of droplets. In this study, it is calculated according to the correlation of Merker et al. [15]:

$$SMD = 6156 \cdot 10^{-6} \nu_l^{0.385} \rho_l^{0.737} \rho_g^{0.06} \triangle p_{inj}^{-0.54} \tag{7.22}$$

where ν_l is the liquid kinematic viscosity, ρ_l is the liquid density, ρ_g is the ambient gas density, and $\triangle p_{inj}$ is the difference between the injection pressure and in-cylinder gas pressure.

The droplet size distribution is then computed according to the method developed in the KIVA program [16] (taken from [12]) by first defining a minimum and maximum droplet diameter and dividing the range into a number of diameter classes n_{class}.

$$d_i = \begin{cases} d_{min} & \text{for } i = 1, \\ d_{i-1} + \frac{d_{max} - d_{min}}{n_{class} - 1} & \text{for } i > 1. \end{cases} \tag{7.23}$$

The number of droplets allocated to each diameter class is determined using a distribution function $G(i)$. This allocation is necessary to achieve the initially computed SMD.

$$G(i) = \frac{d_i^3}{6\bar{d}^4} \cdot exp(-\frac{d_i}{\bar{d}}) \quad \text{with} \quad \bar{d} = \frac{1}{6}SMD \tag{7.24}$$

The minimum and maximum diameters chosen here are 1 μm and 50 μm, respectively, similarly to Frommater [12]. Even though the probability of larger droplets existing in the spray is low, impact on wall wetting would be significant since they encompass a larger mass compared to their smaller counterparts.

7.2.3 Spray model validation

Experimental visualizations of a GDI spray in a constant volume chamber were used to validate the spray model. The measurement campaign was carried out by a previous PhD student at CMT – Clean Mobility & Thermofluids [17]. A 6 orifice Continental GDI injector was used, whose characteristics are summarized in Table 7.1. Iso-octane fuel was injected into a vessel made up of four 180 mm quartz windows allowing for the implementation of optical diagnostics.

Table 7.1: Injector characteristics.

Injector	**Continental**
Number of orifices	6
Orifice geometry	circular
Nozzle geometry	conical
Orifice diameter	170 μm
Orifice length	444 μm
Orifice drill angle	0°
L/D ratio	2.6
Spray umbrella angle	70°

The test matrix chosen to validate the spray model involved a variation of rail pressure, back pressure, and ambient temperature. For more details on how these parameters are controlled in the vessel, the reader is referred to Bautista's doctoral thesis [18]. The test matrix is further depicted in Table 7.2.

Since the measurements were carried out under fixed ambient conditions, the boundary conditions for the simulations were kept constant. This simplifies the calculation since only one injection step is required. Figure 7.4 plots the penetration trends of the four operating conditions tested. The experimental curves are depicted in blue along with the standard deviation, whereas

Table 7.2: Test characteristics.

Parameter	Value	Units
Rail Pressure (P_r)	150/250	bar
Back pressure (P_b)	0.5/1	bar
Ambient temperature	50/100	°C
Fuel temperature	25	°C
Energizing time	0.8	ms
Repetitions per test	10	-

the mass averaged numerical spray penetration in orange. A mean value of the spray penetration is obtained by weighting the penetration values of the diameter classes with their respective masses. This is a common method, especially in 3D CFD codes, where the maximum spray length is defined by setting a threshold based on mass. Both penetration values are taken along the spray plume axis.

A shorter spray length is evident in all operating points, although the simplified spray model shows a good response to changes in chamber conditions. For instance, the increase in spray velocity due to a higher injection pressure is captured by the model. No significant change is evident when increasing chamber temperature and an increase in penetration is observed when chamber backpressure is reduced, in both the experimental and numerical trends. The lower spray penetration is likely attributed to two main simplifications in the spray model, which were also noted in Frommater's thesis [12]. First, the fuel mass fraction in the ambient gas (Y_∞) is set to zero leading to a larger gradient of fuel mass fraction between the droplet surface and the surrounding environment. This might not be true in reality since the spray could re-entrain air and fuel vapor. However, due to the poor evaporative conditions in most of the tests, this is not likely to be the main reason behind the shorter penetration. Second, the drag force the droplets are subjected to does not account for the presence of other droplets with different diameters. In a real spray, the smaller droplets would be shielded by the larger ones that penetrate faster. Larger droplets then absorb most of the drag force thus enabling the smaller droplets to penetrate faster.

To account for the shielding effect larger droplets create on smaller ones, Frommater used non-linear regression analysis based on three supporting points. The result of the analysis is a correction factor for the drag coefficient, reducing it in a progressive way for smaller droplets. The function has the following form:

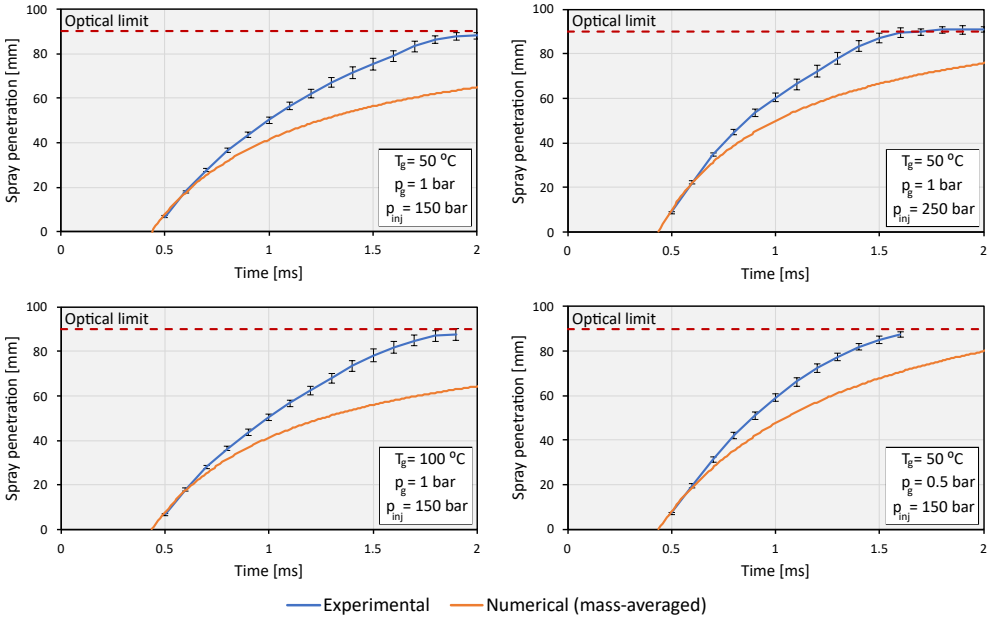

Figure 7.4: Numerical vs experimental spray penetration for four different chamber conditions.

$$f_D(d_i) = f_{D,min} + a_1 \cdot \exp(a_2 \cdot d_i) \tag{7.25}$$

The same function has been utilized in this work with changes to the parameters $f_{D,min}$ and a_1 to better fit the available experimental data. The values adopted in this work were 0.3 for $f_{D,min}$, 6.8841e-04 for a_1, and 0.13851 for a_2. The new drag coefficient is then calculated for each droplet diameter based on the factor f_D. The new values were obtained by a simple sensitivity analysis on one of the operating conditions (T_g=50 °C, p_g=1 bar, p_{inj}=150 bar). The results of the modified drag coefficient are shown in Figure 7.5. Reducing the drag coefficient increases the penetration of the droplets as expected and results in a better agreement with the experimental measurements. However, this adjustment leads to a slight overestimation of penetration velocity during the initial stages of injection. Nonetheless, this is not critical as impingement is anticipated to occur at later timings. The spray model reliability is thus improved and can now be coupled with the spray-wall impingement model, which will be explained in the following section.

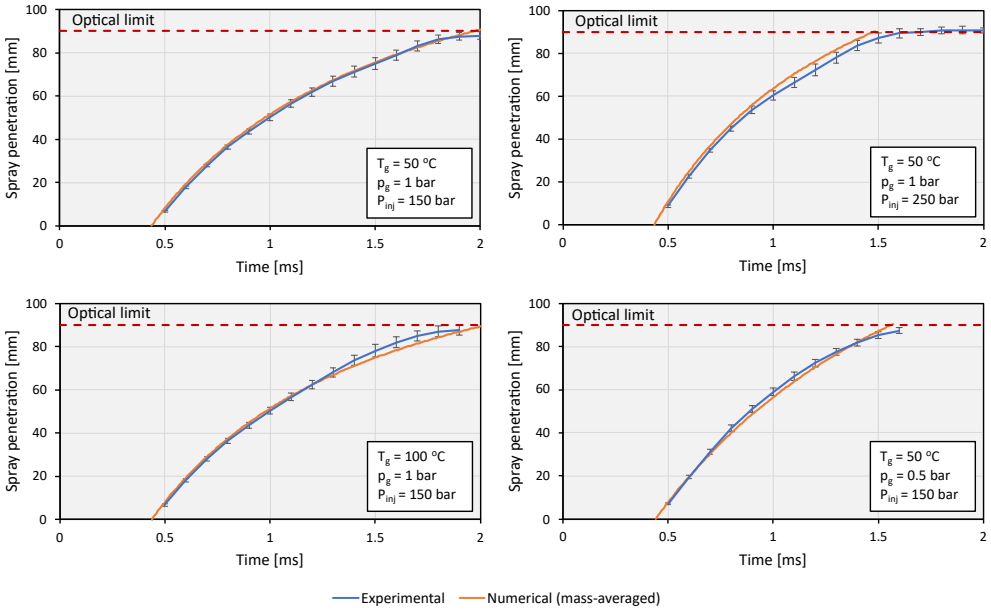

Figure 7.5: Numerical vs experimental spray penetration for four different chamber conditions after modifying drag coefficient.

7.3 Spray-wall impingement

There is a large database in literature investigating fundamental spray-wall impingement phenomena, usually in controlled environments [19–22]. These conditions are close to practical applications of GDI sprays within ICEs. Fundamental studies provide detailed assessments of impingement characteristics which could be transferred to actual engines. For instance, it is recognized that higher injection pressures increase the impact area and velocity of droplets, while also enhancing the flux of small-sized droplets that can be vaporized more easily [23]. The impact features are significantly influenced by both the momentum of the spray upon collision and the angle of inclination at impact [24], which in turn affects secondary droplet characteristics [25]. Additionally, longer injection durations have shown to increase film mass deposition, which motivated researchers to adopt split injection strategies [26].

Modeling film dynamics involves the characterization of different regimes, which include splash, stick, spread, and rebound, depending on various criteria. The criteria are typically based on dimensionless numbers, such as the Weber number of the droplet. For instance, the splash criterion is defined based on a threshold value of the Weber number, or based on more complex

parameters accounting for local film thickness [27]. The Kuhnke model defines the regimes based on a K parameter that is a function both the Weber and Laplace numbers [28], and further distinguishes between dry and wet wall conditions. In the current framework, the model of Bai and Gosman [29] was adopted to model impingement characteristics and compute the total impacted mass. The model has been validated with experimental measurements and is widely used in modeling spray-wall interaction for ICE applications. The formulations of the model are detailed in the following section.

7.3.1 Bai-Gosman formulations

The model has been developed based on single droplet impact studies. It identifies the regimes based on parameters, such as droplet velocity, diameter, temperature, incidence angle, and fluid properties such as viscosity and surface tension. In the context of this work, impact on a dry wall is considered and wall temperature influence on impact characteristics are neglected due to uncertainties in wall temperature values. On the basis of the droplet Weber number, three regimes are identified:

$$\text{Stick:} \quad We_n \leq 2 \tag{7.26}$$

$$\text{Spread:} \quad 2 < We_n \leq We_c \tag{7.27}$$

$$\text{Splash:} \quad We_n > We_c \tag{7.28}$$

where We_n is the normal impact Weber number defined as:

$$We_n = \frac{\rho_l u_n^2 d_d}{\sigma_l} \tag{7.29}$$

and the We_c is the critical Weber number defined as:

$$We_c = 2360 \cdot Oh^{0.36} \tag{7.30}$$

where Oh is the Ohnesorge number. Slow droplets, with very low impact energy, adhere to the wall within the stick regime and are directly added to the wall film mass. Within the spread regime, the droplets impact the wall with moderate velocity and spread. The masses of these droplets are also summed up to the existing wall film mass. In the splash regime, droplets have a higher impact energy and some of the mass is rebounded. The ratio of the rebounded mass with respect to the incoming mass is defined in a stochastic way:

$$\frac{m_{splash}}{m_{income}} = 0.2 + 0.6 \cdot a \tag{7.31}$$

where a is a random number between the interval (0,1). The splashed mass is then subtracted from the initial incoming mass to yield the mass that becomes part of the liquid film. In the model of Bai-Gosman, the splashed mass is broken up into secondary droplets, however, for simplification purposes, those secondary droplets are assumed to evaporate instantaneously and become part of the gas phase.

7.3.2 0D model comparison with CFD

The calibrated 0D spray model was integrated into the engine simulation to replicate spray evolution within the engine across the operating points coupled with the spray-wall impingement model. This impingement model was seamlessly integrated into the framework without additional calibration. It is important to emphasize that comparing the 0D model to CFD will be qualitative, given the reliance of spray-wall impingement models on empirical correlations. Additionally, the CFD spray model was configured with default parameters due to lack of experimental data, meaning that neither spray penetration nor deposited mass have undergone validation against measurements. Nevertheless, evaluating the 0D model's ability to replicate trends across varying engine conditions remains valuable.

Figure 7.6 compares the total deposited mass on the piston and liner. This mass consists of droplets that are within the stick regime and the portion of mass that remains on the wall in the splash regime. Regarding the piston wall, the 0D model captures the trend exhibited by the CFD model, as shown in Figure 7.6a. Deposited mass increases at higher loads with higher fueling rates and longer injection durations. The advanced injection timing at higher loads results in a reduced distance between the injector tip and piston during injection, thus favoring impingement. The model also captures the decrease in deposited mass when moving from 2000 rpm to 3000 rpm, more pronouncedly at higher load (A100 to B100). This decrease could be attributed to the increased spray momentum when coming into contact with the piston wall, due to higher injection pressures, which leads to a greater fraction of droplets that rebound off of the wall. CFD simulations depict comparable deposited mass values for the liner whereas no impact with the liner is detected by the 0D model for most cases except for B50. A possible reason for this could be due to a difference in spray penetration between the 0D model and CFD, which could also explain the smaller values of piston deposited mass observed

in all cases. These values could thus be improved by calibrating the 0D spray model taking CFD simulations as a reference. However, this would further add a level of uncertainty since the spray behavior in the CFD model has not been validated with experimental measurements.

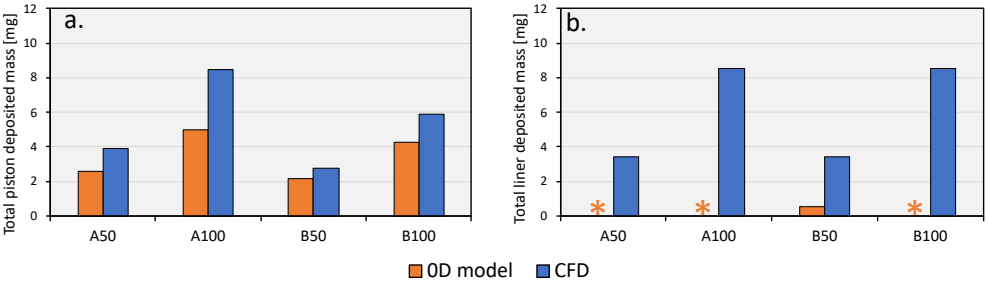

Figure 7.6: Total deposited mass on piston (a) and liner (b). Asterisks denote the absence of impingement.

7.4 Film evaporation

Wall film evaporation is induced by the hot surfaces in the combustion chamber and by the ambient gas. Heat is transferred to the liquid film by conduction from the wall and convection from the gas phase above the film. Additionally, vaporization due to a mass flux by diffusion from the wall film to the bulk gas occurs according to the fuel concentration gradient between the film surface and the gas. The net effect of these processes is a continuously changing film thickness, surface area, and mass, throughout the cycle. In this study, film evaporation is considered to take place at average film properties, such as thickness, temperature, and impact velocity.

The mass transfer rate from the wall film to the bulk gas is calculated using [30]:

$$\dot{m}_{film,g} = A_{film} \frac{Sh_L \rho_g D (Y_{f,film} - Y_{f,\infty})}{L_{ch}(1 - Y_{f,film})} \tag{7.32}$$

where A_{film} is the area covered by the film, Sh_L is the Sherwood number, ρ_g is the density of the ambient gas, D is the fuel/air binary diffusion coefficient, $Y_{f,\infty}$ is the fuel mass fraction in the gas above the film, $Y_{f,film}$ is the fuel mass fraction at the film surface obtained from the Clausius-Clapeyron relation, and L_{ch} is a characteristic length computed as $100 \cdot \bar{h}_{film}$ according to French et al. [31]. The area of the wall film is calculated from the knowledge of the current film mass and the average film thickness according to:

$$A_{film} = \frac{m_{film}}{\rho_l(\bar{T}_d)\bar{h}_{film}} \tag{7.33}$$

where m_{film} is the current film mass, ρ_l is the liquid density computed at the average impact droplet temperature $\bar{T}_d$, and $\bar{h}_{film}$ is the average film thickness computed by the relation of Nagaoka et al. [32]:

$$\bar{h}_{film} = 2\frac{\sigma_{lv}(\bar{T}_d)}{\rho_l(\bar{T}_d)\bar{u}_n^2} \tag{7.34}$$

where σ_{lv} is the surface tension between the liquid and vapor phase and $\bar{u}_n$ is the average normal impact velocity. The Sherwood number Sh_L is calculated by [33]:

$$Sh_L = 0.322Re^{1/2}Sc^{1/3} \tag{7.35}$$

The fuel vapor mass fraction at the film surface $Y_{f,film}$ is obtained from the molar fraction of fuel at the film surface computed according to:

$$X_{f,film} = \frac{p_v(T_{film})}{p_g} \tag{7.36}$$

where p_v is the fuel vapor pressure calculated according to the Extended Antoine Equation with iso-octane coefficients [11]. Here, the film temperature at the surface, T_{film}, is constant and equal to the average temperature of the droplets upon impact $\bar{T}_d$.

Equation 7.32 is used under normal liquid evaporation conditions, in the so-called complete wetting regime, where the wall temperature is less than the fuel saturation temperature.

The vaporization rate of the wall film not only depends on the wall temperature but also on the ambient gas thermodynamic conditions, especially on the in-cylinder pressure that defines the film saturation temperature. Habchi [34] developed a comprehensive liquid film boiling model for ICEs, which distinguishes between three regimes based on the superheating temperature $\triangle T_{w,sat} = T_w - T_{sat}$. The limits of the regimes are defined by liquid saturation temperature T_{sat}, the Nukiyama temperature T_N, and the Leidenfrost temperature T_L. The last two temperatures are normally obtained from controlled experiments that measure the droplet lifetime on a hot plate. The droplet lifetime curve is shown in Figure 7.7.

When the wall temperature is between the saturation temperature and Nukiyama temperatures ($T_{sat} < T_w < T_N$), the liquid becomes overheated

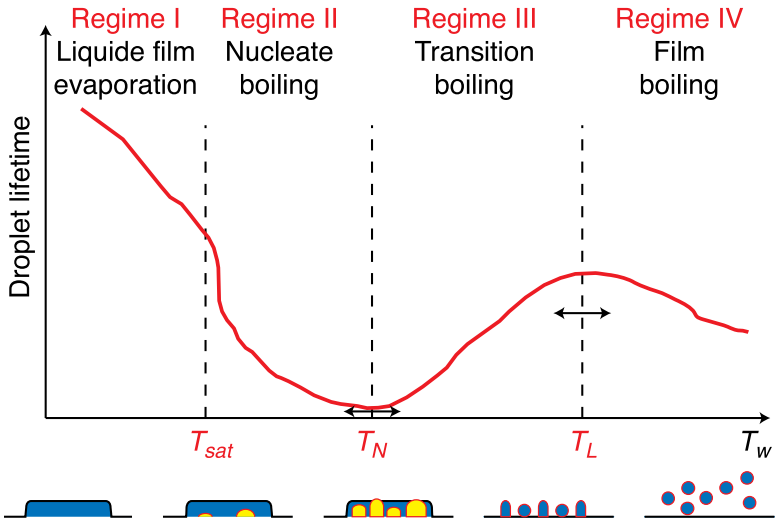

Figure 7.7: Droplet lifetime depicting the four regimes [34].

and forms vapor bubbles in the cavities of the wall. These bubbles accelerate the vaporization of the liquid film as seen by the reduction in the droplet lifetime.

In Regime III ($T_N < T_w < T_L$), the bubbles in the cavities may coalesce and form larger vapor pockets in the liquid film. As a result, a vapor cushion is formed that separates the film from the wall leading to a reduction in heat transfer to the film from the wall. Consequently, droplet lifetime increases.

In Regime IV, or the Leidenfrost regime ($T_w > T_L$), heat conduction passes through a fully developed vapor cushion and then to the liquid, resulting in a relatively lower evaporation rate compared to the preceding regimes.

The physical aspects of the boiling regimes (II-IV) are governed by several parameters. One of which is the dry fraction of the wall α_{dry}, which is the ratio of the cavities to the wetted area in the absence of boiling. This ratio varies between 0 and 1, increasing when wall temperatures rises, reaching about 0.7 to 0.9 when the wall temperature reaches the Nukiyama temperature [34]. Another essential parameter is the length density of the contact lines C_{lld}, which affects the wetted area fraction β_1 (will be shown shortly), between the vapor cavities and the wall. Most of the evaporation takes place on these lines according to the observations of Dhir [35](as cited in [34]). This parameter increases in the Nucleate boiling regime as the bubble diameters increase leading to a larger contact line with wall. It then decreases in the

transition regime towards a minimum value at the Leidenfrost temperature due to the formation of a vapor cushion and detachment of the vapor cavities from the surface. For a detailed description of the parameters and the corresponding formulations, the reader is referred to the paper of Habchi [34].

The estimation of the Nukiyama and Leidenfrost temperatures is done as a function of the gas pressure formulated based on the following expressions:

$$T_{cr} = T_{sat} + \triangle T \tag{7.37}$$

$$\triangle T = \begin{cases} T_{cr|1\text{ bar}} - T_b & \text{if } p_g \leq 1 \text{ bar} \\ \frac{(T_{cr|1\text{ bar}} - T_b) - A}{T_c - T_b}(T_c - T_{sat} + A) & \text{if } p_g > 1 \text{ bar} \end{cases} \tag{7.38}$$

where T_{cr} represents either T_N or T_L, T_b and T_c are the normal boiling temperature and critical temperature, respectively. $A = max(1, T_{cr|1\text{ bar}})$ where $T_{cr|1\text{ bar}}$ represents the Nukiyama and Leidenfrost temperatures at 1 bar, and are computed experimentally by lifetime curves of fuel droplets. The values of T_N and T_L for iso-octane at atmospheric pressure are 395 K and 463 K, respectively. With the knowledge of these temperatures, parameters such as α_{dry} can then be computed.

The rate of vaporization can then be calculated based on the aforementioned parameters, and parameters that are correlated with them, according to the following formulation:

$$\dot{m}_{film,w} = A_{film} \frac{\beta_1(1 - \alpha_{dry})Q_{wl} + \beta_2 \alpha_{dry} Q_{wvl}}{\triangle H_{v,sat}} \tag{7.39}$$

where β_1 is the fraction of the wetted area where most liquid vaporization occurs, β_2 is the fraction of dry area where the liquid film is separated from the wall by a vapor cushion, $H_{v,sat}$ is the fuel latent heat of vaporization at T_{sat}, Q_{wl} is the heat flux per unit area between the wall and liquid in direct contact calculated according to:

$$Q_{wl} = \lambda_{l,sat} \frac{T_w - T_{sat}}{h_{film}} \tag{7.40}$$

where $\lambda_{l,sat}$ is the fuel thermal conductivity at the saturation temperature T_{sat}. Q_{wvl} is the heat flux per unit area from the wall to the liquid through the vapor cushion, which becomes more dominant over Q_{wl} as the wall temperature increases towards the T_L, and is calculated by:

$$Q_{wvl} = \lambda_v \frac{Tw - T_{film}}{\delta_v} \tag{7.41}$$

where λ_v is the thermal conductivity of the vapor and δ_v is the thickness of the vapor cushion. To get acquainted with the main derivations and to obtain a more complete overview of the film boiling model, the reader is directed to the work of Habchi [34].

By integrating the film evaporation model into the spray model and the spray-wall interaction model, the third route to soot formation is finalized. The sub-model computational span extends from the SOI until either complete film evaporation or SOC, whichever occurs first. Any residual film mass at SOC, if present, is subsequently transferred to the main particle model. The residual fuel film mass undergoes analogous treatment to the injector tip wetting model, utilizing the same temperature correction factor and initial fuel molar fraction in the pyrolysis zone.

7.4.1 Film evaporation comparison with CFD

To evaluate the model's capability in estimating the residual film mass at the start of combustion, the evaporation rates calculated by the 0D model are compared with those from the CFD simulation. Given the significance of wall temperatures in film evaporation, it is crucial to acknowledge that the prescribed wall temperatures in both the CFD and 0D simulations are derived from the combustion diagnostic tool and are not directly measured in the engine. These temperature values are averaged over cycles and depend on empirical correlations embedded within the lumped model, which inherently introduces uncertainties. Nevertheless, comparing the evaporation rates provides valuable information regarding the 0D model's ability to account for the physical aspects of film evaporation described previously. Final film mass values can then be assessed based on the contribution to overall particle emissions with respect to measured values.

The film thickness is another crucial parameter affecting the rate of film mass evaporation as it determines the surface area of the wall film. This thickness is calculated considering factors like droplet velocity, surface tension, and density (refer to Equation 7.34), but it doesn't consider the spray cone angle upon impact. As the spray evolves during injection, the spray plume widens as it interacts with the surrounding gas. Consequently, sprays impacting on the walls, such as those with very advanced timings, are likely to form a fuel film with a smaller area compared to later impacts. Given that the film area is inversely proportional to the film thickness, this suggests that early impacts would result in a larger film thickness compared to delayed ones.

To address this phenomenon, Frommater [36] adjusted the film thickness based on a correlation that relates impact time to a calibrated time limit value.

A similar procedure is employed here, wherein an exponential function is used for computing a film thickness multiplication factor based on impact time, as seen in:

$$f_{th} = max(18.571 \cdot exp(-5605 \cdot \triangle t_{impact}), 2.5e-3) \tag{7.42}$$

where $\triangle t_{impact}$ is the time between SOI and impact on the wall. A threshold value is set to avoid excessive and unphysical reduction of film thickness for very late impact times. The coefficients of the exponential function were calibrated based on a comparison between the evaporation rates calculated by the 0D model and CFD simulations.

The piston wall film evaporation rates for the four operating conditions are shown in Figure 7.8. The evaporated mass is normalized by the maximum deposited mass on the piston for each case. All cases show relatively good agreement with the CFD simulations. Moreover, complete film evaporation occurred for the cases at 2000 rpm whereas a residual film mass was detected for both cases at 3000 rpm. The remaining film mass for the B50 case was on the liner wall although a higher deposited film mass was detected on the piston. The liner wall temperature is almost 50 K lower than the piston wall temperature which makes wall-side evaporation, the more dominant evaporation source, less effective. The B100 case had the residual film on the piston surface since no contact with the liner occurred. Here, the time available for evaporating the film is short and the evaporation rate enters the liquid film evaporation regime, the regime with the longest droplet lifetime (Regime I), much sooner than other cases. Although evaporation rates of the 0D model and CFD are similar, the final absolute film mass value reached a stable value during the compression phase in the CFD model, and even slightly increased, possibly due to condensation from the bulk gas to the wall film. Due to the uncertainties previously pointed out, the quality of the CFD simulations in simulating wall impingement processes is limited. To further assess the quality of the CFD model and 0D model, the remaining fuel film mass is provided to the particle model to evaluate the particle size distribution.

7.5 PN/PM based on wall film mass computed by CFD and 0D model

Figure 7.9 provides a summary of the trends observed in particle number and mass concentrations resulting from all the soot pathways investigated in this study. In this context, "Numerical (gas)" pertains to rich zones obtained

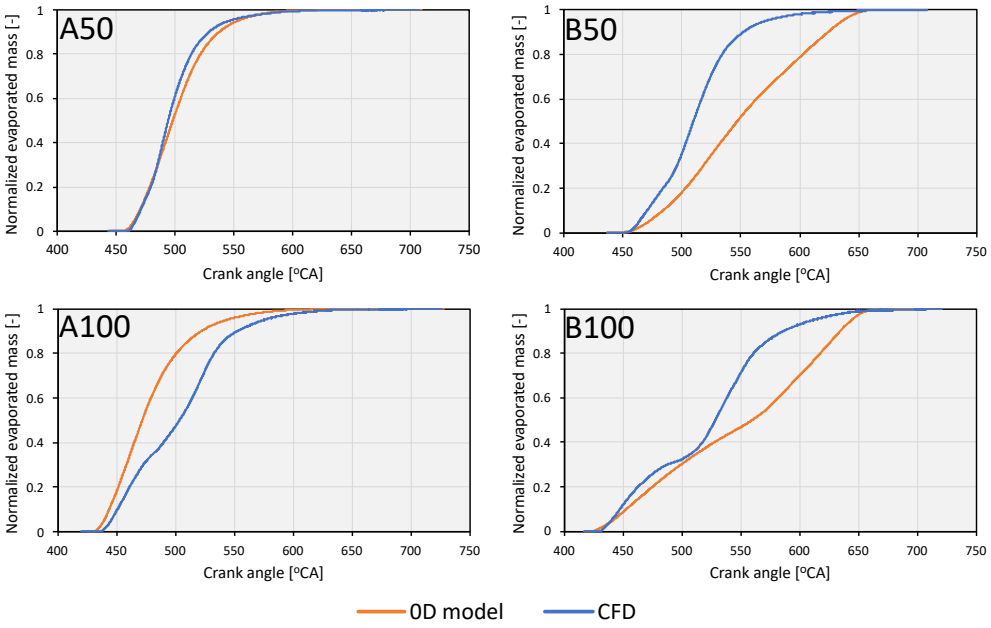

Figure 7.8: Normalized evaporated film mass from the piston computed by the 0D model (orange) and CFD (blue) simulations. Values normalized by the maximum deposited mass for each case.

from the equivalence ratio distribution, while "Numerical (injector)" refers to injector tip wetting. The graphs on the right-hand side illustrate the particle emissions emitted if the final wall film mass values (at SOC) calculated by the CFD simulation were employed. Hence, the total emissions computed by the numerical model encompass, on one hand, the aggregate emissions when utilizing wall film values from the 0D model (depicted by orange bars), and on the other hand, the total emissions when incorporating wall film values from the CFD model (illustrated by green bars). An overestimation in both particle number and mass can be observed when using wall film mass from CFD. Nevertheless, it was mentioned that the CFD model is not completely reliable as far as wall-impingement and film evaporation is concerned. The accuracy of the CFD model could be improved be employing reactive simulations in order to properly calculate wall temperatures. However, this implies a calibration of the combustion model, which was out of the scope of this study. Wall film values obtained by the 0D model are thus deemed reliable in this case since the total particle emissions are in good agreement with measured values.

In the 0D model, a better agreement with measured values is obtained at higher loads. At medium load conditions, the main source of particle emissions

seems to be attributed to the injector, which results in an underestimation of the measured values. Nevertheless, this offset is likely not due to wall films, since medium load conditions operated with relatively more delayed SOI timings. Optical experiments (see section 6.1 and section 7.1) also showed almost no contribution from wall films at similar injection timings (-270 °CA) further supporting this point.

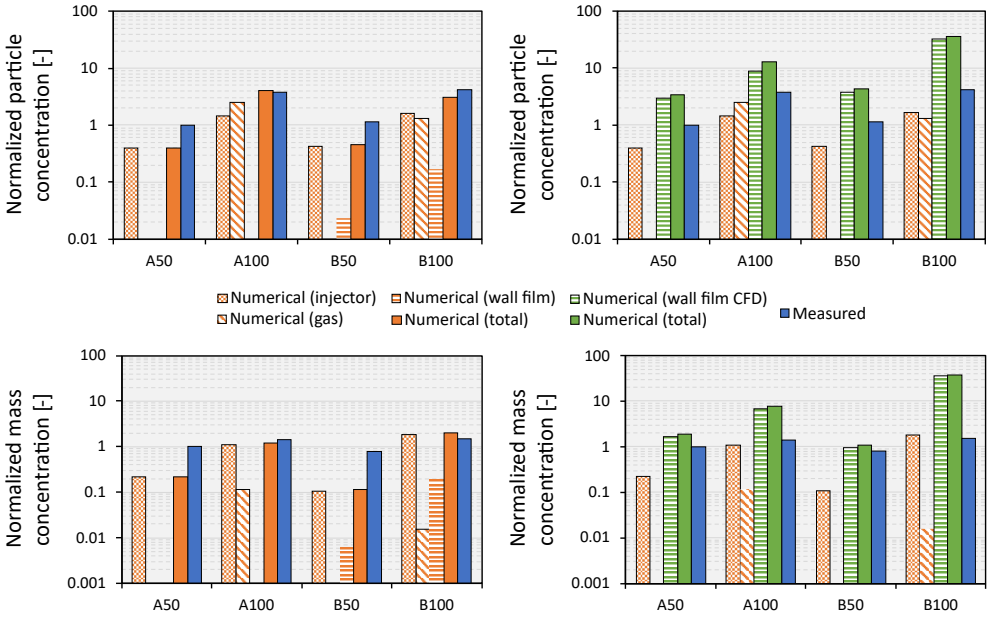

Figure 7.9: Particle concentration and mass concentration comparison between the numerical model and measured values. Values are normalized by the measured particle emissions at A50. Green bars represent particle emissions when using piston wall film mass computed by CFD.

7.6 Summary

To wrap up this chapter, a few remarks should be highlighted. The plausibility of the simplified spray model was demonstrated by comparison with experimental data carried out in a constant volume vessel. A droplet diameter distribution was implemented and considered to represent the complete droplet population of the spray based on the Sauter Mean Diameter, which was computed by an empirical correlation. An estimation of the diameter distribution was essential for the consequent wall-impingement model. With this information, the spray conservation equations were solved to compute spray relevant characteristics, such as penetration, velocity, mass, and temperature.

The Bai-Gosman wall-impingement model was then incorporated into the framework to model droplet impact dynamics. Comparison with CFD simulations revealed that the 0D model is able to describe wall interaction with sufficient accuracy. Total wall film deposited mass on the piston wall was very similar to the computed values by the CFD model. Even though the comparison here was qualitative, since both approaches rely on empirical formulations, the 0D model presents itself as a valid tool for calculating wall film mass deposition.

In order to consider the evaporation of film mass from the walls, a comprehensive boiling model was incorporated. Depending on the degree of wall superheat, one of the four evaporation regimes, three of which involve boiling, dictates the evaporation rate, thereby affecting the final film mass at the start of combustion. The film height emerges as a critical parameter significantly impacting the evaporation rate. To accommodate the expansion of spray width (cone angle), the film height was adjusted by a factor based on the difference between the impact time and the start of injection. Comparing the evaporation rates of 0D and CFD models yielded a satisfactory level of agreement showcasing the ability of the 0D model to account for the physical considerations involved in wall film evaporation.

Despite the consistency observed in evaporation rates, differences in final film mass values result in varied particle emissions. The 0D model predicts complete removal of the wall film for the 2000 rpm cases, thus no particle emissions from wall films are accounted for. On the contrary, a residual fuel film mass at SOC resulted lead to particle emissions from the liner and piston, for the B50 and B100 cases, respectively. Nevertheless, the contribution of wall films was less pronounced compared to the injector tip and gas phase sources. CFD simulation predicts the presence of residual wall film in all cases, leading to an overestimation of particle emissions. Due to uncertainties in wall temperature specification, the evaporation behavior may yield unreliable mass data, necessitating the examination of measured PN/PM values to evaluate the model's accuracy. In this context, the 0D approach demonstrates an advantage, as total particle emissions align more closely with measured values, highlighting that mixture inhomogeneity and injector tip wetting serve as primary sources of soot formation for the tested operating points.

References

[1] Lacey, J. et al. “Generalizing the behavior of flash-boiling, plume interaction and spray collapse for multi-hole, direct injection”. In: *Fuel* 200 (2017), pp. 345–356. DOI: 10.1016/j.fuel.2017.03.057.

[2] Zeng, W., Xu, M., Zhang, G., Zhang, Y., and Cleary, D. J. “Atomization and vaporization for flash-boiling multi-hole sprays with alcohol fuels”. In: *Fuel* 95 (2012), pp. 287–297. DOI: 10.1016/j.fuel.2011.08.048.

[3] He, X. et al. “Impact of coolant temperature on the combustion characteristics and emissions of a stratified-charge direct-injection spark-ignition engine fueled with E30”. In: *Fuel* 309.September 2021 (2022). DOI: 10.1016/j.fuel.2021.121913.

[4] Hiroyasu, H. and Arai, M. “Structures of Fuel Sprays in Diesel Engines”. In: *SAE Technical Paper* (1990). DOI: https://doi.org/10.4271/900475.

[5] Naber, J. D. and Siebers, D. L. “Effects of gas density and vaporization on penetration and dispersion of diesel sprays”. In: *SAE Technical Papers* (1996). DOI: 10.4271/960034.

[6] Dukowicz, J. K. “A particle-fluid numerical model for liquid sprays”. In: *Journal of Computational Physics* 35.2 (1980), pp. 229–253. DOI: 10.1016/0021-9991(80)90087-X.

[7] Paredi, D. et al. “Validation of a comprehensive computational fluid dynamics methodology to predict the direct injection process of gasoline sprays using Spray G experimental data”. In: *International Journal of Engine Research* 21.1 (2020), pp. 199–216. DOI: 10.1177/1468087419868020.

[8] Payri, R., Marti-Aldaravi, P., Abboud, R., and Bautista, A. “Numerical Analysis of GDI Flash Boiling Sprays Using Different Fuels”. In: *Energies* (2021), pp. 1–23.

[9] Adachi, M., McDonell, V. G., Tanaka, D., Senda, J., and Fujimoto, H. “Characterization of fuel vapor concentration inside a flash boiling spray”. In: *SAE Technical Paper Series* (1997). DOI: 10.4271/970871.

[10] Zuo, B., Gomes, A. M., and Rutland, C. J. “Modelling superheated fuel sprays and vaproization”. In: *International Journal of Engine Research* 1.4 (2000), pp. 321–336. DOI: 10.1243/1468087001545218.

[11] Poling, B. E., Prausnitz, J. M., and O'Connell, J. P. *The Properties of Gases and Liquids*. Fifth Edit. New York: McGraw Hill, 2001.

[12] Frommater, S. "Phenomenological modelling of particulate emissions in direct injection spark ignition engines for driving cycle simulations". PhD thesis. TU Darmstadt, 2018.

[13] O'Rourke, P. J. and Amsden, A. A. "The tab method for numerical calculation of spray droplet breakup". In: *SAE Technical Papers 872089* (1987). DOI: 10.4271/872089.

[14] Renksizbulut, M. and Yuen, M. C. "Numerical Study of Droplet Evaporation in a High-Temperature Stream". In: *Journal of Heat Transfer* 105.2 (1983), pp. 389–397. DOI: 10.1115/1.3245591.

[15] Merker, G. P., Schwarz, C., and Teichmann, R. *Combustion Engines Development: Mixture Formation, Combustion, Emissions and Simulation*. Berlin, Heidelberg: Springer-Verlag, 2012. DOI: 10.1007/978-3-642-14094-5.

[16] Amsden, A. A., O'Rourke, P.J, and Butler, T. D. *KIVA-II: A computer program for chemically reactive flows with sprays*. Tech. rep. 1989, LA–11560–MS. DOI: https://doi.org/10.2172/6228444.

[17] Carvallo, C. "Experimental study of the behavior of gasoline direct injection GDI sprays during wall impingement under realistic engine conditions." PhD thesis. Universitat Politècnica de València, 2023.

[18] Bautista Rodríguez, A. "Study of the gasoline direct injection process under novel operating conditions". PhD thesis. Universitat Politècnica de València, 2021.

[19] Park, J., Im, K. S., Kim, H., and Lai, M. C. "Characteristics of wall impingement at elevated temperature conditions on gdi spray". In: *International Journal of Automotive Technology* 5.3 (2004), pp. 155–164.

[20] Mundo, C., Sommerfeld, M., and Tropea, C. "Droplet-wall collisions: Experimental studies of the deformation and breakup process". In: *International Journal of Multiphase Flow* 21.2 (1995), pp. 151–173. DOI: 10.1016/0301-9322(94)00069-V.

[21] Panão, M. and Moreira, A. "Thermo- and fluid dynamics characterization of spray cooling with pulsed sprays". In: *Experimental Thermal and Fluid Science* 30 (2005), pp. 79–96. DOI: 10.1016/j.expthermflusci.2005.03.020.

[22] Weiss, C. "The liquid deposition fraction of sprays impinging vertical walls and flowing films". In: *International Journal of Multiphase Flow* 31.1 (2005), pp. 115–140. DOI: 10.1016/j.ijmultiphaseflow.2004.08.004.

[23] Park, S. W. and Lee, C. S. "Macroscopic and microscopic characteristics of a fuel spray impinged on the wall". In: *Experiments in Fluids* 37.5 (2004), pp. 745–762. DOI: 10.1007/s00348-004-0866-3.

[24] Senda, J. et al. "Measurement and modeling on wall wetted fuel film profile and mixture preparation in intake port of SI engine". In: *SAE Technical Papers* 724 (1999). DOI: 10.4271/1999-01-0798.

[25] Bai, C. and Gosman, A. D. "Development of methodology for spray impingement simulation". In: *SAE Technical Paper Series 950283* (1995). DOI: 10.4271/950283.

[26] Stanton, D. W., Lippert, A.M., Reitz, R. D., and Rutland, C. "Influence of spray-wall interaction and fuel films on cold starting in direct injection diesel engines". In: *SAE Technical Papers 982584* (1998). DOI: 10.4271/982584.

[27] O'Rourke, P. J. and Amsden, A. A. "A spray/wall interaction submodel for the KIVA-3 wall film model". In: *SAE Technical Papers* (2000). DOI: 10.4271/2000-01-0271.

[28] Kuhnke, D. "Spray wall interaction modelling by dimensionless data analysis". PhD thesis. Technische Universität Darmstadt, 2004.

[29] Bai, C., Rusche, H., and Gosman, A. D. "Modeling of gasoline spray impingement". In: *Atomization and Sprays* 12.1-3 (2002), pp. 1–27.

[30] Wang, B. et al. "Modelling soot formation from wall films in a gasoline direct injection engine using a detailed population balance model". In: *Applied Energy* 163 (2016), pp. 154–166. DOI: 10.1016/j.apenergy.2015.11.011.

[31] French, W., Rose, D., Kelly-Zion, P., and Pursell, C. "Analysis of evaporating fuel films using shadowgraph and schlieren imaging techniques". In: *SAE Technical Papers* (2008). DOI: 10.4271/2008-01-2443.

[32] Nagaoka, M., Kawazoe, H., and Nomura, N. "Modeling fuel spray impingement on a hot wall for gasoline engines". In: *SAE Technical Papers 940525* (1994). DOI: 10.4271/940525.

[33] Welty, J., Rorrer, G., and Foster, D. *Fundamentals of momentum, heat, and mass transfer*. Sixth Edit. New Jersey: John Wiley & Sons, 2001.

[34] Habchi, C. "Modeling fuel spray impingement on a hot wall for gasoline engines". In: *Oil and Gas Science and Technology* 65.2 (2010), pp. 331–343. DOI: 10.2516/ogst/2009062.

[35] Dhir, D. "Nucleate and Transition Boiling Heat Transfer Under Pool and External Flow Conditions". In: *International Journal of Heat and Fluid Flow* 12.4 (1991), pp. 290–314. DOI: https://doi.org/10.1016/0142-727X(91)90018-Q.

[36] Frommater, S., Neumann, J., and Hasse, C. "A phenomenological modelling framework for particle emission simulation in a direct-injection gasoline engine". In: *International Journal of Engine Research* 22.4 (2021), pp. 1166–1179. DOI: 10.1177/1468087419895161.

Chapter 8

Model sensitivity to parametric variations

This chapter explores the model applicability with respect to variations in engine parameters, such as injection timing, injection pressure, and injector tip temperature. By doing so, the sensitivity of the model to physical changes associated with parameter variations is evaluated.

8.1 Injection timing sweep

The implications of SOI variation on engine-out particle number and mass concentrations has been previously discussed in Chapter 2. Figure 8.1 plots the change in particle emissions, along with the proportions of varying sources, under five different injection timings. The base value corresponds to particle emissions at A50 (2000 rpm and 9.4 bar BMEP) operating with a SOI of -275 °CA. At the base operating point, particle emissions computed by the model has been shown to be formed solely due to injector tip fuel films.

For advanced injection timings, both particle number and mass emissions are reduced and almost completely eliminated at a SOI of -315 °CA. As SOI is shifted to earlier timings, more time would be available for the evaporation of the liquid fuel from the injector tip. However, at earlier timings, the distance between the injector and the piston is reduced and more impingement is expected. Although more fuel mass is deposited on the piston at earlier timings compared to the base case, only a minor contribution to overall emissions was

evident as the piston film mass was almost completely evaporated at start of combustion. Piston wall temperatures are generally higher than injector tip wall temperatures resulting in improved evaporation rates from the wall-side.

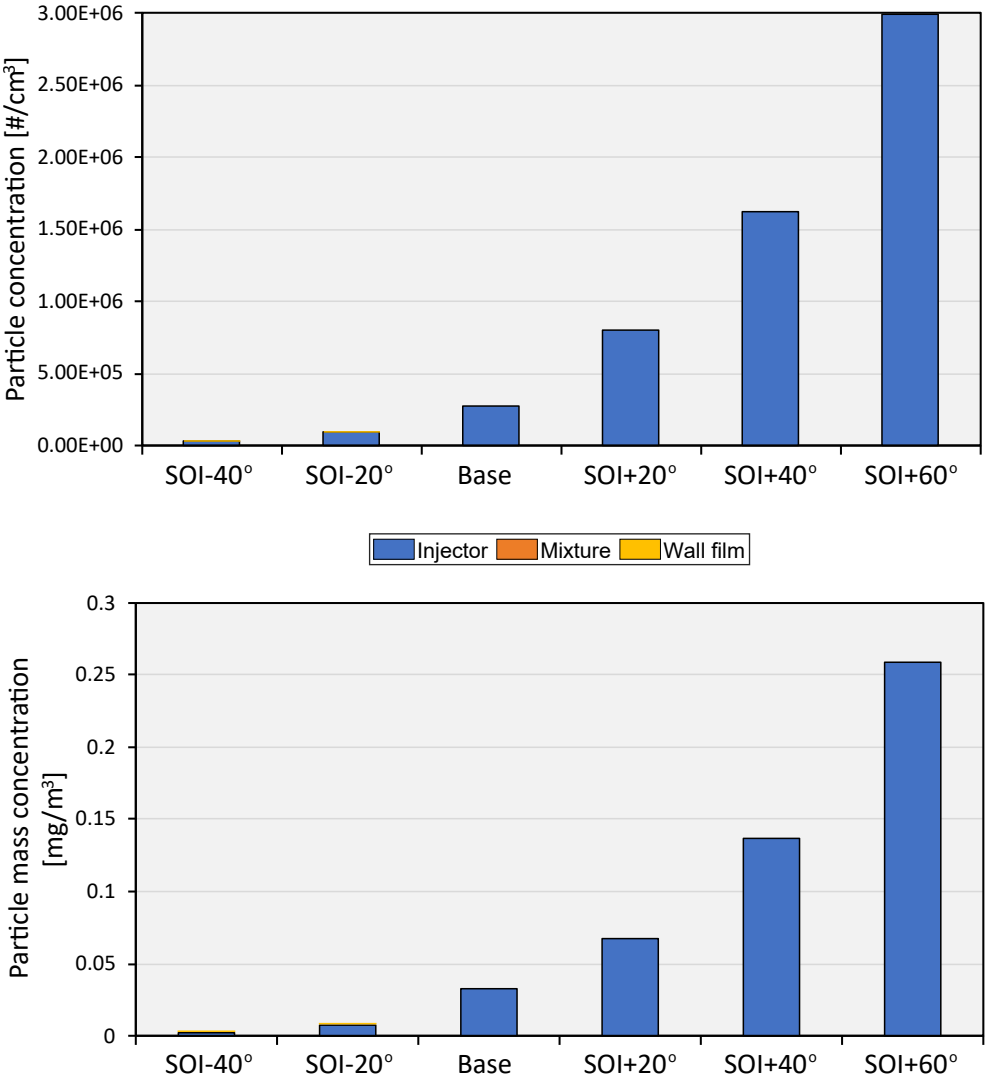

Figure 8.1: Particle number and mass concentrations for a SOI sweep around the base value of -275 °CA. Base condition corresponds to the A50 operating point.

Delayed injection timings showed a consistent increase in injector-induced particle emissions as evaporation time is shortened. Injector fuel films remained the sole contributor even at SOI +60 °CA. Since the mixing time is

shortened, mixture inhomogeneity increased as SOI was delayed, with more zones exceeding the sooting threshold. Nevertheless, the particles formed in gas phase were entirely eliminated due to oxidation processes.

Variations in injection timing are anticipated to have a more significant impact on mixture uniformity at higher loads, which operate with higher fueling rates and longer injection durations. Specifically, at A100, advancing the SOI by 20 °CA resulted in enhanced mixture quality at SOC. This improvement is evidenced by the decrease in mixture-induced particles, as depicted in Figure 8.2a. Furthermore, the reduction in injector-induced particles is also observed due to analogous reasons outlined earlier for the A50 case. Both reductions are illustrated in Figure 8.2b, where a decrease in both the accumulation and nucleation mode peaks are evident. Conversely, retarding injection timing curtails the available mixing duration, consequently leading to more regions surpassing the sooting threshold. At this operating point, the cumulative contribution of mixture-induced particles to the particle number concentration remains predominant over that of injector-induced particles. Similar to A50, advancing the injection timing resulted in a minor residual wall film on the piston, thus exerting a minor influence on total particle emissions. Hence, the model's response to variations in injection timing is logical, indicating that the sub-models are capable of accommodating the effects induced by parameter sweeps.

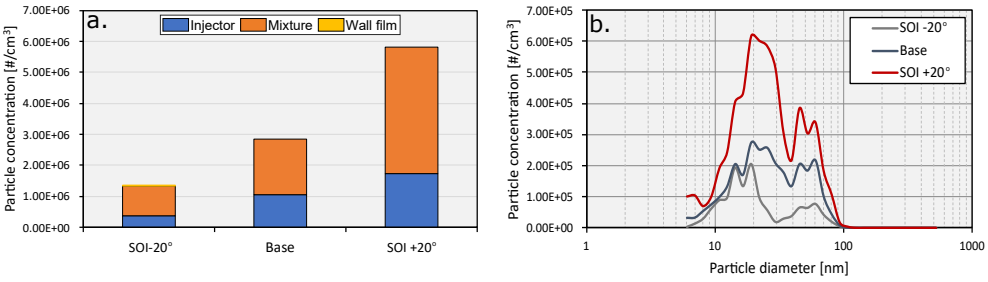

Figure 8.2: Particle number concentration (a) and particle size distribution (b) for a SOI variation of ±20 °CA around the base value of -295 °CA. Base condition corresponds to the A100 operating point.

8.2 Injection pressure sweep

Variations in injection pressure impact all pathways leading to soot formation, contributing to a versatile interaction among them. As indicated by observations from optical engine images, lowering injection pressure may lead

to diminished particle emissions for very advanced injection timings. This outcome stems from diminished wall interactions with the descending piston, which overshadow the negative influence of a decreased mixture quality, derived from a longer injection duration and larger liquid droplets. At the same time, a lower injection pressure could lead to a higher deposited fuel film on the injector tip due to the lower spray momentum when exiting the nozzle.

The A50 operating point operates with the lowest injection pressure among the investigated conditions in this study, set at 80 bar. Despite the relatively low injection pressure, no particles are emitted from the gas phase due to mixture inhomogeneity, nor are particles emitted from wall films. When the injection pressure is raised to 100 bar, the injection mass flow rate increases, resulting in a shorter injection duration. This allows more time for the evaporation of the deposited fuel film on the injector tip. On the one hand, this effect, combined with a higher spray momentum, leads to a significant reduction in particle emissions. On the other hand, a greater amount of residual fuel film remains on the combustion chamber walls, counteracting the benefits of reduced injector tip sooting. Nevertheless, the overall effect is a decrease in total emissions. Further increasing the injection pressure to 120 bar renders the emitted particles from the injector tip negligible. Furthermore, no wall film particles are evident at this pressure due to the higher impact energy of the droplets. This primarily has two effects: at higher impact velocities, a greater proportion of droplets rebound back to the gas phase due to their higher Weber number. Additionally, the higher impact velocities lead to a thinner wall film, resulting in a larger area of evaporation, as accounted for by the assumptions of the wall film evaporation model.

Soot formation originating from gas phase inhomogeneities becomes prominent at lower injection pressures, at 50 bar in this case. Several factors contribute to a diminished mixture quality. Firstly, the injection velocity decreases, leading to reduced air entrainment into the spray, thereby exacerbating the mixing process. Secondly, the shorter mixing time resulting from the prolonged injection duration worsens mixture formation, although this effect may have a lesser impact compared to the former. On the injector side, the decreased fuel momentum is expected to cause greater fuel deposition on the tip, since the fuel exits the nozzle with less momentum and becomes more prone to remain within the layer of deposits. The model addresses this by considering a reduced area for evaporation, consequently leading to higher fuel film mass at ignition.

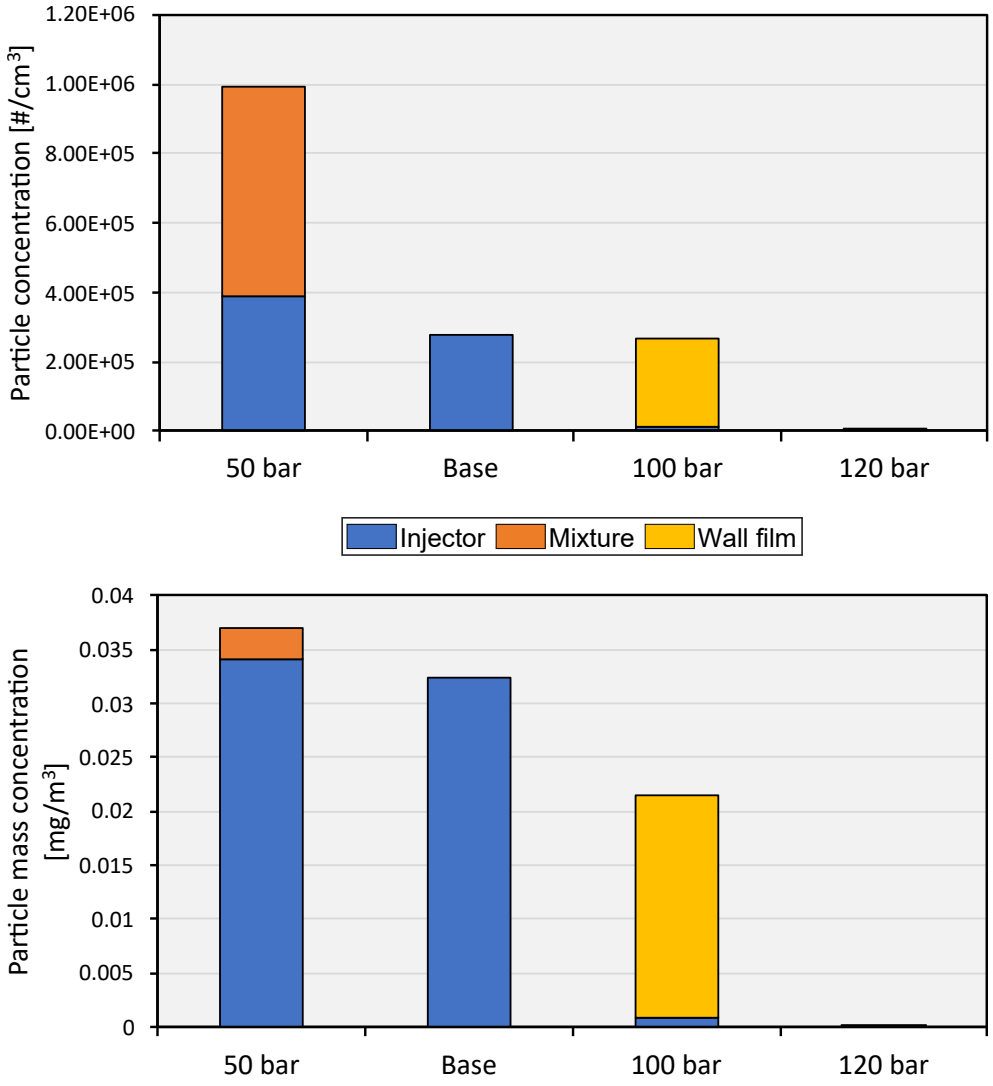

Figure 8.3: Particle number and mass concentrations for an injection pressure sweep around the base value of 80 bar. Base condition corresponds to the A50 operating point.

8.3 Injector tip temperature sweep

As injector-induced particle emissions were observed to be the primary source of soot emissions, particularly concerning soot mass, an examination of injection tip temperature variation was conducted. Due to the physical principles accounted for by the injector tip evaporation model, increasing the temperature is expected to increase the heat transfer by conduction to the fuel film, aiding in the evaporation of the film. This is depicted in Figure 8.4 where an exponential dependency on injector tip temperature can be seen. Increasing the injector tip temperature by 10% results in a significant reduction in injector tip sooting, whereas one order of magnitude increase is evident when the injection tip temperature decreases by 10%.

As depicted in Figure 8.4, alterations in tip temperature solely impact injector-induced particle emissions. However, it is plausible that spray characteristics may also be influenced by tip temperature, potentially leading to a different trend from the observed one here [1]. Furthermore, changes in injection tip temperatures could prompt modifications in the deposit layer on the injector tip. These ramifications are not accommodated for by the sub-models within the modeling framework and necessitate further detailed investigations.

8.4 Summary

A set of parametric variations have been implemented in this chapter highlighting the influence they have on overall particle emissions. The model responded to parameter changes in a plausible way thus proving to be able to account for the main physical aspects involved in sooting pathways. The selected set of engine parameters for the sensitivity analysis were specifically chosen to avoid the need for updated input variables. Modifying other parameters like engine speed, engine load, and ignition timing would impact the combustion process, consequently altering input variables such as in-cylinder pressure and temperature.

Injector tip wetting was the primary factor influencing particle emissions during the medium load case (A50). Various strategies aimed at mitigating emissions originating from this source were highlighted. Raising injection pressure and injector tip temperature demonstrated significant decreases in tip sooting. However, it is imperative to assess their concurrent effect on wall wetting, which could counter the benefit of those strategies.

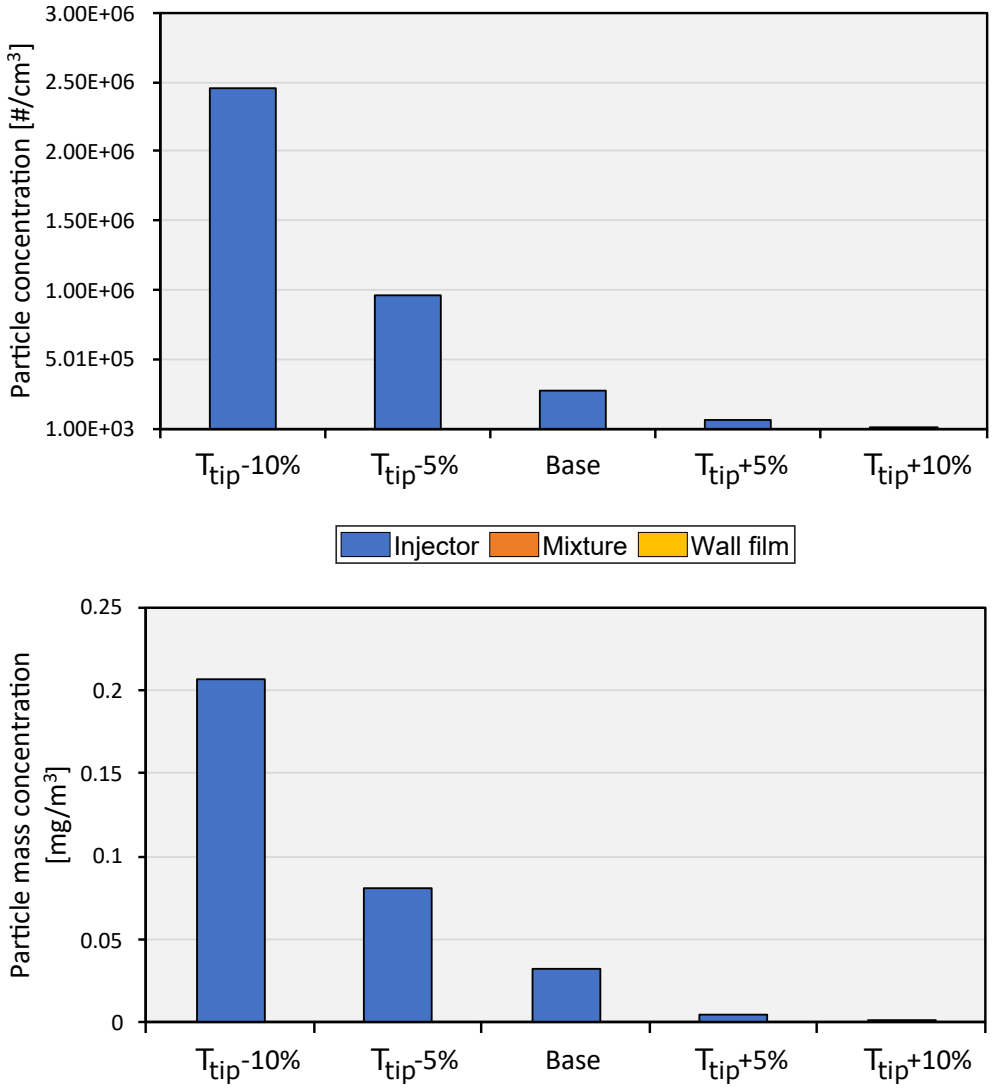

Figure 8.4: Particle number and mass concentrations for a variation of injector tip temperature within ±10% of the base value. Base condition corresponds to the A50 operating point.

Therefore, the comprehensive modeling tool emerges as a valuable asset for exploring strategies aimed at reducing engine-out particle emissions, which is to be a critical aspect in the future of engine development.

References

[1] Moon, S., Choi, J., Abo-Serie, E., and Bae, C. "The effects of injector temperature on spray and combustion characteristics in a single cylinder DISI engine". In: *SAE Technical Papers* (2005). DOI: 10.4271/2005-01-0101.

Chapter 9

Conclusions and future works

This chapter provides a summary of the main scientific contributions of this thesis. It outlines the key takeaways and emphasizes the main constraints and limitations of the model. Additionally, future directions are suggested to broaden the applicability of the modeling tool.

9.1 Summary and conclusions

The main objective of this study was to develop a detailed and computationally efficient modeling tool to estimate particle emissions from modern turbocharged gasoline direct injection engines. This endeavor aimed to establish a virtual platform for particle testing, facilitating the evaluation of engine-out particle emissions under steady-state operating conditions. To achieve this goal, physical sub-models were integrated to address three primary sooting pathways: mixture inhomogeneity, injector tip wetting, and spray-wall impingement. The outputs from the sub-models were integrated with a chemical kinetics solver, which is integrated with the Method of Moments, to evaluate gas-phase species profiles. These profiles were subsequently fed into a stochastic particle dynamics solver to estimate particle number, mass, and size distributions. Engine thermodynamic variables, including pressure and temperature profiles, were acquired from a combustion diagnostic tool that processes the measured in-cylinder pressure. Alternatively, a 1D engine model could also provide the required input variables.

In order to distinguish between sources of particle emissions, an extensive review of the literature highlighted that particles formed through different pathways typically display distinct characteristics, particularly in terms of size. It was found that early injection strategies, which result in significant piston wetting, tend to produce larger soot particles compared to delayed injections. This delay often leads to an elevation in the number of smaller particles, referred to as the nucleation mode.

In all four operating points examined in this study, the measured particle size distribution of the engine displayed a bi-modal shape, featuring one peak in the nucleation mode and another in the accumulation mode. The relative proportions of the two peaks shifted as the engine transitioned from medium to high load, with the nucleation mode becoming more prominent. Consequently, the dynamics of soot formation pathways undergo changes as engine parameters are adjusted to meet specific operating conditions. Thus, the numerical model must consider the physical aspects of soot sources to effectively address soot formation across various conditions.

Mixture quality was evaluated by analyzing the equivalence ratio distribution at ignition. Two methods for computing these distributions were examined. Initially, a 1D spray model (DICOM) was integrated into a MATLAB environment for direct incorporation into the main modeling framework. However, this model exhibited limitations, particularly in its tendency to overpredict mixture formation post-end of injection. To rectify this issue, significant reductions in the spray cone angle were required to slow down the mixing process, ultimately achieving better agreement with CFD simulations at ignition. Despite these adjustments, no clear correlations with injection and mixing parameters were identified, prompting the conclusion that an alternative approach was necessary.

Consequently, an empirical approach was adopted to calculate the equivalence ratio distribution, leveraging an inhomogeneity index dependent on three dimensionless numbers: Weber, Reynolds, and mixing time. Following the calibration of adjustable parameters, this formulation demonstrated improved sensitivity to changes in operating conditions, exhibiting commendable agreement with CFD distributions. Within the multi-zone framework, the equivalence ratio distributions were partitioned into multiple zones surpassing the sooting threshold, where a detailed chemical mechanism facilitated the computation of soot precursors. Under high load conditions, where a fuel enrichment strategy was implemented, an increased number of rich zones were observed. Notably, in conditions where particles were formed, the particles aligned with the first peak of the PSD. A comparison with measured

values revealed a closer agreement with nucleation mode particles, with only a marginal contribution of those particles to soot mass. During the initial phase of particle formation, soot mass was found to be primarily affected by in-cylinder gas temperature, with OH as the predominant oxidation species. Additionally, the numerical particle size distribution demonstrated the impact of the equivalence ratio on particle size, where higher ϕ values led to larger particles due to elevated peaks in nucleation rates, thereby resulting in increased coagulation rates.

Since the measured PSD was only partially represented by mixture-induced particles, injector films were hypothesized to complement these particles primarily in the accumulation mode. For this purpose, an analytical injector film evaporation model was implemented to compute the film mass evolution from end of injection to ignition. Optical engine experiments revealed that increasing engine load resulted in higher injector-induced soot formation due to higher fuel mass remaining on the injector tip aEOI, while higher injection pressures reduced injector-induced soot formation. From these observations, the injector film area for evaporation was scaled based on the injected fuel mass quantity and Weber number. For wall films, soot was considered to be formed by pyrolysis reactions encompassing the burned gas and fuel. In the injector zone, the in-cylinder temperature could not be used in particle formation processes since temperatures near the wall are much lower compared to the bulk gas. A temperature correction factor was used based on the comparison of peak in-cylinder temperature to a temperature threshold and applied to all operating conditions in the same way. Injector zone particles were shown to be mainly dependent on the time available for coagulation, and thus the engine speed. The numerical model was able to reproduce the increase in particle number when moving from 2000 rpm to 3000 rpm, as observed in the measured values. The numerical model captured the bi-modal shape of the particle size distribution by summing mixture-induced and injector-induced particles. However, this was only observed for the higher load cases; at medium load, the model did not calculate any contribution from mixture inhomogeneities.

The evaluation of fuel deposition on the combustion chamber walls involved three sub-models. First, the spray evolution was determined by solving the conservation equations for each diameter class. A pre-defined diameter distribution, based on the sauter mean diameter, was specified. Subsequently, the fuel mass deposited on the walls was calculated using a spray-wall interaction model, which categorizes different impact regimes based on the droplet Weber number. Utilizing the net deposited mass, a film evaporation model incorporating film boiling governed the rate of film evaporation, resulting in the remaining film mass at ignition. Qualitative comparison of film mass

deposition and evaporation with CFD simulations was conducted due to inherent uncertainties in both models. Therefore, measured particle number and mass values served as the means to analyze the absolute film mass values at ignition. When utilizing film values computed by the CFD simulations, an overestimation in total particle number and mass concentrations was evident. Conversely, the 0D model computed complete evaporation of the film mass, hence no contribution to particle formation was observed via this soot pathway.

Overall, the comprehensive 0D model reliably predicts particle size distribution under diverse operating conditions by incorporating physical considerations into its sub-models. This enables the model to accommodate variations in engine parameters such as injection pressure, start of injection timing, and injector tip temperature. However, its phenomenological nature necessitates the calibration of multiple parameters, demanding a comprehensive dataset of measured emissions. Consequently, applying the model directly to a different engine would pose challenges. Additionally, a series of CFD simulations is essential to optimize the parameters of the mixing model, which rely on the mixing characteristics specific to each engine.

9.2 Future research paths

To overcome the limitations identified throughout this study, a set of future research pathways are suggested to broaden the model's applicability to a wider scope. This would facilitate the integration of the model into the automotive research domain, facilitating the exploration of novel strategies for reducing particle emissions and obviating the need for expensive experimental measurements. The proposed future works are listed below:

- Design an experimental campaign with the aim of isolating the sources of soot formation. For instance, measurements could be done with a clean injector with a carefully adjusted injection timing to either target spray-wall impingement (advanced timing) or mixture inhomogeneity (delayed timing). Ideally, metal engine experiments accompanied by a set of optical measurements would provide a global picture of the in-cylinder processes occurring. In this way, the resulting particles that are emitted are quantified and associated to the respective source, enabling a more precise model development.

- Implement a multi-component fuel to represent the aromatic content of gasoline fuel. In this Thesis, the use of iso-octane as the fuel was com-

pensated by adjustments in the initial fuel molar fraction in the pyrolysis zones. Moreover, utilizing a multi-component fuel has important implications on the evaporation rates of the wall films and thus influences final particle emissions values.

- In the context of the injector tip wetting sub-model, a temperature correction factor was used to reduce the temperature of the pyrolysis zone. This most likely necessitates a re-calibration of this threshold for a different engine. Thus, a method should be developed to compute the thermal stratification in the zone instead of relying on a correction factor. Temperature estimations in boundary zones used when modeling NO_x formation in SI engines would be a good start for developing such a method. 3D CFD reactive simulations should be run in parallel in order to provide a set of data for validation.

- Develop sub-models for other soot formation pathways, such as those originating from lubrication oil, which can be particularly significant. These dedicated models should address the reverse blow-by phenomenon, where oil penetrates the combustion chamber and combusts, leading to the formation of soot particles. Additionally, the evaporation of the oil film layer from the cylinder liner could contribute to particulate formation and thus requires further consideration.

- Integrate the modeling framework into a virtual drivetrain. This represents the primary real-world application of this Thesis, enabling the model to estimate particle emissions during a driving cycle such as the World Harmonized Light Duty Test Procedure (WLTP). Achieving this would involve supplying input data to the particle model via an engine model (e.g., a detailed engine model in GT-POWER).

Global Bibliography

ABB Sensyflow. *Thermal air-mass flowmeter for test rigs and quality assurance. Operation and Service manual.* (Cited on page 63).

Adachi, M., McDonell, V. G., Tanaka, D., Senda, J., and Fujimoto, H. "Characterization of fuel vapor concentration inside a flash boiling spray". In: *SAE Technical Paper Series* (1997). DOI: 10.4271/970871 (cited on page 151).

Alessio, A. D., Gambi, G., Minutolo, P., Russo, S., and D'Anna, A. "Optical characterization of rich premixed CH4/O2 flames across the soot formation threshold". In: *Twenty-Fifth Symposium (International) on Combustion* 25.1 (1994), pp. 645–651. DOI: https://doi.org/10.1016/S0082-0784(06)80696-X (cited on pages 23, 74).

Alzahrani, F. M., Fatouraie, M., and Sick, V. "Analytical model for liquid film evaporation on fuel injector tip for the mitigation of injector tip wetting and the resulting particulate emissions in gasoline direct-injection engines". In: *International Journal of Engine Research* 23.1 (2022), pp. 49–63. DOI: 10.1177/1468087420973897 (cited on page 127).

Amann, C. A. and Siegla, D. C. "Diesel particulates—What they are and why". In: *Aerosol Science and Technology* 1.1 (1981), pp. 73–101. DOI: 10.1080/02786828208958580 (cited on pages 11, 17).

Amsden, A. A., O'Rourke, P.J, and Butler, T. D. *KIVA-II: A computer program for chemically reactive flows with sprays.* Tech. rep. 1989, LA–11560–MS. DOI: https://doi.org/10.2172/6228444 (cited on page 155).

Appel, J., Bockhorn, H., and Frenklach, M. "Kinetic modeling of soot formation with detailed chemistry and physics: Laminar premixed flames of C2 hydrocarbons". In: *Combustion and Flame* 121.1-2 (2000), pp. 122–136. DOI: 10.1016/S0010-2180(99)00135-2 (cited on pages 25, 28, 58).

AVL 733S Dynamic Fuel Meter. *AVL LIST GMBH. Graz. User Manual.* (Cited on page 64).

Babajimopoulos, A., Assanis, D. N., Flowers, D. L., Aceves, S. M., and Hessel, R. P. "A fully coupled computational fluid dynamics and multi-zone model with detailed chemical kinetics for the simulation of premixed charge compression ignition engines". In: *International Journal of Engine Research* 6.5 (2005), pp. 497–512. DOI: 10.1243/146808705X30503 (cited on page 74).

Babajimopoulos, A., Lavoie, G. A., and Assanis, D. N. "Modeling HCCI Combustion With High Levels of Residual Gas Fraction – A Comparison of Two VVA Strategies". In: *SAE Technical Paper*. 2003. DOI: https://doi.org/10.4271/2003-01-3220 (cited on page 73).

Bahreini, R. et al. "Characterizing emissions and optical properties of particulate matter from PFI and GDI light-duty gasoline vehicles". In: *Journal of Aerosol Science* 90 (2015), pp. 144–153. DOI: 10.1016/j.jaerosci.2015.08.011 (cited on page 18).

Bai, C. and Gosman, A. D. "Development of methodology for spray impingement simulation". In: *SAE Technical Paper Series 950283* (1995). DOI: 10.4271/950283 (cited on page 159).

Bai, C., Rusche, H., and Gosman, A. D. "Modeling of gasoline spray impingement". In: *Atomization and Sprays* 12.1-3 (2002), pp. 1–27 (cited on page 160).

Balthasar, M. and Kraft, M. "A stochastic approach to calculate the particle size distribution function of soot particles in laminar premixed flames". In: *Combustion and Flame* 133.3 (2003), pp. 289–298. DOI: 10.1016/S0010-2180(03)00003-8 (cited on page 28).

Baratta, M., Ferrari, A., and Zhang, Q. "Multi-zone thermodynamic modeling of combustion and emission formation in CNG engines using detailed chemical kinetics". In: *Fuel* 231 (2018), pp. 396–403. DOI: 10.1016/j.fuel.2018.05.088 (cited on pages 73, 74).

Barone, T., Storey, J., Youngquist, A., and Szybist, J. "An analysis of direct-injection spark-ignition (DISI) soot morphology". In: *Atmospheric Environment* 49 (2012), pp. 268–274. DOI: 10.1016/j.atmosenv.2011.11.047 (cited on page 19).

Bautista Rodríguez, A. "Study of the gasoline direct injection process under novel operating conditions". PhD thesis. Universitat Politècnica de València, 2021 (cited on page 156).

Berndorfer, A., Breuer, S., Piock, W., and Von Bacho, P. "Diffusion combustion phenomena in GDi engines caused by injection process". In: *SAE Technical Papers* 2 (2013). DOI: 10.4271/2013-01-0261 (cited on pages 19, 122).

Berni, F. et al. "Modeling of gaseous emissions and soot in 3D-CFD in-cylinder simulations of spark-ignition engines: A methodology to correlate numerical results and experimental data". In: *International Journal of Engine Research* 24.5 (2023), pp. 2149–2174. DOI: 10.1177/14680874221112564 (cited on page 31).

Biagiotti, F. et al. "Modelling liquid film in modern GDI engines and the impact on particulate matter emissions – Part 1". In: *International Journal of Engine Research* 23.10 (2022), pp. 1634–1657. DOI: 10.1177/14680874211024476 (cited on pages 21, 22).

Bittner, J. D. and Howard, J. B. "Composition profiles and reaction mechanisms in a near-sooting premixed benzene/oxygen/argon flame". In: *Symposium (International) on Combustion* 18.1 (1981), pp. 1105–1116. DOI: 10.1016/S0082-0784(81)80115-4 (cited on page 14).

Blanquart, G., Pepiot-Desjardins, P., and Pitsch, H. "Chemical mechanism for high temperature combustion of engine relevant fuels with emphasis on soot precursors". In: *Combustion and Flame* 156.3 (2009), pp. 588–607. DOI: 10.1016/j.combustflame.2008.12.007 (cited on pages 15, 25, 26, 54, 69).

Bockhorn, H. *Soot Formation in Combustion: Mechanisms and Models*. Ed. by V. I. Toennies, F. P. Goldanskii, and J. P. Schafer. 59. Springer-Verlag, 1994. DOI: 10.1007/978-3-642-85167-4 (cited on pages 12, 13).

Böhm, H. et al. "The influence of pressure and temperature on soot formation in premixed flames". In: *Symposium (International) on Combustion* 22.1 (1989), pp. 403–411. DOI: https://doi.org/10.1016/S0082-0784(89)80047-5 (cited on page 12).

Bönig, M. et al. "Soot formating in premixed C2H4 flat flames at elevated pressure". In: *Symposium (International) on Combustion* 23.1 (1991), pp. 1581–1587. DOI: https://doi.org/10.1016/S0082-0784(06)80429-7 (cited on page 11).

Burton, T. et al. “A Data-Driven Greenhouse Gas Emission Rate Analysis for Vehicle Comparisons”. In: *SAE International Journal of Electrified Vehicles*. Vol. 12. 1. 2022, pp. 91–128. DOI: 10.4271/14-12-01-0006 (cited on page 3).

Cai, L., Ramalingam, A., Minwegen, H., Alexander Heufer, K., and Pitsch, H. “Impact of exhaust gas recirculation on ignition delay times of gasoline fuel: An experimental and modeling study”. In: *Proceedings of the Combustion Institute* 37.1 (2019), pp. 639–647. DOI: 10.1016/j.proci.2018.05.032 (cited on page 31).

Campos, D. “Estudio De Las Emisiones De Escape En Motores De Combustion Interna Alternativos Utilizando Diferentes Sistemas De Control De Contaminantes”. PhD thesis. Universitat Politècnica de València, 2016 (cited on pages 63, 66–68).

Carvallo, C. “Experimental study of the behavior of gasoline direct injection GDI sprays during wall impingement under realistic engine conditions.” PhD thesis. Universitat Politècnica de València, 2023 (cited on page 156).

Chen, L., Liang, Z., Zhang, X., and Shuai, S. “Characterizing particulate matter emissions from GDI and PFI vehicles under transient and cold start conditions”. In: *Fuel* 189 (2017), pp. 131–140. DOI: 10.1016/j.fuel.2016.10.055 (cited on pages 18, 21).

Christianson, M., Bardasz, E., and Nahumck, W. “Impact of lubricating oil condition on exhaust particulate matter emissions from light duty vehicles”. In: *SAE Technical Papers* 3.2 (2010), pp. 476–488. DOI: 10.4271/2010-01-1560 (cited on page 25).

Converge CFD v3.1. https://www.convergecfd.com/. Convergent Science Inc. 2022 (cited on page 50).

Conway, G., Joshi, A., Leach, F., García, A., and Senecal, P. K. “A review of current and future powertrain technologies and trends in 2020”. In: *Transportation Engineering* 5.May (2021). DOI: 10.1016/j.treng.2021.100080 (cited on page 4).

Costa, M., Sorge, U., and Allocca, L. “Numerical study of the mixture formation process in a four-stroke GDI engine for two-wheel applications”. In: *Simulation Modelling Practice and Theory* 19.4 (2011), pp. 1212–1226. DOI: 10.1016/j.simpat.2010.07.006 (cited on page 92).

D’Anna, A. “Combustion-formed nanoparticles”. In: *Proceedings of the Combustion Institute* 32.1 (2009), pp. 593–613. DOI: 10.1016/j.proci.2008.09.005 (cited on page 15).

De Petris, C., Giglio, V., and Police, G. "Some insights on mechanisms of oil consumption". In: *SAE Technical Papers* 412 (1996). DOI: 10.4271/961216 (cited on page 24).

Dec, J. E. "A conceptual model of di diesel combustion based on laser-sheet imaging". In: *SAE Technical Papers* (1997). DOI: 10.4271/970873 (cited on page 115).

DEKATI. *Model FPS-4000. Fine Smart Particle Sampler. User manual* (cited on page 65).

Del Pecchia, M. et al. "Development of a Sectional Soot Model Based Methodology for the Prediction of Soot Engine-Out Emissions in GDI Units". In: *SAE Technical Papers* 2020-April.April (2020). DOI: 10.4271/2020-01-0239 (cited on page 6).

Desantes, J. M., Pastor, J. V., Garcia-Oliver, J. M., and Pastor, J. M. "A 1D model for the description of mixing-controlled reacting diesel sprays". In: *Combustion and Flame* 156.1 (2009), pp. 234–249. DOI: 10.1016/j.combustflame.2008.10.008 (cited on page 96).

Dhir, D. "Nucleate and Transition Boiling Heat Transfer Under Pool and External Flow Conditions". In: *International Journal of Heat and Fluid Flow* 12.4 (1991), pp. 290–314. DOI: https://doi.org/10.1016/0142-727X(91)90018-Q (cited on page 164).

Dobbins, R. A. and Subramaniasivam, H. "Soot Precursor Particles in Flames". In: *Soot Formation in Combustion: Mechanisms and Models*. Ed. by Henning Bockhorn. Berlin, Heidelberg: Springer Berlin Heidelberg, 1994, pp. 290–299. DOI: 10.1007/978-3-642-85167-4_10 (cited on page 18).

Dong, Z., Shuai, S., Wang, Z., and Zhao, H. "CFD Modeling of Mixture Preparation and Soot Formation in a Downsized Gasoline Direct Injection Engine". In: *SAE Technical Paper* (2016). DOI: 10.4271/2016-01-0586 (cited on page 27).

Dukowicz, J. K. "A particle-fluid numerical model for liquid sprays". In: *Journal of Computational Physics* 35.2 (1980), pp. 229–253. DOI: 10.1016/0021-9991(80)90087-X (cited on page 150).

Edelman, R. B. and Harsha, P. T. "Laminar and turbulent gas dynamics in combustors-current status". In: *Progress in Energy and Combustion Science* 4.1 (1978), pp. 1–62. DOI: 10.1016/0360-1285(78)90010-2 (cited on page 27).

Environmental Protection Agency. *Multi-Pollutant Emissions Standards for Model Years 2027 and Later Light-Duty and Medium-Duty Vehicles*. Tech. rep. 2023 (cited on page 5).

Etheridge, J., Mosbach, S., Kraft, M., Wu, H., and Collings, N. "Modelling soot formation in a DISI engine". In: *Proceedings of the Combustion Institute* 33.2 (2011), pp. 3159–3167. DOI: 10.1016/j.proci.2010.07.039 (cited on pages 29, 30).

Etikyala, S. and Dahlander, P. "Soot Sources in Warm-Up Conditions in a GDI Engine". In: *SAE Technical Papers* (2021). DOI: 10.4271/2021-01-0622 (cited on page 116).

European Commission. *Euro 7 proposal from european commission*. Tech. rep. 2022 (cited on page 5).

Farron, C. et al. "Particulate characteristics for varying engine operation in a gasoline spark ignited, direct injection engine". In: *SAE World Congress and Exhibition* (2011). DOI: 10.4271/2011-01-1220 (cited on page 21).

Fischer, A. "Experimental and Numerical Investigation of Injector Tip Wetting in Modern Gasoline Engines as predecessor for particle emissions". PhD thesis. TU Graz, 2018. DOI: 10.51202/9783186807120-725 (cited on page 19).

Fontanesi, S., Del Pecchia, M., Pessina, V., Sparacino, S., and Di Iorio, S. "Quantitative investigation on the impact of injection timing on soot formation in a GDI engine with a customized sectional method". In: *International Journal of Engine Research* 23.4 (2022), pp. 624–637. DOI: 10.1177/1468087421993955 (cited on pages 30, 31).

French, W., Rose, D., Kelly-Zion, P., and Pursell, C. "Analysis of evaporating fuel films using shadowgraph and schlieren imaging techniques". In: *SAE Technical Papers* (2008). DOI: 10.4271/2008-01-2443 (cited on page 162).

Frenklach, M. "Method of moments with interpolative closure". In: *Chemical Engineering Science* 57.12 (2002), pp. 2229–2239. DOI: 10.1016/S0009-2509(02)00113-6 (cited on pages 28, 54).

Frenklach, M., Clary, D. W., Gardiner, W. C., and Stein, S. E. "Detailed kinetic modeling of soot formation in shock-tube pyrolysis of acetylene". In: *Symposium (International) on Combustion* 20.1 (1984), pp. 887–901. DOI: 10.1016/S0082-0784(85)80578-6 (cited on pages 14, 15).

Frenklach, M. and Harris, S. J. "Aerosol dynamics modeling using the method of moments". In: *Journal of Colloid And Interface Science* 118.1 (1987), pp. 252–261. DOI: 10.1016/0021-9797(87)90454-1 (cited on page 28).

Frenklach, M. and Wang, H. "Detailed modeling of soot particle nucleation and growth". In: *Symposium (International) on Combustion* 23.1 (1991), pp. 1559–1566. DOI: 10.1016/S0082-0784(06)80426-1 (cited on pages 14, 15).

Frenklach, M. and Wang, H. "Detailed Mechanism and Modeling of Soot Particle Formation". In: *Soot Formation in Combustion: Mechanisms and Models*. Ed. by Henning Bockhorn. Berlin, Heidelberg: Springer Berlin Heidelberg, 1994, pp. 165–192. DOI: 10.1007/978-3-642-85167-4_10 (cited on pages 15, 28).

Frommater, S. "Phenomenological modelling of particulate emissions in direct injection spark ignition engines for driving cycle simulations". PhD thesis. TU Darmstadt, 2018 (cited on pages 6, 62, 81, 104, 152, 155–157).

Frommater, S., Neumann, J., and Hasse, C. "A phenomenological modelling framework for particle emission simulation in a direct-injection gasoline engine". In: *International Journal of Engine Research* 22.4 (2021), pp. 1166–1179. DOI: 10.1177/1468087419895161 (cited on pages 33–35, 135, 166).

Gelbard, F. and Seinfeld, J. H. "Simulation of multicomponent aerosol dynamics". In: *Journal of Colloid And Interface Science* 78.2 (1980), pp. 485–501. DOI: 10.1016/0021-9797(80)90587-1 (cited on page 28).

Giovannoni, N. et al. "CFD Analysis of the Effects of Fuel Composition and Injection Strategy on Mixture Preparation and Fuel Deposit Formation in a GDI Engine". In: *SAE Technical Papers* 2015-September.September (2015). DOI: 10.4271/2015-24-2408 (cited on page 32).

Gong, J. and Rutland, C. "A quasi-dimensional NOx emission model for spark ignition direct injection (SIDI) gasoline engines". In: *SAE Technical Papers* (2013). DOI: 10.4271/2013-01-1311 (cited on page 104).

Goodwin, D. G., Moffat, H. K., Schoegl, I., Speth, R. L., and Weber, B. W. *Cantera: An Object-oriented Software Toolkit for Chemical Kinetics, Thermodynamics, and Transport Processes*. https://www.cantera.org. Version 3.0.0. 2023. DOI: 10.5281/zenodo.8137090 (cited on page 53).

Guido, C., Di Maio, D., Napolitano, P., and Beatrice, C. "Sub-23 particle control strategies towards Euro VII HD SI natural gas engines". In: *Transportation Engineering* 10 (2022), p. 100132. DOI: 10.1016/j.treng.2022.100132 (cited on pages 24, 25).

Guinther, G. and Smith, S. "Formation of Intake Valve Deposits in Gasoline Direct Injection Engines". In: *SAE International Journal of Fuels and Lubricants* 9.3 (2016), pp. 558–566. DOI: 10.4271/2016-01-2252 (cited on page 19).

Habchi, C. "Modeling fuel spray impingement on a hot wall for gasoline engines". In: *Oil and Gas Science and Technology* 65.2 (2010), pp. 331–343. DOI: 10.2516/ogst/2009062 (cited on pages 163–166).

Hageman, M. and Rothamer, D. "Sensitivity analysis of particle formation in a spark-ignition engine during premixed operation". In: *8th US National Combustion Meeting 2013* 1 (2013), pp. 500–514 (cited on page 23).

Haynes, B.S. and Wagner, H.Gg. "Soot formation". In: *Progress in Energy and Combustion Science* 7.4 (1981), pp. 229–273. DOI: https://doi.org/10.1016/0360-1285(81)90001-0 (cited on pages 11–13, 16).

He, X., Ratcliff, M. A., and Zigler, B. T. "Effects of gasoline direct injection engine operating parameters on particle number emissions". In: *Energy and Fuels* 26.4 (2012), pp. 2014–2027. DOI: 10.1021/ef201917p (cited on page 18).

He, X. et al. "Impact of coolant temperature on the combustion characteristics and emissions of a stratified-charge direct-injection spark-ignition engine fueled with E30". In: *Fuel* 309.September 2021 (2022). DOI: 10.1016/j.fuel.2021.121913 (cited on page 149).

Held, F., Reusch, J., Salenbauch, S., and Hasse, C. "A 3D computational study of the formation, growth and oxidation of soot particles in an optically accessible direct-injection spark-ignition engine using quadrature-based methods of moments". In: *Fuel Processing Technology* 254.February 2023 (2024). DOI: 10.1016/j.fuproc.2023.107923 (cited on page 6).

Herdman, J. D. and Miller, J. H. "Intermolecular potential calculations for polynuclear aromatic hydrocarbon clusters". In: *Journal of Physical Chemistry A* 112.28 (2008), pp. 6249–6256. DOI: 10.1021/jp800483h (cited on page 15).

Heywood, J. B. *Internal Combustion Engine Fundamentals*. New York: McGraw-Hill, 1988 (cited on pages 11, 15).

Hiroyasu, H. and Arai, M. "Structures of Fuel Sprays in Diesel Engines". In: *SAE Technical Paper* (1990). DOI: https://doi.org/10.4271/900475 (cited on page 150).

Hiroyasu, H. and Kadota, T. "Models for Combustion and Formation of Nitric Oxide and Soot in Direct Injection Diesel Engines." In: *SAE Prepr* 760129 (1976). DOI: 10.4271/760129 (cited on pages 27, 32).

Homann, K.H. "Carbon formation in Pre-Mixed flames". In: *Combustion and Flame* 11.4 (1967), pp. 265–287. DOI: https://doi.org/10.1016/0010-2180(67)90017-X (cited on page 16).

HORIBA MEXA 1230-PM. *Particle Matter Exhaust Gas Analyzer. HORIBA GmbH. user Manual* (cited on page 65).

Imaoka, Y., Hashizume, Y., Inoue, T., and Shiraishi, T. "A Study of Particulate Emission Formation Mechanism from Injector Tip in Direct-Injection Gasoline Engines". In: *SAE International Journal of Advances and Current Practices in Mobility* 2.1 (2020), pp. 376–384. DOI: 10.4271/2019-01-2244 (cited on pages 19, 20).

Jiao, Q. and Reitz, R. "Modeling of equivalence ratio effects on particulate formation in a spark-ignition engine under premixed conditions". In: *SAE Technical Papers* (2014). DOI: 10.4271/2014-01-1607 (cited on pages 23, 32, 74).

Jiao, Q. and Reitz, R. D. "Modeling soot emissions from wall films in a direct-injection spark-ignition engine". In: *International Journal of Engine Research* 16.8 (2015), pp. 994–1013. DOI: 10.1177/1468087414562008 (cited on page 32).

Jung, H., Kittelson, D. B., and Zachariah, M. R. "The influence of engine lubricating oil on Diesel nanoparticle emissions and kinetics of oxidation". In: *SAE Technical Papers* 724 (2003). DOI: 10.4271/2003-01-3179 (cited on page 24).

Kayes, D. and Hochgreb, S. "Mechanisms of particulate matter formation in spark-ignition engines. 1. Effect of engine operating conditions". In: *Environmental Science and Technology* 33.22 (1999), pp. 3968–3977. DOI: 10.1021/es981100w (cited on page 21).

Kennedy, I. M. "Models of soot formation and oxidation". In: *Progress in Energy and Combustion Science* 23.2 (1997), pp. 95–132. DOI: 10.1016/S0360-1285(97)00007-5 (cited on pages 27, 28).

Kennedy, I. M., Yam, C., Rapp, D. C., and Santoro, R. J. "Modeling and measurements of soot and species in a laminar diffusion flame". In: *Combustion and Flame* 107.4 (1996), pp. 368–382. DOI: 10.1016/S0010-2180(96)00092-2 (cited on page 28).

Khan, I.M., Greeves, G., and Probert, D.M. "Prediction of soot and nitric oxide concentrations in diesel engine exhaust". In: *Air Pollution Control in Transport Engines C* 142 (1971), pp. 205–217 (cited on page 27).

Kim, N., Vuilleumier, D., and Sjoberg, M. "Effects of Injection Timing and Duration on Fuel-Spray Collapse and Wall-Wetting in a Stratified Charge SI Engine". In: *SAE Technical Paper* (2021). DOI: 10.4271/2021-01-0544 (cited on page 18).

Kleeman, M. J., Riddle, S. G., Robert, M. A., and Jakober, C. A. "Lubricating oil and fuel contributions to particulate matter emissions from light-duty gasoline and heavy-duty diesel vehicles". In: *Environmental Science and Technology* 42.1 (2008), pp. 235–242. DOI: 10.1021/es071054c (cited on page 24).

Knop, V. and Essayem, E. "Comparison of PFI and DI operation in a downsized gasoline engine". In: *SAE International Journal of Engines*. Vol. 6. 2. 2013, pp. 941–952. DOI: 10.4271/2013-01-1103 (cited on page 17).

Kodavasal, J. et al. "An accelerated multi-zone model for engine cycle simulation of homogeneous charge compression ignition combustion". In: *International Journal of Engine Research* 14.5 (2013), pp. 416–433. DOI: 10.1177/1468087413482480 (cited on page 74).

Kong, S. C., Senecal, P. K., and Reitz, R. D. "Developments in spray modeling in diesel and direct-injection gasoline engines". In: *Oil and Gas Science and Technology* 54.2 (1999), pp. 197–204. DOI: 10.2516/ogst:1999015 (cited on page 51).

Kuhnke, D. "Spray wall interaction modelling by dimensionless data analysis". PhD thesis. Technische Universität Darmstadt, 2004 (cited on page 160).

Lacey, J. et al. "Generalizing the behavior of flash-boiling, plume interaction and spray collapse for multi-hole, direct injection". In: *Fuel* 200 (2017), pp. 345–356. DOI: 10.1016/j.fuel.2017.03.057 (cited on page 149).

Lahaye, J. "Mechanisms of soot formation". In: *Polymer Degradation and Stability* 30.1 (1990), pp. 111–121. DOI: 10.1016/0141-3910(90)90121-M (cited on page 17).

Lee, K. O., Seong, H., Sakai, S., Hageman, M., and Rothamer, D. "Detailed morphological properties of nanoparticles from gasoline direct injection engine combustion of ethanol blends". In: *11th International Conference on Engines & Vehicles*. Vol. 6. SAE International, 2013. DOI: 10.4271/2013-24-0185 (cited on page 21).

Leick, P., Bork, B., and Geiler, J. N. "Experimental characterization of tip wetting in gasoline DI injectors". In: *ICLASS 2018 - 14th International Conference on Liquid Atomization and Spray Systems* July (2018) (cited on pages 19, 130, 132).

Lenhert, D. B. and Manzello, S. L. "Effects of benzene and naphthalene addition on soot inception in a well-stirred reactor/plug flow reactor". In: *Proceedings of the Combustion Institute* 32.1 (2009), pp. 657–664. DOI: 10.1016/j.proci.2008.07.016 (cited on page 79).

Liang, L., Naik, C. V., Puduppakkam, K. V., Modak, A. U., and Meeks, E. "Application of Detailed Soot-Particle Model to Simulations of Fundamental Spray Experiments and GDI Engine". In: *International Multidimensional Engine Modeling User's Group Meeting* (2014) (cited on page 31).

Lindstedt, R. and Skevis, G. "Benzene Formation Chemistry in Premixed 1,3-Butadiene Flames". In: *Twenty-Sixth Symposium (International) on Combustion/The Combustion Institute* 26.1 (1996), pp. 703–709 (cited on page 14).

Mansurov, Z.A. "Soot formation in combustion processes (Review)". In: *Combustion, Explosion, and Shock Waves* 41.6 (2005), pp. 727–744. DOI: 10.1007/s10573-005-0083-2 (cited on page 11).

Manzello, S. L. et al. "Soot particle size distributions in a well-stirred reactor/plug flow reactor". In: *Proceedings of the Combustion Institute* 31.1 (2007), pp. 675–683. DOI: 10.1016/j.proci.2006.07.013 (cited on page 79).

Martinez, S., Merola, S., and Irimescu, A. "Flame front and burned gas characteristics for different split injection ratios and phasing in an optical GDI engine". In: *Applied Sciences* 9.3 (2019). DOI: 10.3390/app9030449 (cited on page 116).

McGraw, R. "Description of aerosol dynamics by the quadrature method of moments". In: *Aerosol Science and Technology* 27.2 (1997), pp. 255–265. DOI: 10.1080/02786829708965471 (cited on page 28).

Medina, M., Alzahrani, F. M., Fatouraie, M., Wooldridge, M. S., and Sick, V. "Mechanisms of fuel injector tip wetting and tip drying based on experimental measurements of engine-out particulate emissions from gasoline direct-injection engines". In: *International Journal of Engine Research* 22.6 (2021), pp. 2035–2053. DOI: 10.1177/1468087420916052 (cited on pages 19, 122).

Merker, G. P., Schwarz, C., and Teichmann, R. *Combustion Engines Development: Mixture Formation, Combustion, Emissions and Simulation*. Berlin, Heidelberg: Springer-Verlag, 2012. DOI: 10.1007/978-3-642-14094-5 (cited on page 155).

Miller, J. A. and Klippenstein, S. J. "The Recombination of Propargyl Radicals and Other Reactions on a C6H6 Potential". In: *Journal of Physical Chemistry A* 107.39 (2003), pp. 7783–7799. DOI: https://doi.org/10.1021/JP030375H (cited on page 14).

Moon, S., Choi, J., Abo-Serie, E., and Bae, C. "The effects of injector temperature on spray and combustion characteristics in a single cylinder DISI engine". In: *SAE Technical Papers* (2005). DOI: 10.4271/2005-01-0101 (cited on page 180).

Morgan, N. et al. "Mapping surrogate gasoline compositions into RON/MON space". In: *Combustion and Flame* 157.6 (2010), pp. 1122–1131. DOI: 10.1016/j.combustflame.2010.02.003 (cited on page 25).

Mueller, M. E., Blanquart, G., and Pitsch, H. "Hybrid Method of Moments for modeling soot formation and growth". In: *Combustion and Flame* 156.6 (2009), pp. 1143–1155. DOI: 10.1016/j.combustflame.2009.01.025 (cited on pages 15, 28).

Mueller, M.E., Blanquart, G., and Pitsch, H. "A joint volume-surface model of soot aggregation with the method of moments". In: *Proceedings of the Combustion Institute* 32.1 (2009), pp. 785–792. DOI: 10.1016/j.proci.2008.06.207 (cited on page 15).

Mundo, C., Sommerfeld, M., and Tropea, C. "Droplet-wall collisions: Experimental studies of the deformation and breakup process". In: *International Journal of Multiphase Flow* 21.2 (1995), pp. 151–173. DOI: 10.1016/0301-9322(94)00069-V (cited on page 159).

Naber, J. D. and Siebers, D. L. "Effects of gas density and vaporization on penetration and dispersion of diesel sprays". In: *SAE Technical Papers* (1996). DOI: 10.4271/960034 (cited on page 150).

Nagaoka, M., Kawazoe, H., and Nomura, N. "Modeling fuel spray impingement on a hot wall for gasoline engines". In: *SAE Technical Papers 940525* (1994). DOI: 10.4271/940525 (cited on page 163).

Napolitano, P., Di Maio, D., Guido, C., Merlone Borla, E., and Torbati, R. "Experimental investigation on particulate filters for heavy-duty natural gas engines: Potentialities toward EURO VII regulation". In: *Journal of Environmental Management* 331 (2023), p. 117204. DOI: 10.1016/j.jenvman.2022.117204 (cited on page 24).

National Research Council. *Cost, effectiveness, and deployment of fuel economy technologies for light-duty vehicles*. Washington, DC: The National Academies Press, 2015. DOI: 10.17226/21744 (cited on page 17).

Netzell, K., Lehtiniemi, H., and Mauss, F. "Calculating the soot particle size distribution function in turbulent diffusion flames using a sectional method". In: *Proceedings of the Combustion Institute* 31 I.1 (2007), pp. 667–674. DOI: 10.1016/j.proci.2006.08.081 (cited on pages 28, 31).

Ó Conaire, M., Curran, H. J., Simmie, J. M., Pitz, W. J., and Westbrook, C. K. "A comprehensive modeling study of hydrogen oxidation". In: *International Journal of Chemical Kinetics* 36.11 (2004), pp. 603–622. DOI: 10.1002/kin.20036 (cited on page 26).

O'Rourke, P. J. and Amsden, A. A. "The tab method for numerical calculation of spray droplet breakup". In: *SAE Technical Papers 872089* (1987). DOI: 10.4271/872089 (cited on page 152).

O'Rourke, P. J. and Amsden, A. A. "A spray/wall interaction submodel for the KIVA-3 wall film model". In: *SAE Technical Papers* (2000). DOI: 10.4271/2000-01-0271 (cited on page 160).

Panão, M. and Moreira, A. "Thermo- and fluid dynamics characterization of spray cooling with pulsed sprays". In: *Experimental Thermal and Fluid Science* 30 (2005), pp. 79–96. DOI: 10.1016/j.expthermflusci.2005.03.020 (cited on page 159).

Paredi, D. et al. "Validation of a comprehensive computational fluid dynamics methodology to predict the direct injection process of gasoline sprays using Spray G experimental data". In: *International Journal of Engine Research* 21.1 (2020), pp. 199–216. DOI: 10.1177/1468087419868020 (cited on page 150).

Park, J., Im, K. S., Kim, H., and Lai, M. C. "Characteristics of wall impingement at elevated temperature conditions on gdi spray". In: *International Journal of Automotive Technology* 5.3 (2004), pp. 155–164 (cited on page 159).

Park, S. W. and Lee, C. S. "Macroscopic and microscopic characteristics of a fuel spray impinged on the wall". In: *Experiments in Fluids* 37.5 (2004), pp. 745–762. DOI: 10.1007/s00348-004-0866-3 (cited on page 159).

Pastor, J. V., García-Oliver, J. M., Pastor, J. M., and Vera-Tudela, W. "One-dimensional diesel spray modeling of multicomponent fuels". In: *Atomization and Sprays* 25.6 (2015), pp. 485–517. DOI: 10.1615/AtomizSpr.2014010370 (cited on page 96).

Pastor, J. V., Lopez, J. J., Garcia-Oliver, J. M., and Pastor, J. M. "A 1D model for the description of mixing-controlled inert diesel sprays". In: *Fuel* 87.13-14 (2008), pp. 2871–2885. DOI: 10.1016/j.fuel.2008.04.017 (cited on pages 96, 97).

Pastor, J. V., Payri, R., Garcia-Oliver, J. M., and Nerva, J. G. "Schlieren measurements of the ECN-spray a penetration under inert and reacting conditions". In: *SAE Technical Papers*. 2012. DOI: 10.4271/2012-01-0456 (cited on page 96).

Patterson, R. I., Singh, J., Balthasar, M., Kraft, M., and Wagner, W. "Extending stochastic soot simulation to higher pressures". In: *Combustion and Flame* 145.3 (2006), pp. 638–642. DOI: 10.1016/j.combustflame.2006.02.005 (cited on page 60).

Patterson, R.I. and Celnik, M. *SWEEP2: Cambridge Soot Simulator*. http://como.cheng.cam.ac.uk. 2006 (cited on pages 59, 62).

Payri, F., Galindo, J., Martín, J., and Arnau, F. J. "A simple model for predicting the trapped mass in a DI diesel engine". In: *SAE Technical Papers* 2007.724 (2007). DOI: 10.4271/2007-01-0494 (cited on page 48).

Payri, F., Margot, X., Gil, A., and Martin, J. "Computational study of heat transfer to the walls of a DI diesel engine". In: *SAE Technical Papers* 2005.724 (2005). DOI: 10.4271/2005-01-0210 (cited on page 48).

Payri, F., Molina, S., Martín, J., and Armas, O. "Influence of measurement errors and estimated parameters on combustion diagnosis". In: *Applied Thermal Engineering* 26.2-3 (2006), pp. 226–236. DOI: 10.1016/j.applthermaleng.2005.05.006 (cited on page 48).

Payri, F., Olmeda, P., Martín, J., and García, A. "A complete 0D thermodynamic predictive model for direct injection diesel engines". In: *Applied Energy* 88.12 (2011), pp. 4632–4641. DOI: 10.1016/j.apenergy.2011.06.005 (cited on page 48).

Payri, R., Marti-Aldaravi, P., Abboud, R., and Bautista, A. "Numerical Analysis of GDI Flash Boiling Sprays Using Different Fuels". In: *Energies* (2021), pp. 1–23 (cited on page 150).

Pejpichestakul, W. et al. "Examination of a soot model in premixed laminar flames at fuel-rich conditions". In: *Proceedings of the Combustion Institute* 37.1 (2019), pp. 1013–1021. DOI: 10.1016/j.proci.2018.06.104 (cited on page 25).

Pirjola, L. et al. "Effects of fresh lubricant oils on particle emissions emitted by a modern gasoline direct injection passenger car". In: *Environmental Science and Technology* 49.6 (2015), pp. 3644–3652. DOI: 10.1021/es505109u (cited on page 24).

Pitz, W. J. et al. "Development of an experimental database and chemical kinetic models for surrogate gasoline fuels". In: *SAE Technical Papers* 2007.724 (2007), pp. 776–790. DOI: 10.4271/2007-01-0175 (cited on page 25).

Poling, B. E., Prausnitz, J. M., and O'Connell, J. P. *The Properties of Gases and Liquids*. Fifth Edit. New York: McGraw Hill, 2001 (cited on pages 104, 128, 129, 152, 163).

Prado, G. and Lahaye, J. "Physical Aspects of Nucleation and Growth of Soot Particles". In: *Particulate Carbon: Formation During Combustion*. Ed. by Donald C. Siegla and George W. Smith. Boston, MA: Springer US, 1981, pp. 143–175. DOI: 10.1007/978-1-4757-6137-5_6 (cited on page 16).

Price, P., Twiney, B., Stone, R., Kar, K., and Walmsley, H. "Particulate and hydrocarbon emissions from a spray guided direct injection spark ignition engine with oxygenate fuel blends". In: *SAE Technical Papers* 724 (2007), pp. 776–790. DOI: 10.4271/2007-01-0472 (cited on page 24).

Ranzi, E. et al. "Hierarchical and comparative kinetic modeling of laminar flame speeds of hydrocarbon and oxygenated fuels". In: *Progress in Energy and Combustion Science* 38.4 (2012), pp. 468–501. DOI: 10.1016/j.pecs.2012.03.004 (cited on page 25).

Reizer, E., Viskolcz, B., and Fiser, B. "Formation and growth mechanisms of polycyclic aromatic hydrocarbons: A mini-review". In: *Chemosphere* 291 (2022), p. 132793. DOI: 10.1016/j.chemosphere.2021.132793 (cited on pages 14, 15).

Renksizbulut, M. and Yuen, M. C. "Numerical Study of Droplet Evaporation in a High-Temperature Stream". In: *Journal of Heat Transfer* 105.2 (1983), pp. 389–397. DOI: 10.1115/1.3245591 (cited on page 153).

Revzan, K. L., Brown, N. J., and Frenklach, M. http://www.me.berkeley.edu/soot/. 1999 (cited on pages 55, 59, 83).

Richter, H. and Howard, J. B. "Formation of polycyclic aromatic hydrocarbons and their growth to soot-a review of chemical reaction pathways". In: *Progress in Energy and Combustion Science* 26.4 (2000), pp. 565–608. DOI: 10.1016/S0360-1285(00)00009-5 (cited on page 13).

Rivas Perea, M. E. "Assessment of fuel consumption reduction strategies on a gasoline turbocharged direct injection engine with a cooled EGR system". PhD thesis. Universitat Politècnica de València, 2016 (cited on pages 47, 48).

Sabathil, D., Koenigstein, A., Schaffner, P., Fritzsche, J., and Doehler, A. "The influence of DISI engine operating parameters on particle number emissions". In: *SAE World Congress and Exhibition*. 2011. DOI: 10.4271/2011-01-0143 (cited on pages 19–21).

Salenbauch, S. et al. "Modeling soot formation in premixed flames using an Extended Conditional Quadrature Method of Moments". In: *Combustion and Flame* 162.6 (2015), pp. 2529–2543. DOI: 10.1016/j.combustflame.2015.03.002 (cited on page 29).

Schug, K. P., Manheimer-Timnat, Y., Yaccarino, P., and Glassman, I. "Sooting Behavior of Gaseous Hydrocarbon Diffusion Flames and the Influence of Additives". In: *Combustion Science and Technology* 22.5-6 (1980), pp. 235–250. DOI: 10.1080/00102208008952387 (cited on page 13).

Seinfeld, J. H., Pandis, S. N., and Noone, K. "Atmospheric Chemistry and Physics: From Air Pollution to Climate Change". In: *Physics Today* 51.10 (1998), pp. 88–90. DOI: 10.1063/1.882420 (cited on page 56).

Senda, J. et al. "Measurement and modeling on wall wetted fuel film profile and mixture preparation in intake port of SI engine". In: *SAE Technical Papers* 724 (1999). DOI: 10.4271/1999-01-0798 (cited on page 159).

Short, D. Z., Vu, D., Durbin, T. D., Karavalakis, G., and Asa-Awuku, A. "Components of Particle Emissions from Light-Duty Spark-Ignition Vehicles with Varying Aromatic Content and Octane Rating in Gasoline". In: *Environmental Science and Technology* 49.17 (2015), pp. 10682–10691. DOI: 10.1021/acs.est.5b03138 (cited on page 24).

Shukla, B., Miyoshi, A., and Koshi, M. "Role of Methyl Radicals in the Growth of PAHs". In: *Journal of the American Society for Mass Spectrometry* 21.4 (2010), pp. 534–544. DOI: 10.1016/j.jasms.2009.12.019 (cited on page 14).

Singh, E. et al. "Particulate Matter Emissions in Gasoline Direct-Injection Spark-Ignition Engines: Sources, Fuel Dependency, and Quantities". In: *Fuel* 338.October 2022 (2023). DOI: 10.1016/j.fuel.2022.127198 (cited on pages 24, 31, 134).

Smith, G. P. et al. *http://www.me.berkeley.edu/gri_mech/*. Accessed on 2023-11-06 (cited on page 26).

Smith, O.I. "Fundamentals of soot formation in flames with application to diesel engine particulate emissions". In: *Progress in Energy and Combustion Science* 7:4 (1981). DOI: 10.1016/0360-1285(81)90002-2 (cited on pages 11, 14, 16).

Sonntag, D. B., Bailey, C. R., Fulper, C. R., and Baldauf, R. W. "Contribution of lubricating oil to particulate matter emissions from light-duty gasoline vehicles in Kansas City". In: *Environmental Science and Technology* 46.7 (2012), pp. 4191–4199. DOI: 10.1021/es203747f (cited on page 24).

Stanton, D. W., Lippert, A.M., Reitz, R. D., and Rutland, C. "Influence of spray-wall interaction and fuel films on cold starting in direct injection diesel engines". In: *SAE Technical Papers 982584* (1998). DOI: 10.4271/982584 (cited on page 159).

Stevens, E. and Steeper, R. "Piston wetting in an optical DISI engine: Fuel films, pool fires, and soot generation". In: *SAE Technical Papers* 2001.724 (2001). DOI: 10.4271/2001-01-1203 (cited on page 19).

Tan, J. Y., Bonatesta, F., Ng, H. K., and Gan, S. "Developments in computational fluid dynamics modelling of gasoline direct injection engine combustion and soot emission with chemical kinetic modelling". In: *Applied Thermal Engineering* 107 (2016), pp. 936–959. DOI: 10.1016/j.applthermaleng.2016.07.024 (cited on page 27).

Tan, J. Y., Bonatesta, F., Ng, H. K., and Gan, S. "Numerical Investigation of Particulate Matter Processes in Gasoline Direct Injection Engines through Integrated Computational Fluid Dynamics-Chemical Kinetic Modeling". In: *Energy and Fuels* 34.4 (2020), pp. 4909–4924. DOI: 10.1021/acs.energyfuels.9b03945 (cited on pages 23, 30).

Tesner, P. A., Smegiriova, T. D., and Knorre, V. G. "Kinetics of dispersed carbon formation". In: *Combustion and Flame* 17.2 (1971), pp. 253–260. DOI: 10.1016/S0010-2180(71)80168-2 (cited on page 27).

Thomson, M. J. "Modeling soot formation in flames and reactors: Recent progress and current challenges". In: *Proceedings of the Combustion Institute* 39.1 (2023), pp. 805–823. DOI: 10.1016/j.proci.2022.07.263 (cited on pages 25, 26).

Torregrosa, A. J., Olmeda, P., Martín, J., and Romero, C. "A tool for predicting the thermal performance of a diesel engine". In: *Heat Transfer Engineering* 32.10 (2011), pp. 891–904. DOI: 10.1080/01457632.2011.548639 (cited on page 48).

Tree, D. R. and Svensson, K. I. "Soot processes in compression ignition engines". In: *Progress in Energy and Combustion Science* 33.3 (2007), pp. 272–309. DOI: 10.1016/j.pecs.2006.03.002 (cited on page 16).

TSI. *Engine Exhaust Particle Sizer Spectrometer Model 3090 Spec Sheet.* (Cited on page 67).

TSI. *Model DCS-100. Diffusion charging sensor. Operation and Service Manual* (cited on page 65).

TSI. *Model EEPS-3090. Engine Exhaust Particle Sizer Spectrometer. Operation and Service Manual.* (Cited on page 66).

U.S. Energy Information Administration. *International Energy Outlook 2023.* Tech. rep. 2023 (cited on pages 1–3, 5).

United Nations, Department of Economic and Social Affairs, Population Division. *World Population Prospects 2022: Summary of Results*. Tech. rep. 2022 (cited on page 1).

Vasudev, A., Mikulski, M., Balakrishnan, P. R., Storm, X., and Hunicz, J. "Thermo-kinetic multi-zone modelling of low temperature combustion engines". In: *Progress in Energy and Combustion Science* 91 (2022), p. 100998. DOI: 10.1016/j.pecs.2022.100998 (cited on page 73).

Vishwanathan, G. and Reitz, R. D. "Development of a practical soot modeling approach and its application to low-temperature diesel combustion". In: *Combustion Science and Technology* 182.8 (2010), pp. 1050–1082. DOI: 10.1080/00102200903548124 (cited on page 32).

Vuilleumier, D. and Sjöberg, M. "The Use of Transient Operation to Evaluate Fuel Effects on Knock Limits Well beyond RON Conditions in Spark-Ignition Engines". In: *SAE Technical Paper*. 2017. DOI: 10.4271/2017-01-2234 (cited on page 117).

Wallesten, J., Lipatnikov, A., and Chomiak, J. "Simulations of Fuel / Air Mixing , Combustion , and Pollutant Formation in a Direct Injection Gasoline Engine". In: *SAE Technical Paper Series* (2002) (cited on page 29).

Wang, B. et al. "Modelling soot formation from wall films in a gasoline direct injection engine using a detailed population balance model". In: *Applied Energy* 163 (2016), pp. 154–166. DOI: 10.1016/j.apenergy.2015.11.011 (cited on pages 29, 162).

Wang, E. and Ding, J. "Reaction between the i-C4H5 radical and propargyl radical (C3H3): A theoretical study". In: *Chemical Physics Letters* 768 (2021), p. 138407. DOI: 10.1016/j.cplett.2021.138407 (cited on page 14).

Wang, Y., Raj, A., and Chung, S. H. "A PAH growth mechanism and synergistic effect on PAH formation in counterflow diffusion flames". In: *Combustion and Flame* 160.9 (2013), pp. 1667–1676. DOI: 10.1016/j.combustflame.2013.03.013 (cited on page 25).

Warnatz, J., Mass, U., and Dibble, R.W. *Combustion: Physical and Chemical Fundamentals, Modeling and Simulation, Experiments, Pollutant Formation*. Springer Berlin Heidelberg New York, 2006 (cited on page 12).

Weiner, A. M. and Harris, S. J. "Optical detection of large soot precursors". In: *Combustion and Flame* 77.3-4 (1989), pp. 261–266. DOI: 10.1016/0010-2180(89)90133-8 (cited on page 15).

Weiss, C. "The liquid deposition fraction of sprays impinging vertical walls and flowing films". In: *International Journal of Multiphase Flow* 31.1 (2005), pp. 115–140. DOI: 10.1016/j.ijmultiphaseflow.2004.08.004 (cited on page 159).

Welty, J., Rorrer, G., and Foster, D. *Fundamentals of momentum, heat, and mass transfer*. Sixth Edit. New Jersey: John Wiley & Sons, 2001 (cited on page 163).

Woods, P. M., Millar, T. J., Zijlstra, A. A., and Herbst, E. "The Synthesis of Benzene in the Proto–planetary Nebula CRL 618". In: *The Astrophysical Journal* 574.2 (2002), pp. L167–L170. DOI: 10.1086/342503 (cited on page 14).

Wu, S., Zhou, D., and Yang, W. "Implementation of an efficient method of moments for treatment of soot formation and oxidation processes in three-dimensional engine simulations". In: *Applied Energy* 254.July (2019). DOI: 10.1016/j.apenergy.2019.113661 (cited on page 6).

Yakhot, V. and Orszag, S. "Renormalization group analysis of turbulence. I. Basic theory". In: *Journal of scientific computing* 1.1 (1986), pp. 3–51. DOI: 10.1007/BF01061452 (cited on page 51).

Yuan, C. and Fox, R. O. "Conditional quadrature method of moments for kinetic equations". In: *Journal of Computational Physics* 230.22 (2011), pp. 8216–8246. DOI: 10.1016/j.jcp.2011.07.020 (cited on page 29).

Yuan, C., Laurent, F., and Fox, R. O. "An extended quadrature method of moments for population balance equations". In: *Journal of Aerosol Science* 51 (2012), pp. 1–23. DOI: 10.1016/j.jaerosci.2012.04.003 (cited on page 29).

Zeng, W., Xu, M., Zhang, G., Zhang, Y., and Cleary, D. J. "Atomization and vaporization for flash-boiling multi-hole sprays with alcohol fuels". In: *Fuel* 95 (2012), pp. 287–297. DOI: 10.1016/j.fuel.2011.08.048 (cited on page 149).

Zhang, F. et al. "Formation of the phenyl radical [C6H5(X 2A1)] under Single collision conditions: A crossed molecular beam and ab initio study". In: *Journal of the American Chemical Society* 132.8 (2010), pp. 2672–2683. DOI: 10.1021/ja908559v (cited on page 14).

Zhao, F., Lai, M. C., and Harrington, D. L. "Automotive spark-ignited direct-injection gasoline engines". In: *Progress in Energy and Combustion Science* 25.5 (1999), pp. 437–562. DOI: 10.1016/S0360-1285(99)00004-0 (cited on page 17).

Zuo, B., Gomes, A. M., and Rutland, C. J. “Modelling superheated fuel sprays and vaproization”. In: *International Journal of Engine Research* 1.4 (2000), pp. 321–336. DOI: 10.1243/1468087001545218 (cited on page 151).